NON-LINEAR DYNAMIC EXTENSION OF CONSISTENT SHELL

ELEMENT AND ANALYSES OF LIQUID-FILLED CONICAL TANKS

by

ASHRAF EL DAMATTY, B.Sc., M.Sc.

A Thesis

Submitted to the School of Graduate Studies

in Partial Fulfilment of the Requirements

for the Degree

Doctor of Philosophy

McMaster University

Hamilton, Ontario, Canada

March 1995

TO MY DEAR WIFE

DINA

DOCTOR OF PHILOSOPHY (1992)   McMASTER UNIVERSITY
(Civil Engineering)   Hamilton, Ontario

TITLE   : Non-Linear Dynamic Extension of Consistent Shell Element and Analyses
      of Liquid-Filled Conical Tanks

AUTHOR : Ashraf El Damatty,   B.Sc. (CAIRO UNIVERSITY)
               M.Sc. (CAIRO UNIVERSITY)

SUPERVISORS : Dr. R.M.Korol and Dr.F.A.Mirza

NUMBER OF PAGES : xxiii, 248

ABSTRACT

Conical steel shells are fairly widely used as elevated water tanks. However, the current code of practice in North America for the design of such reservoir structures provides an obsolete method for ascertaining their adequacy to resist hydrostatic loadings. Moreover, there are no provisions available for handling liquid-filled conical tanks subjected to seismic forces. The lack of appropriate design methods could not have been demonstrated more vividly when in December of 1990, an elevated conical water tower failed by buckling when being filled for the first time. The steel vessel, located in Fredericton, New Brunswick, is claimed to have "exploded" by eyewitnesses.

The work of this thesis, then, was motivated by this failure. It involves non-linear stability analysis of liquid-filled conical steel vessels possessing geometric imperfections and residual stresses, and which can be subjected to hydrostatic and seismic loading. To achieve this, a finite element formulation is developed based on a consistent shell element which is free from spurious shear modes known to exist in the isoparametric shell elements. The consistent shell element employed also exhibits excellent performance in the analysis of plates and shells in the small displacement range. This element is extended to include both geometric and material non-linearities as well as non-linear dynamic analysis. The non-linear finite element model developed is general and can be applied to any thin or thick shell problem. Numerical testing of the non-linear model through static and dynamic analysis of different plate and shell problems indicates the continued

excellent performance of the consistent shell element in the non-linear range.

Hydrostatically loaded conical steel vessels are modelled using the consistent shell element. Static stability analyses of conical shells with different geometric imperfection patterns are undertaken and the results indicate that the presence of axisymmetric imperfections leads to the lowest limit load for the structure. The sensitivity of the hydrostatically loaded conical vessels to geometric imperfections and residual stresses is investigated by considering three cases: (i) analysis of perfect vessels, (ii) same as case (i) but with axisymmetric geometric imperfections of the order of the thickness of the shell, (iii) same as case (ii) but with the addition of residual stresses due to welding. The results from these analyses indicate that the liquid-filled conical shells are significantly sensitive to geometric imperfections, and that yielding precedes elastic buckling for tanks having practical dimensions.

The non-linear dynamic (stability) analysis of elevated liquid-filled conical vessels subjected to both horizontal and vertical accelerations, but free from rocking motion, is then considered. The boundary integral method is used to formulate the fluid added-mass matrix resulting from the impulsive component of the hydrodynamic pressure. This is added to the mass matrix of the shell structure to perform free vibration as well as non-linear time history analyses for elevated liquid-filled conical tanks treated as either perfect or axisymmetrically imperfect. Tanks with different dimensions and imperfection levels are subjected to an appropriately scaled real input ground motion. Some of these

v

elevated structures exhibit inelastic behaviour and generally develop a localized buckle near the bottom of the vessel which leads to the overall instability of the structure. In general, time history analyses indicate that liquid-filled conical tanks, often possessing apparently adequate safety factors under hydrostatic loading, may not be safe under seismic loading. Therefore, a proper modelling procedure along with time dependent analysis must be followed in order to design such tanks safely. The finite element model developed in this thesis is a means provided for such a purpose.

ACKNOWLEDGEMENT

I would like to express my sincere appreciation to my research supervisors, Dr. F. A. Mirza and Dr. R. M. Korol for their valuable guidance and encouragement throughout the course of this thesis. It has been a privilege and a pleasure to work under their supervision.

I am greatly indebted to Dr. J. C. Wilson and Dr. D. S. Weaver, the other members of my supervisory committee, for their valuable comments and suggestions and also their time in reviewing this thesis.

My personal involvement with the study would not have been possible without the financial support of McMaster University, the Natural Sciences and Engineering Council of Canada and the Ontario Graduate Council.

I would like to express special thanks to my friends and colleagues Mr. M. El Attar and Mr. A. Biddah for their great effort helping in preparing the figures in this thesis.

Finally, to my father, mother and brother Mohamed whom their guidance and moral support made this work possible, my very special thanks.

This thesis is dedicated to my wife Dina and my daughter May for their great sacrifices during the period of this study.

TABLE OF CONTENTS

LIST OF TABLES

LIST OF FIGURES

LIST OF SYMBOLS

All symbols are defined at their first appearance

The principal symbols used are listed below:

x, y, z $\quad\quad\quad$ = Global cartesian coordinates

r, s, t $\quad\quad\quad$ = Curvilinear coordinates

x', y', z' $\quad\quad$ = Local cartesian coordinates

ΔV_n, ΔV_n, ΔW_n $\quad$ = Incremental displacement degrees of freedom

$\Delta \alpha_n$, $\Delta \beta_n$, $\Delta \phi_n$, $\Delta \psi_n$ = Incremental rotational degree of freedom

N_n, $\bar{N}_n$ $\quad\quad$ = Quadratic and cubic interpolation functions

M_{1n}, M_{2n} $\quad\quad$ = Through thickness interpolation functions

v_{1n}, v_{2n}, v_{3n} $\quad$ = consistent shell element nodal unit vectors

h_n $\quad\quad\quad\quad$ = Thickness of the shell at node n

$[\theta]$ $\quad\quad\quad\quad$ = Transformation matrix relating local axes x', y' and z' to

$\quad\quad\quad\quad\quad\quad$ global axes x, y and z

l_{ij}, i=1,3 and j=1,2 = Direction cosines

S_{ij} $\quad\quad\quad\quad$ = Second Piola-Kirchhoff stress tensor

ϵ_{ij} $\quad\quad\quad\quad$ = Green-Lagrangian strain tensor

$[K_L]$ $\quad\quad\quad$ = Sum of the linear and the initial strain stiffness matrices

$[K_\sigma]$ $\quad\quad\quad$ = Initial stress stiffness matrix

$\{F\}$ $\quad\quad\quad$ = Unbalanced load vector

$\{R\}$	= External Load vector
$[D']$	= Elasticity matrix in local coordinate system
E, ν	= Elastic modulus and poisson's ratio
$[D_p']$	= Inelastic constitutive matrix in local coordinate system
r_1	= Radius at the base of the cone
h	= Height of the cone
θ_v	= Angle of inclination of the generator of the cone with the vertical
t	= Thickness of the cone
l_r	= Wave length of the buckle adjoining the base of the cone
S	= Distance measured along the generator of the cone
w_o	= Amplitude of the imperfection wave
p	= Static load factor
p_{cr}	= Critical static load factor
$[M_s]$	= Mass matrix of the shell
$[K^*]$	= Effective stiffness matrix
$[C]$	= Damping matrix
P_d	= Hydrodynamic pressure
P_s	= Convective component of the hydrodynamic pressure
P_I	= Impulsive component of the hydrodynamic pressure
$H_{in}(r, \theta, z)$	= Shape functions of the hydrodynamic pressure
$A_{in}(T), B(T)$	= Amplitude functions of the hydrodynamic pressure

[DM]	= Fluid added-mass matrix
[DM]$_H$	= Fluid added-mass matrix resulting from the horizontal ground accelerations
[DM]$_v$	= Fluid added-mass matrix resulting from the vertical ground accelerations
[M]	= Effective mass matrix
[K$_{Tan}$]	= Tangential stiffness matrix
a$_H^T$	= Horizontal component of the ground acceleration at time T
a$_v^T$	= Vertical component of the ground acceleration at time T
K$_h$	= Stiffness of the horizontal spring simulating the supporting frames
K$_v$	= Stiffness of the vertical spring simulating the supporting frame

CHAPTER ONE

INTRODUCTION

.

1-1 Motivation of the Study

Conical steel tanks with cylindrical upper section caps are widely used as containment vessels for elevated water tower structures. A typical cross section of an elevated conical tank is shown in Figure 1.1 where the conical steel vessel is typically welded to a steel circular plate at its bottom, with the latter anchored to a reinforced concrete slab which in turn is supported by a reinforced concrete tower. The steel vessel is normally constructed from cylindrical panels, butt welded together along circumferential and longitudinal edges.

In December 1990, a conical shape water tower built in Fredericton, New Brunswick, Canada, failed when it was filled with water for the first time. As reported by Korol (1991) and then by Dawe (1993), the failure of the tank was due to the buckling of the wall of the steel vessel as a result of inadequate thickness for the shell. Current standards of practice for water containment structures in North America are generally based on the AWWA D-100 (1984) specification. Unfortunately, this code does not provide a rational and up-to-date design methodology for these types of structures. A consequence of this shortfall in appropriate guideline information may have played a role in the demise of the failed structure. The designer of the Fredericton tank relied on

a formula for the buckling strength of axially compressed and internally pressurized closed conical vessels given in Roark and Young (1989), obviously for a different loading type from the case of hydrostatically loaded shell. In addition, the design formula given in Roark and Young (1989) assumes that the conical shell has a near perfect shape as might be expected in the aerospace industry. It neither takes into account the geometric imperfections of a large civil engineering type of structure, nor the residual stresses due to welding. Clearly, there is also the issue of tolerance limits, which are usually more restrictive in the aerospace engineering sector than in civil engineering construction due to cost factors. As such, it seemed imperative that an extensive research investigation be undertaken to study the stability of liquid-filled conical tanks which have both geometric imperfections and residual stresses due to on site welding. Although the Fredericton tank failed under static conditions, it was also decided to incorporate a seismic analysis of elevated liquid-filled conical tanks to broaden the scope of the project. This is important when attempting a rational design in a seismically active region.

1-2 Current Codes of Practice for Design of Liquid-Filled Conical Tanks

The current codes of practice for the design of water structures do not directly specify the design rules for liquid-filled conical tanks. Some European codes, like the Danish standards DNV (1982) and the German code DAST (1980), as well as the industrial standards in North America based on the AWWA D-100 (1984) specifications suggest the use of an equivalent cylinder when studying the stability of conical tanks subject to hydrostatic pressure. According to these codes, the safety of liquid-filled conical vessels against instability can be checked by calculating the compressive strength

of an equivalent cylinder which is then compared to the maximum compressive stresses induced in the liquid-filled conical shell. These design methods, although simple, are not based on any rational experimental or analytical studies. Recently, the European recommendations related to shell buckling, published by the Convention for Constructional Steel Work (1988), incorporated some design equations based on an extensive experimental investigation of buckling of small scale conical shells filled with liquids (Vandepitte et al.,1982). While the current codes of practice provide some suggestions for the design of conical tanks against hydrostatic forces, there is no proposed method for handling earthquake-type loads.

1-3 Literature Review

1-3-1 Shell Elements and Geometric Non-Linearities

It is decided to use the finite element method to study the stability of liquid-filled conical tanks under static and seismic loads. Of course, this involves the choice of a suitable finite element to model the shell structures. A survey of shell elements in the literature shows that a considerable number of these have been developed since the late sixties. Such shell finite elements can be categorized according to the basic concepts used in the formulation; (i) shell elements based on membrane and bending actions, (ii) the degenerated shell elements derived from a three dimensional continuum, (iii) transitional finite element, (iv) stress, mixed and hybrid elements. A complete survey of shell elements is given by Gilewski and Radwanska (1991) and Mackerie (1993).

The degenerated shell elements obtained from a three dimensional continuum

represent a simple and general approach to solve plate and shell problems. The simplicity of this category of shell elements arises from the fact that it requires only C_o continuity. This simplicity has great merit when dealing with non-linear problems. The idea of the degenerated shell element was first introduced by Ahmad et al. (1970) through the eight and the nine node shell elements which are based on the Mindlin plate bending theory (1951). These elements resulted in overly stiff solutions when used to model thin plates and shells. Meanwhile, the predicted transverse shear stresses were found to be very large for both thin and thick plates and shells with arbitrary magnitudes. This behaviour is also referred to as the "locking phenomena", and is actually due to the presence of spurious transverse shear modes in the elements formulation. To overcome these problems, a reduced integration technique was proposed by Zeinkiewicz et al. (1971) which employs a lower order integration scheme to integrate the stiffness matrix. As reported by Parish, (1979), the use of the reduced integration technique leads to the presence of zero energy modes different from the rigid body modes which the elements have to produce. Different attempts have been made to suppress these zero energy modes as given by Briassoulis (1988), Belytschko et al. (1989) and Vu-Quoc and Mora (1989). None of these methods have been successful in their general applications. Furthermore, these are usually complicated, hard to implement and their accuracy in the non-linear range is highly doubtful.

A consistent subparametric triangular shell element has been recently formulated by Koziey (1993). One of the main features of this shell element is that it is free from

the spurious shear modes associated with the isoparametric shell elements. This has been achieved by approximating displacements using the cubic interpolation functions, while the rotations are approximated by the quadratic shape functions. The consistent element consists of thirteen nodes, ten nodes of which are used to achieve a complete cubic polynomial for the displacements, and six nodes are used to obtain a complete quadratic polynomial for the rotations. The geometry of the shell is interpolated quadratically, therefore, the element is subparametric. Another specific feature of this shell element is that it includes special rotational degrees of freedom which lead to cubic variation of the displacements through the thickness of the shell. As such, the quadratic distribution of the transverse shear stress can be accurately represented by the element and hence, the shear correction factor κ is not needed. In fact, these special rotational degrees of freedom are important when modelling thick plates or shells where the shear deformation is significant. The small displacement formulation of this element was presented by Koziey (1993), where a convergence study was carried out showing the excellent performance of the element. The behaviour of a number of plates and shells using the consistent shell element was presented in the same study and compared to those available in the literature proving its superior performance in the small displacement range. In the present study, the task has been undertaken to extend the formulation of this element to include geometric non-linearities as well as non-linear dynamic analysis. Once these are included in the formulation, together with an appropriate plasticity model for steel, the non-linear stability analysis for conical steel tanks under static or seismic loading can be

undertaken. It should be mentioned that the special rotational degrees of freedom which provide a cubic variation of the displacement through the thickness might not be important when studying the performance of thin conical vessels. However, the non-linear formulation of the element is kept general and includes these degrees of freedom, so that it can be applied for the non-linear static and dynamic analysis for both thin and thick shells. A detailed description about the large displacement formulation and the non-linear dynamic analysis using the finite element method in general can be found in Bathe (1982).

1-3-2 Stability of Liquid-Filled Conical Tanks

Several studies concerning the stability of conical shells under different load combinations have been reported in research conducted in the field of aerospace engineering. However, none of these studies dealt with hydrostatically loaded conical tanks. The first known attempt to estimate the buckling strength of a simply supported cone under compressive force was conducted by Seide (1956). This analysis predicted that the buckling load of the cone is the same as that of a cylinder having a thickness equal to the projection of the cone thickness in a plane perpendicular to the longitudinal axis of the cone. The elastic stability analysis of conical shells under combined internal pressure and the axial compressive force was also investigated by Seide et al. (1965). The increase in buckling strength due to the stabilizing effect of the internal pressure was obtained analytically and then verified by a number of tests. It should be noted that the formulae for buckling of internally pressurized conical tanks, which were used by the

designer of the failed Fredericton tank, and were incorporated in Roark and Young (1989), are based on the work of Seide et al. (1965).

The most relevant research investigation concerning the stability of hydrostatically loaded conical tanks was conducted at Ghent University in Belgium, after the collapse of a conical steel water tower. An extensive experimental study was carried out by Vandepitte et al. (1982), in which hundreds of model cones were tested. The imperfection shapes existing in the cones were determined before loading. The cones were classified as "good" or "poor" according to their imperfection level. The model cones were filled with water until they collapsed and the height of water at which each model buckles was detected. A numerical study restricted to the elastic stability of the perfect cones was also conducted in the same study using a large displacement finite difference analysis. Based on a lower bound of the test results, design curves were suggested for hydrostatically loaded cones having different imperfection levels. As was mentioned by Vandepitte et al. (1982), the suggested design curves are applicable under the assumption that the behaviour of the vessel is purely elastic. Also noteworthy is the method of construction of the models tested by Vandepitte et al. (1982). This includes only one longitudinal seam, which is quite different from the method of construction of conical vessels in practice which includes longitudinal and circumferential welding of cylindrical panels. As such, the imperfection patterns in the models reported by Vandepitte et al. are different from those expected in practice.

A stability analysis of a liquid-filled conical vessel, clamped at its base, was

carried out by Bornscheuer et al.(1983) using a degenerated shell element to model the vessel. The investigation shows that the axisymmetric imperfections have a larger effect in reducing the buckling strength of the structure than do the non-axisymmetric ones. Their study also shows that by including an elasto-plastic material model, yielding precedes the elastic buckling resulting in an inelastic limit load for the cone. As stated by the author, additional studies are needed to generalize the above statements.

Recently, an investigation of the collapse of the Fredericton tank has been carried out by Dawe et al. (1993), which involves an assessment of different components of the structure. According to the National Building Code of Canada NBCC (1990) and the Canadian Portland Cement Association CAN3-A23.3 (1985), the foundation, the reinforced concrete supporting shaft and the floor slab have been found to be safe. The thickness of the storage vessel has also been checked and evaluated according to the different practical guidelines presented in Section 1-1-2. The predicted factors of safety for the storage vessel have been found to be all less than unity. Therefore, it has been concluded that the collapse was a buckling failure in the lower cone of the tank due to inadequate thickness.

1-3-3 Geometric Imperfections and Residual Stresses due to Welding

Geometric imperfections have been identified as the main cause of the large discrepancies between the experimental and the theoretical buckling or limit loads for both cylindrical and conical shells subjected to either pure compression, or a combination of compressive force and an internal pressure. It has been observed experimentally that

the higher the internal pressure, the less sensitive is the shell to geometric imperfections.

Early work on imperfect cylindrical shells was done by Koitter (1963). This study assumed an imperfection in the form of the axisymmetric first buckling mode of the cylinder under pure compression. Subsequently, an asymptotic relation for buckling loads of imperfect cylinders was derived. Localized imperfections were considered by Hutchinson et al. (1971) and Amazigo and Budiansky (1972); their conclusion was that a dimple-type profile superimposed onto the perfect shape would cause a lesser amount of reduction in the buckling load of cylinders having an imperfection wave similar to the first buckling mode extending over the entire length. Recently, attempts have been made to obtain realistic patterns of imperfection in aerospace structures. As far as is known, two initial imperfection data banks exist, one at Delft University of Technology prepared by Arbocz and Abramovich (1979), and the other at the Technion in Haifa given by Singer et al (1978). It should be noted here that such imperfection data are representative of small shells and depend on the method of construction of these shells. Therefore, these data banks are not applicable to liquid-filled conical tanks. In civil engineering construction, silos and tanks are constructed from rolled steel plates which are joined together by longitudinal and circumferential welding. Bornsheuer and Hafner (1983) made some measurements to investigate the shape adjacent to a circumferential weld and concluded that the weld joint depressions occurring in practice are of the order of one wall thickness. Rotter and Tang (1989) modelled the axisymmetric weld depression by two different shapes which represent the upper and lower bounds for the expected

depression. However, their model has not been verified through field measurements.

Conical steel vessels are usually constructed from steel cylindrical panels welded together using circumferential and longitudinal welds. Residual stresses are expected as a result of the welding process. These stresses develop due to the cooling of the weldments and heat affected zones of the parent material. During this cooling, the welds tend to shrink while the material remote from the weldments remains cool and prevents shrinkage. This process introduces tensile stresses in the vicinity of the weld zone and compressive stresses away from the weld. Based on some experimental results, the residual stress distribution around a weldment in a cylindrical shell was idealized by Bornscheuer and Hafner (1983) using three different mathematical models. With some modifications, one of these models is used in the present study to represent the expected residual stresses arising from welded conical shells. Furthermore, the lack of geometric imperfection data for large civil engineering steel shell structures necessitated selecting a suitable model without reasonable undue complexity. As such, it has been decided to take Koitter's approach in this study, and to assume imperfection shapes having the same wave length as that of the first buckling mode of the perfect shell. This assumption is expected to result in a conservative estimate of the actual buckling or limit load for the structure.

1-3-4 Seismic Analysis of Liquid-Filled Conical Tanks

A large number of studies concerning the seismic analysis and design of liquid-filled cylindrical tanks can be found in the literature. The performance of cylindrical

tanks during actual earthquakes was recorded in a number of investigations, e.g. Niwa and Clough (1982), Manos and Clough (1985) and Manos et al. (1989). One of the common forms of damage found to occur in cylindrical tanks after a seismic event is buckling of the walls of such cylindrical shells near their bases. This phenomenon was described as "elephant foot buckling" because the buckling was found to be localized in a shape having such an appearance. This localized instability is mainly due to the overturning moment which is exerted by the hydrodynamic pressure resulting from the horizontal component of an earthquake motion. Early analytical work concerning the evaluation of the hydrodynamic pressure developed inside such tanks was conducted by Housner (1955). In this study, the hydrodynamic pressure was divided into two components; the impulsive component resulting from the movement of the walls of the tank, and the convective component due to the surface wave developing at the top of the tank. Assuming that its walls are rigid, a mechanical model representing both components of the fluid's hydrodynamic pressure was developed for different shapes of the container. Based on Housner's model, the typical procedure for designing cylindrical tanks has usually been to first estimate the maximum overturning moment induced by the components of the model due to a horizontal ground acceleration. The axial stresses due to this overturning effect are then calculated and compared to the classical buckling strength of the cylinder divided by an appropriate factor of safety.

Now, it has been recognized that the flexibility of the walls of such tanks has an important effect on the impulsive component of the hydrodynamic pressure. As such, a

large number of numerical and analytical studies have focused on the interaction between flexible walls and the contained fluid. An analytical approach of including the fluid-structure interaction for flexible tanks based on the assumption of a prescribed mode of deformation of the tank wall was developed by Velestos (1974). Balendra et al. (1982) interpolated both the displacement of the shell structure and the dynamic pressure using the finite element method. The coupled system was then solved to obtain some design charts which can be used to estimate the base shear, the overturning moment and the required free board for cylindrical tanks subjected to horizontal acceleration and which are free from rocking. The displacement finite element method to model both the structure and the fluid was used by Barton and Parker (1987). The latter was treated as a solid having a very small shear resistance. Since the early eighties, a considerable number of studies have been conducted by Haroun and his co-authors to study the response of flexible cylinders under seismic loading. These investigations led to a significant improvement in the design of flexible cylindrical tanks. Tanks subjected to horizontal acceleration and free from rocking motion were considered by Haroun (1980). In this study, the cylindrical shell was modelled using the axisymmetric shell element with harmonic oscillations. Meanwhile, the boundary integral method was used to derive the fluid added-mass resulting from the hydrodynamic pressure. The natural frequencies and the mode shapes resulting from a $\cos \theta$-type vibration, i.e. vibration in which the cylinder remains circular, were obtained for the liquid-shell system. The influence of the $\cos n\theta$-modes of the dynamic pressure which can be excited in a tank having

circumferential imperfections was also investigated. In the same study, Haroun also considered the effect of sloshing on shell vibration. One of the conclusions in Haroun's study (1980) involves the decoupling between the shell vibrations and the sloshing modes as a valid assumption when studying the behaviour of the shell. A vibration test of a full scale liquid-filled cylinder showed good agreement between the natural frequencies of the liquid-shell system and those obtained from Haroun's numerical study. Also, in that investigation, Haroun studied the dynamic buckling of a scaled model vibrating on a shake table. The dynamic test showed that the stability of the tank depends mainly on the $\cos\theta$ component of the fluid pressure. Shortly afterwards, Haroun and Housner (1981) suggested a mechanical model simulating the hydrodynamic pressure developing inside a flexible cylindrical tanks subjected to a horizontal excitation without rocking. The formulation was based on the boundary integral method and the fundamental mode shape of vibration of cylindrical tanks. This mechanical model was extended by Haroun and Ellaithy (1985a) to account for the rocking motion at the base. The extended model was then used by Haroun and Ellaithy (1985b) to study the response of elevated cylindrical tanks. Two examples were considered in their study; a small capacity tank resting on a cross braced frame and a larger tank supported by a pedestal tower. The periods of the structures, the maximum displacements, the base shears and the overturning moments were all calculated using both the response spectrum and the time history analyses. The effect of different parameters, tank flexibility, sloshing modes, and the rotation of the base of the vessel were all investigated in this study. Results of the analyses show that

the flexibility of the tank is important for large capacity cylindrical tanks. Analyses also indicate that the rotation has an important effect on the behaviour of the pedestal type supported tanks.

The effect of the vertical ground acceleration on the behaviour of liquid-filled cylinders was also investigated about the same time by Haroun and Tayel (1985 a-b-c). In the first two studies, the natural frequencies and the corresponding mode shapes due to the axisymmetric vibrations, caused by this type of ground motion, were considered both through a closed form analytical solution and numerically, followed by complete response (Haroun and Tayel, 1985c). In this latter investigation, it was concluded that the axial stresses induced by the vertical acceleration component can be neglected compared to those resulting from the horizontal acceleration. However, they also mentioned that the increase of hoop stresses due to the vertical acceleration would be important when accounting for material non-linearity. It should be pointed out here that all of the above described investigations concerning liquid-filled cylindrical tanks were limited to the linear elastic range of behaviour.

The dynamic instability of liquid-filled cylindrical tanks under horizontal, vertical and rocking motion was studied by Liu and Uras (1989 a-b). The fluid structure interaction was taken care of using the concept of added-mass, and the structure was modelled using ring finite elements with harmonic oscillations. An eigen value analysis limited to small deformation elastic response was carried out to determine the critical mode shapes resulting from different types of excitations. Their analyses show that the

horizontal component of the ground acceleration is responsible for the dynamic buckling of the structure. Zhou et al. (1992) used the non-linear shell theory to predict the elephant foot buckling of liquid storage cylindrical tanks under horizontal excitation. The boundary solution technique was employed in the fluid region, while ring finite elements with fourier oscillations were used to discretize the structure. In their study, the effect of the $\cos(n\theta)$ modes of the shell vibration on the elastic stability of the liquid-filled cylindrical vessels was investigated.

To the best of the author's knowledge, no attempts have been made to study the seismic response of liquid-filled conical tanks. As would be the case for cylindrical tanks, the horizontal ground accelerations are expected to cause significant overturning moment at the base of the vessel. This overturning moment will have an amplified effect on the stability of conical vessels due to the small radius at the bottom part of the cone. Also, due to the inclination of the walls of the cone, vertical accelerations are expected to induce both axial and hoop stresses in the shell. As such, the vertical component of the ground acceleration may have an important effect on the tank stability, and hence needs to be considered in any seismic analysis.

It should be noted that previous studies have shown that the stresses at the base of cylindrical tanks resulting from seismic motion are usually less than the yield stress of the steel. As such, it seems reasonable to consider only the linear response of such structures in seismic analysis. However, for the case of liquid-filled conical steel tanks, the axial stresses due to hydrostatic pressure, when added to those resulting from

seismic excitation, may indeed lead to yielding of steel. This yielding, together with a localized large deformation near the base, may cause premature local buckling near the bottom of the tank, followed by an overall instability of the structure. It seems prudent, therefore, to include geometric and material non-linearities when performing seismic analysis on liquid-filled conical tanks.

1-4 Objective and Scope

The objectives of the present study, then, are as follows :

1-   Extend the formulation of the consistent shell element to include geometric non-linearities as well as non-linear dynamic analysis to solve thin and thick shell problems in general.

2-   Use the consistent shell element to model hydrostatically loaded conical tanks and study the state of instability of such structures including the influence of geometric and material non-linearities, the geometric imperfections and the residual stresses due to welding

3-   Employ the non-linear formulation of the consistent shell element together with the boundary integral technique to investigate the stability of liquid-filled conical tanks, as a part of elevated water tower structures, under the effects of both the horizontal and the vertical components of a seismic motion.

In Chapter Two, the formulation of the consistent shell element is extended to geometric non-linearities. A strain hardening plasticity model, capable of simulating the loading and unloading behaviour is also included. The formulation is general and can be

applied to any thin or thick plate or shell problems. Several examples are presented and comparisons are made with the available numerical and experimental results in the literature to evaluate the performance of the element in the non-linear range.

In Chapter Three, liquid-filled conical steel vessels are modelled using the consistent shell element. Two categories of tanks are considered. These are specified as tall or broad tanks according to the ratio of height to bottom radius of the conical vessel. Elastic stability analyses are first performed on perfect shells and the results are compared to the numerical results available in the literature. Tanks with different imperfection patterns are then elastically analyzed to determine the imperfection shape which leads to the lowest limit load. Then, material non-linearities are included in the analysis. Here, the effect of both hoop and meridional residual stresses on the inelastic stability of liquid-filled conical shells are studied. Following that, the sensitivity of the liquid-filled conical shells to geometric imperfections and residual stresses are investigated by performing inelastic analyses for: 1) perfect tanks, 2) tanks having only geometric imperfections, and 3) tanks with both geometric imperfections and residual stresses due to welding. Finally, the tank that failed in Fredericton, Canada, is analyzed and the results are compared with those obtained from design checks employing different codes and with other independent investigations.

In Chapter Four, the formulation of the consistent shell element is extended to non-linear dynamic analysis. The mass matrix and the linear stiffness matrix of the consistent shell element are incorporated into an eigen value analysis to solve for the

natural frequencies and mode shapes of shells. The non-linear dynamic and the free vibration analysis models are verified using the analysis of different plate and shell problems. The boundary integral technique is then used to obtain the fluid added-mass due to the impulsive components resulting from both the lateral and vertical excitations acting on a liquid-filled conical vessel which is prevented from rocking at its base. The fluid added-mass is added to the mass matrix of the structure to perform free vibration and non-linear dynamic analyses of the liquid-shell system. In this context, the added-mass formulation is verified by performing free vibration analyses on liquid-filled cylindrical tanks.

Finally, a number of conical tanks, supported on rigid frames, are considered. Both free vibration and non-linear time history analyses are performed on these elevated tanks using the horizontal and the vertical accelerations of a real earthquake chosen to have frequency content matching the fundamental frequencies of the tanks to be analyzed.
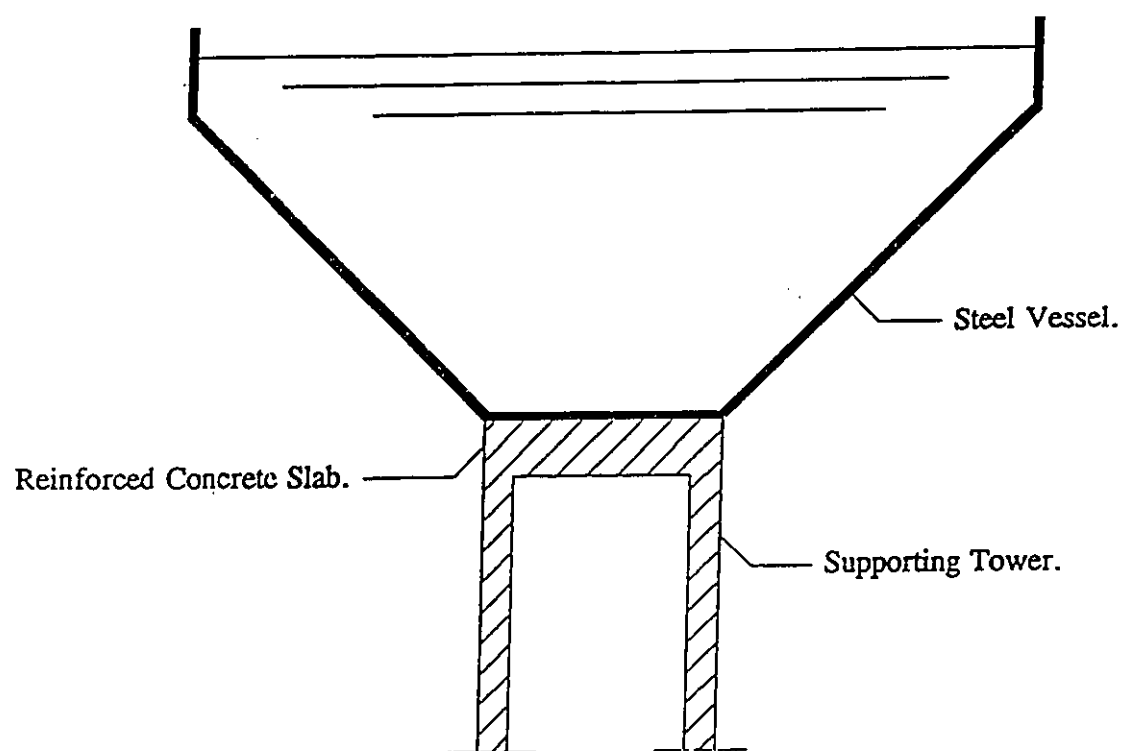
Figure 1.1 Cross Sectional Elevation of Elevated Conical Tanks.

CHAPTER TWO

NON-LINEAR FORMULATION OF CONSISTENT SHELL ELEMENT

2-1 Introduction

The excellent performance of the consistent shell element for small deformations has encouraged the author to use the element in modelling of conical shells in order to study their stability. The consistent subparametric triangular shell element was formulated by Koziey (1993). The element employs cubic polynomials for approximations of displacements and quadratic polynomials for approximations of rotations. This ensures a consistent formulation and eliminates the spurious transverse shear modes and the shear locking phenomenon found to exist in both eight node and nine node isoparametric shell elements when used to model thin plates and shells. Thus, the consistent shell element does not require the use of the reduced integration technique as used in the isoparametric shell elements. The consistent element employs two types of variations in rotations. The first is constant through the thickness and the second varies quadratically. The latter gives a parabolic distribution of the transverse shear strains through the depth of the element and, as such, the shear factor κ which is usually required to correct the assumption of constant shear strain across the depth, is not needed in the consistent shell element formulation.

The buckling of liquid filled conical shells is expected to be associated with large displacements and large rotations. This behaviour necessitated an extension of the consistent shell element to include geometric non-linearities. The total Lagrangian approach is first applied to a three dimensional finite element formulation to obtain expressions for the non-linear stiffness matrix and the unbalanced load vector. These are then used in the large deformation formulation of the consistent shell element degenerated from a solid element. The material non-linearities are also included through isotropic strain hardening, the Von Mises yield criterion and an associated flow rule. The incremental load method is employed for the non linear analysis and uses the Newton-Raphson method for iterations within each load increment. The extended formulation is verified through use of various examples. These include the large deformation analysis of a simply supported square plate, a cylindrical panel and a shallow arch. The results obtained from the analyses are then compared with those available in the literature and show excellent agreement, thus confirming a superior performance. Finally, the non-linear formulation of the consistent shell element is verified using experimental results. This is done by modelling W-shaped cantilever steel beams using the consistent shell element and performing inelastic stability analysis for such beams. The limit loads obtained from these analyses are then compared with those resulting from an experimental investigation carried out by Daali and Korol (1994).

2-2 Element Description

2-2-1 Coordinate Systems and Geometry

The coordinate systems employed in the formulation of the consistent shell

element as used by Koziey (1993) are shown in Figure 2.1. These are defined in the following manner:

1. x, y and z are the global cartesian coordinates.

2. r, s and t are the curvilinear coordinates, where r and s are tangent to the surface at t=constant while t may be so disturbed to waive the requirement of normality to the r-s tangent plane.

3. x´, y´ and z´ are the local cartesian coordinates used to define local strains and stresses, with z´ always normal to the surface at t=constant and x´ and y´ tangent to the surface.

A curvilinear transformation in terms of the parent r and s coordinates and a linear transformation in terms of the t coordinate are employed for geometric distortion. The following interpolation can then be used to determine the location of any point within the element in terms of the coordinates of the nodal points (x_n, y_n and z_n) and the vector V_{3n} at each node:

$$\begin{Bmatrix} x \\ y \\ z \end{Bmatrix} = \sum N_n \begin{Bmatrix} x_n \\ y_n \\ z_n \end{Bmatrix} + \sum N_n \frac{t}{2} V_{3n} \tag{2.1}$$

where the interpolation functions N_n are quadratic and are presented in Appendix A. The thickness vector V_{3n} is obtained via the top and bottom global coordinates of the nodal points as:

$$V_{3n} = \left\{ \begin{array}{c} x_n \\ y_n \\ z_n \end{array} \right\}_{\text{TOP}} \quad - \quad \left\{ \begin{array}{c} x_n \\ y_n \\ z_n \end{array} \right\}_{\text{BOTTOM}} . \tag{2.2}$$

2-2-2 Displacement Field

In non-linear analysis, solutions are normally carried out incrementally using a time step ΔT, where the time T for static analysis is only a convenient variable which represents different intensities of the load applications and correspondingly different configurations. Iterations within each load increment are performed until an equilibrium state is achieved. The displacement $u^{T\ (k)}$ at the kth iteration of the configuration T is related to the displacement $u^{T\ (k-1)}$ at the previous iteration of the same configuration in the following manner:

$$u_i^{T\ (k)} = u_i^{T\ (k-1)} + \Delta u_j^{(k)} . \tag{2.3}$$

In the non-linear formulation of the consistent shell element, the incremental displacement Δu_i is expressed using the incremental global displacement degrees of freedom ΔU_n, ΔV_n and ΔW_n directed along axes x, y and z, respectively, together with four incremental rotations $\Delta\alpha_n$, $\Delta\beta_n$, $\Delta\phi_n$, and $\Delta\psi_n$, about the local axes. Rotations $\Delta\alpha$ and $\Delta\phi$ are about the local y' axis and rotations $\Delta\beta$ and $\Delta\psi$ are about the local x' axis. The consistency of the formulation is achieved by interpolating the displacements using cubic polynomials and the rotations using quadratic polynomials. To obtain cubic approximations for ΔU, ΔV and ΔW, the incremental displacement degrees of freedom at the corner, one third side nodes and the center node are used. Quadratic

approximations for $\Delta\alpha$, $\Delta\beta$, $\Delta\phi$ and $\Delta\psi$ are achieved using the incremental rotational

degrees of freedom at the corner and mid-side nodes as shown in Figure 2.1. The

number of degrees of freedom are not the same for all nodes. The total number of

degrees of freedom per element is fifty four. However, the formulation of the consistent

shell element is performed by assuming that each node has all seven degrees of freedom,

and that the interpolation function which corresponds to a non-active degree of freedom

is equal to zero. It should be noted that the rotations $\Delta\alpha$ and $\Delta\beta$ are constant through the

depth of the element while rotations $\Delta\phi$ and $\Delta\psi$ vary quadratically. Therefore, $\Delta\alpha$ and

$\Delta\beta$ lead to a linear variation of Δu, Δv and Δw, while $\Delta\phi$ and $\Delta\psi$ provide a cubic

variation of Δu, Δv and Δw across the thickness.

The incremental global displacements (Δu, Δv, Δw) can now be written in terms

of the nodal incremental degrees of freedom as

$$\begin{Bmatrix} \Delta u \\ \Delta v \\ \Delta w \end{Bmatrix} = \sum_{n=1}^{13} \bar{N}_n \begin{Bmatrix} \Delta U_n \\ \Delta V_n \\ \Delta W_n \end{Bmatrix} + \sum_{n=1}^{13} N_n \ M_{1n} \ [V_n] \begin{Bmatrix} \Delta \alpha_n \\ \Delta \beta_n \end{Bmatrix} + \sum_{n=1}^{13} N_n \ M_{2n} \ [V_n] \begin{Bmatrix} \Delta \phi_n \\ \Delta \psi_n \end{Bmatrix} \qquad (2.4)$$

where N and $\bar{N}$ are the quadratic and cubic shape functions, respectively. These are

presented in Appendix A. The matrix $[V_n]$ is given by v_{1n} and v_{2n} as $[V_n]=[v_{1n},-v_{2n}]$

where the unit vectors v_{1n} and v_{2n} are directed along the x´ and y´ axes, respectively and

are orthogonal to the unit vector v_{3n} at the nth node.

The procedure for construction of the orthogonal basis (v_{1n}, v_{2n}, v_{3n}) due to Koziey

(1993), appears in Appendix C. The shape functions M_{1n} and M_{2n} are used for

approximating displacements through the depth due to both the constant and the quadratic

rotations, respectively, and are of the following form:

$$M_{1n} = \frac{h_n t}{2} \ , \quad M_{2n} = \frac{h_n t \, (1 - t^2)}{2}$$

(2.5)

where h_n is the thickness of the shell at the node n.

The details of the through thickness displacement approximation due to quadratic rotations $\Delta\phi$ and $\Delta\psi$, as derived by Koziey (1993), are presented in Appendix B. It has to be noted that the consistent shell element is a subparametric element because of the cubic displacement field and quadratic geometry transformation.

The transformation matrix for relative direction cosines between the local and the global axes at the point where a displacement is to be transformed is also needed. This matrix [θ] can be established using the Jacobian matrix as given below

$$[\theta] = \begin{bmatrix} l_{11} & l_{12} & l_{13} \\ l_{21} & l_{22} & l_{23} \\ l_{31} & l_{32} & l_{33} \end{bmatrix} .$$

(2.6)

The derivative of [θ], by Koziey (1993), is presented in Appendix C. Using this matrix and the global incremental displacements in Equation 2.4, the local incremental displacements can be written in terms of the nodal incremental degrees of freedom as

$$\begin{Bmatrix} \Delta u' \\ \Delta v' \\ \Delta w' \end{Bmatrix} = \sum_{n=1}^{13} \bar{N}_n [\theta] \begin{Bmatrix} \Delta U_n \\ \Delta V_n \\ \Delta W_n \end{Bmatrix} + \sum_{n=1}^{13} N_n \, M_{1n} [C_n] \begin{Bmatrix} \Delta \alpha_n \\ \Delta \beta_n \end{Bmatrix} + \sum_{n=1}^{13} N_n \, M_{2n} [C_n] \begin{Bmatrix} \Delta \phi_n \\ \Delta \psi_n \end{Bmatrix}$$

(2.7)

where [C_n] takes the following form

$$[C_n] = [\theta][V_n]$$

or

$$[C_n] = \begin{bmatrix} C_n^{11} & C_n^{12} \\ C_n^{21} & C_n^{22} \\ C_n^{31} & C_n^{32} \end{bmatrix} = \begin{bmatrix} (l_{11}l_{11}^n + l_{12}l_{12}^n + l_{13}l_{13}^n) & (-l_{11}l_{21}^n - l_{12}l_{22}^n - l_{13}l_{23}^n) \\ (l_{21}l_{11}^n + l_{22}l_{12}^n + l_{23}l_{13}^n) & (-l_{21}l_{21}^n - l_{22}l_{22}^n - l_{23}l_{23}^n) \\ (l_{31}l_{11}^n + l_{32}l_{12}^n + l_{33}l_{13}^n) & (-l_{31}l_{21}^n - l_{32}l_{22}^n - l_{33}l_{23}^n) \end{bmatrix}. \quad (2.8)$$

Note that for large displacement problems, the components of the matrix $[\theta]$ change with the displacement history. Therefore, the components of matrix $[C_n]$ will also change due to incremental loading. For a detailed description of the consistent shell element and its small displacement formulation, the reader is referred to Koziey (1993).

2-3 Stress and Strain Tensors

In large displacement analysis, the current configuration of the structure is different from its initial configuration. As such, it is not possible to use the Cauchy stress tensor and the corresponding engineering strain tensor. A suitable stress measure for a total Lagrangian formulation is the second Piola-Kirchhoff stress tensor S_{ij} which is related to the Cauchy stress tensor τ_{mn} by the following relation (Bathe, 1982)

$$S_{ij} = \frac{\rho_o}{\rho_t} \frac{\partial X_i}{\partial x_m} \frac{\partial X_j}{\partial x_n} \tau_{mn}. \quad (2.9)$$

In the equation above, ρ_o and ρ_t represent the mass densities at the initial and current configurations, respectively; X and x are the coordinates in the initial and current configurations, respectively. The second Piola-Kirchhoff tensor can be physically defined as the internal force per undeformed unit area directed along the current axes.

The corresponding strain tensor is the Green-Lagrangian strain tensor which is defined as follows:

$$e_{ij} = \frac{\partial u_i}{\partial X_j} + \frac{\partial u_j}{\partial X_i} + \frac{\partial u_k}{\partial X_i} \frac{\partial u_k}{\partial X_j} \qquad (2.10)$$

where u_i is the displacement vector in the initial configuration.

It was proven by Bathe (1982) that the second Piola-Kirchhoff stress tensor is the energy conjugate of the Green-Lagrangian strain tensor because of the following internal virtual work equality, i.e.

$$\int_{V_o} S_{ij} \delta (e_{ij}) \, dV = \int_{V} \tau_{mn} \delta (e_{mn}) \, dV \qquad (2.11)$$

where V_o and V are the volumes of the structure in the initial and the current configuration, respectively; e_{mn} is the engineering strain tensor while δ denotes the virtual quantities. The virtual work on the left hand side of Equation 2.11 is in fact the basis of the total Lagrangian formulation. The difficulty with the right hand side lies in the determination of the current volume V for the domain integration.

It was also proven by Bathe (1982) that both the second Piola-Kirchhoff stress tensor and the Green-Lagrangian strain tensor are invariant under rigid body motion. This implies, as stated by Bathe, that "any material description which has been developed for infinitesimal displacement analysis using engineering stress and strain measures can directly be employed in large displacement and large rotation but small strain analysis, provided that the second Piola Kirchhoff stress and the Green-Lagrangian strain are used". More details about the stress and strain measures in non-linear analysis can be

found in Bathe (1982) and Crisfield (1991).

2-4 Total Lagrangian Non-Linear Formulation

The non-linear formulation of the consistent shell element is based on the total

Lagrangian approach. A detailed description of the total Lagrangian in the finite element

context is presented by Bathe (1982). The formulation is based on incremental loading

and an iterative technique employed until equilibrium is reached within each load

increment. The equilibrium solution at a prescribed time (T-ΔT) as well as the kinematic

variables corresponding to the (k-1)th iteration at time T are assumed to be known. The

solution then proceeds to the next iteration (kth) of the same time T. The following steps

are applied in order to obtain a piecewise linearized equation of motion corresponding

to the kth iteration of the time T.

(a) Equation of Motion:

According to the virtual work principle, the virtual work form of the equation of

motion can be written as:

$$\int_{V_o} S_{ij}^T \delta \left(e_{ij}^T \right) dV = W^T \tag{2.12}$$

where S_{ij} and ϵ_{ij} as described in Section 2.3 are the second Piola-Kirchhoff stress tensor

and the Green-Lagrangian strain tensor, respectively and W is the virtual work done by

the external forces. Note that the superscript T corresponds to the value of the variable

for the equilibrium solution at the time T.

(b) Incremental Stresses and Strains

As the stress tensor S_{ij} and the strain tensor ϵ_{ij} refer to the original configuration,

incremental versions of both tensors can be applied as follows:

$$S_{ij}^{T}{}^{(k)} = S_{ij}^{T}{}^{(k-1)} + \Delta S_{ij} \tag{2.13}$$

$$e_{ij}^{T}{}^{(k)} = e_{ij}^{T}{}^{(k-1)} + \Delta e_{ij} + \Delta \eta_{ij} \tag{2.14}$$

where ΔS_{ij} is the incremental second Piola Kirchhoff stress tensor; Δe_{ij} and $\Delta \eta_{ij}$ are the linear and non-linear parts of the incremental Green-Lagrangian strain tensor, respectively, and are given by the following:

$$\Delta e_{ij} = \frac{1}{2} \left(\Delta u_{i,j} + \Delta u_{j,i} + u_{q,i}^{T}{}^{(k-1)} \Delta u_{q,j} + u_{q,j}^{T}{}^{(k-1)} \Delta u_{q,i} \right) \tag{2.15}$$

$$\Delta \eta_{ij} = \frac{1}{2} \left(\Delta u_{q,i} \Delta u_{q,j} \right) . \tag{2.16}$$

The superscripts T $(k-1)$ and T (k) used with the variables above denote evaluated magnitudes at the $(k-1)^{th}$ and the kth iteration at time T, respectively.

C) Linearized Equations of Motion

In order to linearize the equations of motion, the non linearities in Equation 2.14 are assumed negligible for the virtual strain increment to give

$$\delta \Delta (e_{ij}) = \delta (\Delta e_{ij}) . \tag{2.17}$$

Also the incremental stresses are assumed to be related to the incremental strains by the following incremental constitutive equation

$$\Delta S_{ij} = C_{ijrs} \Delta e_{rs} \tag{2.18}$$

where C_{ijn} is a fourth order material tensor.

Substitution of Equations 2.13, 2.14, 2.17 and 2.18 into Equation 2.12 yields the following linearized virtual work form of the equations of motion

$$\int_{V_o} C_{ijrs} e_{rs}^{T\ (k-1)} \delta\ (\Delta e_{ij})\ dV + \int_{V_o} S_{ij}^{T\ (k-1)} \delta\ (\Delta \eta_{ij})\ dV = W^T - \int_{V_o} S_{ij}^{T\ (k-1)} \delta\ (\Delta e_{ij})\ dV.$$

(2.19)

2-4-1 Application to a General 3-D Finite Element Discretization

Assume the following general finite element discretization:

$$\Delta u_i = \psi_n \Delta U_i^n \qquad (2.20)$$

where Δu_i is the incremental displacement in the ith direction; ΔU^n_i is the incremental degree of freedom of the node n in the ith direction and ψ_n is the interpolation function for the node n.

After substituting 2.20, 2.15 and 2.16 into Equation 2.19, the linearized equation of motion (Equation 2.19) can be written as

$$\int_{V_o} C_{ijrs} \psi_{n,i}\ (\delta_{jq} + u_{q,j}^{T\ (k-1)})\ \psi_{p,r}\ (\delta_{st} + u_{t,s}^{T\ (k-1)})\ \Delta U_t^p\ \delta\ (\Delta U_q^n)\ dV \qquad +$$

$$\int_{V_o} S_{ij}^T \psi_{m,j} \psi_{n,i}\ \Delta U_q^m \delta\ (\Delta U_q^n)\ dV \qquad =$$

$$W^T - \int_{V_o} S_{ij}^{T\ (k-1)} \psi_{n,i}\ [\delta_{jq} + u_{q,j}^{T\ (k-1)}]\ \delta\ (\Delta U_q^n)\ dV.$$

(2.21)

Realizing arbitrary $\delta(\Delta U_q^n)$, Equation 2.21 then leads to the following equations of motion in the matrix form:

$$[K_L^{T\ (k-1)} + K_S^{T\ (k-1)}]\{\Delta U\} = \{R^T\} - \{F^{T\ (k-1)}\} \tag{2.22}$$

where $[K_L]$ is the sum of the linear and the initial strain stiffness matrices; $[K_S]$ is the initial stress stiffness matrix; $\{F\}$ is the unbalanced load vector; and $\{\Delta U\}$ is the load vector which includes the incremental degrees of freedom. The $[K_L]$, $[K_S]$ and $\{F\}$ matrices and the other associated matrices are evaluated in the following manner.

$$[K_L^{T\ (k-1)}] = \int_{V_o} [B_L^{T\ (k-1)}]^{TRANS} [D] [B_L^{T\ (k-1)}]\, dV \tag{2.23}$$

$$[K_S^{T\ (k-1)}] = \int_{V_o} [B_S]^{TRANS} [S^{T\ (k-1)}] [B_S]\, dV \tag{2.24}$$

$$\{F^{T\ (k-1)}\} = \int_{V_o} [B_L^{T\ (k-1)}]^{TRANS} \{S^{T\ (k-1)}\} dV \tag{2.25}$$

$$
\left[B_L^{T\ (k-1)}\right]_{(6\cdot 3,N)} = \sum_{n=1}^{N}
\begin{bmatrix}
\psi_{n,1}(1+u_{1,1}^{T\ (k-1)}) & \psi_{n,1}(0+u_{2,1}^{T\ (k-1)}) & \psi_{n,1}(0+u_{3,1}^{T\ (k-1)}) \\[2ex]
\psi_{n,2}(0+u_{1,2}^{T\ (k-1)}) & \psi_{n,2}(1+u_{2,2}^{T\ (k-1)}) & \psi_{n,2}(0+u_{3,2}^{T\ (k-1)}) \\[2ex]
\psi_{n,3}(0+u_{1,3}^{T\ (k-1)}) & \psi_{n,3}(0+u_{2,3}^{T\ (k-1)}) & \psi_{n,3}(1+u_{3,3}^{T\ (k-1)}) \\[2ex]
\begin{array}{c}\psi_{n,1}(0+u_{1,2}^{T\ (k-1)})\\+\\\psi_{n,2}(1+u_{1,1}^{T\ (k-1)})\end{array} & \begin{array}{c}\psi_{n,1}(1+u_{2,2}^{T\ (k-1)})\\+\\\psi_{n,2}(0+u_{2,1}^{T\ (k-1)})\end{array} & \begin{array}{c}\psi_{n,1}(0+u_{3,2}^{T\ (k-1)})\\+\\\psi_{n,2}(0+u_{3,1}^{T\ (k-1)})\end{array} \\[4ex]
\begin{array}{c}\psi_{n,1}(0+u_{1,3}^{T\ (k-1)})\\+\\\psi_{n,3}(1+u_{1,1}^{T\ (k-1)})\end{array} & \begin{array}{c}\psi_{n,1}(0+u_{2,3}^{T\ (k-1)})\\+\\\psi_{n,3}(0+u_{2,1}^{T\ (k-1)})\end{array} & \begin{array}{c}\psi_{n,1}(1+u_{3,3}^{T\ (k-1)})\\+\\\psi_{n,3}(0+u_{3,1}^{T\ (k-1)})\end{array} \\[4ex]
\begin{array}{c}\psi_{n,2}(0+u_{1,3}^{T\ (k-1)})\\+\\\psi_{n,3}(0+u_{1,2}^{T\ (k-1)})\end{array} & \begin{array}{c}\psi_{n,2}(0+u_{2,3}^{T\ (k-1)})\\+\\\psi_{n,3}(1+u_{2,2}^{T\ (k-1)})\end{array} & \begin{array}{c}\psi_{n,2}(1+u_{3,3}^{T\ (k-1)})\\+\\\psi_{n,3}(0+u_{3,2}^{T\ (k-1)})\end{array}
\end{bmatrix}
$$

$$(2.26)$$

$$[B_S]_{9*3N} = \sum_{n=1}^{N} \begin{bmatrix} \psi_{n,1} & 0 & 0 \\ 0 & \psi_{n,1} & 0 \\ 0 & 0 & \psi_{n,1} \\ \psi_{n,2} & 0 & 0 \\ 0 & \psi_{n,2} & 0 \\ 0 & 0 & \psi_{n,2} \\ \psi_{n,3} & 0 & 0 \\ 0 & \psi_{n,3} & 0 \\ 0 & 0 & \psi_{n,3} \end{bmatrix}$$

$$(2.27)$$

$$[S^{T(k-1)}]_{9*9} = \begin{bmatrix} S_{11}^{T(k-1)} & 0 & 0 & S_{12}^{T(k-1)} & 0 & 0 & S_{13}^{T(k-1)} & 0 & 0 \\ 0 & S_{11}^{T(k-1)} & 0 & 0 & S_{12}^{T(k-1)} & 0 & 0 & S_{13}^{T(k-1)} & 0 \\ 0 & 0 & S_{11}^{T(k-1)} & 0 & 0 & S_{12}^{T(k-1)} & 0 & 0 & S_{13}^{T(k-1)} \\ S_{12}^{T(k-1)} & 0 & 0 & S_{22}^{T(k-1)} & 0 & 0 & S_{23}^{T(k-1)} & 0 & 0 \\ 0 & S_{12}^{T(k-1)} & 0 & 0 & S_{22}^{T(k-1)} & 0 & 0 & S_{23}^{T(k-1)} & 0 \\ 0 & 0 & S_{12}^{T(k-1)} & 0 & 0 & S_{22}^{T(k-1)} & 0 & 0 & S_{23}^{T(k-1)} \\ S_{13}^{T(k-1)} & 0 & 0 & S_{23}^{T(k-1)} & 0 & 0 & S_{33}^{T(k-1)} & 0 & 0 \\ 0 & S_{13}^{T(k-1)} & 0 & 0 & S_{23}^{T(k-1)} & 0 & 0 & S_{33}^{T(k-1)} & 0 \\ 0 & 0 & S_{13}^{T(k-1)} & 0 & 0 & S_{23}^{T(k-1)} & 0 & 0 & S_{33}^{T(k-1)} \end{bmatrix}$$

$$(2.28)$$

$$\{S^{T(k-1)}\}^{TRANS} = \{S_{11}^{T(k-1)} \quad S_{22}^{T(k-1)} \quad S_{33}^{T(k-1)} \quad S_{12}^{T(k-1)} \quad S_{13}^{T(k-1)} \quad S_{23}^{T(k-1)}\}$$

$$(2.29)$$

where N in Equations 2.26 and 2.27 is the number of nodes per element.

Matrix [D] is a general three dimensional constitutive matrix which relates the incremental strain vector $\{\Delta e\}$ to the incremental stress vector $\{\Delta S\}$

$$\{\Delta S\} = [D]\{\Delta e\}. \tag{2.30}$$

Meanwhile, the incremental stress and strain vectors are of the following form:

$$\{\Delta S\}^{TRANS} = \{\Delta S_{11} \quad \Delta S_{22} \quad \Delta S_{33} \quad \Delta S_{12} \quad \Delta S_{13} \quad \Delta S_{23}\} \tag{2.31}$$

$$\{\Delta e\} = [B_L^{T\ (k-1)}]\{\Delta U\}. \tag{2.32}$$

2-5 Degeneration to the Consistent Shell Element

2-5-1 Expressions for [D], [S], {S} and {ΔS} Matrices

The formulation of the consistent shell element is referred to the local axes x', y' and z'. According to the usual assumption used in shell theory, the stress component normal to the surface can be neglected and hence $\Delta S_{z'z'} = 0$. The corresponding elasticity matrix [D '] for a linear elastic material is of the following form:

$$[D'] = \frac{E}{1-v^2}
\begin{bmatrix}
1 & v & 0 & 0 & 0 \\
 & 1 & 0 & 0 & 0 \\
 & & \dfrac{1-v}{2} & 0 & 0 \\
Symmetry & & & \dfrac{1-v}{2} & 0 \\
 & & & & \dfrac{1-v}{2}
\end{bmatrix}. \tag{2.33}$$

Here, E and v are the elastic modulus and Poisson's ratio, respectively. It should be noted that the shear correction factor κ is not required in [D '] because of the parabolic approximation of the transverse shear strains through the thickness.

Expressions for the matrix $[S^{T\,(k-1)}]$ and the stress vectors $\{S^{T\,(k-1)}\}$ and $\{\Delta S\}$ for the consistent shell element formulation are given in Appendix D1 and can in fact be used for any other shell finite element.

2-5-2 Expressions for [B$_L$] and [B$_S$]

Because the effect of the strain component normal to the surface of the shell has been incorporated into the constitutive equation through imposition of zero stress normal to the surface, the calculation of this normal strain is not required and hence is ignored. Therefore, the matrix [B$_L$] has five rows instead of six.

In order to obtain expressions for both the [B$_L$] and [B$_S$] matrices, the derivatives of the incremental local displacements with respect to the local axes are required. Using Equation 2.7, the derivatives of the incremental local displacements with respect to the parent coordinates (r, s, t) can be obtained by the following:

$$
\begin{Bmatrix} \Delta u'_{i,r} \\ \Delta u'_{i,s} \\ \Delta u'_{i,t} \end{Bmatrix} = \sum_{n=1}^{13} [A_n] \begin{Bmatrix} \Delta U_n \\ \Delta V_n \\ \Delta W_n \\ \Delta \alpha_n \\ \Delta \beta_n \\ \Delta \phi_n \\ \Delta \psi_n \end{Bmatrix}
\qquad (2.34)
$$

where

$$[A_n] = \begin{bmatrix} l_{11}\overline{N}_{n,r} & l_{12}\overline{N}_{n,r} & l_{13}\overline{N}_{n,r} & C_n^{11}N_{n,r}M_{1n} & -C_n^{12}N_{n,r}M_{1n} & C_n^{11}N_{n,r}M_{2n} & -C_n^{12}N_{n,r}M_{2n} \\ l_{11}\overline{N}_{n,s} & l_{12}\overline{N}_{n,s} & l_{13}\overline{N}_{n,s} & C_n^{11}N_{n,s}M_{1n} & -C_n^{12}N_{n,s}M_{1n} & C_n^{11}N_{n,s}M_{2n} & -C_n^{12}N_{n,s}M_{2n} \\ 0 & 0 & 0 & C_n^{11}N_n dM_{1n} & -C_n^{12}N_n dM_{1n} & C_n^{11}N_n dM_{2n} & -C_n^{12}N_n dM_{2n} \end{bmatrix}$$

$$(2.35)$$

$u'_1 = u'$, $u'_2 = v'$, $u'_3 = w'$ and the functions dM_{1n} and dM_{2n} are the derivatives of the through thickness interpolation functions M_{1n} and M_{2n} with respect to the coordinate t.

The partial derivatives with respect to local x', y', z' coordinates can be written in terms of derivatives in the curvilinear coordinate system using:

$$\left\{ \begin{array}{c} \dfrac{\partial}{\partial x'} \\ \dfrac{\partial}{\partial y'} \\ \dfrac{\partial}{\partial z'} \end{array} \right\} = \begin{bmatrix} \dfrac{\partial r}{\partial x'} & \dfrac{\partial s}{\partial x'} & \dfrac{\partial t}{\partial x'} \\ \dfrac{\partial r}{\partial y'} & \dfrac{\partial s}{\partial y'} & \dfrac{\partial t}{\partial y'} \\ \dfrac{\partial r}{\partial z'} & \dfrac{\partial s}{\partial z'} & \dfrac{\partial t}{\partial z'} \end{bmatrix} \left\{ \begin{array}{c} \dfrac{\partial}{\partial r} \\ \dfrac{\partial}{\partial s} \\ \dfrac{\partial}{\partial t} \end{array} \right\} = [J']^{-1} \left\{ \begin{array}{c} \dfrac{\partial}{\partial r} \\ \dfrac{\partial}{\partial s} \\ \dfrac{\partial}{\partial t} \end{array} \right\}$$

$$(2.36)$$

where the Jacobian matrix $[J']$ relates the derivatives in the curvilinear coordinate system to the derivatives in the local coordinate system and is given by:

$$[J'] = \begin{bmatrix} \dfrac{\partial x'}{\partial r} & \dfrac{\partial y'}{\partial r} & \dfrac{\partial z'}{\partial r} \\ \dfrac{\partial x'}{\partial s} & \dfrac{\partial y'}{\partial s} & \dfrac{\partial z'}{\partial s} \\ \dfrac{\partial x'}{\partial t} & \dfrac{\partial y'}{\partial t} & \dfrac{\partial z'}{\partial t} \end{bmatrix}.$$

$$(2.37)$$

The components of $[J']$ are determined using Equation 2.1, the matrix of direction cosines $[\theta]$ and the chain rules as:

$$\frac{\partial a'_i}{\partial r} = \frac{\partial x}{\partial r}\frac{\partial a'_i}{\partial x} + \frac{\partial y}{\partial r}\frac{\partial a'_i}{\partial y} + \frac{\partial z}{\partial r}\frac{\partial a'_i}{\partial z} = l_{i1}\frac{\partial x}{\partial r} + l_{i2}\frac{\partial y}{\partial r} + l_{i3}\frac{\partial z}{\partial r}$$

$$\frac{\partial a'_i}{\partial s} = \frac{\partial x}{\partial s}\frac{\partial a'_i}{\partial x} + \frac{\partial y}{\partial s}\frac{\partial a'_i}{\partial y} + \frac{\partial z}{\partial s}\frac{\partial a'_i}{\partial z} = l_{i1}\frac{\partial x}{\partial s} + l_{i2}\frac{\partial y}{\partial s} + l_{i3}\frac{\partial z}{\partial s}$$

$$\frac{\partial a'_i}{\partial r} = \frac{\partial x}{\partial t}\frac{\partial a'_i}{\partial x} + \frac{\partial y}{\partial t}\frac{\partial a'_i}{\partial y} + \frac{\partial z}{\partial t}\frac{\partial a'_i}{\partial z} = l_{i1}\frac{\partial x}{\partial t} + l_{i2}\frac{\partial y}{\partial t} + l_{i3}\frac{\partial z}{\partial t} \qquad (2.38)$$

where $a'_1 = x'$, $a'_2 = y'$ and $a'_3 = z'$. Since the components of the inverse of the Jacobian matrix will be used in a later derivation, the components of this inverted Jacobian matrix are taken as $J^\bullet_{ij}$, i.e.

$$[J']^{-1} = \begin{bmatrix} J^\bullet_{11} & J^\bullet_{12} & J^\bullet_{13} \\ J^\bullet_{21} & J^\bullet_{22} & J^\bullet_{23} \\ J^\bullet_{31} & J^\bullet_{32} & J^\bullet_{33} \end{bmatrix}. \qquad (2.39)$$

From Equations 2.34 and 2.37, the derivatives of the local incremental displacements with respect to the local coordinate system can be obtained from the following equations:

$$\begin{Bmatrix} \Delta u'_{i,x'} \\ \Delta u'_{i,y'} \\ \Delta u'_{i,z'} \end{Bmatrix} = \sum_{n=1}^{13} [A'_n] \begin{Bmatrix} \Delta U_n \\ \Delta V_n \\ \Delta W_n \\ \Delta \alpha_n \\ \Delta \beta_n \\ \Delta \phi_n \\ \Delta \psi_n \end{Bmatrix} \qquad (2.40)$$

where $[A'_n]$ and its components are given by the following:

$$[A'_n] = \begin{bmatrix} l_{i1}h_{n,1} & l_{i2}h_{n,1} & l_{i3}h_{n,1} & C_n^{i1}H_n^1 & -C_n^{i2}H_n^1 & C_n^{i1}G_n^1 & -C_n^{i2}G_n^1 \\ l_{i1}h_{n,2} & l_{i2}h_{n,2} & l_{i3}h_{n,2} & C_n^{i1}H_n^2 & -C_n^{i2}H_n^2 & C_n^{i1}G_n^2 & -C_n^{i2}G_n^2 \\ l_{i1}h_{n,3} & l_{i2}h_{n,3} & l_{i3}h_{n,3} & C_n^{i1}H_n^3 & -C_n^{i2}H_n^3 & C_n^{i1}G_n^3 & -C_n^{i2}G_n^3 \end{bmatrix} \qquad (2.41)$$

$$h_{n,i} = J_{i1}^{*}\, \overline{N}_{n,r} + J_{i2}^{*}\, \overline{N}_{n,s} \qquad (2.42)$$

$$H_n^i = (J_{i1}^{*}\, N_{n,r} + J_{i2}^{*}\, N_{n,s})\, M_{1n} + J_{i3}^{*}\, N_n\, dM_{1n} \qquad (2.43)$$

$$G_n^i = (J_{i1}^{*}\, N_{n,r} + J_{i2}^{*}N_{n,s})\, M_{2n} + J_{i3}^{*}\, N_n\, dM_{2n}. \qquad (2.44)$$

Using matrix [A'$_n$] above and the general three dimensional expression for the matrices [B$_L$] and [B$_S$] in Equations 2.26 and 2.27, the corresponding [B$_L$] and [B$_S$] matrices for the consistent shell element are obtained. This is achieved by replacing $\psi_{n,i}$ in Equations 2.26 and 2.27 with a corresponding row from [A'$_n$] according to the following table:

Column Position of $\psi_{n,i}$ in Equations 2.26 and 2.27		
	First Column	Second Column	Third Column
$\psi_{n,1}$	First row of $[A'_n]$ with $i=1$	First row of $[A'_n]$ with $i=2$	First row of $[A'_n]$ with $i=3$
$\psi_{n,2}$	Second row of $[A'_n]$ with $i=1$	Second row of $[A'_n]$ with $i=2$	Second row of $[A'_n]$ with $i=3$
$\psi_{n,3}$	Third row of $[A'_n]$ with $i=1$.	Third row of $[A'_n]$ with $i=2$	Third row of $[A'_n]$ with $i=3$

After the above mentioned substitutions and multiplications with the bracketed factors for the initial strain terms, e.g. $(1 + u^{T\,(k-1)}_{1,1})$, the corresponding columns according to the same degree of freedom are added (i.e. 1 and 8, 2 and 9, 3 and 10, etc.) to obtain a matrix resulting in seven columns for Equations 2.26 and 2.27. The above operation leads to a five by seven matrix for a single node. After repeating the procedure for all thirteen nodes, the final size of the $[B_L]$ and $[B_S]$ matrices will be five by ninety one. Expressions for the matrices $[B_L]$ and $[B_S]$ of the consistent shell element are given in Appendix E.

2-5-3 Evaluation of Initial Strains

The matrix $[B_L]$ includes terms consisting of partial derivatives of the local displacements $(u^{T\,(k-1)}, v^{T\,(k-1)}, w^{T\,(k-1)})$ with respect to the local axes (x', y', z'). These

derivatives represent the components of the local initial strains at the kth iteration of the configuration T. In order to evaluate these local strains, expressions for the total global displacements ($u^{T\,(k-1)}$, $v^{T\,(k-1)}$, $w^{T\,(k-1)}$) at the $(k-1)^{th}$ iteration at the time T have to be first obtained by considering the following.

The effect of the incremental global displacement degrees of freedom ΔU_n, ΔV_n and ΔW_n on the total global displacements $u^{T\,(k-1)}$, $v^{T\,(k-1)}$ and $w^{T(k-1)}$ can be obtained through the total global displacement degrees of freedom $U_n^{T(k-1)}$, $V_n^{T\,(k-1)}$ and $W_n^{T\,(k-1)}$, respectively. These are obtained by a simple vector addition of the incremental displacements occurring during different iterations which precede the kth iteration of the configuration T, as given by the following equations:

$$U_n^{T\,(k-1)} = \sum^{\Delta T} \Delta U_n \qquad\qquad (2.45)$$

$$V_n^{T\,(k-1)} = \sum^{\Delta T} \Delta V_n \qquad\qquad (2.46)$$

$$W_n^{T\,(k-1)} = \sum^{\Delta T} \Delta W_n . \qquad\qquad (2.47)$$

The contributions of the local rotational degrees of freedom ($\Delta\alpha_n$ and $\Delta\beta_n$), occurring at different iterations to the total accumulated global displacements $u^{T\,(k-1)}$, $v^{T(k-1)}$, $w^{T\,(k-1)}$ can be expressed using the terms $\alpha x_n^{T\,(k-1)}$, $\alpha y_n^{T(k-1)}$ and $\alpha z_n^{T(k-1)}$, respectively. These terms represent special rotations which when multiplied by the shape functions M_{ln} lead to the components of the through thickness accumulated displacements in the global

x, y and z axes, respectively, and are evaluated using the following equations:

$$\alpha x_n^{T\ (k-1)} = \sum^{\Delta T} l_{11}^n \Delta \alpha_n - l_{21}^n \Delta \beta_n \tag{2.48}$$

$$\alpha y_n^{T\ (k-1)} = \sum^{\Delta T} l_{12}^n \Delta \alpha_n - l_{22}^n \Delta \beta_n \tag{2.49}$$

$$\alpha z_n^{T\ (k-1)} = \sum^{\Delta T} l_{13}^n \Delta \alpha_n - l_{23}^n \Delta \beta_n . \tag{2.50}$$

Similarly, the contributions of the local rotational degrees of freedom ($\Delta \phi_n$ and $\Delta \psi_n$) occurring at different iterations to the total global displacements $u^{T\ (k-1)}$, $v^{T\ (k-1)}$, $w^{T\ (k-1)}$, can be expressed using the terms $\beta x_n^{T\ (k-1)}$, $\beta y_n^{T\ (k-1)}$, $\beta z_n^{T\ (k-1)}$, respectively, which are evaluated using the following equations:

$$\beta x_n^{T\ (k-1)} = \sum^{\Delta T} l_{11}^n \Delta \phi_n - l_{21}^n \Delta \psi_n \tag{2.51}$$

$$\beta y_n^{T\ (k-1)} = \sum^{\Delta T} l_{12}^n \Delta \phi_n - l_{22}^n \Delta \psi_n \tag{2.52}$$

$$\beta z_n^{T\ (k-1)} = \sum^{\Delta T} l_{13}^n \Delta \phi_n - l_{23}^n \Delta \psi_n . \tag{2.53}$$

In view of the above considerations, the total global displacements at the (k-1)th iteration at time T can be given by:

$$\begin{Bmatrix} u^{T\ (k-1)} \\ v^{T\ (k-1)} \\ w^{T\ (k-1)} \end{Bmatrix} = \sum_{n=1}^{13} \bar{N}_n \begin{Bmatrix} U_n^{T(k-1)} \\ V_n^{T(k-1)} \\ W_n^{T(k-1)} \end{Bmatrix} + \sum_{n=1}^{13} N_n\ M_{1n} \begin{Bmatrix} \alpha x_n^{T(k-1)} \\ \alpha y_n^{T(k-1)} \\ \alpha z_n^{T(k-1)} \end{Bmatrix} + \sum_{n=1}^{13} N_n\ M_{2n} \begin{Bmatrix} \beta x_n^{T(k-1)} \\ \beta y_n^{T(k-1)} \\ \beta z_n^{T(k-1)} \end{Bmatrix} . \quad (2.54)$$

Using the transformation matrix $[\theta]$ defined in Section 2-2-2, the total local displacements at the $(k-1)^{th}$ iteration can be obtained from the following equations:

$$\begin{Bmatrix} u'^{T(k-1)} \\ v'^{T(k-1)} \\ w'^{T(k-1)} \end{Bmatrix} = \sum_{n=1}^{13} \bar{N}_n\ [\theta] \begin{Bmatrix} U_n^{T(K-1)} \\ V_n^{T(K-1)} \\ W_n^{T(K-1)} \end{Bmatrix} + \sum_{n=1}^{13} N_n\ M_{1n}\ [\theta] \begin{Bmatrix} \alpha x_n^{T(k-1)} \\ \alpha y_n^{T(k-1)} \\ \alpha z_n^{T(k-1)} \end{Bmatrix} + \sum_{n=1}^{13} N_n\ M_{2n}\ [\theta] \begin{Bmatrix} \beta x_n^{T(k-1)} \\ \beta y_n^{T(k-1)} \\ \beta z_n^{T(k-1)} \end{Bmatrix}$$

$$(2.55)$$

Using Equation 2.55 and the same procedure described in Section 2-5-2, the derivatives of the total local displacements with respect to the local axes can be obtained and are given in the following form:

$$\begin{Bmatrix} u'^{T\ (k-1)}_{i,x'} \\ u'^{T\ (k-1)}_{i,y'} \\ u'^{T\ (k-1)}_{i,z'} \end{Bmatrix} = \sum_{n=1}^{13} [B'_n] \begin{Bmatrix} U_n^{T\ (k-1)} \\ V_n^{T\ (k-1)} \\ W_n^{T\ (k-1)} \\ \alpha x_n^{T\ (k-1)} \\ \alpha y_n^{T\ (k-1)} \\ \alpha z_n^{T\ (k-1)} \\ \beta x_n^{T\ (k-1)} \\ \beta y_n^{T\ (k-1)} \\ \beta z_1^{T\ (k-1)} \end{Bmatrix} \qquad\qquad (2.56)$$

where $u'_1 = u'$, $u'_2 = v'$ and $u'_3 = w'$ and

$$[B'_n] = \begin{bmatrix} l_{i1}h_{n,1} & l_{i2}h_{n,1} & l_{i3}h_{n,1} & l_{i1}H_n^1 & l_{i2}H_n^1 & l_{i3}H_n^1 & l_{i1}G_n^1 & l_{i2}G_n^1 & l_{i3}G_n^1 \\ l_{i1}h_{n,2} & l_{i2}h_{n,2} & l_{i3}h_{n,2} & l_{i1}H_n^2 & l_{i2}H_n^2 & l_{i3}H_n^2 & l_{i1}G_n^2 & l_{i2}G_n^2 & l_{i3}G_n^2 \\ l_{i1}h_{n,3} & l_{i2}h_{n,3} & l_{i3}h_{n,3} & l_{i1}H_n^3 & l_{i2}H_n^3 & l_{i3}H_n^3 & l_{i1}G_n^3 & l_{i2}G_n^3 & l_{i3}G_n^3 \end{bmatrix}$$

(2.57)

Note that $h_{n,i}$, H_n^i and G_n^i are defined by Equations 2.42 to 2.44.

It should be pointed out that a simple algebraic summation for the incremental displacement degrees of freedom obtained from all incremental solutions can be performed since these degrees of freedom are all directed along the same axis. However, an algebraic summation of the incremental rotations resulting from the incremental solutions is not possible because the direction cosines of the axes, about which these rotations are taken, vary because of the large deformations. This explains why Equations 2.48 to 2.53 have been considered in calculating the contributions of the incremental rotational degrees of freedom to the total displacements at time T.

Although a Total Lagrangian approach is used in this formulation, it is necessary to update the geometry. Therefore, the direction cosines between the local and the global axes l_{ij} are updated after each iteration. This ensures that the rotation degrees of freedom are always about the local axes which inturn are tangent to the middle surface during the iterations performed for each load increment.

2-6 Strain Hardening Plasticity Model

To perform inelastic analyses of liquid-filled conical steel tanks under both static and seismic loads, it was decided to incorporate a plasticity model for structural steel

which is able to simulate both the loading and the unloading behaviour. The non-linear behaviour for steel can be realistically described through the use of a bilinear isotropic strain hardening constitutive model and a yield criterion which is independent of the hydrostatic pressure. Using the Huber/Von-Mises yield criterion and its associated flow rule, non-linear behaviour of the material, as given by Chen and Han (1988), can be modelled using the following steps:

1) The effective plastic strain ϵ_p is equated to zero at the first iteration of the first load increment.

2) The stress deviator $\overline{S}_{ij}$ and its second invariant J2 are calculated using the following equations:

$$\overline{S}_{ij} = S_{ij} - \frac{1}{3} \delta_{ij} S_{kk}$$

$$J2 = \frac{1}{2} \overline{S}_{ij} \overline{S}_{ij}.$$

3) Using the uniaxial stress-strain relation, the effective stress is dependent on the effective plastic strain in the strain hardening region and is given by the following relation:

$$\sigma_e = \epsilon_p \left(\frac{E_T \, E}{E - E_T} \right) + \sigma_Y.$$

4) Both the yield surface F and the variation d(J2) of the second invariant J2 are calculated using the following equations:

$$F = J2 - \frac{\sigma_e^2}{3}$$

$$d(J2) = \overline{S}_{ij} \Delta S_{ij}.$$

Three possibilities may occur here depending on the calculated values of F and d(J2). These are presented below.

a) F < 0

The material is still in the elastic range and the constitutive relation can be described by the elasticity matrix [D'] given by Equation 2.33.

b) F ≥ 0 and dJ2 < 0

The material is subjected to unloading and the constitutive relation is still given by the stress reversal matrix [D'] given by Equation 2.33 for elastic increments.

c) F ≥ 0 and dJ2 > 0

The yield surface is reached and the material is under a plastic loading condition, hence the constitutive matrix is given by:

$$[D'_{eff}] = [D'] + [D'_p]$$

where [D'$_p$] is the inelastic constitutive matrix which results as a consequence of plastic deformations. Using the three dimensional expression for the elasto-plastic matrix [D$_p$] given by Chen and Han (1988), the corresponding matrix [D'$_p$] for a shell element is presented in Appendix D2. The incremental plastic strain tensor and the effective incremental plastic strain are then calculated using the following expressions:

$$de^P_{ij}=\frac{1}{4H_p}\ \sigma^2_e\ S_{ij}\ dJ2$$

$$de_p=\sqrt{\frac{2}{3}de^P_{ij}\ de^P_{ij}}$$

where H_p is as defined in Appendix D2.

This effective incremental plastic strain is then used to update the total effective plastic strain as:

$$e_p=e_p+de_p.$$

Steps 2 to 4 are repeated at each iteration of the time step ΔT until a convergent solution within a certain tolerance is achieved.

2-7 Solution Technique

The matrices $[B_L^{T\,(k-1)}]$, $[B_S^{T\,(k-1)}]$, $[S^{T\,(k-1)}]$, $\{S^{T\,(k-1)}\}$ and the appropriate constitutive matrix ($[D']$ or $[D'_{eff}]$) are substituted into Equations 2.23 to 2.25 to evaluate the stiffness matrices $[K_L^{T\,(k-1)}]$ and $[K_S^{T\,(k-1)}]$ and the unbalanced load vector $\{F^{T\,(k-1)}\}$ at the kth iteration at time T for each element. The external load vector $\{R^T\}$, which depends on the type of the applied external load, can also be evaluated using the expression for the work done by the external loads. It should be noted here that the dimensions of the stiffness matrices and the load vectors are 91 by 91 and 91 by 1, respectively. However, these dimensions include a large number of zero terms which correspond to the inactive degrees of freedom at certain nodes as explained in Section 2-2-2.

The stiffness matrices and the load vectors are obtained through numerical

integration using the Gaussian Quadrature scheme. Seven integration points in the r-s plane (tangent plane) and five integration points along t (perpendicular to the tangent plane) are used. Note here that all terms in the matrices $[B_L^{T\,(k-1)}]$ and $[B_S^{T\,(k-1)}]$ which have either a superscript or a subscript n are evaluated at the nodal points, while the rest of the terms are evaluated at the integration points.

The frontal solution method (Irons 1970, Hintin and Owen 1977) is used to assemble the stiffness matrices $[K_L^{T\,(k-1)}]$ and $[K_S^{T(k-1)}]$ and the load vectors $\{F^{T(k-1)}\}$ and $\{R^T\}$ for all elements. These are then substituted into Equation 2.22 to solve for $\{\Delta U\}$ using the Newton-Raphson method. During each load increment corresponding to a time interval ΔT, the external load vector $\{R\}$ is kept constant. However, both the stiffness matrices $[K_L]$ and $[K_S]$ as well as the unbalanced load vector $\{F\}$ are updated during each iteration in this time interval until a convergent solution within a specified tolerance is achieved.

To update the stiffness matrices and the unbalanced load vector for the kth iteration, the following steps are performed.

1)   The incremental displacement and rotational degrees of freedom obtained from the solution of the $(k-1)^{th}$ iteration are used to update the global coordinates $(x_n, y_n$ and $z_n)$ and the vector V_{3n} at each node of the element.

2)   The updated nodal coordinates and vectors are used, as described in Appendix C, to obtain the updated components of the matrices $[\theta]$ and $[V_n]$ which represent the relative direction cosines between the local and the global axes at the integration points and at the nodes, respectively. These are then used to update the matrix

$[C_n]$ given by Equation 2.8.

3) The incremental degrees of freedom corresponding to the solution from the $(k-1)^{th}$ iteration are also used to update Equations 2.45 to 2.57 in order to obtain the components of the initial strains $u'_{i,j}{}^{T\,(k-1)}$ prior to the kth iteration. These, together with the updated matrix $[C_n]$, are used to update the matrix $[B_L{}^{T\,(k-1)}]$ which is given in Appendix E.

4) The incremental stresses at the integration points resulting from the $(k-1)^{th}$ iteration are obtained using Equations 2.30 to 2.32 and are used to update the matrix $[S^{T\,(k-1)}]$ and the vector $\{S^{T\,(k-1)}\}$ given by Equations 2.28 and 2.29.

5) Using both the updated total and the incremental stresses, and following the procedure given in section 2.6, the appropriate constitutive matrix $[D']$ for elastic behaviour or $[D'_{eff}]$ for inelastic behaviour is determined.

6) The appropriate constitutive matrix, the updated matrices $[B_L{}^{T\,(k-1)}]$, $[S^{T\,(k-1)}]$ and stress vector $\{S^{T\,(k-1)}\}$ as well as the constant matrix $[B_S]$ are substituted into Equations 2.23 to 2.25 to obtain both the updated stiffness matrices $[K_L{}^{T(k-1)}]$ and $[K_S{}^{T(k-1)}]$ and the updated load vector $\{F^{T(k-1)}\}$. These, together with the external load vector $\{R^T\}$, are substituted into Equation 2.22 to solve for the incremental displacements corresponding to the kth iteration.

The solution proceeds in an iterative manner until a convergent solution within a specified tolerance is reached. The energy tolerance, as described by Bathe (1982), is employed to check the convergence of the solution and uses the ratio of the work done during the iteration to the work done during the first iteration.

Assume that M iterations are needed to reach equilibrium, within a specified tolerance, at the configuration T. The equilibrium solution $\{U^T\}$ at time T is obtained using the equilibrium solution $\{U^{T-\Delta T}\}$ at the previous time (T-ΔT) and the solutions resulting from those M iterations as follows:

$$\{U^T\}=\{U^{T-\Delta T}\}+[\{\Delta U^{(1)}\}+\{\Delta U^{(2)}\}+.+.+. \qquad .\{\Delta U^{(M)}\}].$$

This equilibrium solution $\{U^T\}$ is then used to obtain the initial strains and stresses for the first iteration of the following configuration (T+ΔT). The solution then proceeds in the same iterative manner to achieve equilibrium at time (T+ΔT).

2-8 Numerical Examples

2-8-1 Large Deflection of Simply Supported Plate Under Uniform Load

A square plate with simply supported edges and subjected to a uniformly distributed load is analyzed using the consistent triangular shell element with large displacements. The elastic properties of the plate are: the Modulus of elasticity E=71020.0 MPa and the Poisson 's ratio ν=0.316. The plate dimensions are taken as 16" * 16" * 1/2" (406.4 * 406.4 * 12.7 mm) as shown in Figure 2.2. Due to the double symmetry in geometry and loading, only one quarter of the plate is considered in the analysis. It should be noted that for this particular plate problem, the local x´ and y´ axes coincide with the global x and y axes, respectively. For the simply supported boundary conditions of the quarter plate, the following boundary conditions result for edge displacements and rotations consistent with the physical constraints of the problem.

$u=v=w=\beta=\psi=0$ along AB

$u = v = w = \alpha = \phi = 0$ along BC

$u = \alpha = \phi = 0$ along OC

$v = \beta = \psi = 0$ along OA.

The central deflection w resulting from the analysis, using thirty two consistent shell elements to model one quarter of the plate, is plotted against the load intensity q in Figure 2.3 using the dimensionless parameters (qa^4/Eh^4) and (w/h). Here, a and h are the length and the thickness of the plate, respectively. The corresponding load-deflection curves resulting from an analytical solution by Lin et al. (1972) and a finite element study carried out by Ostrowski (1984), using the non conforming plate bending element, are also presented. A comparison of the load-deflection curves indicates good agreement between the results of the analysis carried out using the consistent shell elements and the other finite element and analytical solutions. Two grids, one with eight elements and the other with seventy two elements, are used in the analysis using the consistent shell element. It is interesting that the eight element (2*2) grid yields about identical results as those obtained by Ostrowski using thirty six non conforming plate bending elements. Of interest, also, is that the eight, thirty two and seventy two consistent shell element grids result in almost identical curves which indicates excellent efficiency of the element in handling elastic plate bending problems.

2-8-2 Large Deflection of a Shallow Arch

The elastic stability analysis of a clamped shallow arch due to a point load at its apex is carried out by performing a large deflection analysis of the arch, again using the consistent shell element. The arch dimensions and its material properties are shown in

Figure 2.4. The apex deflections resulting from the analysis using twenty consistent shell elements to model one half of the arch are plotted versus the point load intensities in Figure 2.5. Alternative solutions given by Bathe et al.(1975) using eight nodes isoparametric shell element and by Mallet and Berhe (1966) employing four 'equilibrium-based ' element, are also plotted in the figure. Excellent agreement in the magnitudes of the apex deflections resulting from the consistent shell element analysis and those obtained by Mallet et al. and Bathe et al. can be observed. It can also be concluded from Figure 2.5 that the limit of the buckling load obtained from the analysis using the consistent shell element and the one given by Mallet et al. are almost identical. An experimental study for the same arch was carried out by Gjelsvik and Bodner (1962). They obtained a buckling load which is about 10% lower than the predicted value by the consistent shell element. However, it should be noted that there would have been imperfections in the experiment which are not considered in the finite element analysis. Therefore, the author believes that the results obtained in this study are satisfactory.

2-8-3 Large Deflection of a Clamped Cylindrical Panel

Large displacement analysis of a cylindrical panel, subjected to uniform normal pressure and clamped at all four boundaries, is also being undertaken. The panel is assumed to have a thickness of 0.125" (3.175 mm) while the other dimensions of the shell are shown in Figure 2.6. The elastic material properties used in the analysis are: Modulus of Elasticity E=450,000 psi and the Poisson's ratio ν=0.3. Due to the double symmetry in geometry and loading, only one quarter of the panel is considered in the finite element analysis. The quarter panel is modelled using eight and thirty two

consistent shell elements. The boundary conditions along the four edges of the quarter

panel are described by displacements along the global axes and rotations about the local

axes in the following manner:

$u=v=w=\alpha=\beta=\phi=\psi$ along AB and BC

$u=\alpha=\phi=0$ along OC

$v=\beta=\psi=0$ along OA.

Central deflection resulting from the consistent shell element analyses is plotted

versus the normal pressure intensity in Figure 2.7. It should be mentioned here that the

eight and thirty two consistent shell element analyses yield identical results for the central

displacement. This problem was also studied by Brebbia and Connor (1969) in which

they used sixty four non-confirming rectangular plate bending elements to model one

quarter of the panel. Comparison of the results obtained from the consistent shell element

analyses with those given by Brebbia and Connor shows a very good agreement in the

load deflection curves. Again, it is important to note that fewer consistent shell elements

give either comparable or perhaps even a more accurate response compared with the non

conforming rectangular plate element analysis.

2-9 Comparison of the Consistent Shell Element Analysis with Experimental Results

In an experimental program conducted by Daali and Korol (1994), test specimens

were fabricated as cantilever beams and had the geometric properties as given in Table

2.1. These specimens were subjected to a downward tip loading as shown in Figure 2.8.

The limit load, at which the stiffness of each specimen vanishes, was recorded. The

stiffness degradation in this problem results from the spread of plasticity in the region adjacent to the support and also due to the geometric effect in the form of local large deformations at both the bottom part of the web and the bottom flange in the form of local buckling.

Daali and Korol's specimens are again modelled using the consistent shell element. The finite element mesh used is shown in Figure 2.8. The double node concept is used at the intersections between the web and the top and bottom flanges where compatibility in the displacements and in the rotations about the common axis between the flange and the web (y-axis in Figure 2.8) are imposed. The rotations about the other in plane local axes of the web (z) and the flange (x) are assumed independent. The initial geometric imperfections which existed in the beams before loading were measured by Daali and Korol. These have been incorporated into the finite element analysis as initial strains.

As was obtained in the experiments, the finite element results also show that the limit loads for the specimens are reached after spread of plasticity near the support. The limit loads obtained from the finite element analysis are tabulated in Table 2.1 and are compared to the corresponding values obtained from the experiments indicating very good agreement. The localized buckling of the bottom flange near the support, as observed in the experiments by Daali and Korol, are also obtained in the finite element simulations.

Specimen	Cross Section	Length (mm)	Limit Loads (KN) (Experiment.)	Limit loads (KN) (Analysis)
A0	W 310*21	2100	48.16	50
P1	W 310*39	2100	113.59	116
B0	W 310*21	1200	86.29	96

Table 2.1 Comparison Between Numerical and Experimental Results

for the Limit Loads of Cantilever Beams.
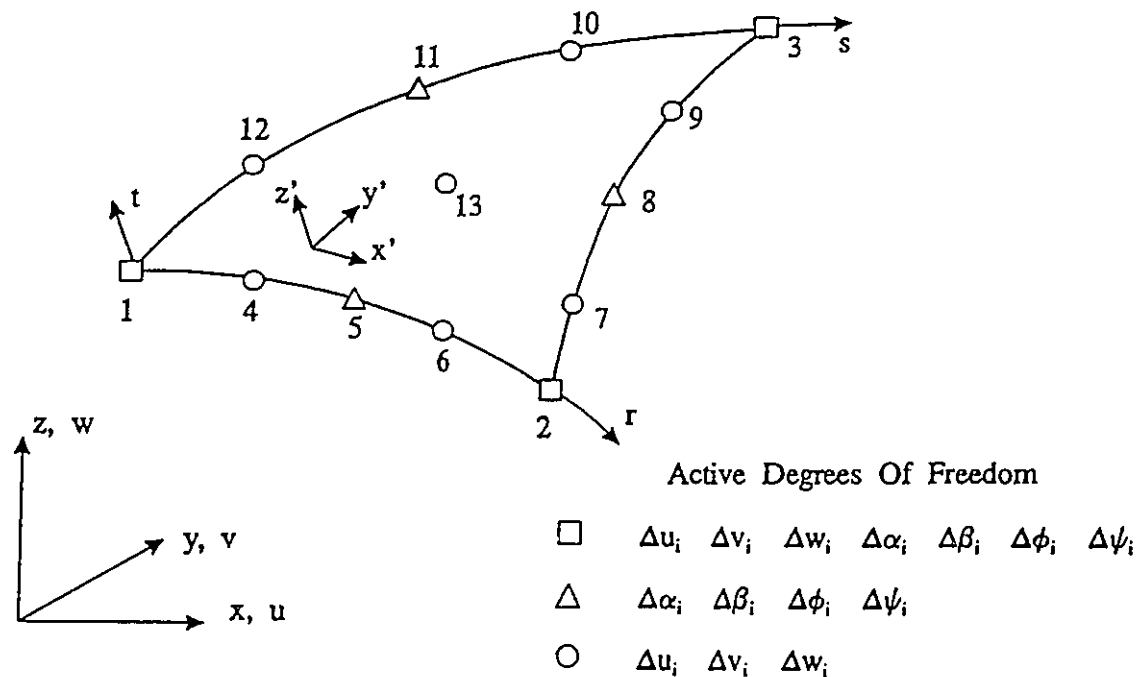
Figure 2.1 Consistent Shell Element Coordinate Systems and Nodal

Degrees of Freedom.
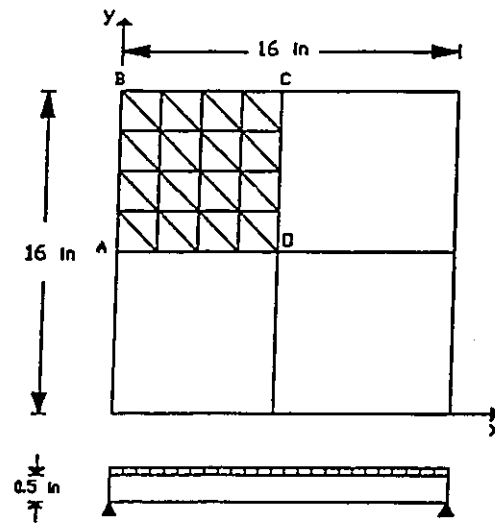
(1 in = 25.4 mm)

Figure 2.2 Simply Supported Square Plate Under Uniform Load (32 Elements).
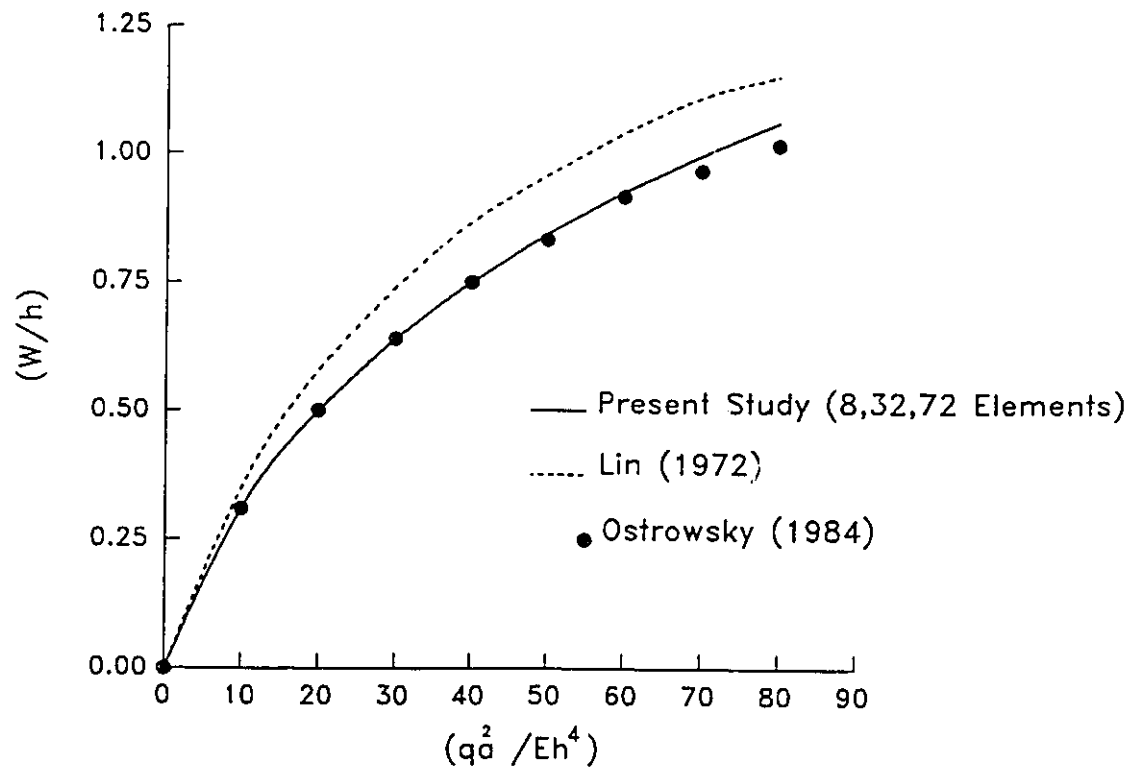
Figure 2.3 Large Deflection Behavior of the Square Plate.
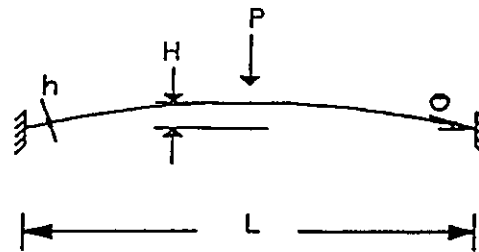
R=133.14 in
h=3/16 in
b=1.0 in (width)
L=34.0 in
H=1.09 in
θ=7.3397°
A=0.188 in^2
I=0.00055 in^4
E=10*10^6 psi   (1 in=25.4mm)
ν=0.2   (1 psi=6895 N/m^2)

Figure 2.4 Shallow Arch Subjected to a Point Load at its Apex.
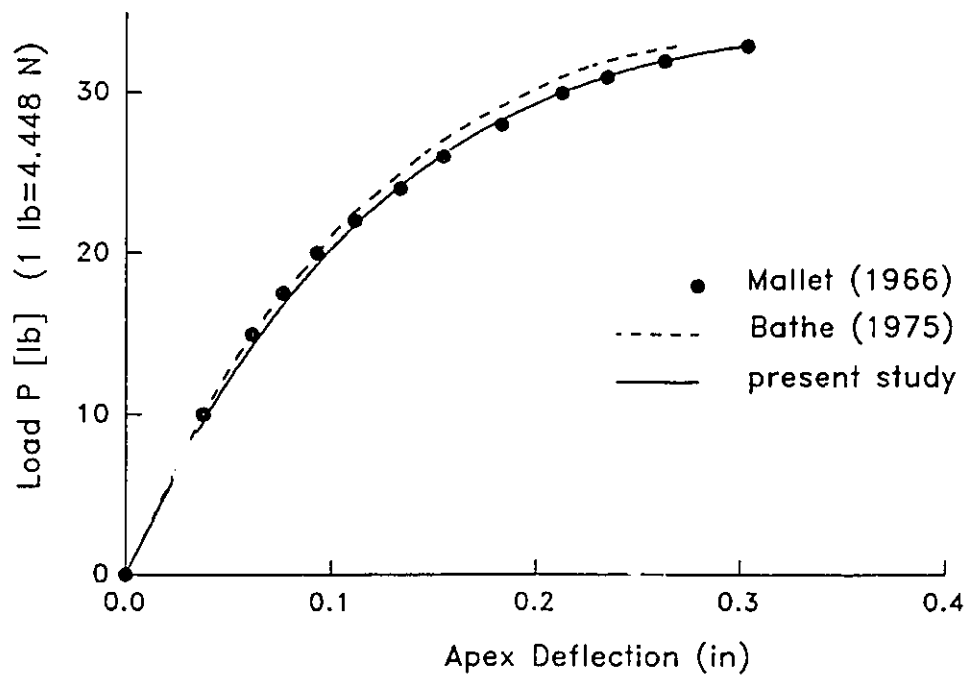
Figure 2.5 Load Deflection Curves for the Shallow Arch.
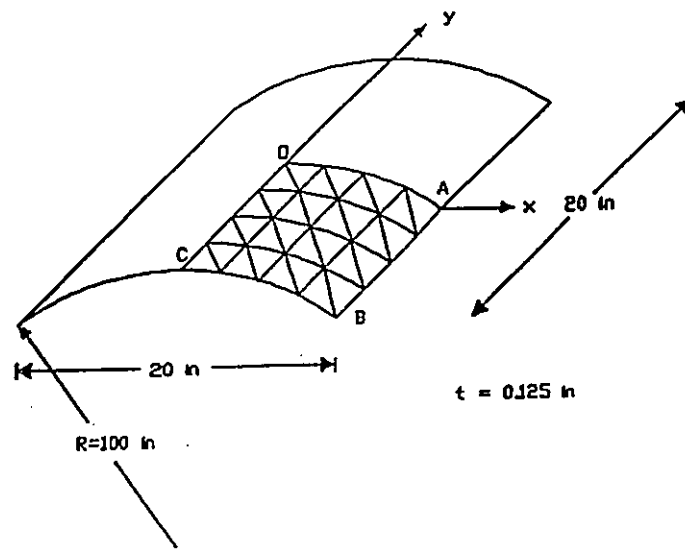
Figure 2.6 Clamped Cylindrical Panel Subjected to Normal Uniform Pressure.

Central Deflection (in)   (1 in = 25.4 mm)
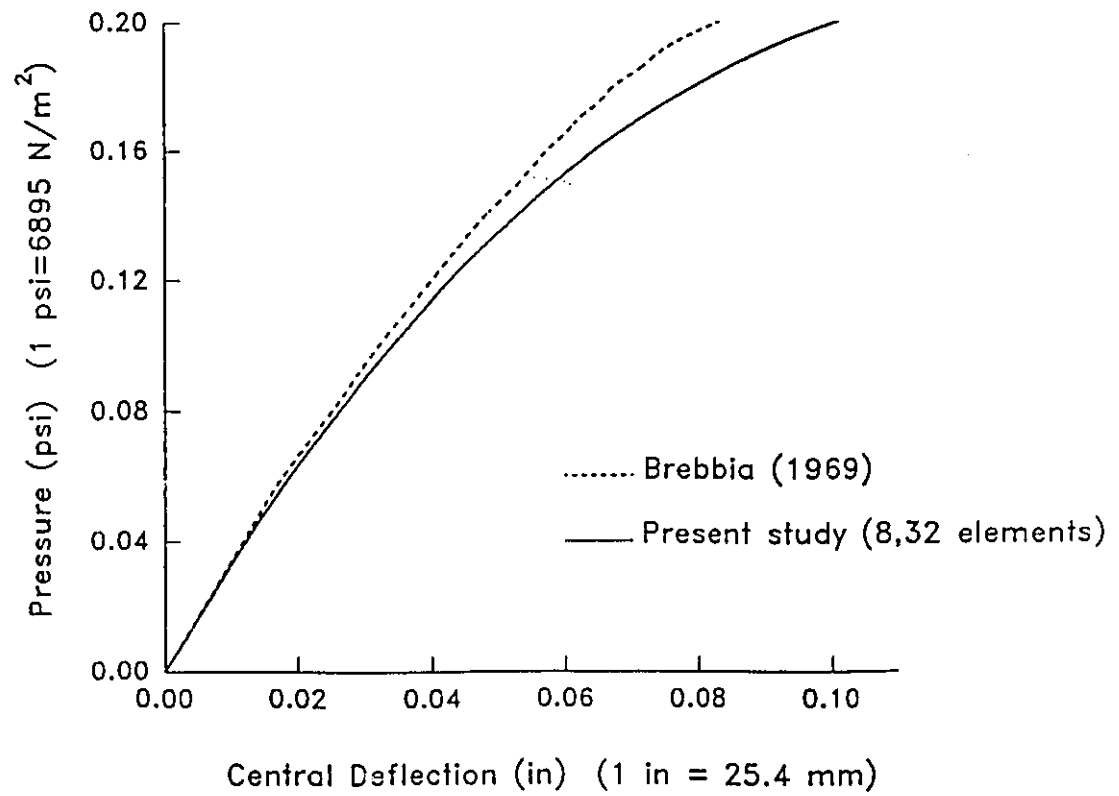
Figure 2.7 Load Deflection Curves for the Clamped Cylindrical Panel
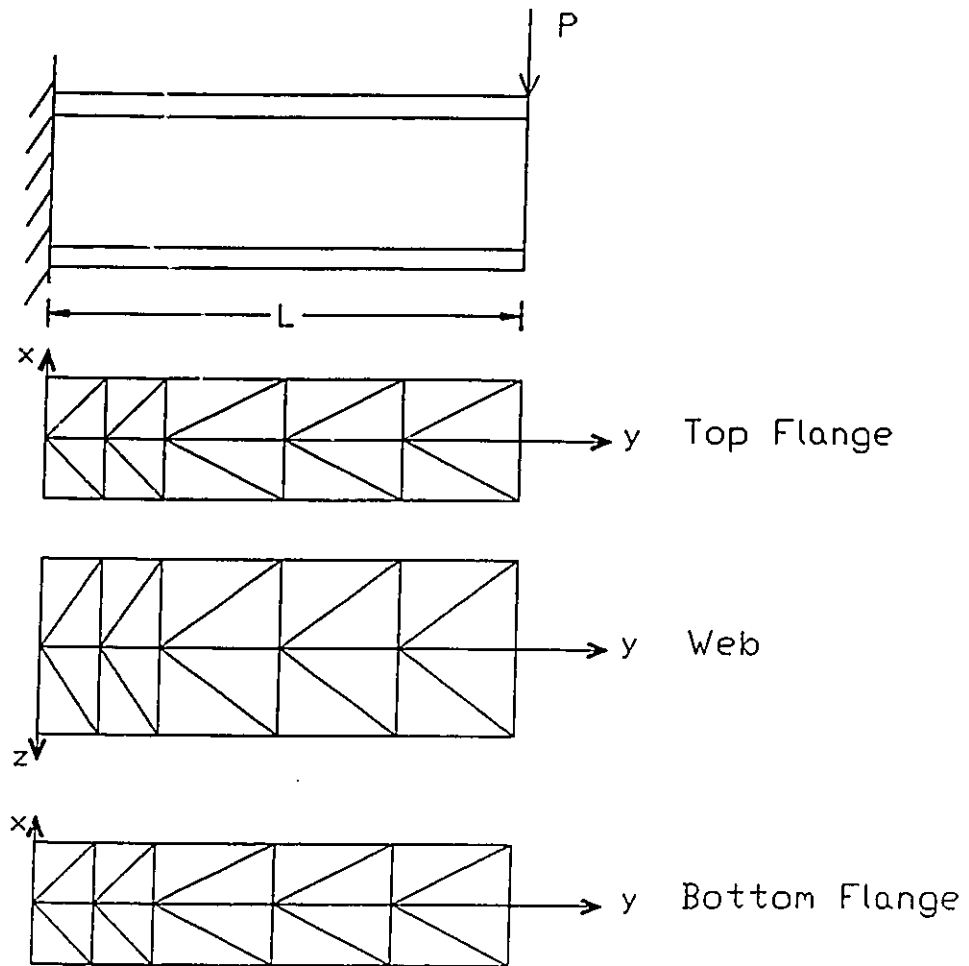
Figure 2.8 Finite Element Mesh for a W-Shaped Cantilever Beam.

CHAPTER THREE

STABILITY OF IMPERFECT LIQUID FILLED CONICAL TANKS

3-1 Introduction

The consistent triangular shell element presented in Chapter Two, is now used to model the liquid-filled conical tanks and to study the stability of such tanks under static loading. The ensuing finite element model includes geometric and material non-linearities and is capable of modelling both initial geometric imperfections and residual stresses due to welding.

The finite element model is first used for elastic stability analyses of liquid-filled perfect tanks and the numerical results obtained are then compared with those available in the literature. Because of geometric imperfections usually present in shell structures and which appear in some random pattern, it has been decided to determine the imperfection shape that would lead to the lowest limit load. As such, tanks with different imperfection patterns are analyzed to determine the critical imperfection shape. Limit loads resulting from the elastic stability analyses of tanks with critical imperfection shapes are then compared with the results obtained from the experimental study for a large number of model cones loaded hydrostatically (Vandepitte et al. 1982).

A strain hardening plasticity model is employed and the resulting limit loads from the inelastic stability analyses undertaken are predicted for perfect tanks. To study the

sensitivity of liquid-filled conical tanks to geometric imperfections and welding residual stresses, these limit loads are compared to those resulting from the analyses of two different cases; the first is the case of tanks with only geometric imperfections, and the second case involves tanks having both geometric imperfections and residual stresses due to welding. Finally, inelastic stability analyses are performed for the tank which failed in Fredericton, and both the limit loads and transverse meridional deflection resulting from the analyses are compared to those given by Vandepitte (1990) in a special report written in response to study the collapse of the structure.

3-2 Cause of Failure of Conical Tanks

As was mentioned in Chapter One, this study was motivated by the failure of a liquid-filled elevated water tank in Fredericton, New Brunswick, Canada in December 1990. It was reported by Korol (1991) and then by Dawe et al. (1993) that the collapse of this structure was precipitated by a buckling failure in the lower cone of the steel water storage cell. This was as a result of inadequate thickness of the steel containment cell. In order to understand the cause of failure, consider a conical shell with a vertical axis and radius r_1 at the lower end which is simply supported. (See Figure 3.1). The upper rim of the shell is assumed to be free. The cone is partly filled with a liquid of specific weight γ. Considering the toroidal volume bounded by the wall of the shell and the cylindrical surface defined by the vertical generators 1-2 and 1´-2´, the weight of the liquid in this volume of revolution is equilibrated by the compressive meridional stresses σ_{act} acting along the circle 1´-1 as shown in Figure 3.1. Since the weight of the toroidal volume increases and the perimeter of the horizontal circle decreases at progressively

lower sections, very high meridional compressive forces develop near the base of the shell. It should be also noted that there are tensile hoop stresses in the circumferential direction. When the level of the liquid in the conical vessel is elevated, large compressive stresses will develop and may cause the bottom part of the shell to buckle despite the stabilizing effect of the circumferential tensile stresses. The geometric imperfections, usually present in real shell structures, will induce more bending in the structure. This in conjunction with large compressive meridional stress may precipate instability of the tank at a lower level of liquid than for the case of a perfect tank. It should be also noted that for the case of strain hardening material behaviour, yielding may precede buckling. In this case, the residual stresses due to welding will also contribute to inelastic buckling and hence reduce the limit load of the shell even further.

3-3 Practice Design Codes for the Stability of Conical Tanks

As previously mentioned in Chapter One, the current codes of practice for the design of water structures do not directly specify design rules for liquid-filled conical tanks. Some design codes like the Danish standard DNV (1982) and the German code DAST (1980), as well as the industrial standards in North America based on the AWWA D-100 (1984) specifications, suggest the use of an equivalent cylinder when studying the stability of conical tanks subject to hydrostatic pressure. A brief description about the DNV code is given by Ellinas et al. (1984). In all of the above-mentioned codes and specifications, the geometry of the equivalent cylinder shell is given by:

$$r_{eq} = \frac{r_1 + r_2}{2\cos\theta_v}, \qquad h_{eq} = \frac{h}{\cos\theta_v}, \qquad t_{eq} = t,$$

where r_1 is the radius at the base of the cone; r_2 is the radius at the top of the cone; r_{eq} is the radius of the equivalent cylinder; θ_v is the inclination of the wall of the cone with the vertical; h is the height of the cone; h_{eq} is the height of the equivalent cylinder; t is the thickness of the cone and t_{eq} is the thickness of the equivalent cylinder.

According to the DNV code and the AWWA standards, the maximum permissible compressive stress of the equivalent cylinder σ_{cr}, can be calculated using the equations presented in Appendix F. Note that these equations incorporate the effect of instability, plasticity and imperfections.

For liquid-filled conical tanks, the maximum membrane meridional stress can be calculated using the following equation:

$$\sigma_{act} = \frac{P}{2\pi\, r_1\, t\, \cos\theta_v}$$

where P is defined as the sum of the vertical forces acting on a section at the base of the vessel.

The stability of the liquid-filled conical tank can be studied according to any of the above mentioned codes, by comparing the above calculated meridional compressive stress σ_{act} to the maximum permissible compressive stress σ_{cr} of the equivalent cylinder. According to this method, the tank is presumed safe against instability if $\sigma_{act} \leq \sigma_{cr}$.

3-4 Experimental Study at Ghent University

An extensive experimental investigation of buckling of conical shells filled with liquids was carried out by Vandepitte et al. (1982). This experimental study led to design guide lines in the form of diagrams and design formulae which can be used directly in

the design of such shells. These diagrams are used for comparison with the results obtained from the numerical analyses carried out in this study.

In their experimental program, hundreds of model cones covering a wide range of the parameters θ_v and $r_1/(t \cos\theta_v)$ were tested. Initial imperfections had been measured for each specimen by Vandepitte et al. before testing. They classified the specimens as good or poor cones according to the deviation from perfect geometry ratio $(\overline{w}/l_r)$ as noted in Figure 3.2, where r_1 is the lower radius of the cone; t is the thickness of the wall of the cone; θ_v is the angle of inclination of the wall of the cone with the vertical axis; l_r is the mean calculated total meridional wave length of the buckle adjoining the support of the cone based on numerical analysis and $\overline{w}$ is the largest inward amplitude of any dent or depression.

Following the analysis of Vandepitte et al., the average buckling wave length was found to be given by

$$l_r = 3.6 \sqrt{\left(\frac{r_1 t}{\cos\theta_v}\right)} . \qquad (3.1)$$

In their assessment, when :

$\overline{w} \le 0.008 \, l_r$, the shell is considered a good cone.

$0.02 \, l_r > \overline{w} > 0.008 \, l_r$, the shell is classified a poor cone.

Each specimen was gradually filled with water until it collapsed with the height of water h at buckling recorded. The results of the experiments were presented through use of two dimensionless parameters, ψ and ω, where

$$\psi = \frac{\sigma_{act} \, t \, \sin\theta_v}{\gamma r_1^2} = \frac{1}{2} \, (1 + \frac{h \, \tan\theta_v}{3r_1}) \, (\frac{h \, \tan\theta_v}{r_1})^2 \qquad (3.2)$$

$$\omega = 1000 \, (\frac{2\gamma r_1^3 \sqrt{1-\gamma^2}}{Et^2 \sin(2\theta_v)})^{\frac{1}{2}} . \qquad (3.3)$$

E and ν are the modulus of elasticity and the Poisson's ratio, respectively, for the material used. In the equations above, σ_{act} is the meridional stresses at the bottom of the cone, given by

$$\sigma_{act} = \frac{\gamma h^2 (r_1 + \frac{h \, \tan\theta_v}{3}) \, \tan\theta_v}{2 \, r_1 \, t \, \cos\theta_v} . \qquad (3.4)$$

Figure 3.3 shows the Vandepitte relation between the dimensionless parameters ω and ψ expressed in logarithmic form. The upper dashed straight line (short dashes) represents results of finite difference analyses for perfect cones using the program BOSOR4 (Bushnell, 1974). This program assumes linear elastic behaviour for the material and takes account of the non-linear relationships between deformations and displacements. The line itself is described by the following equation:

$$\psi = 43400\omega^{-1.946} . \qquad (3.5)$$

The dots represent the experimental results of Vandepitte at al. (1982), while the lower solid straight line represents the lower limit of the experimental results such that ψ has a 99% probability of being surpassed by the experimental points. The lower dashed line has the same description as the previous straight line except for 99.9% probability of experimental results surpassing it. Also, based on these experimental results, the

following expressions relating ω and ψ were suggested:

$$\psi = 37500\omega^{-1.710} \quad \text{(poor cone)} \tag{3.6}$$

$$\psi = 37900\omega^{-1.686} \quad \text{(good cone)} \tag{3.7}$$

Vandepitte et al.(1982) suggested the use of Equations 3.6 and 3.7 to design liquid-filled conical tanks which have a certain degree of expected initial imperfections. As a matter of fact, these equations are incorporated in the European Recommendations relating to shell buckling, published by the Convention for Constructional Steelwork (1988). It must be realized that the meridional stresses σ_{act} calculated by Equation 3.4, just before the collapse of the models, were found to be less than half the yield stress of the material (σ_y /2). The investigators (Vandepitte et al.) predicted that the meridional stress and the hoop stress together will give an effective stress which is less than σ_y. Therefore, it is incumbent that they assumed elastic buckling for the collapse. This particular point will be elaborated upon later in the light of the finite element model results.

3-5 Geometric Imperfections

Geometric imperfections play an important role in determining the limit load capacities of real shells. The initial imperfection pattern depends on the method of construction of the shell. As was mentioned in Chapter One, the reported measurements of imperfections in civil engineering shell structures are quite rare. To be on the conservative side in the design, the imperfection pattern can be assumed as a wave having the same wave length as of the first buckling mode of a perfect tank. This is

expected to lead to the lowest limit load for the corresponding imperfect tank.

In this study, two imperfection patterns are assumed. The first shape is an axisymmetric imperfection described by the following equation:

$$w^* = w_o \sin\left(\frac{2\pi S}{l_r}\right)$$ (3.8)

where w^* is the imperfection perpendicular to the tank surface; w_o is the amplitude of the imperfection wave; S is the distance measured along a generator of the tank; l_r is the wave length of the imperfection and it is assumed equal to the wave length of the first buckling mode of the perfect tank. (See Figure 3.4).

The second shape consists of a circumferential imperfection wave superimposed on the above described axisymmetric imperfection. The resulting deviation pattern is described by the following equation:

$$w^* = w_o \sin\left(\frac{2\pi S}{l_r}\right) \cos(n\theta) .$$ (3.9)

Here, n is the circumferential wave number of the assumed imperfection shape.

These imperfections are introduced into the finite element model through the terms $u'_{i,j}$ which are included in the non-linear stiffness matrix and represent the initial strain after each iteration. Using equations 3.8 and 3.9, the initial strains, before applying the load, are given by:

$$w'_{,x'}=0 \qquad\qquad\qquad \text{axisymmetric} \qquad (3.10)$$

$$w'_{,y'}=w_o\frac{2\pi}{l_r}\cos\left(\frac{2\pi S}{l_r}\right) \qquad\qquad \text{axisymmetric} \qquad (3.11)$$

$$w'_{,x'}=-\frac{w_o n}{R}\sin\left(\frac{2\pi S}{l_r}\right)\sin(n\theta) \qquad \text{asymmetric} \qquad (3.12)$$

$$w'_{,y'}=w_o\frac{2\pi}{l_r}\cos\left(\frac{2\pi S}{l_r}\right)\cos(n\theta) \qquad \text{asymmetric} \qquad (3.13)$$

where R is the radius of the cross section at which the circumferential imperfections are located; w' is the displacement normal to the surface; x' and y' are the components of the local coordinate system as defined in Section 2-2. Note here that in the finite element analysis the vertical axis of the tank is taken as the global y-axis. As such, the local axis y' coincides with the direction S.

It should be also noted here that the above imperfections amplitude w_o corresponds to $(\bar{w}/2)$ where $\bar{w}$ is the imperfection measure given by Vandepitte et al.(1982) and presented in Section 3-4. Therefore, according to Vandepitte's classification, a conical tank can be considered as a "good cone" if $w_o \le 0.004\ l_r$ and as a "poor cone" if $0.004\ l_r < w_o < 0.01\ l_r$.

3-6 Residual Stresses Due to Welding

Conical steel vessels are usually constructed from steel cylindrical panels which are welded together using circumferential and longitudinal welds. Residual stresses are expected as a result of the welding process and will generally induce an inelastic response

and hence necessitate an inelastic instability analysis of the structure. Such stresses develop as a result of cooling of the weldments and heat affected zones of the parent material. During this cooling, the weld tends to shrink, while the material remote from the weldments remains cool and prevents shrinkage. This process introduces tensile stresses in the vicinity of the welding zone and compressive stresses away from the weld. From statics, both the tensile and compressive stresses are self equilibrating. A mathematical model describing the distribution of residual stresses σ_b around the weld line of a cylinder has been given by Bornscheuer and Hafner (1983). As shown in Figure 3.5, the assumed distribution is parabolic with maximum tensile and compressive stresses equal to two third and one third of the yield stress, respectively. These stresses are localized over a width (transverse to the weldment) equal to sixty times the shell thickness. Based on the above residual stress distribution, the residual stresses arising in conical tanks due to circumferential and longitudinal welding are assumed according to the descriptions below.

3-6-1 Residual Stresses due to Circumferential Welding

Circumferential welding will introduce hoop stresses in the conical shell. These stresses are axisymmetric in magnitude and vary along the tank generator. The stress model proposed by Bornscheuer and Hafner (1983) will not be self-equilibrated if it is assumed to act on conical tanks. This is due to the variation of the surface area along the generator. To overcome this, the proposed stress model is multiplied by a weight function f(y) which decreases with the increase in the surface area. As such, self-equilibrated stresses can be obtained. The resulting residual stresses σ_{rc} and the weight

function are shown in Figure 3.6.

3-6-2 Residual Stresses due to Longitudinal Welding

Longitudinal welding will induce meridional stresses in the conical tank. These are localized over a small circumferential width about the longitudinal weld line. The Bornscheuer model can be used here without modification as shown in Figure 3.7.

Both hoop and meridional stresses are introduced in the finite element model in the form of initial stresses present in the structure before loading.

3-7 Modelling of Conical Tanks

Elevated conical tanks are usually steel vessels consisting of a cylinder superimposed on a cone which is supported by a steel plate resting on a heavily reinforced concrete slab supported in turn by a reinforced concrete tower. (See Figure 3.8). Since the focus of this study is the stability of the steel vessel, the finite element modelling is limited to consideration of the inclined walls of the tank. The reason for this limitation is to confine the study to conical shell behaviour. However, if one were to simulate the response of the cylindrical capped conical shell, the cone could serve as a basis for a conservative design. Consider two vessels having the same height, the first being a full cone and the second consisting of a cylinder superimposed on a cone as shown in Figure 3.9. If the two vessels are filled with the same liquid, it is clear that the volume of the liquid supported by section $1'-1'$ in the first vessel is larger than the volume supported by section 1-1 at the same elevation for the second vessel. Hence, it implies that the expected compressive meridional stresses generated in the second vessel will also be larger. However, the tensile hoop stresses will remain the same.

Nonetheless, it can be concluded that the full cone is more critical to buckling.

The bottom of the steel cone is usually welded to a circular steel plate which is anchored to a heavily reinforced concrete slab. Because of rigid diaphragm action, the horizontal displacements at the cone bottom are ignored. The weldments also provide some partial rotational restraint which may be ignored. As such, the cone is assumed simply supported at the base. This assumption also tends to be conservative and leads to lower limit loads.

The top of the cone is assumed free in spite of the presence of a circular rim at the top of the vessel. This assumption is employed because of the fact that the hydrostatic load acting near the top of the cone is very small, which leads to a negligible horizontal movement of the top. Therefore, it is believed that the results of the analysis will not be significantly affected whether the top of the tank is assumed to be free or restricted. As will be seen later, this assumption is justifiable.

For the analyses of tanks which have either axisymmetric or an even wave number n of circumferential imperfections, only one quarter of the cone is modelled because of the double symmetry of geometry and loading. However, for tanks which have an odd wave number n, only single symmetry in geometry exists, and hence one half of the tank must be modelled in the finite element analysis. Typical finite element meshes for the one quarter and the one half of the cone are shown in Figures 3.10(a) and 3.10 (b), respectively, where 128 elements are used to model both the quarter and the half regions of the cone. A finer mesh at the bottom of the tank is used because of expected higher stresses. The element length l_e is taken less than one quarter of the wave

length l, as defined in Section 3-4. This is to ensure that the lowest buckling mode which is localized near the bottom of the tank is not missed in the analysis.

3-8 Method of Analysis

The inclusion of geometric non-linearities in the shell element formulation allows non-linear stability analysis of a liquid-filled conical tanks in both the elastic and the inelastic ranges to be performed. This is achieved by gradually increasing the load acting on the tank wall. The stiffness of the tank will correspondingly decrease with the increase in load until the limit load is reached, i.e. the stiffness vanishes. The load acting on the walls of the liquid-filled conical tank is due to hydrostatic triangular pressure having a maximum value of γh at the bottom, where γ is the specific weight of the fluid and h is the height of the fluid in the tank.

In this study, the structure is assumed to be filled with water. To start the numerical analysis, the hydrostatic pressure is multiplied by a load factor p which is increased until the structure reaches its limit load at $p = p_{cr}$. (The latter being defined as the critical load factor). As such, $p_{cr} = 1$ corresponds to the real situation of a tank filled with water and on the verge of failure. If p_{cr} is less than unity, then the structure cannot sustain the hydrostatic load. When p_{cr} is larger than unity, this signifies that the hydrostatic load acting on the tank can be multiplied by any value up to p_{cr} prior to the tank becoming unsafe. Hence, p_{cr} is a measure of the factor of safety for the tank when it is filled with water. It should be mentioned here, that it is very difficult to determine exactly the limit load in a load control non-linear analysis. However, a very careful attempt has been made to determine the limit load by choosing reasonably small load

increments in its vicinity.

3-9 Tank Layouts

To study the behaviour of conical-shaped tanks, seven different geometries are considered. Four of these are taken as broad tanks (B1-B2-B3-B4) and the other three as tall tanks (T1-T2-T3). All dimensions are shown in Tables.3.1 and 3.2 and Figure 3.11. Material properties for all containment vessels are taken as follows:

Modulus of Elasticity, $E=2*10^5$ (MPa)

Tangent Modulus , $E_T= 6*10^3$ (MPa)

Yield Stress , $\sigma_y= 300$ (MPa)

Poisson's Ratio , $\nu=0.3$.

It has to be noted here that the 45° degree angle between the generator of the tall tanks and the vertical is a common value in practice. It is also important to clarify that the dimensions of the category of tall tanks are close to those of the Fredericton tank to achieve a practical range of values. The reason behind the choice of the broad tank category having a wider generator angle θ_v and a smaller height h, is that these cases provide a high compressive meridional force at the bottom relative to the induced stabilizing pressure. As such, the result could lead to a critical situation in terms of the tank stability and infer the need to use caution when contemplating an increase in generator angle.

The following notations are used to describe the results for the different types of analyses undertaken :

EP=   elastic analysis of perfect tanks,

PP= inelastic analysis of perfect tanks,

EI= elastic analysis of tanks with axisymmetric imperfection,

PI= inelastic analysis of tanks with axisymmetric imperfections,

PIR= inelastic analysis of tanks with axisymmetric imperfections and axisymmetric

residual stresses.

3-10 Elastic Analysis

3-10-1 Perfect Tanks

Non-linear stability analyses (EP) are performed for all seven liquid-filled tanks.

The critical load factor p_{cr} corresponding to the limit load of each tank is obtained. In

order to compare these critical load factors with the numerical analyses performed by

Vandepitte et al. (1982), parameters r_1, t, h, θ_v, E and ν for each tank are substituted into

Equations 3.2, 3.3 and 3.5 to obtain a corresponding value for γ. The limit load factor

p_{cr} is obtained by dividing the above calculated γ by the specific weight of water γ_w. The

calculated critical load factors p_{cr} based on both analyses are then compared and tabulated

in Table 3.3. Excellent agreement, generally within 5%, can be observed for each case.

The buckling modes resulting from the analyses are all axisymmetric. Figures 3.12 to

3.14 show plots of the meridional transverse deflections for all tanks near buckling (at

the last load increment which corresponds to a convergent solution) versus the distance

S measured along the generator. A localized buckling pattern near the support, having

a small wave length l_r, can be observed. The buckling wave lengths resulting from the

analyses are measured and are compared in Table 3.3 to those calculated from Equation

3.1 (Vandepitte et al. 1982). The comparison indicates good agreement. The horizontal

deflections of tanks T2 and B2, near buckling, are plotted in Figures 3.15 and 3.16. These plots show that the horizontal deflections at the top of the tank are very small. This observation justifies the assumption made in Section 3.7 that the tanks can be assumed to be free at the top.

3-10-2 Influence of Imperfection Shapes

The stability of thin shell structures may be greatly affected by the initial geometric imperfections which are usually present in real shell structures. These geometric imperfections can have random shapes and magnitudes. In order to determine the critical imperfection shape, i.e. the shape which leads to the lowest limit load, non-axisymmetric imperfections of different wave numbers n as well as axisymmetric imperfections (n=0) are considered for two tanks (B1 and T1). For purpose of this comparison, imperfection amplitudes equal to 0.01 l_r are employed, where l_r is the buckling wave length of the perfect tank as obtained in Section 3-10-1. The load factors resulting from the analyses (EI) are tabulated in Tables 3.4 and 3.5. It can be concluded from these results that the elastic stability analysis of hydrostatically loaded conical shells is more sensitive to axisymmetric than to the non-axisymmetric imperfections.

In order to explain this conclusion, consider the bottom part of a conical tank bounded by the lower end and a horizontal section having the ordinate S equal to $l_r/2$, as shown in Figure 3.16. It is clear from the buckling mode of the perfect cone that this region is the location where most of the energy is dissipated when the buckling forms. For tanks having an axisymmetric imperfection of wave length l_r, this part of the structure can be treated as an assembly of cylindrical panel having a vertical axis and a

concave inward curvature in the longitudinal direction as shown in Figure 3.17. Each panel can be thought of as subjected to a compressive vertical force P_v and a radially outward pressure P_h. It is clear that both forces will tend to deflect the panel outwardly with respect to the vertical axis. Now consider a tank with non-axisymmetric imperfections. The same portion of the tank, as considered for the axisymmetric imperfections, is now treated as a combination of partial panels with concave inward curvature as shown in Figure 3.17 and partial panels with concave outward curvature in the longitudinal direction as shown in Figure 3.18. When these outward panels are subjected to the vertical force P_v and the radially outward pressure P_h, the bending effects are in opposite directions. The vertical force will tend to bend the panel in the inward direction while the pressure has the tendency to bend it outwardly. The effects of both forces tend to cancel each other and as a consequence, less energy is dissipated in this partial panel as opposed to the adjacent one. This explains why less energy is dissipated in the non-axisymmetric mode resulting from the non-axisymmetric imperfections and hence means that the axisymmetric mode associated with the axisymmetric imperfections is more critical.

Figure 3.19 shows the transverse meridional displacements for the broad tank B1, at a location coinciding with maximum amplitude section (S =0.235 m), for n=2,4 and 8, respectively. Meanwhile, in Figure 3.20 the transverse meridional displacements for the tall tank T1 at a similar section (located at a distance S =0.22 m), are also plotted for n=2,4 and 8, respectively. Note that these transverse displacements are measured relative to the perfect circumference of the tanks. It can be concluded from these figures

that the buckling modes are approximately the same shape as those of the imperfection patterns. The deflection magnitude indicates that the regions where the imperfections have a concave shape, the deflections are larger than those in the regions where the imperfections have a convex shape.

3-10-3 Cones with Axisymmetric Imperfections

Because the presence of axisymmetric imperfections leads to the lowest limit loads for liquid-filled conical tanks, tanks T1, T2, B1 and B2 are elastically analyzed with axisymmetric imperfections of the same wave length as obtained for the buckling modes of their perfect counterparts. The amplitude of imperfections w_o is taken equal to 0.01 l_r, where l_r is the buckling wave length obtained from the analysis of a perfect tank. Therefore, the tanks can be considered to be poor cones (with respect to fabrication) according to the classification given by Vandepitte et al. (1982). The critical load factors p_{cr} obtained from these analyses are compared to the corresponding values which were found from the tests results by Vandepitte et al. (1982). The critical load factors, based on the experimental results by Vandepitte, are obtained for each tank by applying the following steps:

a)   Using Equation 3.2 and the tank dimensions r_1 ,h and θ_v, the dimensionless parameter ψ is calculated.

b)   Using Figure 3.3 and the above calculated parameter ψ, values for ω which correspond to the upper and lower dots are obtained as ω_{upp} and ω_{low}, respectively.

c)   Substitution of ω_{upp} and ω_{low} into Equation 3.3 yields two values of γ, i.e. γ_{upp} and

γ_{low}.

d)   Dividing γ_{upp} and γ_{low} by the specific weight of the water γ_{w} results in the load

factors p_{cr} which represent upper and lower limits.

The values of p_{cr} obtained from the finite element analyses for the four tanks are

tabulated in Table 3.6 and compared to the corresponding upper and lower p_{cr} limits of

the experiments. It can be observed from the table that the numerical results are within

the limits of the experimental range. However, it is also noted that the lower limits from

the experiments underestimate the elastic buckling of liquid-filled conical tanks. The low

values of the experimental results may have been due to an early plastification that might

have occurred before the elastic buckling could have been reached. This certainly would

lead to limit loads lower than the elastic buckling loads. It was previously mentioned in

Section 3-4 that Vandepitte et al. (1982) assumed that elastic buckling took place for all

tested specimens. This assumption was based on a comparison between the induced

membrane stresses and the yield stress of the material. However, from the plots of the

meridional deflections of tanks B1, B2, T1 and T2 obtained from the finite element

analyses and given in Figures 3.21 to 3.22, large local bending effects near the bottom

of the tanks can be easily noticed which were ignored by Vandepitte et al.(1982). The

bending stresses induced, when added to the membrane stresses may indeed cause

yielding in the material, especially in the extreme fibre near the bottom of the tank.

Another possible cause for diminished limit load values of the experimental results is that

the bottoms of the specimens might not have been sufficiently restrained against lateral

movement during the tests. Since buckling is localized near the support, any small lateral

movement of the support itself could have caused a noticeable reduction in the buckling capacity of the experimental tested models. Therefore, it appears reasonable that the limit loads obtained from the non-linear elastic stability analysis using the finite element model tend to be larger than those obtained from the experimental investigation.

3-11 Inelastic Analysis

In all of the previous analyses reported so far, the material has been assumed to be elastic. There are two objectives for performing the non-linear elastic stability analysis. The first is to compare the results of the finite element analysis with the numerical and the experimental results available in the literature. The second objective is to determine the critical imperfection shape.

By including a realistic strain hardening constitutive equations in the finite element model, a non-linear stability analysis including both geometric and material non-linearities can be performed for a liquid-filled conical tank. However, the effects of different residual stress distribution are first studied, before a complete non-linear inelastic analysis is undertaken. The material properties used in all the subsequent analyses are listed in Section 3-9.

3-11-1 Effect of Residual Stresses

As was mentioned in Section 3-6, two types of residual stresses can be present in a shell structure - hoop stresses resulting from a circumferential weld with the stress distribution shown in Figure 3.6, and/or meridional stresses resulting from a longitudinal weld with the distribution shown in Figure 3.7. The effect of these stresses on the limit loads of liquid-filled conical tanks is determined by performing inelastic stability analysis

for the following cases.

a) Tank T3 Without Residual Stresses

Tank T3, free from initial residual stresses is treated first. It is found that a critical load factor p_{cr} of 2.4 is obtained from the inelastic analysis. This result compares with the value of 3.9 for the purely elastic case (Table 3.3), thus showing a considerable reduction in strength when material non-linearities are accounted for. The inelastic analysis indicates that material yielding precedes the attainment of the limit load.

b) Tank T3 with Meridional Residual Stresses Only

Two longitudinal weld lines are considered to exist in one quarter of the tank. Two meridional stress distributions, similar to the one given in Figure 3.7, are located along each weld line. The total residual stress distribution due to the weld lines, acting on one quarter of a circular cross section is shown in Figure 3.23. Note that these stresses act along the entire height of the tank. A critical load factor p_{cr} of 2.5 is obtained from the finite element analysis. The small increase in the critical load factor compared to case (a) above, may be explained by the presence of high tensile stresses about the line of weldment which reduces the compressive meridional stresses resulting from the weight of the water. On the other hand, added compressive residual stresses of lower intensity and further away from the weld area would tend to reduce the vessel's strength capacity.

c) Tank T3 with Hoop Residual Stresses Only

Two circumferential welds 3m apart are considered. One of the weldments is located near the base of the tank and has an ordinate $S = 30t$, where t is the thickness of the tank. Two hoop stress distributions similar to the one given in Figure 3.6 are

assumed around each weld. The total initial stress distribution acting on a vertical (meridional) cross section of the tank is shown in Figure 3.24. Note that these stress distributions are axisymmetric. A critical load factor p_{cr} of magnitude 2.1 results from the finite element model. Comparison with case (a) indicates that the initial hoop stresses resulting from the circumferential welding reduce the limit load of the liquid-filled conical tank by about twelve percent. In this case, the initial large tensile hoop stresses amplify the tensile hoop stresses resulting from the water pressure alone and thus cause yielding of the material at a lower load factor. The same analysis is done by considering only the bottom weld. The critical load factor is found to be unchanged, i.e. 2.1. This result indicates that the residual stresses further away from the bottom region of the tank have little or no effect on the stability of liquid-filled conical tanks.

From the results of the above analyses, it is clear that a conservative load factor for a liquid-filled conical tank can be obtained by assuming only initial hoop stresses at the bottom of the tank.

3-11-2- Sensitivity of Conical Tanks to Geometric and Material Imperfections

Following the inelastic analyses of the above three cases, inelastic stability analyses are performed for all the seven tank geometries. For each tank, three cases are considered. These are the perfect shell (PP), the tank with axisymmetric imperfections with the same wave length as the buckling wave length of the corresponding perfect tank (PI), and the case of self-equilibrated residual hoop stresses (material imperfections) at the bottom of an axisymmetrically imperfect tank (PIR). The maximum amplitude of the imperfections w_o is assumed equal to the thickness of the tank. Such tanks can be

considered as poor cones according to the Vandepitte classification (1982).

The analyses above indicate that all of the seven tanks buckle inelastically, i.e. yielding precedes buckling. Figures 3.25 and 3.26 show the variation of the critical load factor p_{cr} with the thickness for both the tall and broad tanks, respectively. It can be concluded from the figures that a unit thickness imperfection can reduce the limit load by about 35% to 40% and that the residual stresses can introduce an additional reduction of about 5% to 10%.

Figure 3.27 shows the axial deflection, the transverse deflection, the axial (meridional) stress and the hoop stress at the middle surface for the perfect tank T1 versus the distance S measured along the generator. Similar deflection plots and stress distributions for the other six tanks, that include both the perfect (PP) and imperfect (PI) cases, are shown in Figures 3.28 to 3.40. Results of the inelastic analyses for perfect tanks indicate that the tall tanks can sustain larger compressive meridional stresses than the broad tanks. This observation can be interpreted due to the effect of the stabilizing tensile hoop stresses which are relatively larger in the case of tall tanks. Comparison between the responses of a perfect tank and the similar imperfect one indicates that the imperfections lead to an increase in the values of the transverse displacements and a reduction in the axial displacements at the limit load. Also, it can be concluded that the presence of imperfections decreases the resistance of the tanks to the compressive meridional stresses. Meanwhile, these imperfections introduce extra hoop stresses. The percentage in reduction of the strength of the tall and broad tanks due to the presence of a unit thickness imperfection are tabulated in Table 3.7. It clear from these results that

the tall tanks are more sensitive to geometric imperfections than the broad tanks. It can be also concluded from the table that tanks which have small thickness are generally more affected by geometric imperfections than those which have larger thickness.

Considering the magnitudes of the meridional stresses at the limit loads of the imperfect tanks, and knowing that plastification precedes these limit loads, it can be concluded that yielding of the material occurs when the meridional stresses are less than $\sigma_y/2$. This observation indicates that the stress level ($\sigma_{act} < \sigma_y/2$) which was found at the middle surface of the experimental models during the tests performed by Vandepitte (1982), does not ensure elastic buckling. This confirms the present author's belief that during testing of the models, early plastification would have occurred prior to buckling.

As mentioned previously in Section 3-10-3, upper and lower values for the load factor of tanks T1, T2, B1 and B2, can be obtained using the results of the experimental investigation carried out by Vandepitte el al.(1982). These values can now be compared with the corresponding critical load factors obtained from the inelastic stability analysis of the imperfect tanks using the finite element model. The comparison is given in Table 3.6 and shows that the critical load factors from inelastic analyses are very close to the lower bound values obtained from the experimental studies.

3-12 Discussion about the Design of the Fredericton Tank

As previously mentioned in Chapter One, this study was motivated by the failure of an elevated conical tank in Fredericton, New Brunswick, Canada on December 19, 1990. The vessel of the failed tank consisted of a steel cylindrical shell superimposed on top of a steel conical shell of variable thickness. The dimensions of the tank and the

variation of the thickness along a generator of the tank are shown in Figure 3.41. The designer of the tank claimed that these thicknesses provided a safe design for the tank when the tank is filled with water and that a factor of safety of 4.12 was provided against instability.

In the following sections, the stability of the failed tank is checked using different methods. First, the results of an investigation undertaken by Vandepitte (1992) to study stability of the tank are presented. Then, the results of a numerical stability analysis using the consistent shell element are given, followed by an assessment undertaken with the Danish code DNV (1982) and the American AWWA D-100 (1984) specifications. In all these checks, the stability of the tank is studied at section B´-B´ (critical section) shown in Figure 3.41. The vertical downward forces acting on section B´-B´ are assumed the same as those given by the designer of the tank and presented in the design report of the tank (Connors, 1990). The pertinent data applicable to the Fredericton water tower are given as follows:

the weight of water = 16399 kN,

snow load = 489 kN,

the weight of the roof and steel shell = 650 kN.

The material properties of the tank are taken as:

Modulus of Elasticity $E=2*10^5$ (MPa)

Yield Stress $\sigma_y=250$ (MPa)

3-12-1 Study of the Tank by Vandepitte

As a response to the collapse of the tank, a report was written by Vandepitte

(1992) in which he discussed the correctness of the calculations used in the design of the tank. In the same report, Vandepitte questioned the value of the factor of safety given by the designer using the following methods:

a) Design Formulae

The buckling strength of the failed tank was calculated using the design formulae obtained from the results of the experiments carried out by Vandepitte et al. (1982) and presented in Section 3-4. Two different levels of imperfections were assumed to exist in the tank before loading and the buckling strength of the tank was calculated for each. According to the classification given in Section 3-4, the tank having the first level of imperfections was a "good cone", while the tank having the second imperfection level was "a poor cone". The calculated buckling strength σ_{cr} for each case was given as:

$\sigma_{cr} = 70.6$ MPa (good cone)

$\sigma_{cr} = 65.8$ MPa (poor cone)

The meridional membrane compressive stress σ_{act} acting on section B´-B´ is given by the following equation:

$$\sigma_{act} = \frac{P}{2\pi\, r_1\, t\, \cos\theta_v}$$

where P is the sum of the vertical forces acting on the section; r_1 and t are the radius of the cone and its thickness at section B´-B´, respectively; and θ_v is the inclination of the wall of the tank with the vertical.

Using the tank dimensions and the sum of the vertical forces acting on section B´-B´ as given by Connors (1990), the meridional compressive stress σ_{act} at the same section

was found to be: $\sigma_{act} = 103.8$ MPa.

From the above calculated stresses, it is apparent that the values of the buckling strength of the tank would be considerably lower than the acting compressive meridional stress. As such, employing the design formulae suggested by Vandepitte at al. (1982), would indicate that the design of the tank was unsafe against instability.

b) Computer Analysis Done by Vandepitte

Vandepitte also presented in his report the results of a numerical stability analysis done at the University of Ghent. Details of this analysis are given in a report prepared by Van Impe (1992) indicating that the calculations were performed using the computer program FO4BOB developed by Essingler et al.(1984). This program is based on the finite difference method and includes geometric non-linearities, an elasto-plastic material model and initial axisymmetric imperfections. Three cases were considered in the analysis; these are: the perfect tank, the tank with "good cone" axisymmetric imperfections, and the tank with "poor cone" axisymmetric imperfections. Critical load factors resulting from these analyses are given in Table 3.8.

All these analyses show that yielding of the material occurred before the limit load had been reached. Also, the critical load factor obtained from the analysis of the third case indicates that if the initial imperfections existing in the tank were large enough, thus classifying the shell as a poor cone, the design of the tank would be unsafe against stability.

3-12-2 Numerical Analysis of the Tank Using the Shell Element

The failed tank is also modelled using the consistent shell element. The variation

in thickness along the generator of the tank is properly considered in the modelling. The tank is first analyzed elastically to give a buckling wave length (l_r=1.40m). Following that, three inelastic analyses are performed: 1) perfect tank, 2) tank with axisymmetric imperfections of maximum amplitude equal to 0.04 l_r (good cone), 3) tank with axisymmetric imperfections of maximum amplitude equal to 0.01 l_r (poor cone). The critical load factors obtained, and those resulting from the numerical analyses carried out by Van Imp (1992) are tabulated in Table 3.8. It can be observed from the table that excellent agreement in critical load factors between the two sets of analyses is achieved. It has to be noted that, like the results of the finite difference analysis, the limit loads obtained from the finite element analysis are reached after yielding of the material has happened. In Figure 3.42, the meridional transverse deflections prior to the limit load resulting both from the finite element and the finite difference analyses (Van Imp, 1992) of the perfect tank are presented. The deflection patterns show that both analyses lead to the same buckling wave length localized at the bottom of the tank. From the finite element results given in Table 3.8, it can be concluded that if the imperfections in the tank were high enough to classify the tank as a poor cone, the corresponding critical load factor in this case is equal to 0.9. This load factor is expected to be reduced by 10 % by inclusion of the residual stresses due to welding. Hence, the critical load factor in this case would approximately be 0.8. Therefore, it can be stated that the design of the tank would be unsafe against instability if a high level of imperfections and residual stresses were present in the tank before filling.

3-12-3 Check for the Design of the Tank Using Different Codes

The Danish code DNV (1982) and the industry standards in North America based on the AWWA D-100 (1984) specifications are herein used to check the safety of the design of the failed reservoir against instability. The maximum compressive strength of liquid-filled conical tanks, according to both the DNV and the AWWA, is based on the buckling strength of an equivalent cylinder under compressive force as described in Section 3-3.

Based on each code, the maximum compressive strength of the equivalent cylinder σ_{cr} is calculated. Then, this buckling strength is compared to the meridional compressive stress σ_{act} induced in the conical tank at section B´-B´. This stress was shown earlier to be equal to 103.8 MPa as calculated by Vandepitte (1990).

Following the equations given in Section 3-3, the dimensions of the equivalent cylinder are obtained. The maximum compressive strength of this cylinder, based on the DNV (1982) and the AWWA (1984), are calculated as follows:

σ_{cr} = 16.57 (MPa)   (DNV)

σ_{cr} = 12.74 (MPa)   (AWWA)

Comparison of the above calculated buckling strengths of the equivalent cylinder σ_{cr} with the actual membrane meridional stress σ_{act} indicates that according to both the DNV code and the AWWA specifications, the Fredericton tank was vastly unsafe against instability .

According to each design method, a load factor can be calculated by dividing the actual membrane meridional stress σ_{act} by the buckling strength of the cone σ_{cr}. This load

factor means that the hydrostatic load acting on the tank can be multiplied by any value up to this load factor prior to the tank becoming unsafe. The lower the load factor, the more conservative the design method used to obtain this load factor. Three load factors are calculated and are presented in Table 3.9. These correspond to the buckling strengths of the tank based on the following:

a)   Design formulae suggested by Vandepitte et al. (1982) when the cone is considered "poor".

b)   The buckling strength of the equivalent cylinder as defined by DNV (1982).

C)   The buckling strength of the equivalent cylinder as defined by AWWA D-100 (1984).

Comparison of the load factors with those resulting from the finite element analysis given in Table 3.8 indicates that although the DNV (1982) code and the AWWA D-100 (1984) design formulae are not based on any numerical or experimental modelling for liquid-filled conical tanks, they both provide overly conservative designs for this type of structure. On the other hand, the design formulae suggested by Vandepitte et al. (1982), which are based on a rational basis, provide a reasonably conservative design.

$r_1 = 3.0m \quad h = 4.5m \quad \theta_v = 60°$

Tank	Thickness (mm)
B1	7.0
B2	8.0
B3	9.0
B4	10.0

Table 3.1 Dimensions of the Broad Tanks.

$r_1 = 3.0m \quad h = 9.0m \quad \theta_v = 45°$

Tank	Thickness (mm)
T1	8.0
T2	10.0
T3	12.5

Table 3.2 Dimensions of the Tall Tanks.

* Please refer to Figure 3.11 for the notations description.

TANK	p_{cr} Analysis	p_{cr} (Vandepitte)	l_r (m) Analysis	l_r (m) (Vandepitte)
B1	1.5	1.55	0.94	0.74
B2	1.9	2.02	1.05	0.78
B3	2.4	2.56	1.08	0.83
B4	2.9	3.16	1.150	0.88
T1	1.8	1.62	0.88	0.66
T2	2.6	2.53	1.05	0.74
T3	3.9	3.95	1.17	0.82

Table 3.3 Results of the Elastic Analyses of the Perfect Tanks.

n	p_{cr}
0	1.0
1	1.2
2	1.2
4	1.25
8	1.5

Table 3.4 Limit Load Factors for Different Circumferential

Wave Numbers n for the Tall Tank B1.

n	p_{cr}
0	1.3
1	1.5
2	1.4
4	1.45
8	1.6

Table 3.5 Limit Load Factors for Different Circumferential

Wave Numbers n for the Broad Tank T1.

Tank	p_{cr} (Elastic Analysis)	p_{cr} (Inelastic Analysis)	p_{cr} Vandepitte (1982)
T1	1.3	0.7	0.72-1.1
T2	1.9	1.0	1.2-1.85
B1	1.0	0.9	0.8-1.29
B2	1.2	1.1	1.04-1.68

Table 3.6 Results of the Analysis of Tanks Having Axisymmetric Imperfections.

Tank	Percentage of Reduction in Strength	Tank	Percentage of Reduction in Strength
B1	19.6	T1	40
B2	16.0	T2	34.7
B3	19.0	T3	28.5
B4	15.0		

Table 3.7 Percentage of Reduction in Strength Due to Unit Thickness Imperfection.

Case	p_{cr} (Analysis)	p_{cr} (Vandepitte)
Perfect Tank	1.7	1.8
Imperfect "Good Cone"	1.3	1.31
Imperfect "Poor Cone"	0.9	0.957

Table 3.8 Results of the Inelastic Analysis of the Fredericton Tank.

Design Method	Limit Load Factor
Vandepitte et al. (1982)	0.634
DNV Code (1982)	0.160
AWWA (1984)	0.122

Table 3.9 Limit Load Factors for the Fredericton Tank

Based on Different Design Methods.
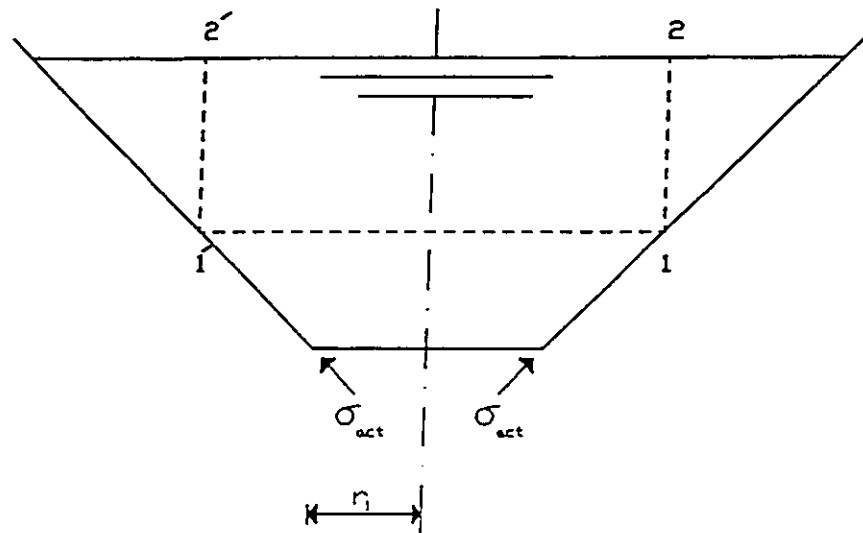
Figure 3.1 Cause of Failure of Conical Tanks.
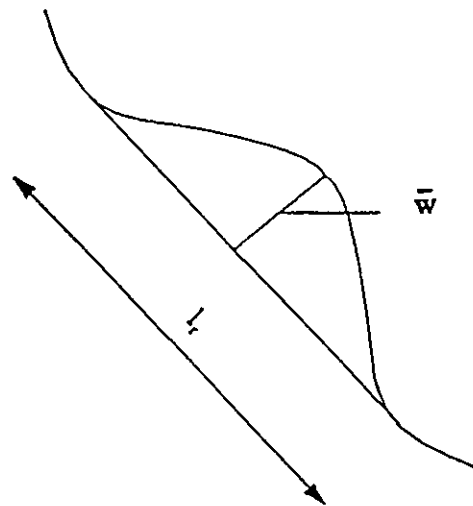
Figure 3.2 Vandepitte's Measure of Imperfections

Figure 3.3 Design Charts for Liquid-Filled Conical Tanks Suggested by Vandepitte et al. (1982).
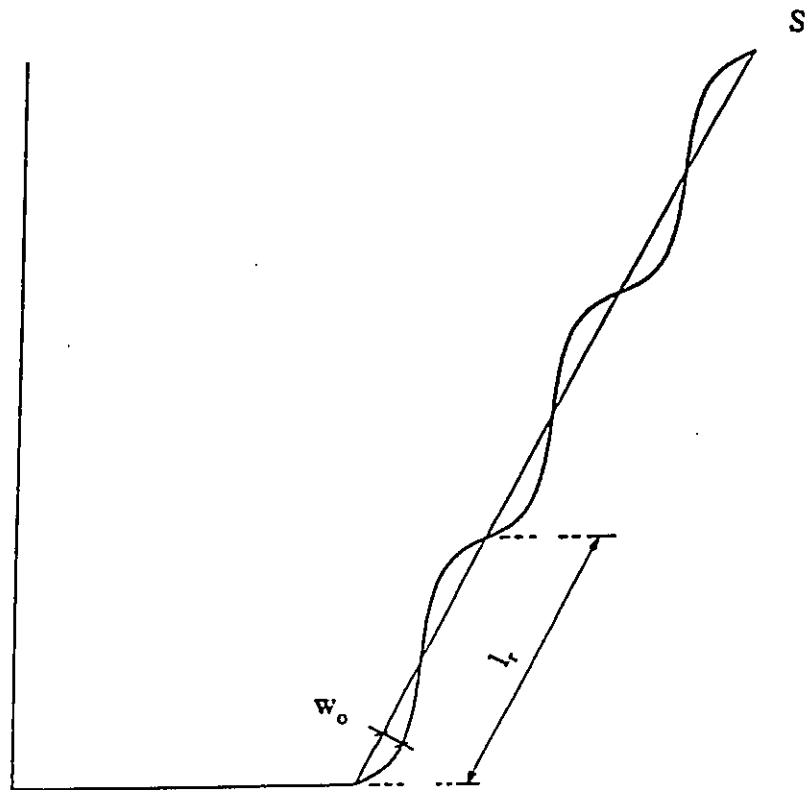
(a) Axisymmetric Imperfections through the Generator.
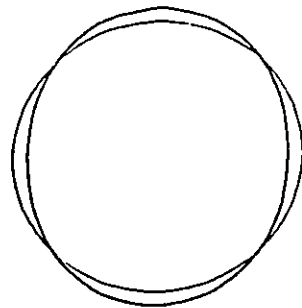
(b) Non-axisymmetric Imperfections

in the Circumferential Direction

Figure 3.4 Ass ned Imperfection Patterns for Conical Tanks.

$$\sigma_b = \sigma_y \left[2 \left(\frac{\bar{Y}}{L}\right)^2 - \frac{4}{3} \left(\frac{\bar{Y}}{L}\right) \right]$$

for $0 \leq Y \leq L$ $\bar{Y} = Y$

for $L \leq Y \leq 2L$ $\bar{Y} = (2L - Y)$

$$\sigma_{max} = \frac{2}{3} \sigma_y$$

$$\sigma_{min} = \frac{2}{9} \sigma_y$$
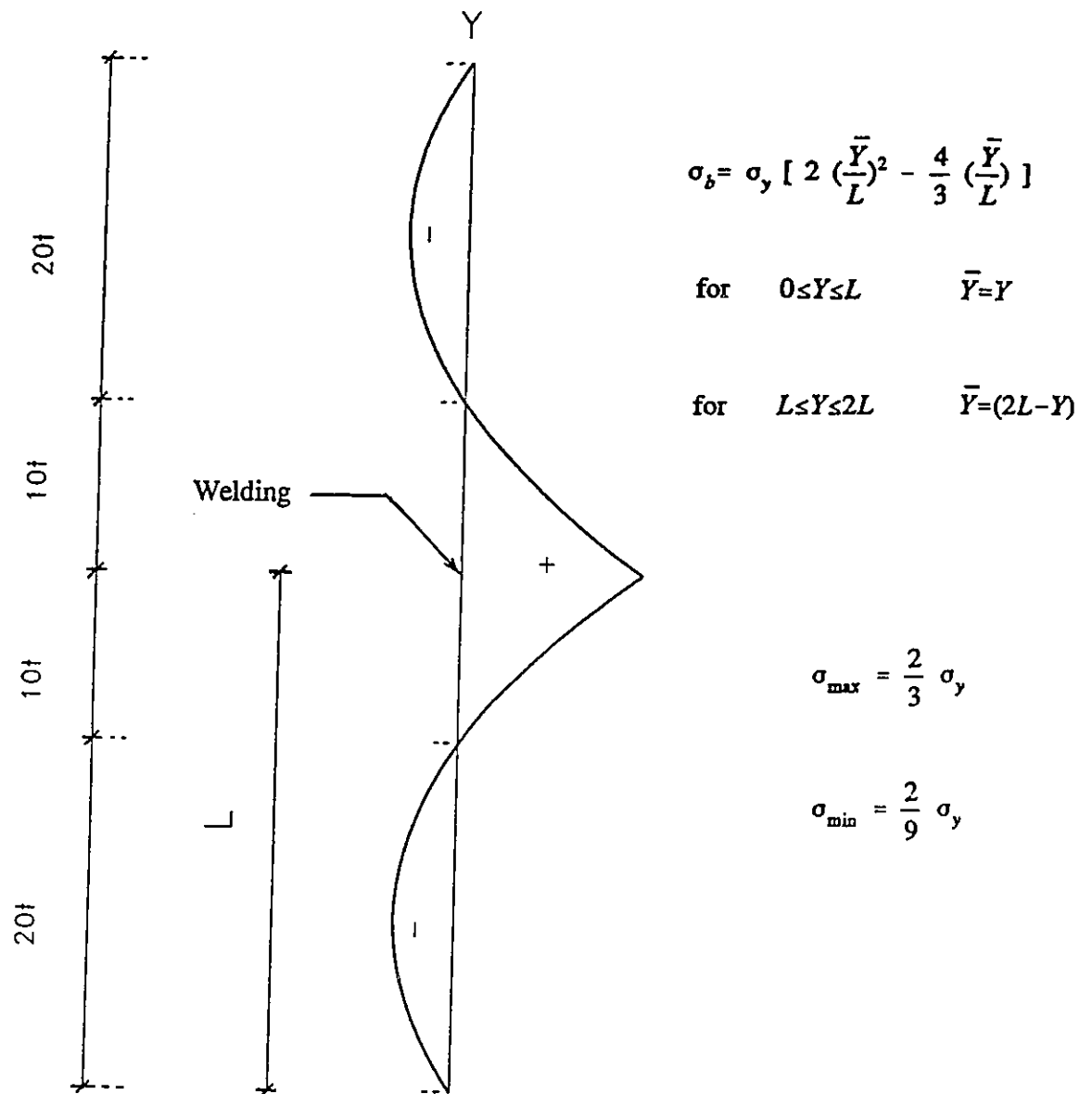
Figure 3.5 Bornscheuer's Model for Residual Stresses in Cylinders.

$$\sigma_{res} = \sigma_b \left[\frac{R}{R(Y)} \right]$$
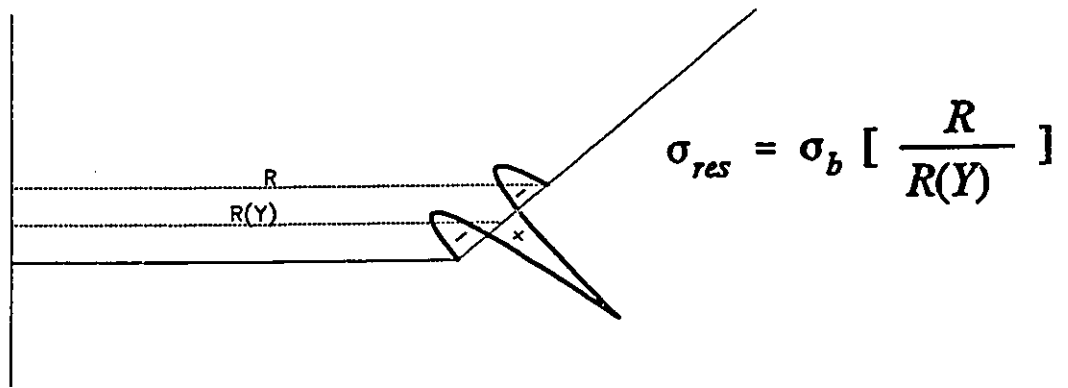
Figure 3.6 Hoop Residual Stress Distribution for Conical Tanks

$$\sigma_{res} = \sigma_b$$
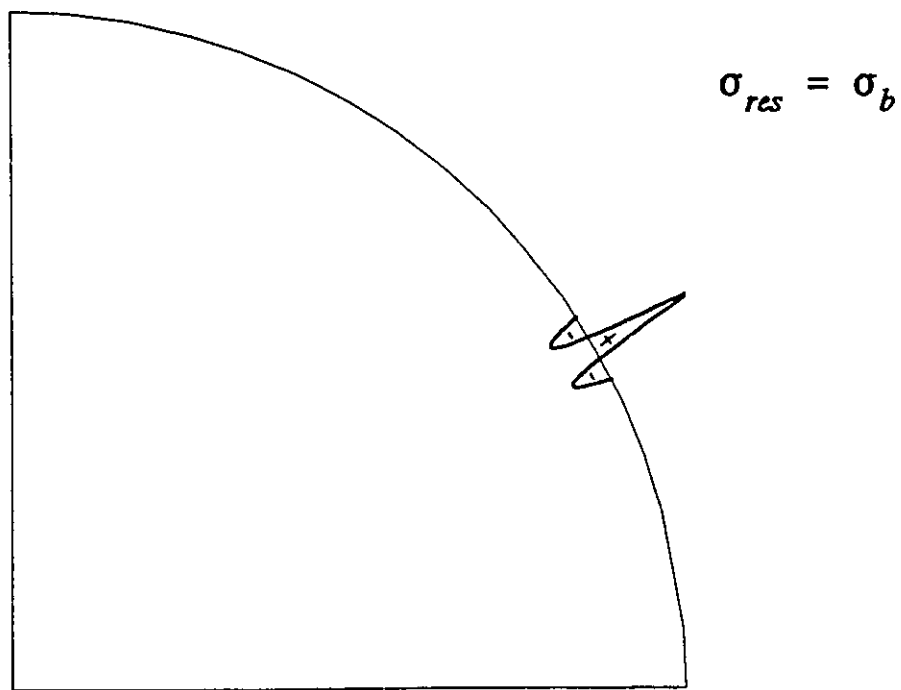
Figure 3.7 Meridional Residual Stress Distribution for Conical Tanks
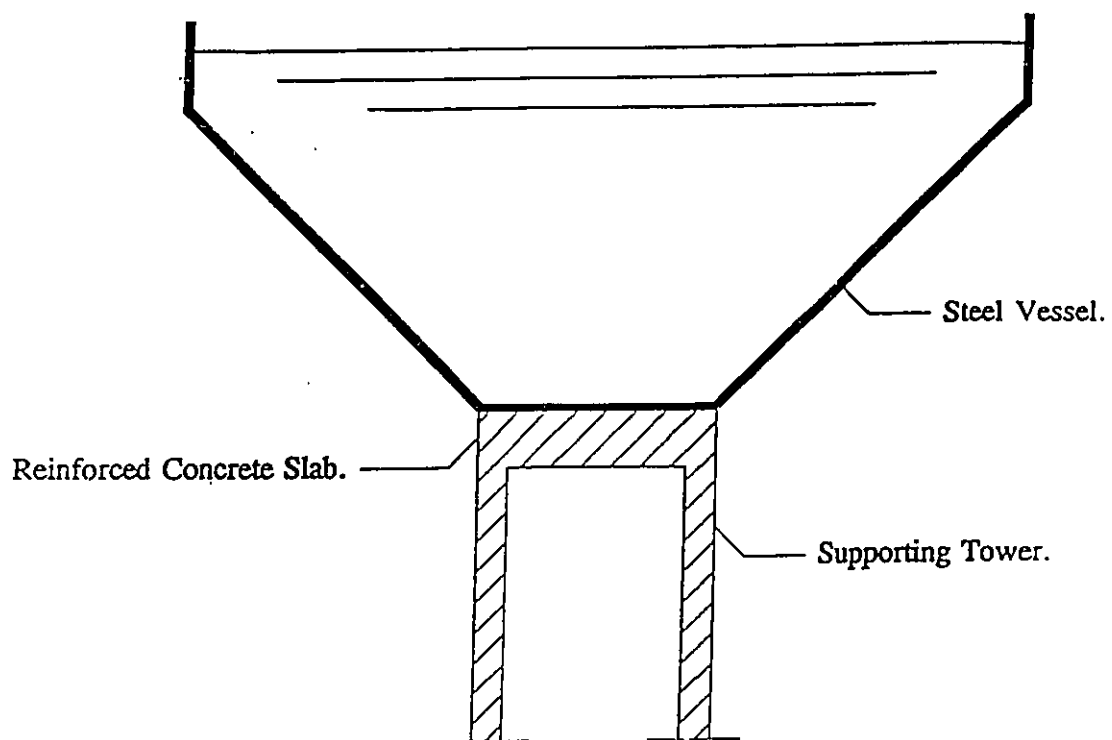
Figure 3.8 Cross Sectional Elevation of Elevated Conical Tanks.
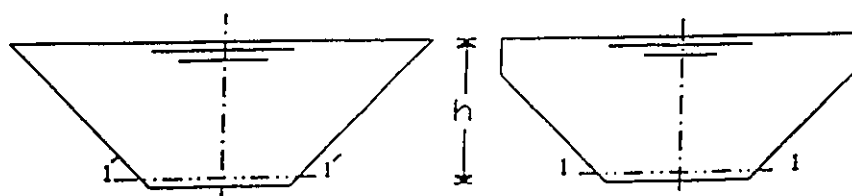
Figure 3.9 Comparison Between Full Cone and Cylindrical Capped Cone.
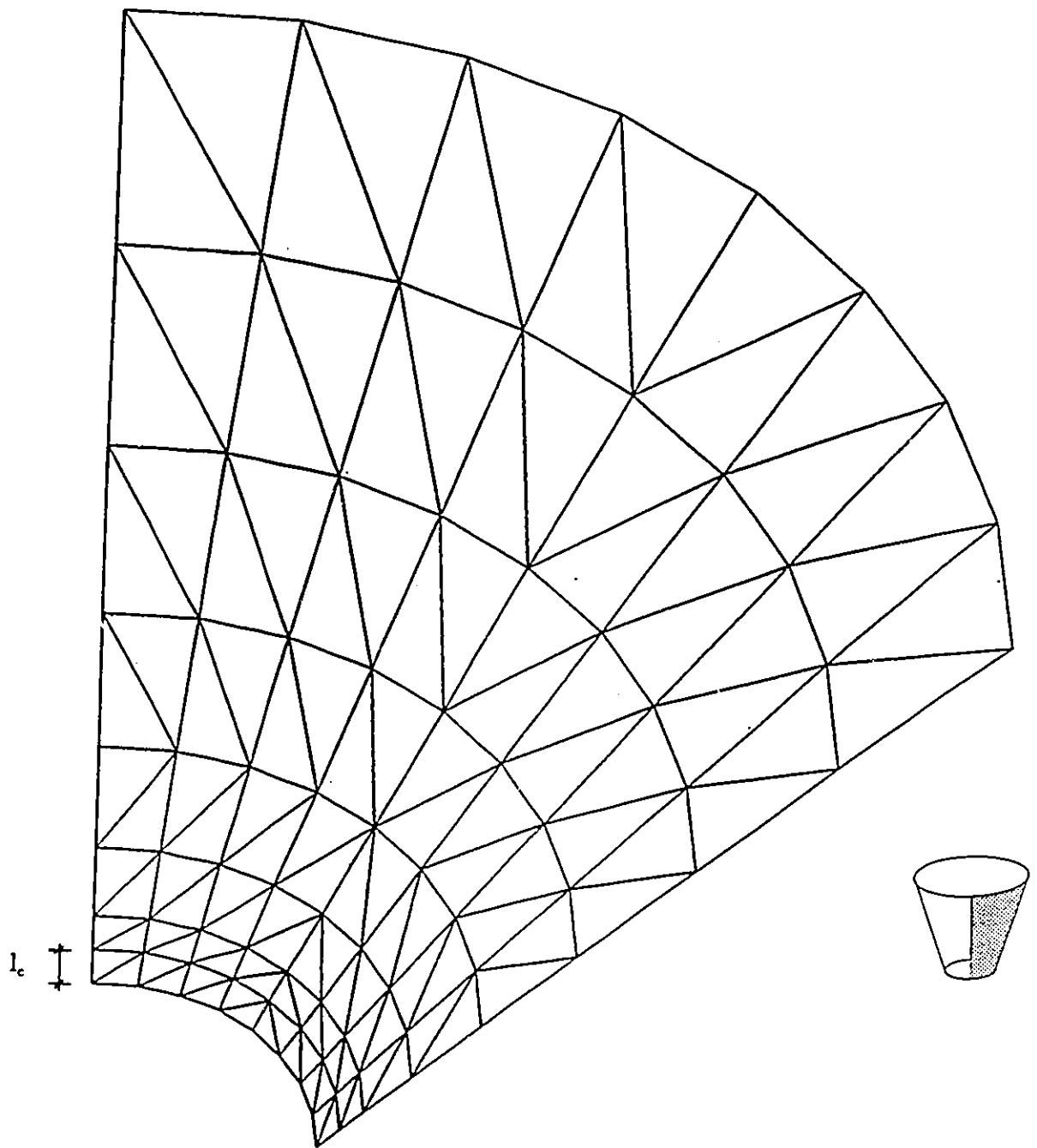
Figure 3.10 (a) Finite Element Mesh for Static Analysis (Quarter Cone).
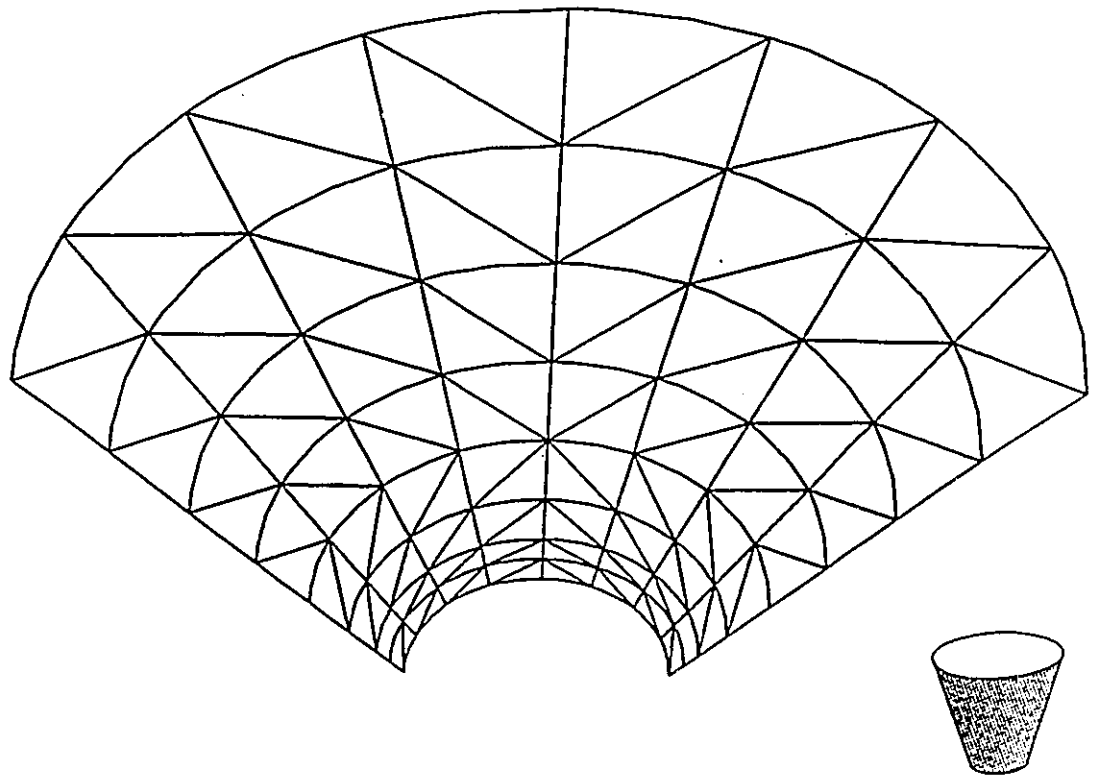
Figure 3.10 (b) Finite Element Mesh for Static Analysis (Half Cone).
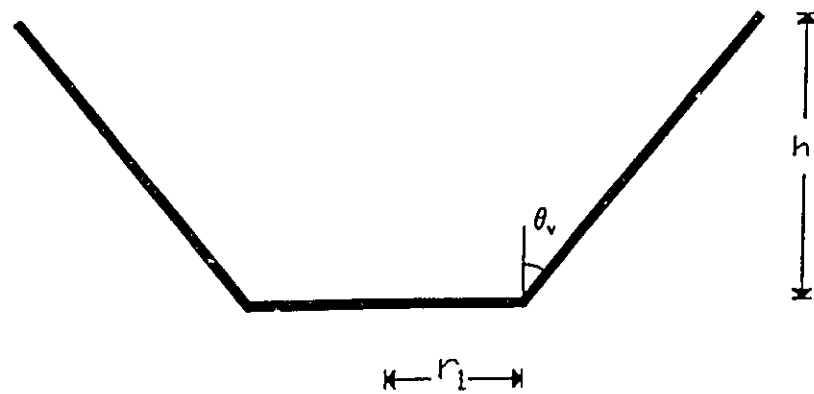
Figure 3.11 Notations Describing the Dimensions of Conical Tanks.
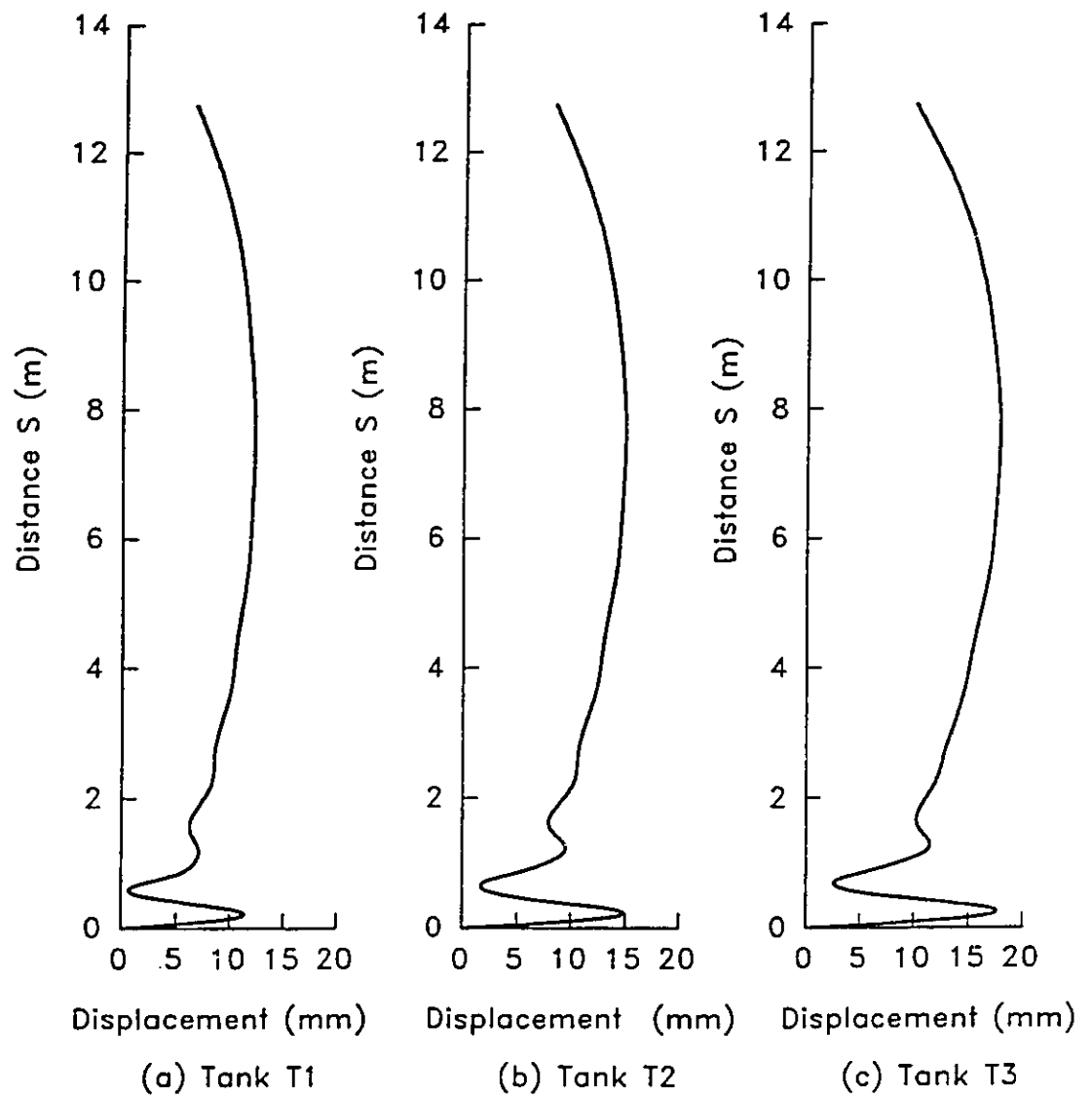
Figure 3.12 Transverse Displacements of the Tall Tanks Near Buckling. (Elastic Perfect Case—EP)
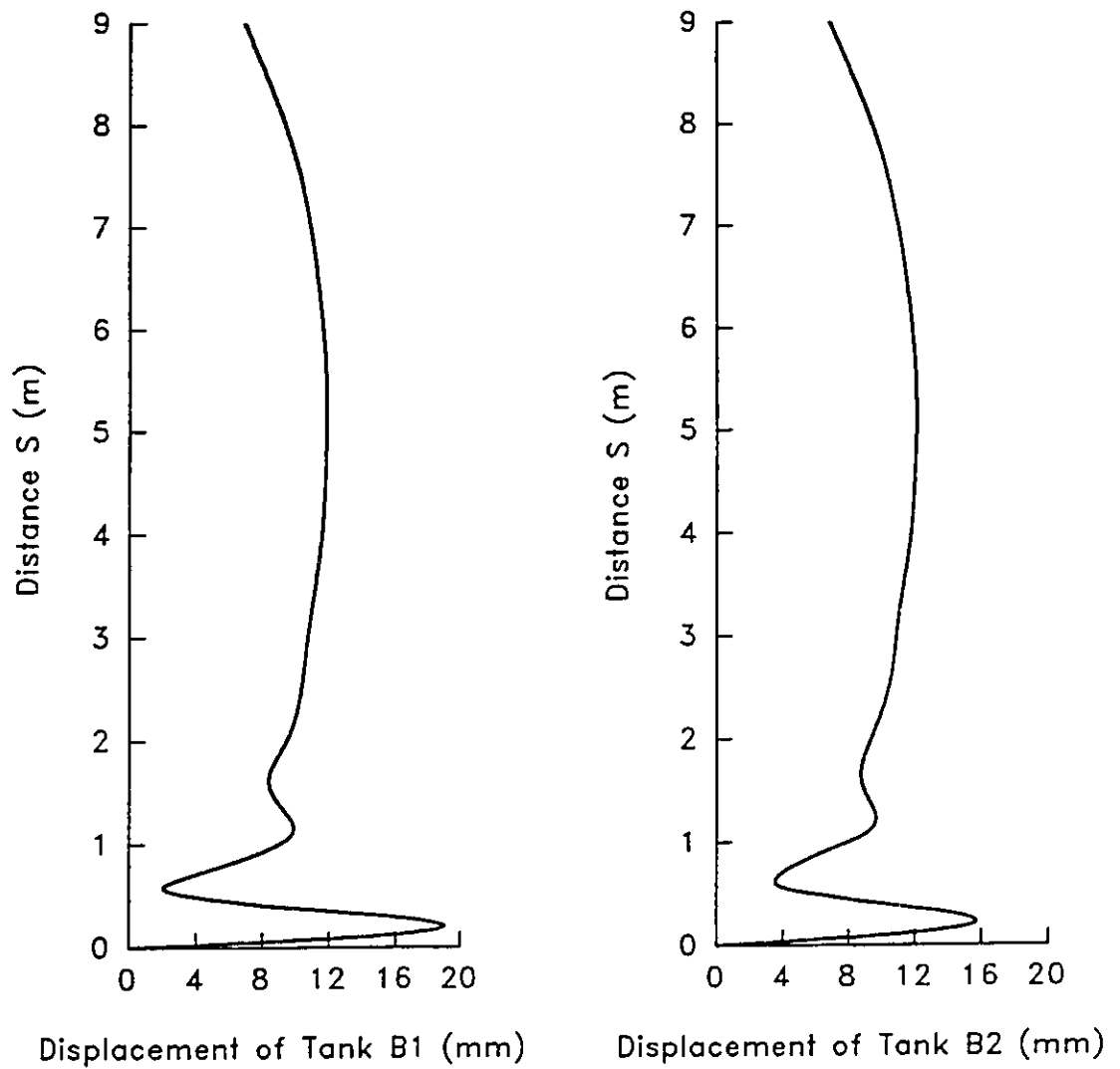
Figure 3.13 Transverse Displacements of Tanks B1,B2 Near Buckling.

(Elastic Perfect Case–EP)
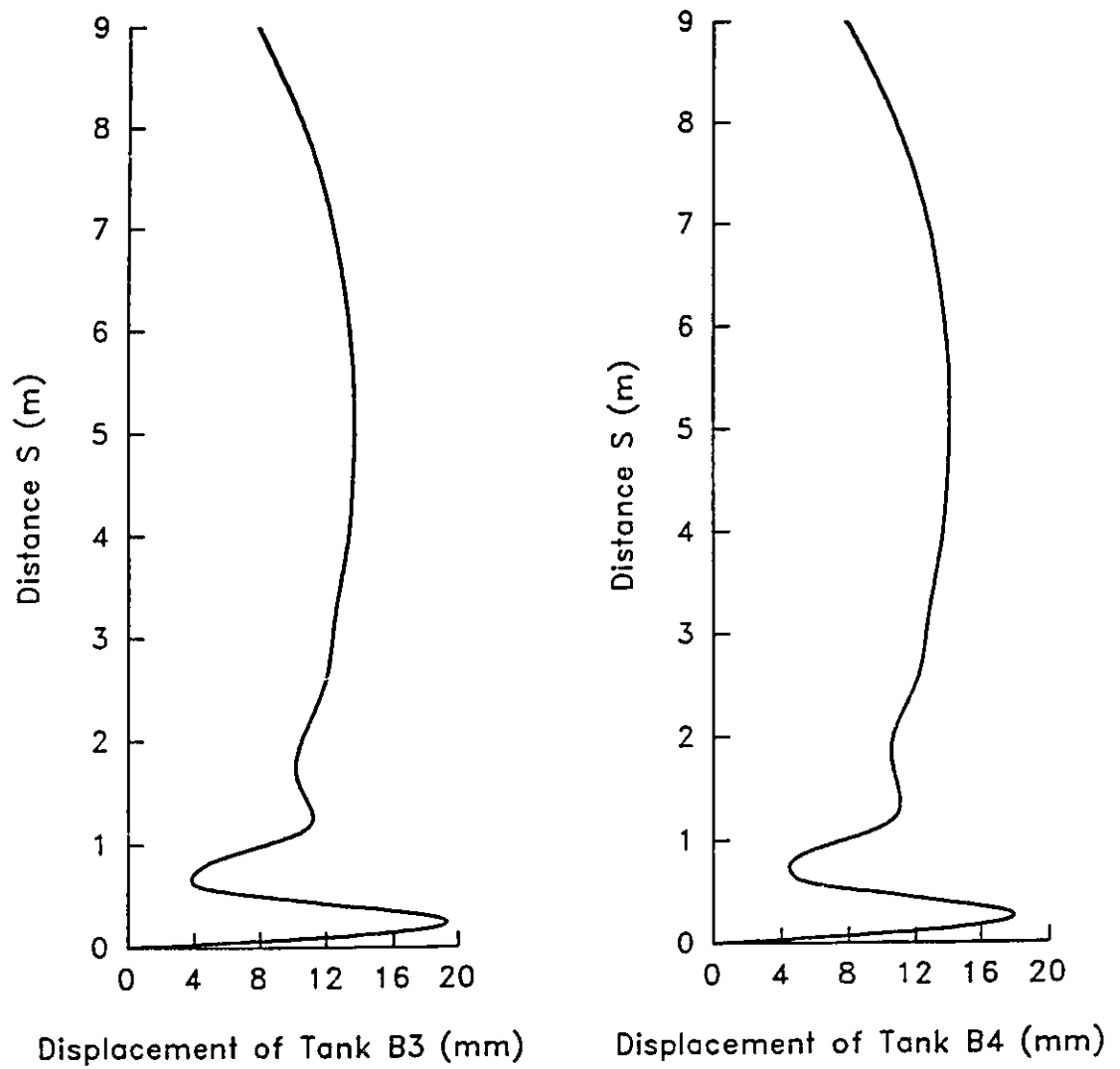
Figure 3.14 Transverse Displacements of Tanks B3,B4 Near Buckling.

(Elastic Perfect Case—EP)
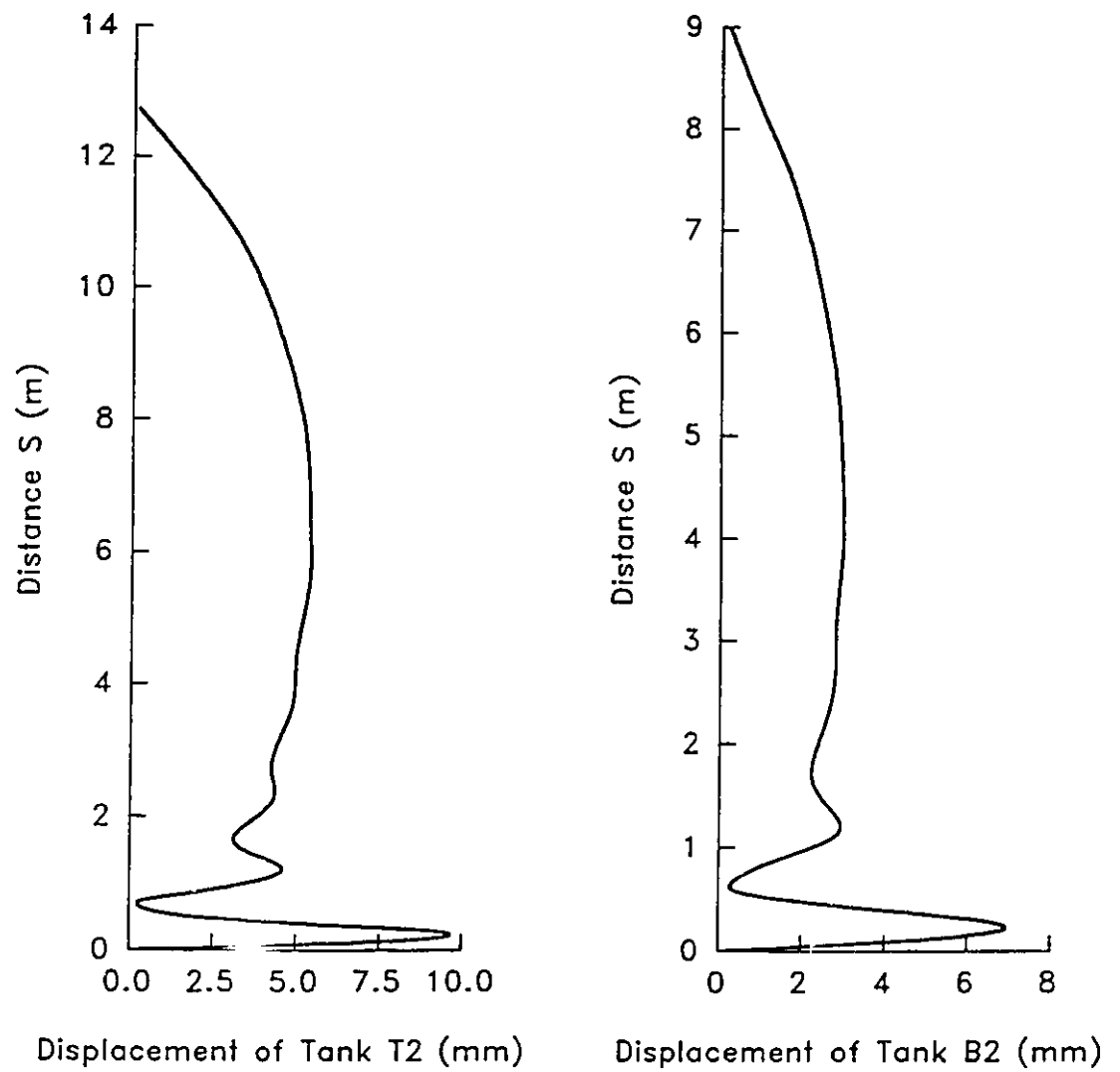
Figure 3.15 horizontal Displacements of Tanks T2,,B2 Near Buckling.

(Elastic Perfect Case—EP)
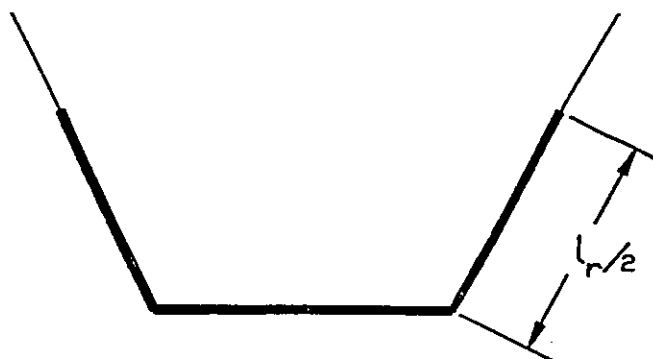
Figure 3.16 Critical Region in Conical Tanks.
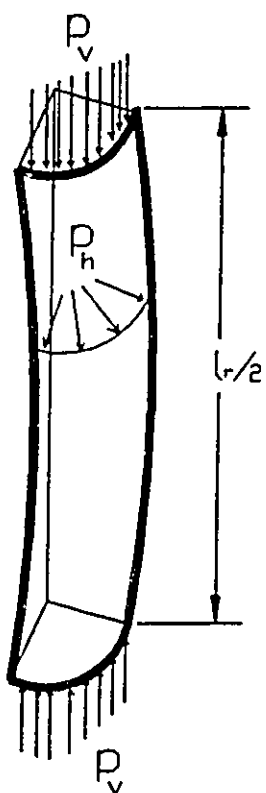
Figure 3.17 Concave Inward Panel.
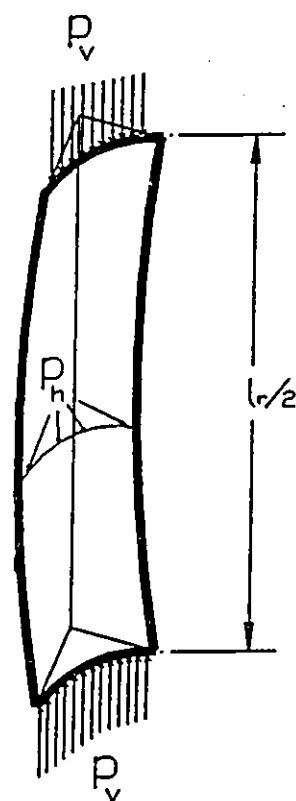
Figure 3.18 Concave Outward Panel.
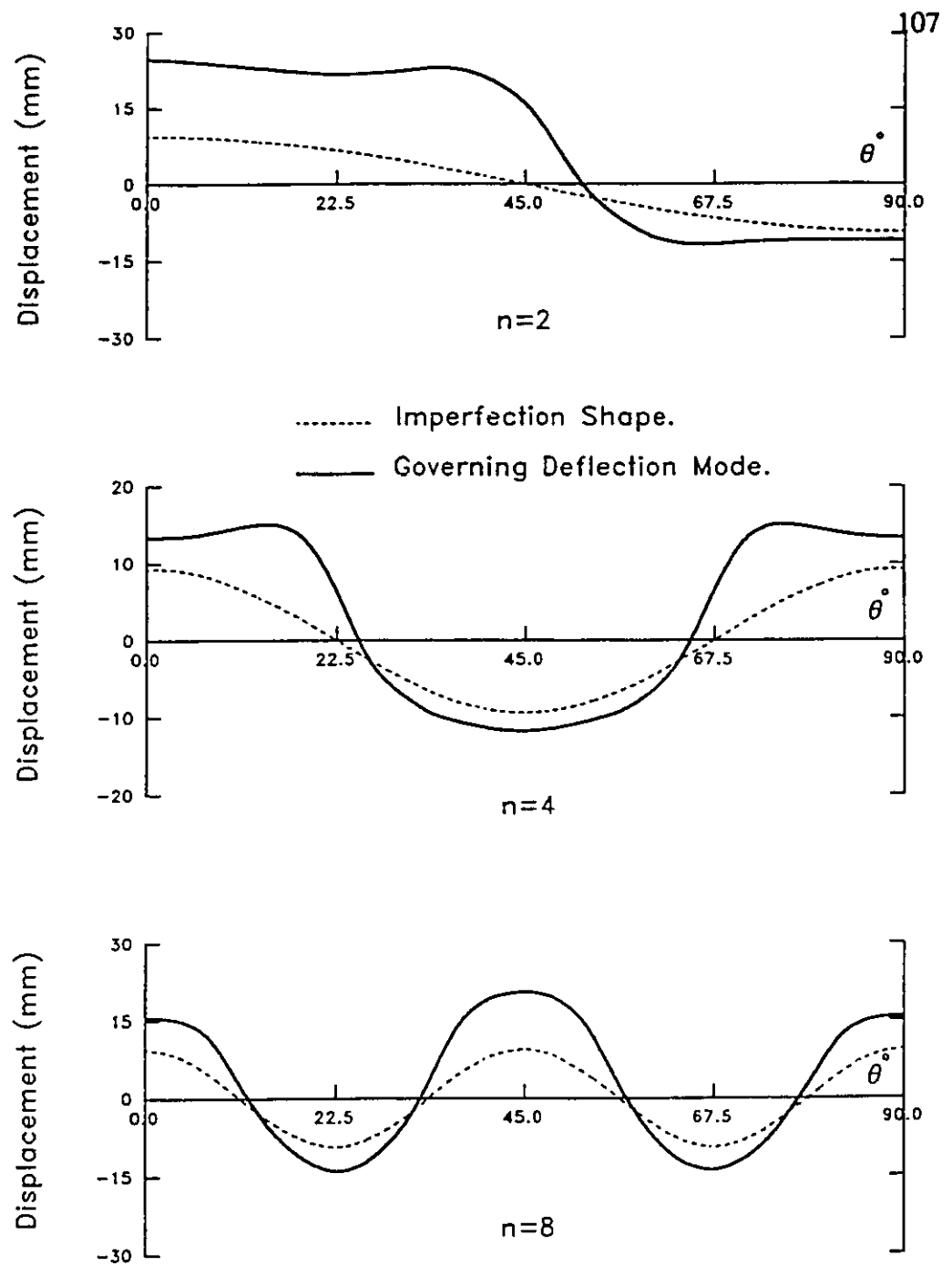
Figure 3.19 Transverse Displacements for Imperfection Wave

Numbers n of Tank B1 (S=0.235 m).
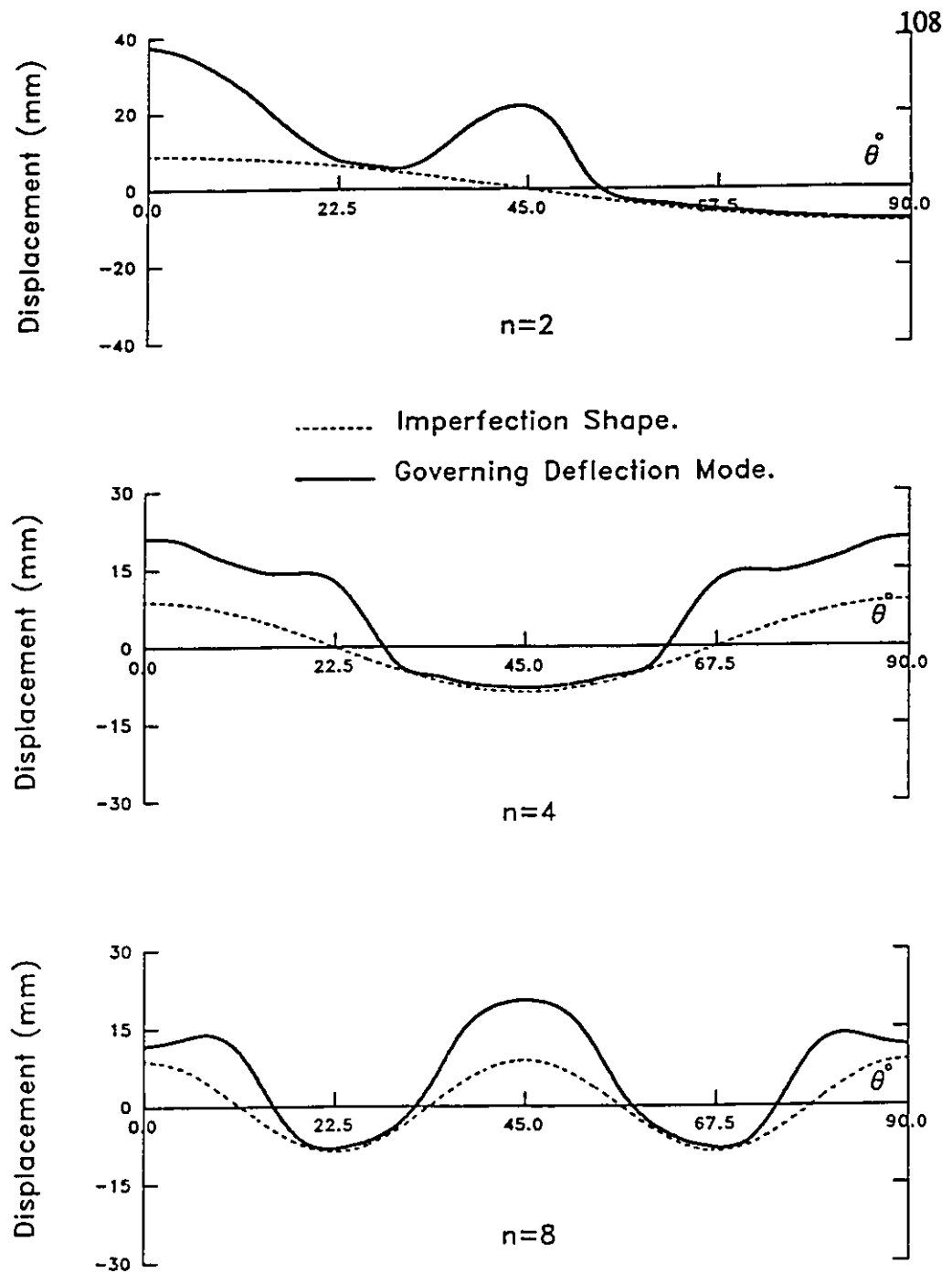
Figure 3.20 Transverse Displacements for Imperfection Wave
Numbers n of Tank T1 (S=0.22 m).
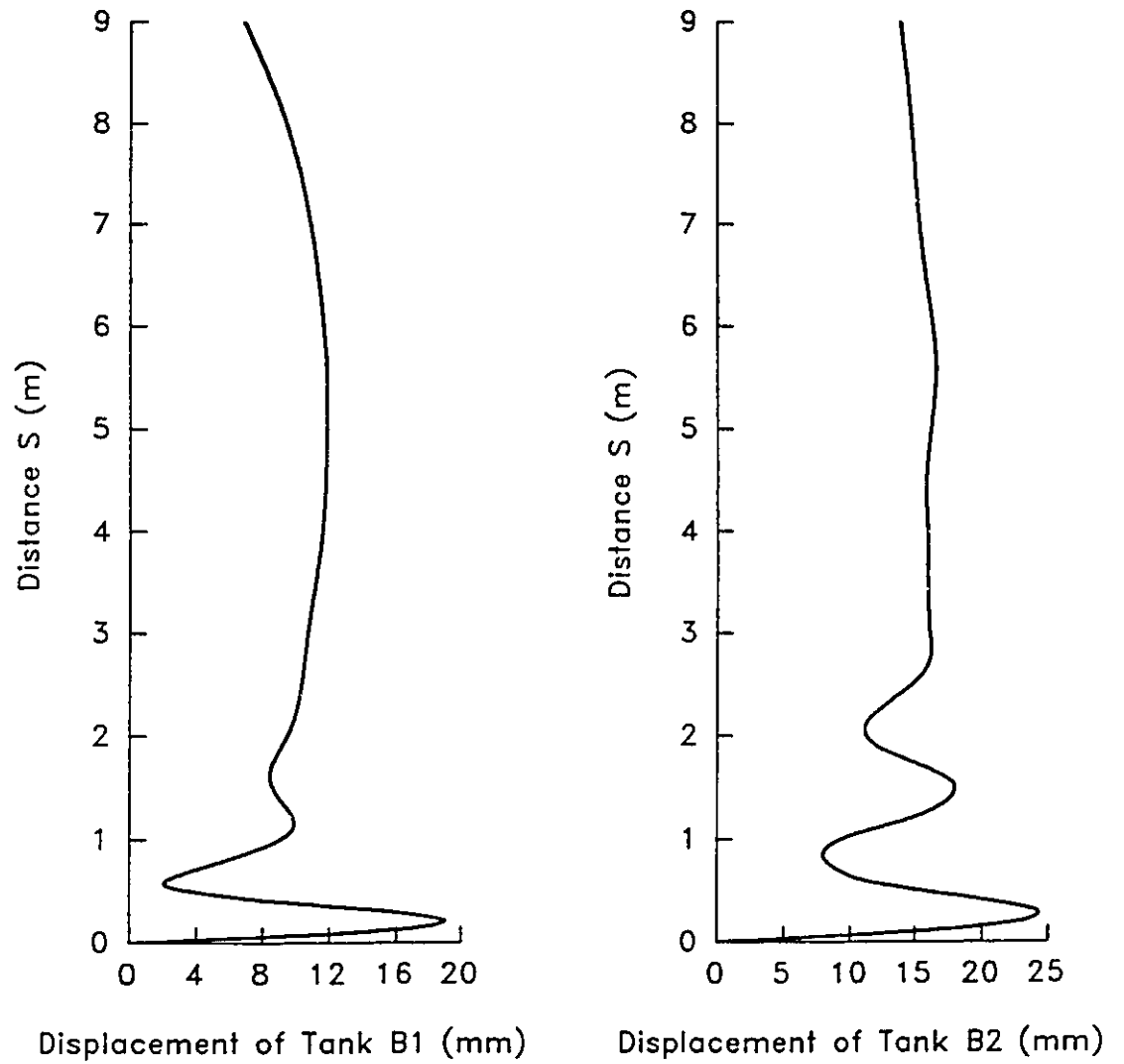
Figure 3.21 Transverse Displacements of Tanks B1,B2 Near Buckling.

(Elastic Imperfect Case—EI)
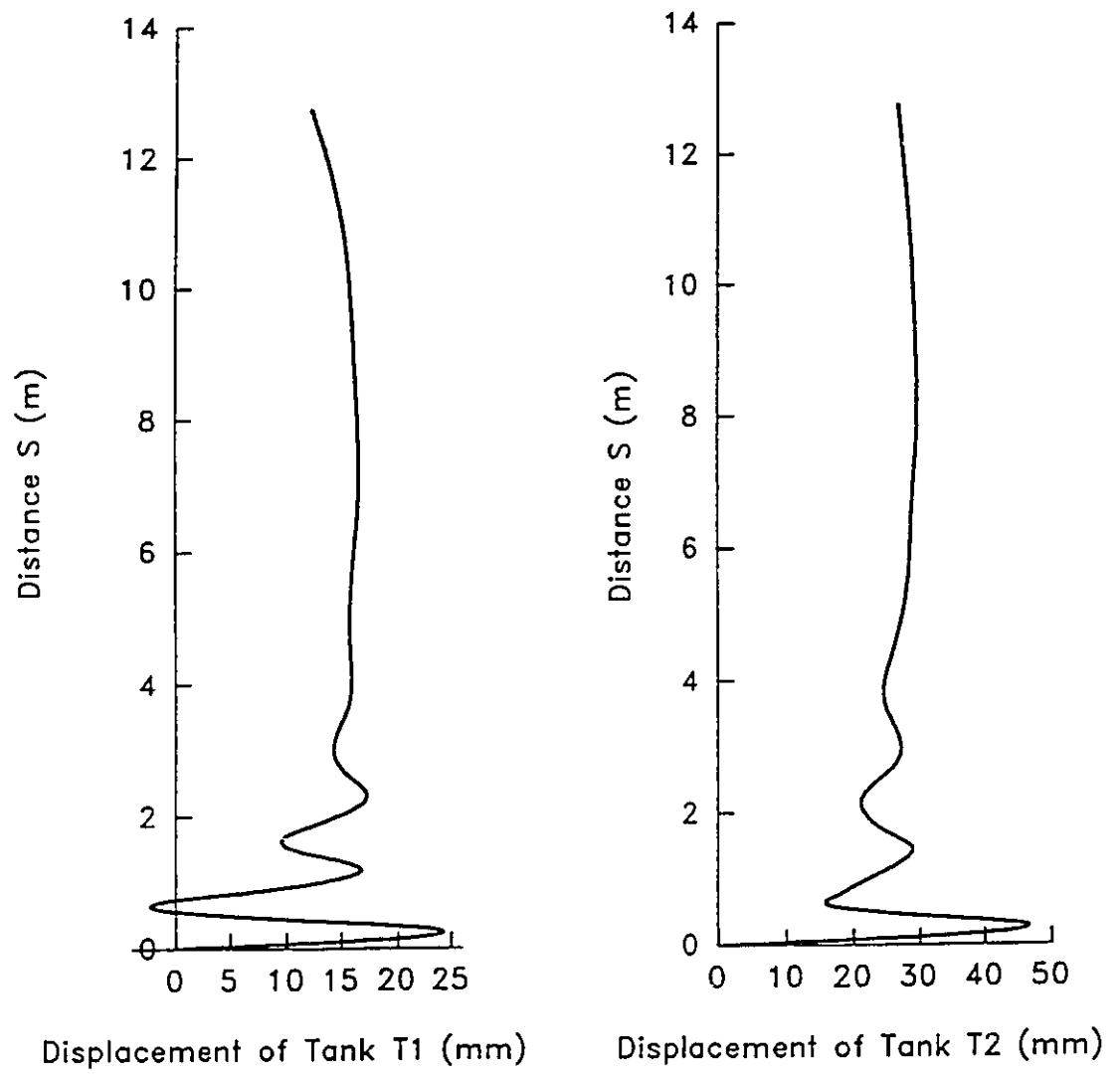
Figure 3.22 Transverse Displacements of Tanks T1,T2 Near Buckling.

(Elastic Imperfect Case−EI)
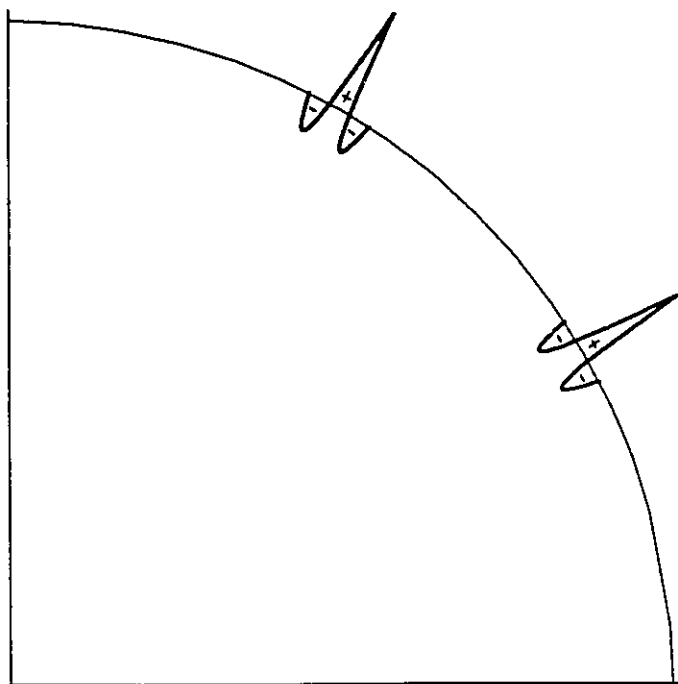
Figure 3.23 Meridional Residual Stresses due to Two Longitudinal Weldments.
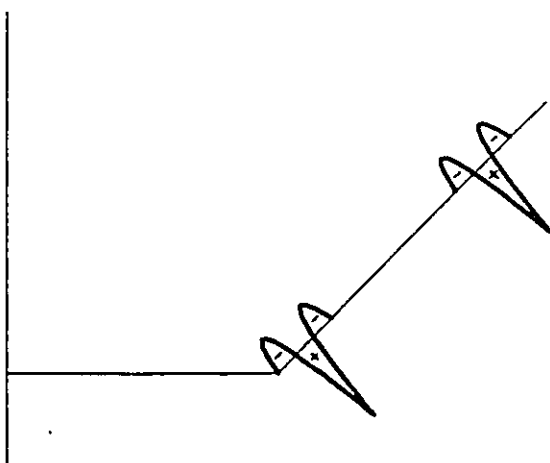
Figure 3.24 Hoop Residual Stresses due to Two Circumferential Weldments.
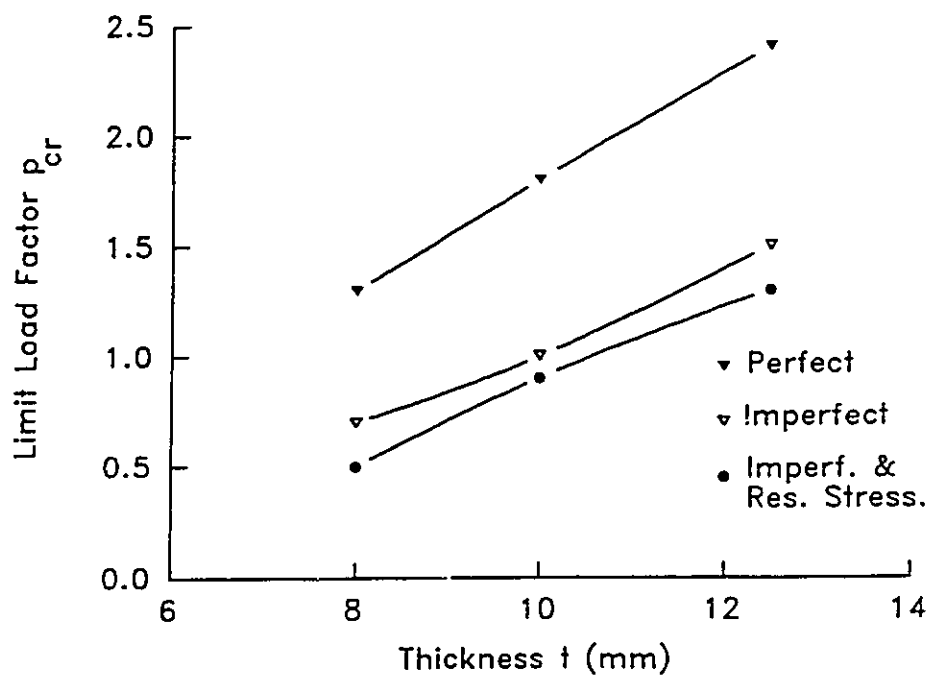
Figure 3.25 Limit Load Factor Versus Thickness for Tall Tanks
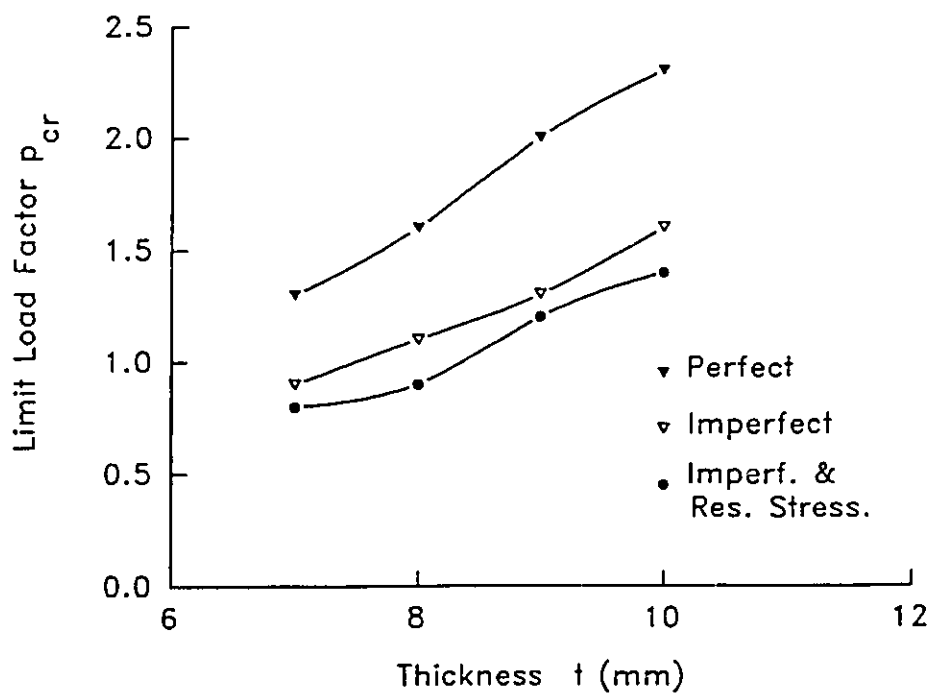
Figure 3.26 Limit Load Factor Versus Thickness for Broad Tanks

(a) Transverse Displacement (mm)

(b) Axial Displacement (mm)

(c) Hoop Stress (MPa)

(d) Axial Stress (MPa)
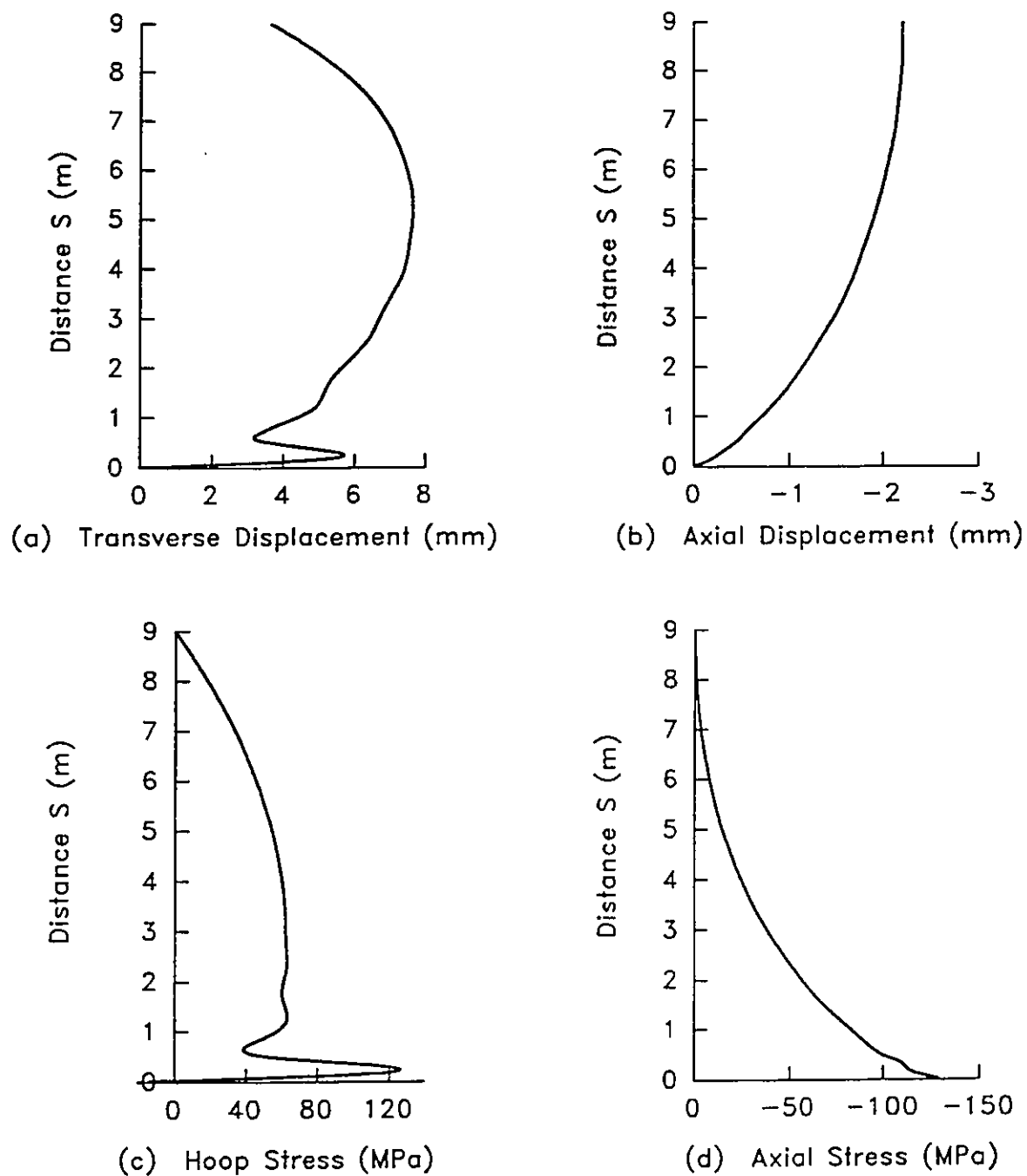
Figure 3.27 Response of Tank B1 Near Limit Load.

(Inelastic Perfect Case—PP)
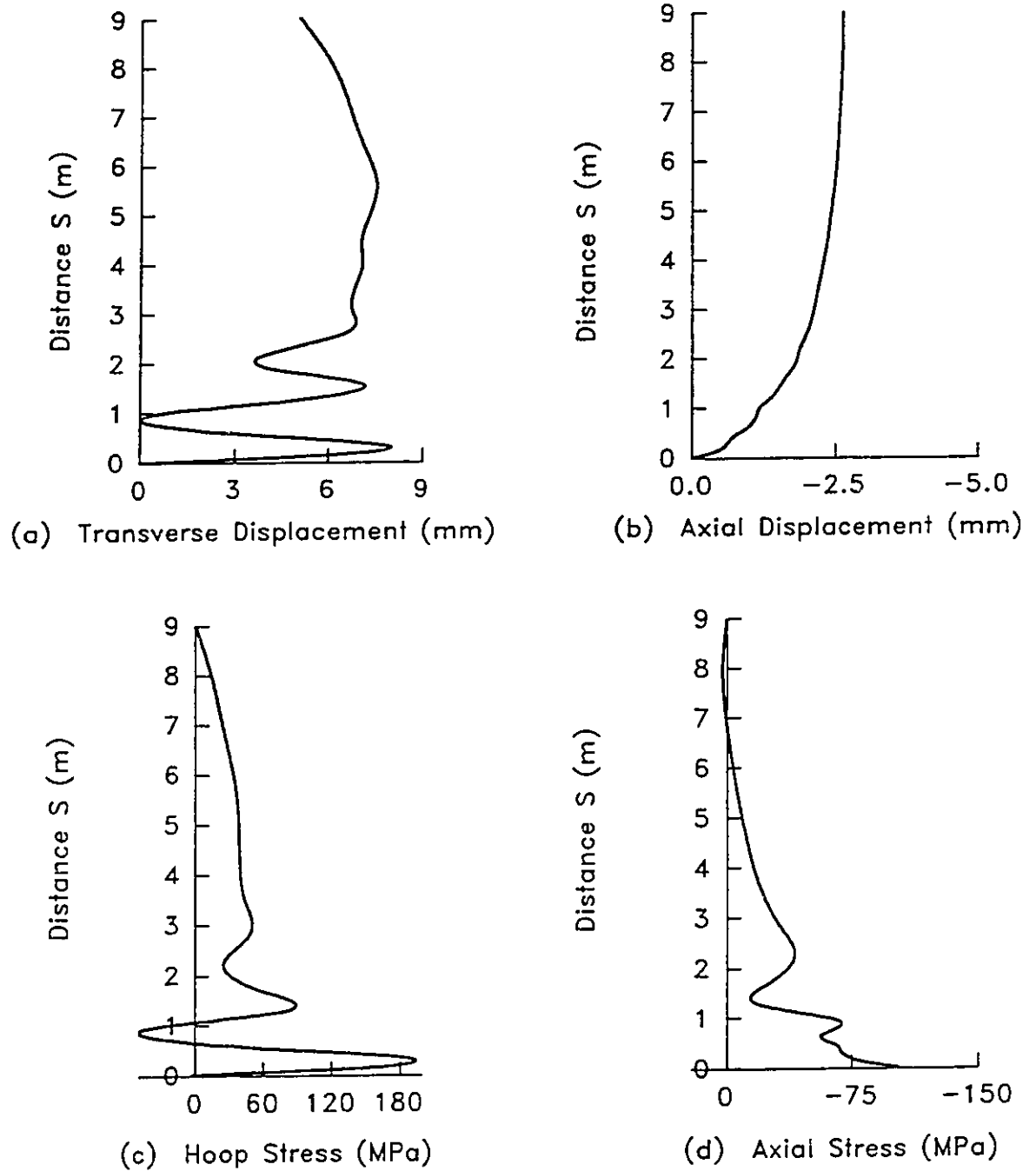
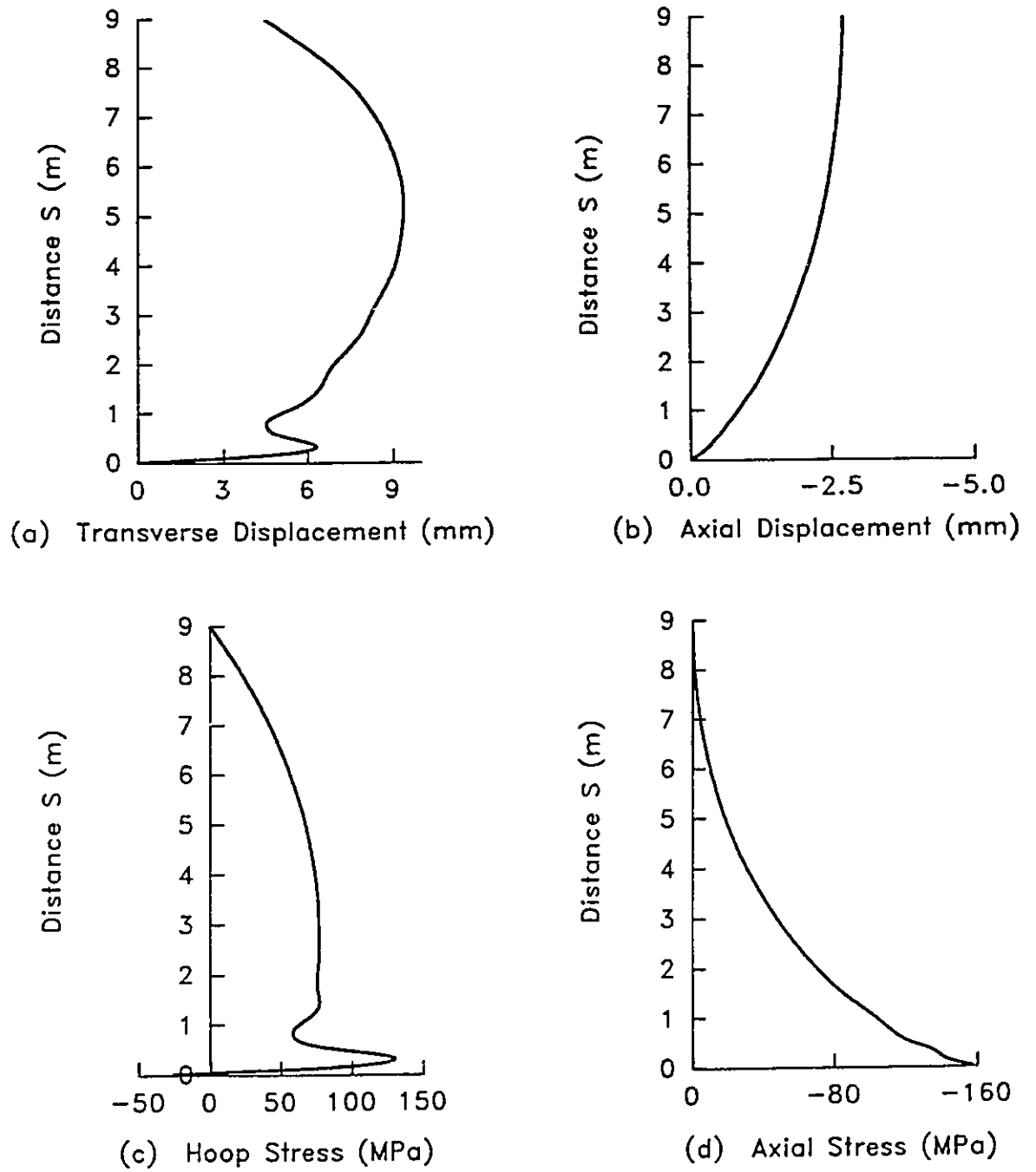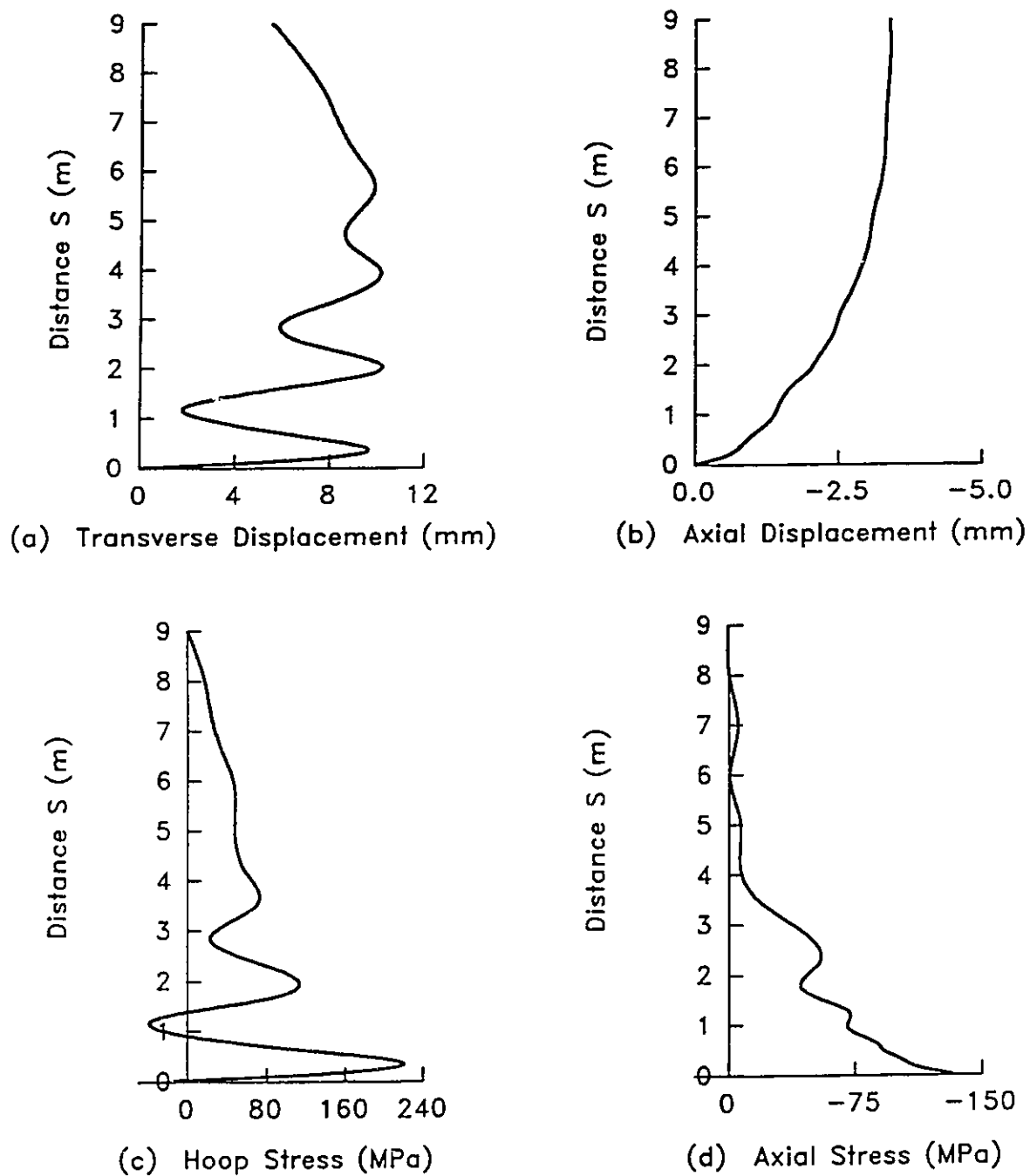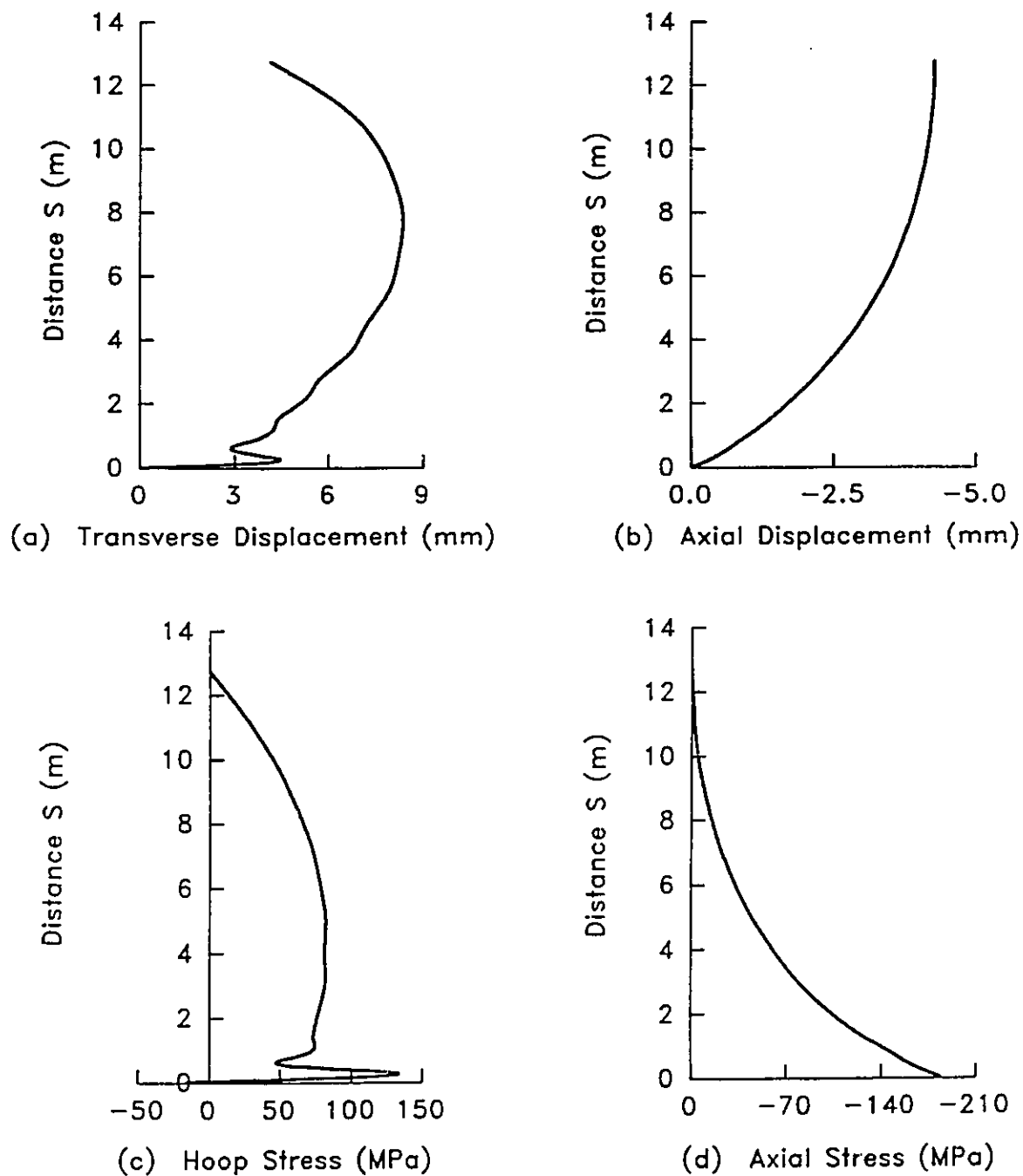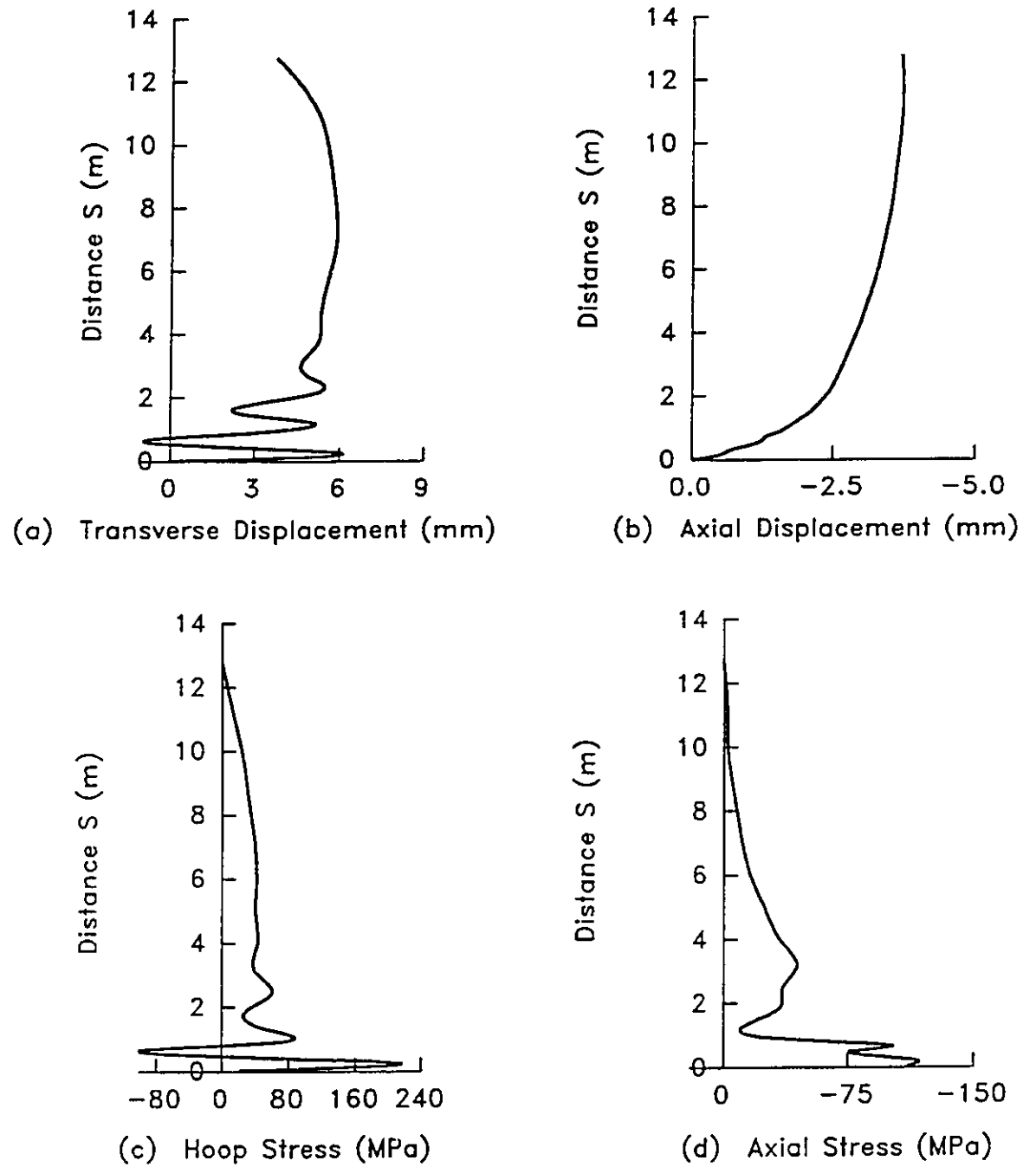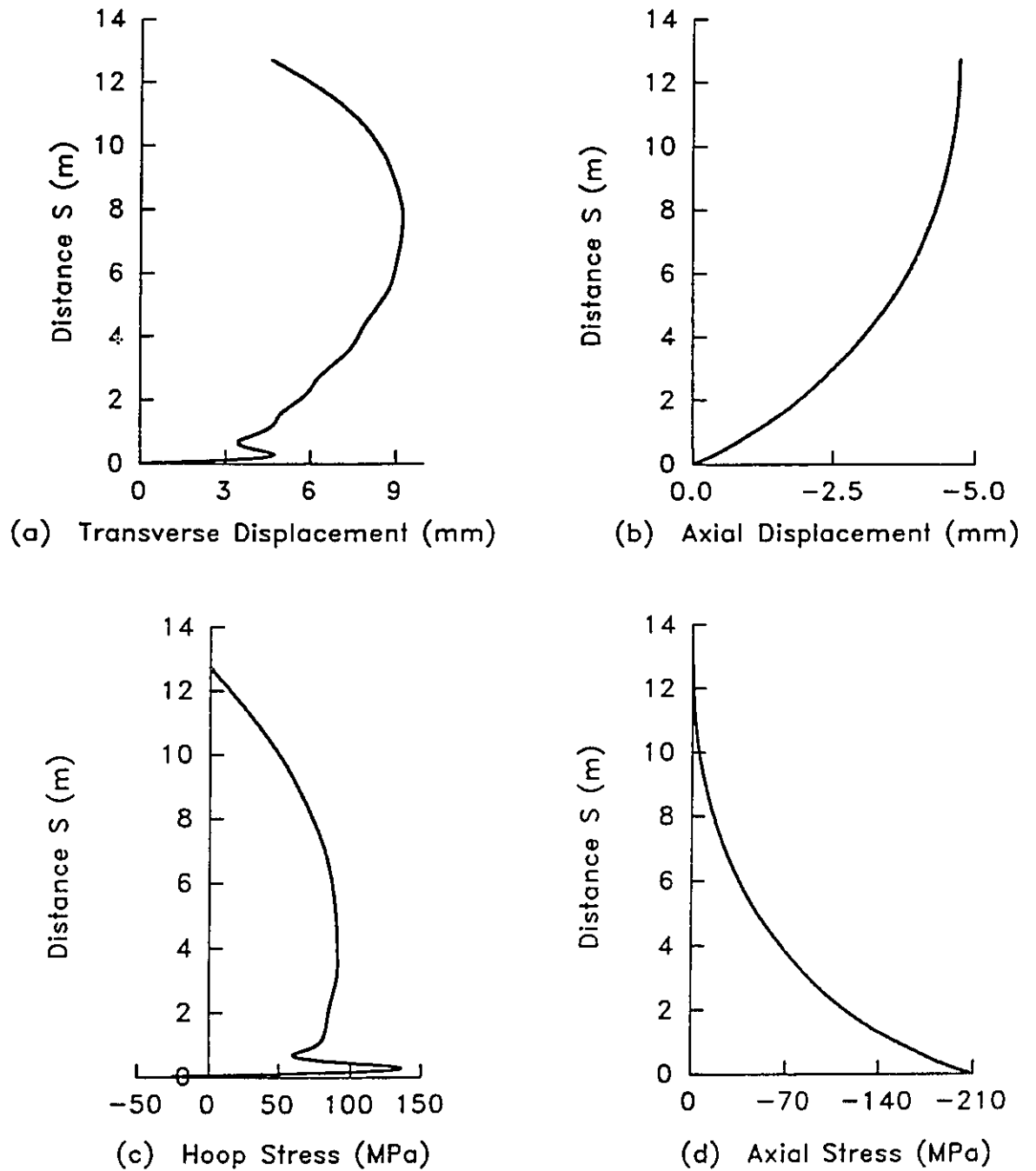Figure 3.28 Response of Tank B1 Near Limit Load.

(Inelastic Imperfect Case—PI)

(a) Transverse Displacement (mm)

(b) Axial Displacement (mm)

(c) Hoop Stress (MPa)

(d) Axial Stress (MPa)
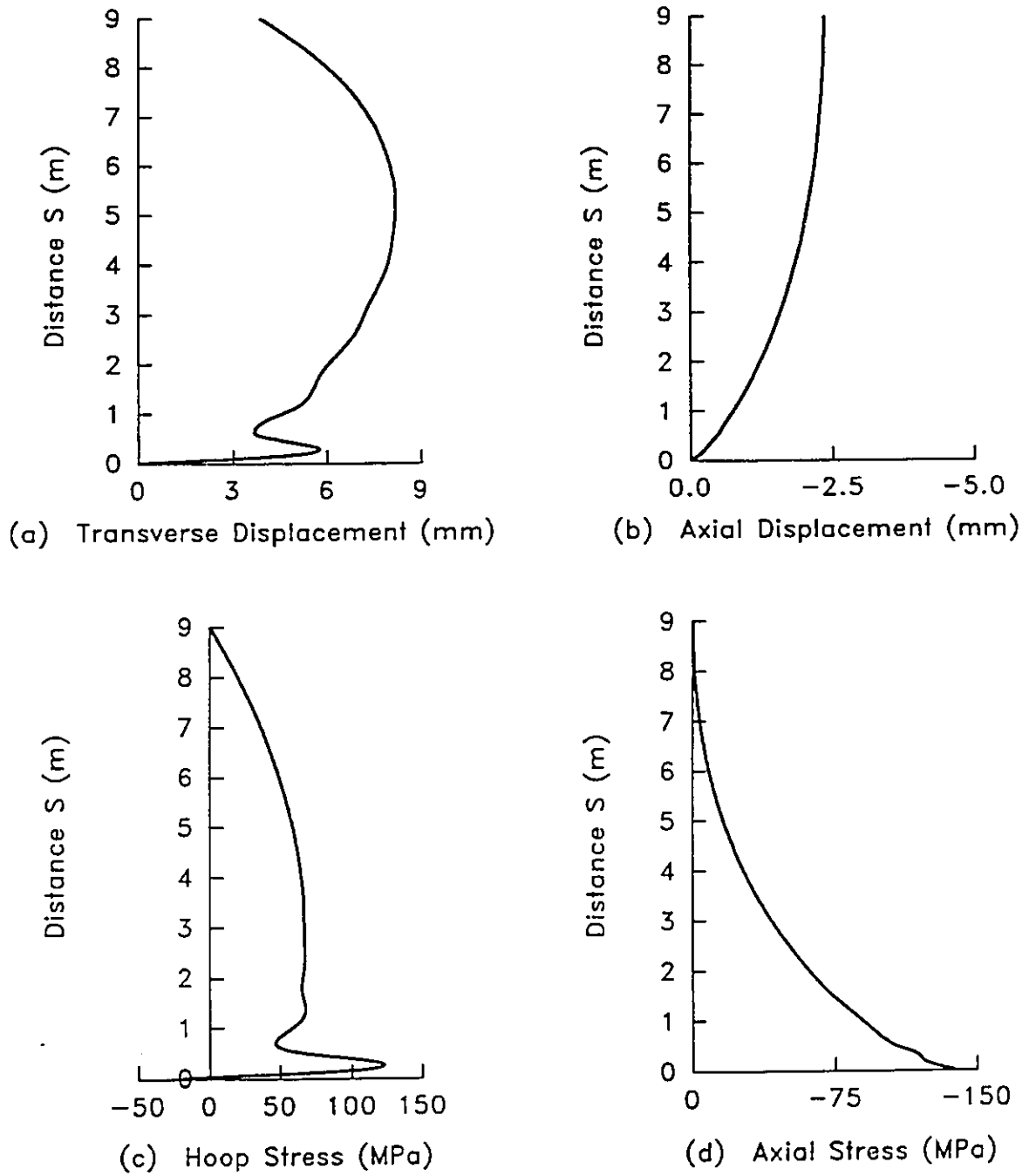
Figure 3.29 Response of Tank B2 Near Limit Load.

(Inelastic Perfect Case—PP)

(a) Transverse Displacement (mm)

(b) Axial Displacement (mm)

(c) Hoop Stress (MPa)

(d) Axial Stress (MPa)
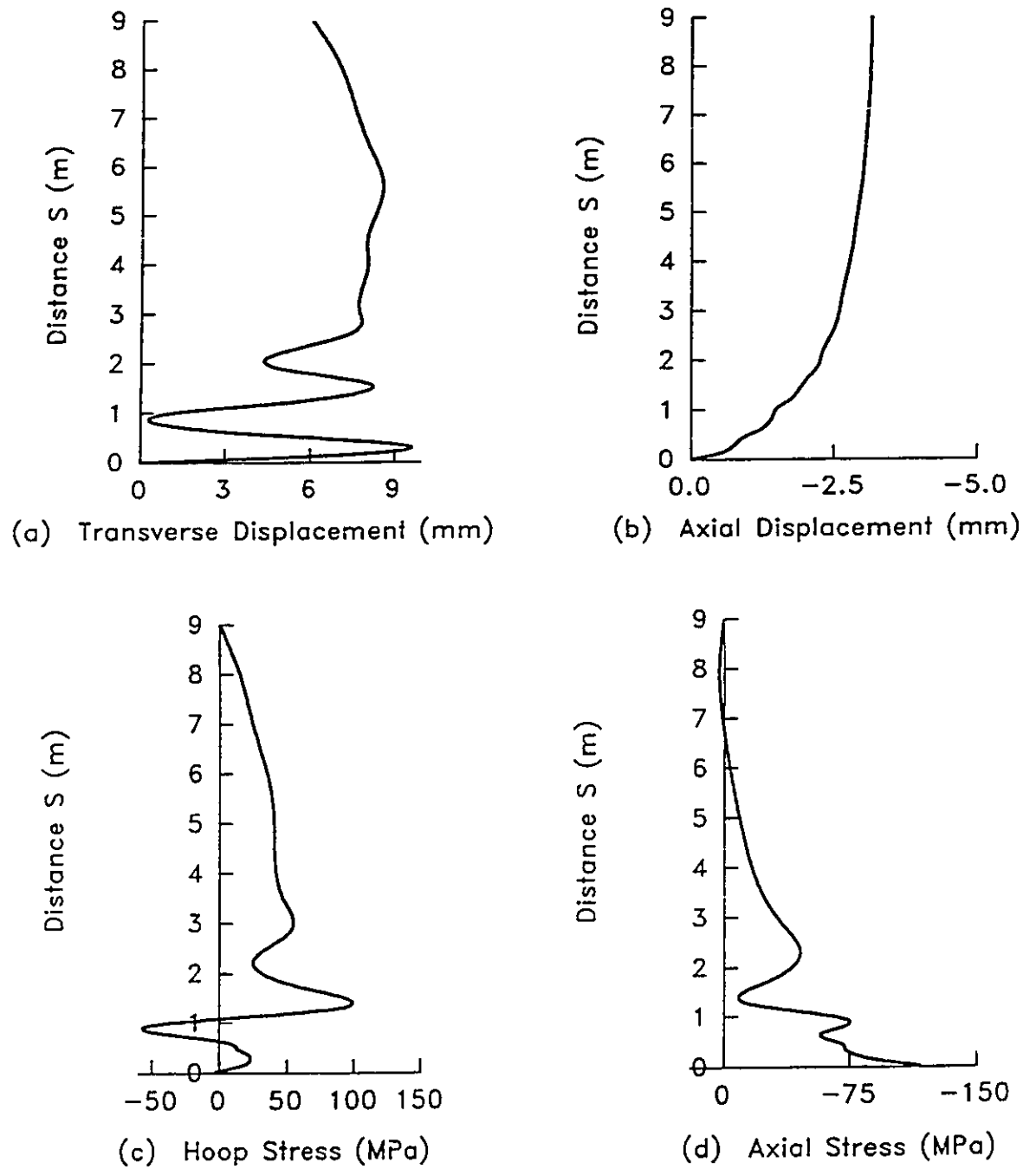
Figure 3.30 Response of Tank B2 Near Limit Load.

(Inelastic Imperfect Case–PI)

(a) Transverse Displacement (mm)

(b) Axial Displacement (mm)

(c) Hoop Stress (MPa)

(d) Axial Stress (MPa)
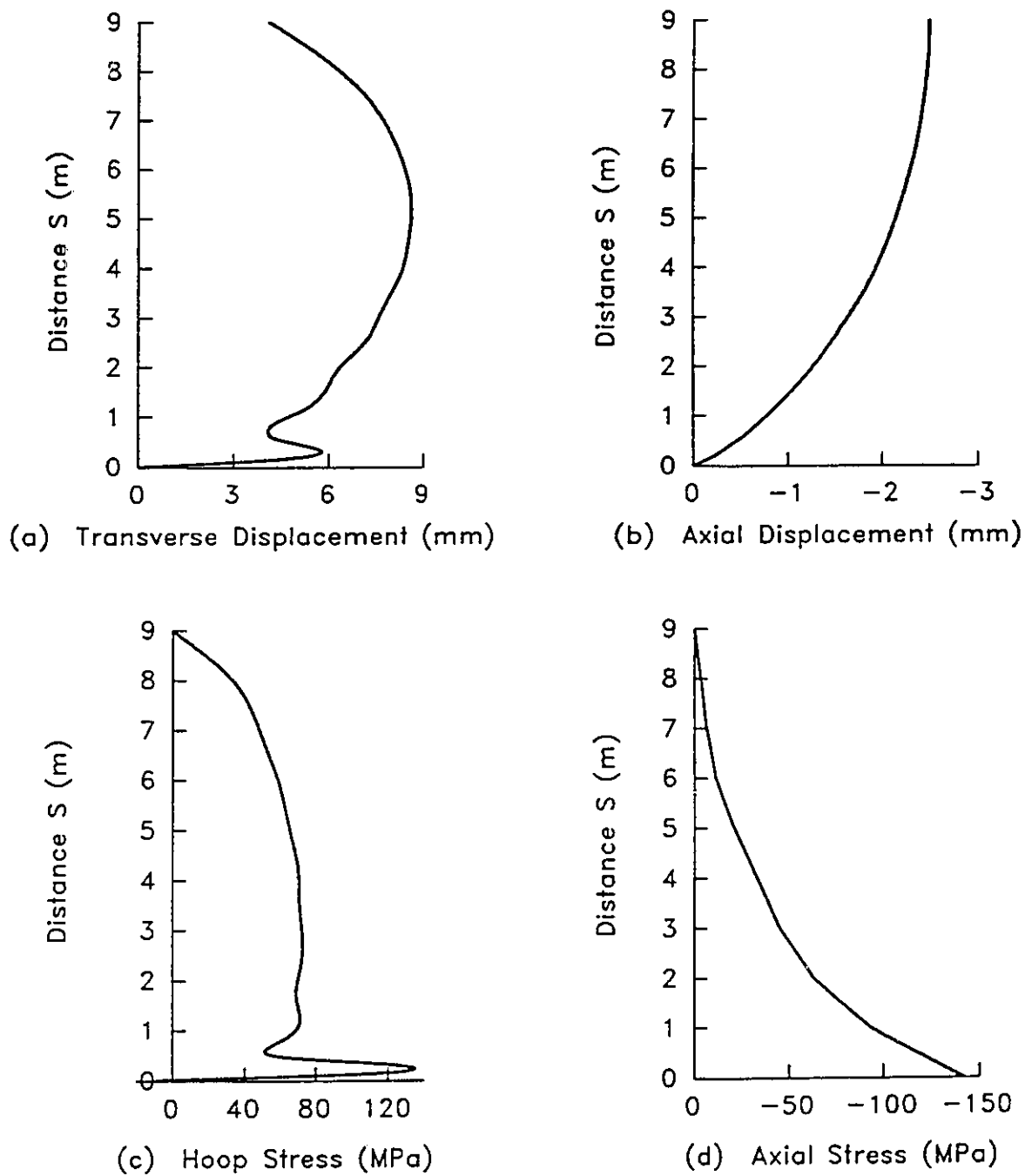
Figure 3.31 Response of Tank B3 Near Limit Load.

(Inelastic Perfect Case–PP)

(a) Transverse Displacement (mm)

(b) Axial Displacement (mm)

(c) Hoop Stress (MPa)

(d) Axial Stress (MPa)
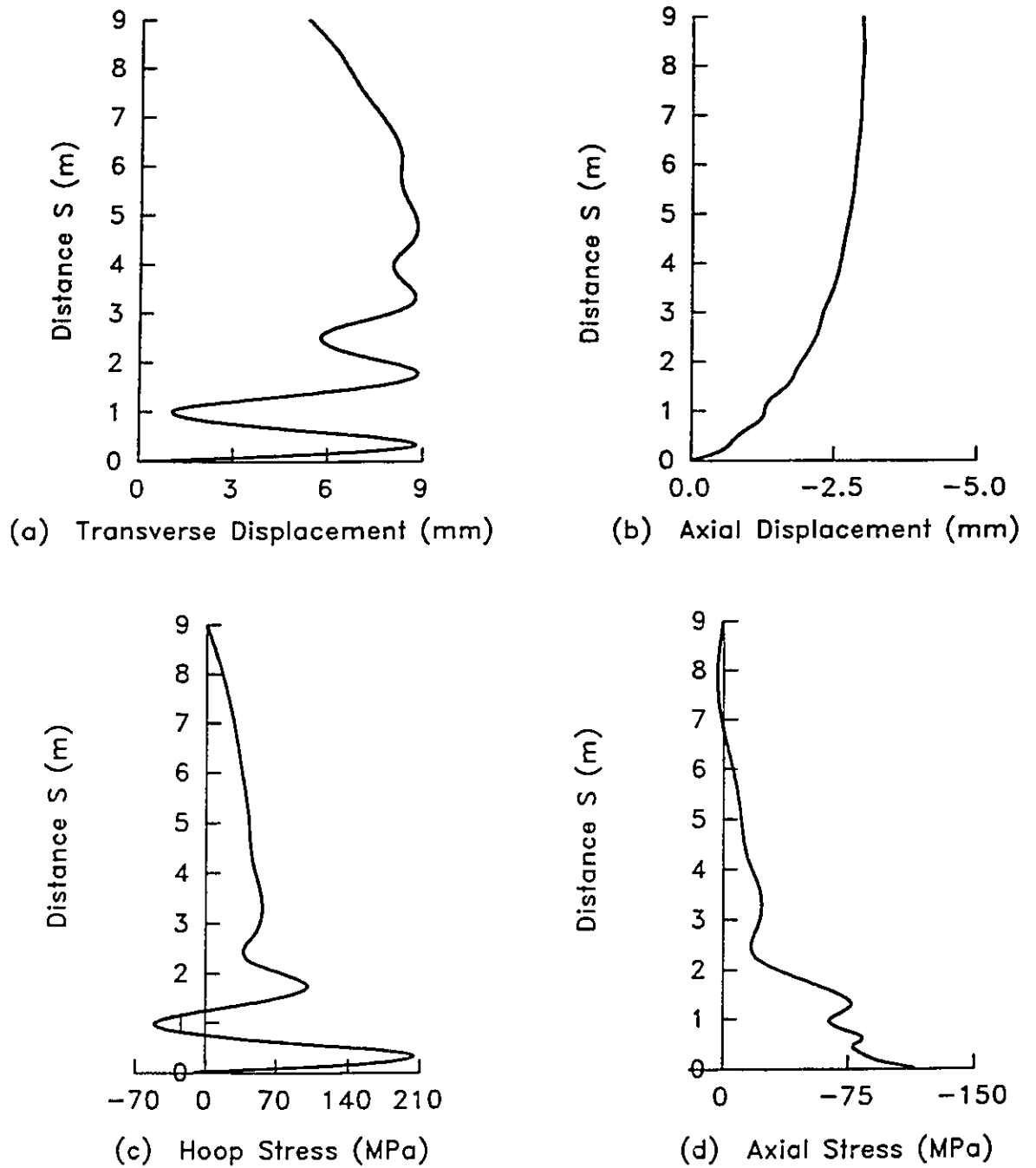
Figure 3.32 Response of Tank B3 Near Limit Load.

(Inelastic Imperfect Case-PI)

(a)   Transverse Displacement (mm)

(b)   Axial Displacement (mm)

(c)   Hoop Stress (MPa)

(d)   Axial Stress (MPa)

Figure 3.33 Response of Tank B4 Near Limit Load.

(Inelastic Perfect Case–PP)

(a) Transverse Displacement (mm)

(b) Axial Displacement (mm)

(c) Hoop Stress (MPa)

(d) Axial Stress (MPa)

Figure 3.34 Response of Tank B4 Near Limit Load.

(Inelastic Imperfect Case—PI)

(a) Transverse Displacement (mm)

(b) Axial Displacement (mm)

(c) Hoop Stress (MPa)

(d) Axial Stress (MPa)

Figure 3.35 Response of Tank T1 Near Limit Load.

(Inelastic Perfect Case—PP)

(a) Transverse Displacement (mm)

(b) Axial Displacement (mm)

(c) Hoop Stress (MPa)

(d) Axial Stress (MPa)

Figure 3.36 Response of Tank T1 Near Limit Load.

(Inelastic Imperfect Case–PI)

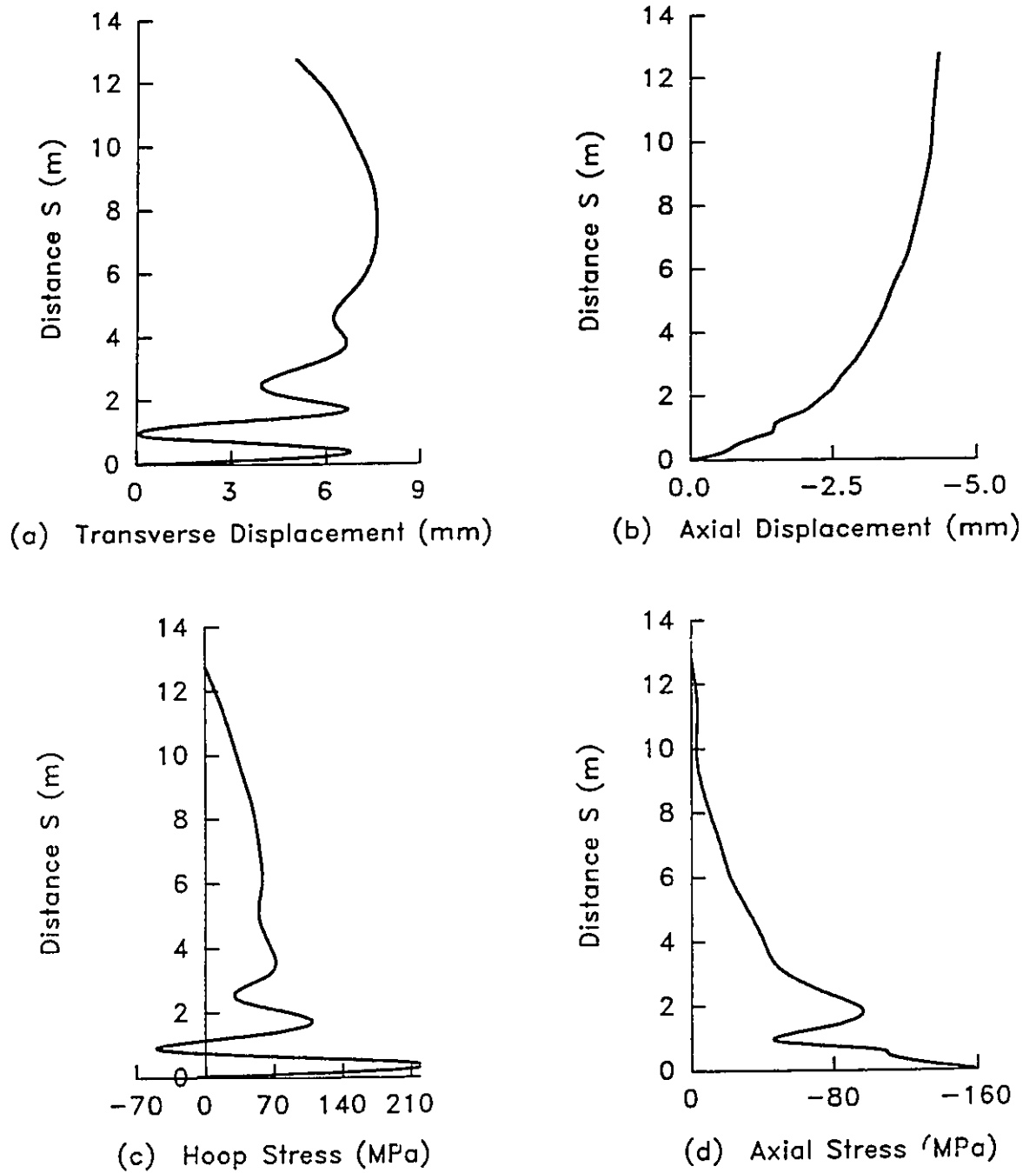Figure 3.37 Response of Tank T2 Near Limit Load.

(Inelastic Perfect Case-PP)
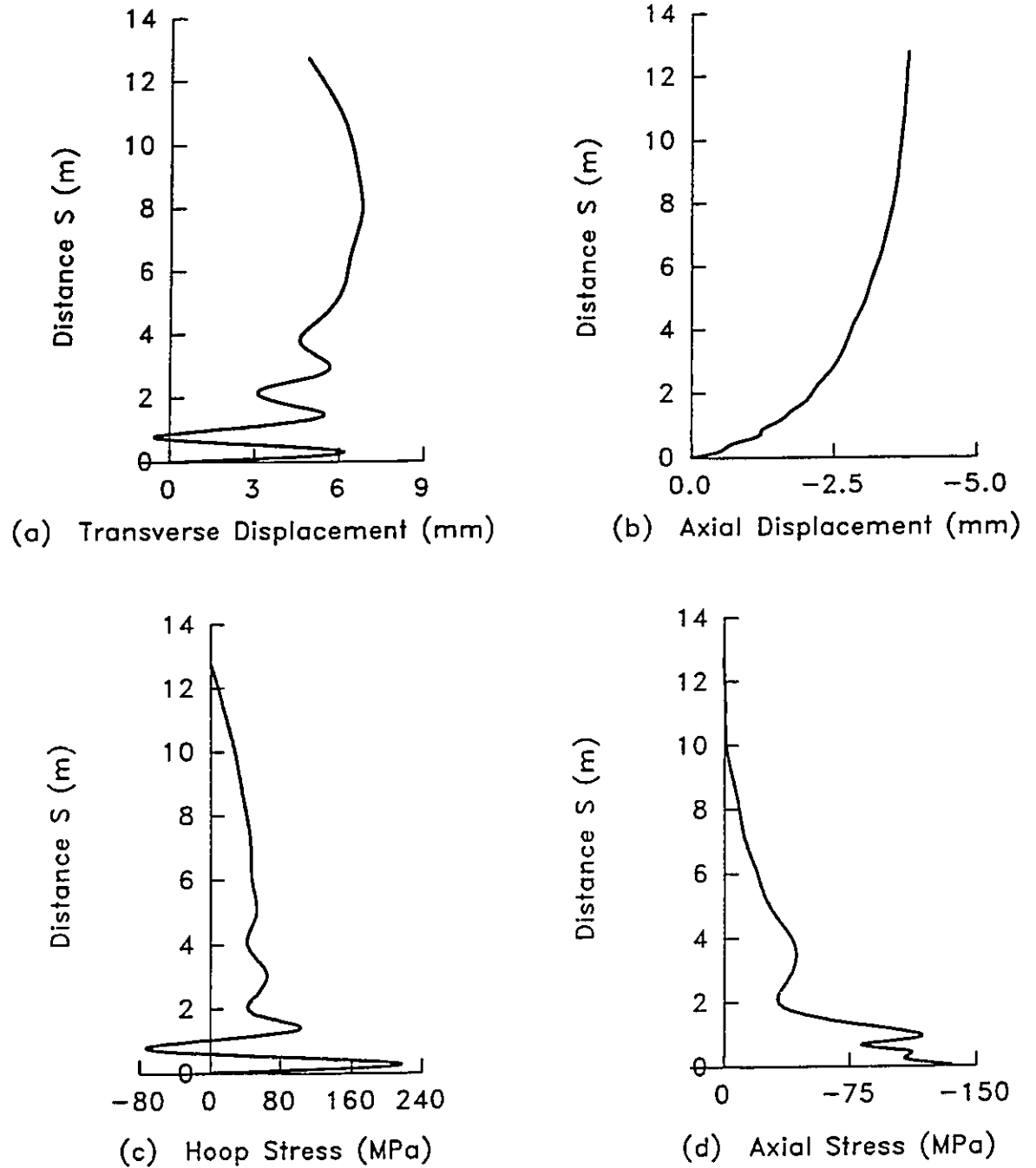
Figure 3.38 Response of Tank T2 Near Limit Load.
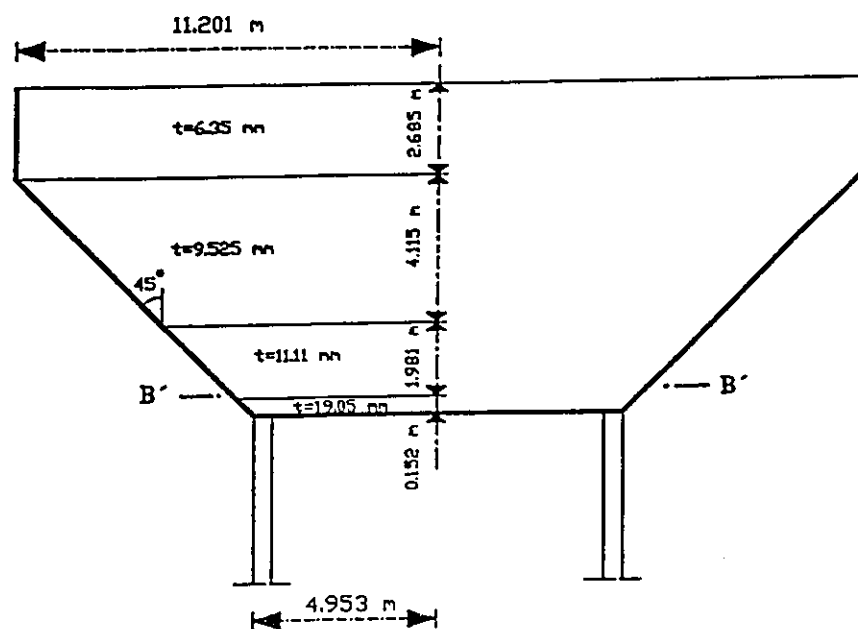
(Inelastic Imperfect Case—PI)

(a) Transverse Displacement (mm)

(b) Axial Displacement (mm)

(c) Hoop Stress (MPa)

(d) Axial Stress (MPa)
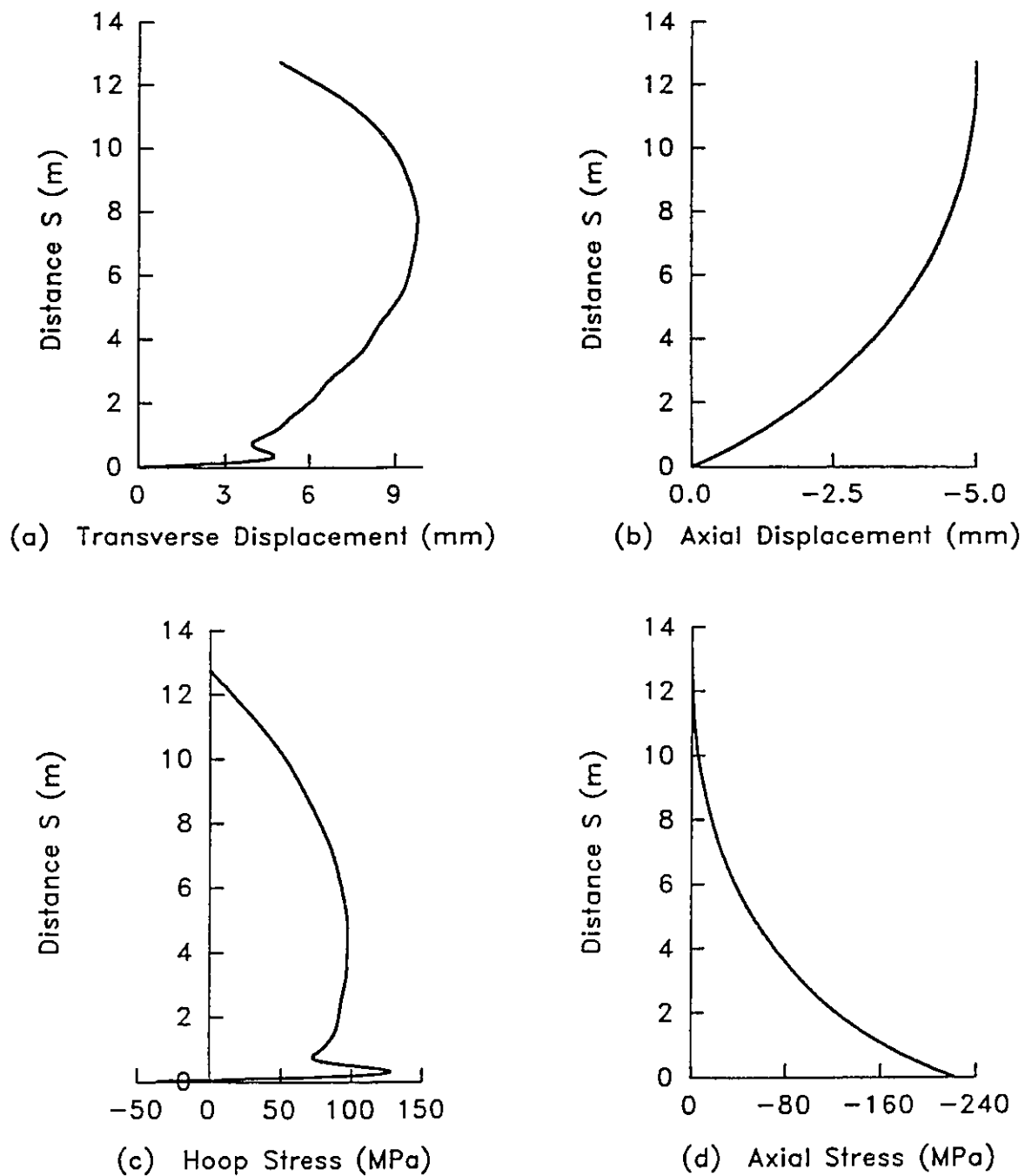
Figure 3.39 Response of Tank T3 Near Limit Load.

(Inelastic Perfect Case-PP)

(a) Transverse Displacement (mm)

(b) Axial Displacement (mm)

(c) Hoop Stress (MPa)

(d) Axial Stress (MPa)

Figure 3.40 Response of Tank T3 Near Limit Load.

(Inelastic Imperfect Case—PI)

Figure 3.41 Dimensions of the Fredericton Tank.
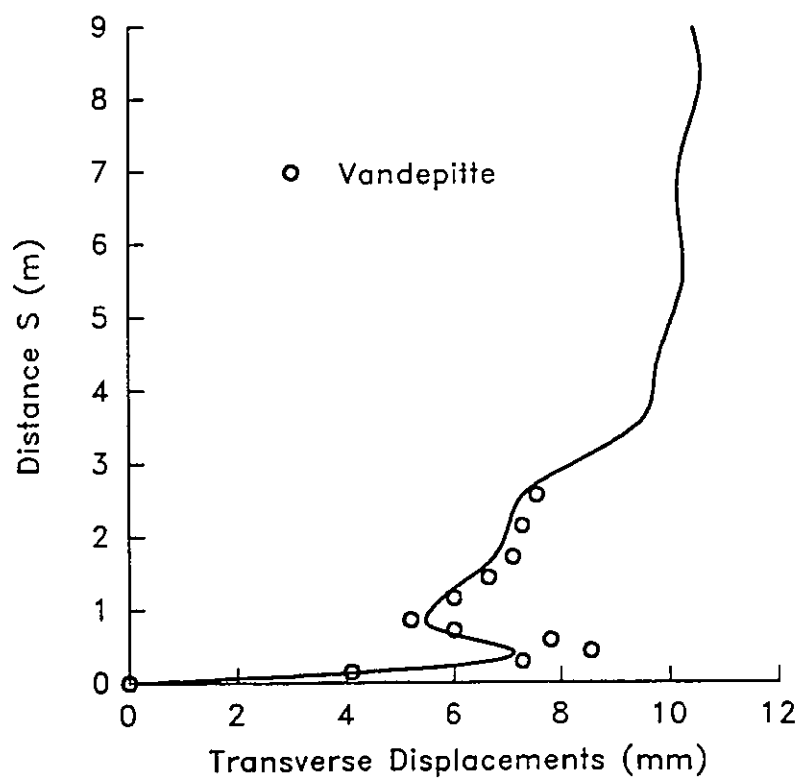
Figure 3.42 Displacement Pattern of the Fredericton Tank Near Buckling
(Inealstic Perfect Analysis)

CHAPTER FOUR

SEISMIC ANALYSIS OF LIQUID-FILLED CONICAL TANKS

4-1 Introduction

The design of elevated liquid-filled conical tanks, which are located in an active seismic zone, has to account for the dynamic instability which might occur during a strong earthquake. In this chapter, the seismic response of a liquid-filled conical tank is studied using the consistent shell element to model the structure and the boundary integral method to model the fluid.

The formulation of the consistent shell element, presented in Chapter Two, is first extended to non-linear dynamic analysis. This is achieved by deriving the mass matrix for the consistent shell element using the virtual work done by the inertia forces. The mass matrix is then incorporated into a non-linear time history analysis which uses Newmark's method to perform time integration and the Newton-Raphson method to iterate within each time step until dynamic equilibrium is achieved. A procedure for free vibration analysis is also formulated using the mass matrix and the linear stiffness matrix of the consistent shell element. The dynamic formulation is then verified by performing the free vibration and the non-linear time history analyses of a simply supported plate and a cylindrical shell. The results of the analyses are then compared with those available in the literature.

Two components of the hydrodynamic pressure develop inside a liquid-filled vessel that is subjected to a seismic excitation. These are the impulsive pressure which results from the vibrations of the walls of the tank and the convective pressure due to the free surface motion. Based on the previous investigations concerning liquid-filled cylindrical tanks, the convective component of pressure due to the free surface motion is neglected and only the impulsive component is considered in the analyses reported in this thesis. The hydrodynamic pressure distributions resulting from horizontal and vertical excitations acting on a liquid-filled tank, prevented from rocking at its base, are obtained using the boundary integral formulation. This leads to a fluid added-mass which when multiplied with the acceleration of the structure gives the inertia force resulting from the dynamic pressure. The fluid added-mass is combined with the mass matrix of the structure to perform both free vibration and non-linear time history analyses for a liquid-filled tank. The fluid added-mass formulation is verified by performing free vibration analyses of liquid-filled cylindrical tanks under both horizontal and vertical excitations. The resulting natural frequencies from the analyses are compared to those given by Haroun (1980) and Haroun and Tayel (1985b).

In order to study the sensitivity of liquid-filled conical tanks to seismic motion, free vibration analyses are first performed for seven elevated liquid-filled conical tanks which are supported on rigid frames and have different dimensions and magnitudes of axisymmetric imperfections. Following this, a real earthquake, which includes the natural frequencies of the liquid-filled conical tanks in its dominant frequency content, is applied as an input ground motion to perform non-linear time history analyses of all seven liquid-

filled elevated conical tanks.

4-2 Dynamic Extension of the Consistent Shell Element Formulation

4-2-1 Derivation of the Consistent Mass Matrix

The consistent mass matrix of the subparametric shell element is derived using the virtual work quantity V_M done by the inertia forces. In the mass matrix formulation, the rotationary inertia involving the rotational degrees of freedom α, β, ϕ and ψ is neglected. Therefore, the virtual work quantity V_M at a time T can be given as

$$V_M = \int_S \rho_s h(s) \, [\ddot{u}^T \delta(\Delta u) + \ddot{v}^T \delta(\Delta v) + \ddot{w}^T \delta(\Delta w)] \, dS \qquad (4.1)$$

where ρ_s is the density of the shell material; h(s) is the thickness of the shell; $\ddot{u}^T$, $\ddot{v}^T$, $\ddot{w}^T$ are the components of the acceleration at time T along the global coordinates x, y and z, respectively; $\delta(\Delta u)$, $\delta(\Delta v)$ and $\delta(\Delta w)$ are the components of the virtual incremental displacements along the global directions x, y and z, respectively. Due to the assumption of negligible rotationary inertia, the rotational degrees of freedom can be ignored in the expressions for the incremental and total displacements of the consistent shell element given by Equations 2.4 and 2.54, respectively. Therefore, the components of the virtual global incremental displacements and those of the total global accelerations can be given by the following equations:

$$\delta(\Delta u) = \sum_{n=1}^{13} \bar{N}_n \delta(\Delta U_n) \qquad (4.2)$$

$$\delta(\Delta v) = \sum_{n=1}^{13} \bar{N}_n \delta(\Delta V_n) \qquad (4.3)$$

$$\delta(\Delta w) = \sum_{n=1}^{13} \overline{N}_n \delta(\Delta W_n) \qquad (4.4)$$

$$\ddot{u}^{(T)} = \sum_{n=1}^{13} \overline{N}_n \ddot{U}^T \qquad (4.5)$$

$$\ddot{v}^{(T)} = \sum_{n=1}^{13} \overline{N}_n \ddot{V}^T \qquad (4.6)$$

$$\ddot{w}^{(T)} = \sum_{n=1}^{13} \overline{N}_n \ddot{W}^T \qquad (4.7)$$

where $\overline{N}_n$ are the cubic interpolation functions as given in Appendix A; ΔU_n, ΔV_n and ΔW_n are the components of the incremental displacement degrees of freedom of the nth node along the global directions x, y and z, respectively; $\ddot{U}_n^T$, $\ddot{V}_n^T$ and $\ddot{W}_n^T$ are the components of the total acceleration of the nth node along the global directions x, y and z, respectively, at time T. Substituting Equations 4.2 to 4.7 into the expression of the virtual work done by the inertia forces given by expression 4.1, leads to the inertia force F_I of the consistent shell element and is given by the following:

$$\{F_I\} = \sum^{NEL} [M_S]_{91 \bullet 91} \{\Delta \ddot{U}^T\}_{91 \bullet 1} \qquad (4.8)$$

where NEL is the number of elements.

The components of the mass matrix $M_S{}^{ij}$ can be obtained by relating the indices i and j to the variables k_1, l_1, k_2 and l_2 in the following manner:

$$i = 7 * (k_1 - 1) + l_1 \qquad\qquad (4.9)$$

$$j = 7 * (k_2 - 1) + l_2 \qquad\qquad (4.10)$$

In the equations above, k_1 and k_2 can take on values from 1 to 13, while l_1 and l_2 take on values from 1 to 7. The numerical values 13 corresponds to the number of nodes per element while 7 relates to the number of degrees of freedom per node. Any combination of k_1, k_2, l_1 and l_2 corresponds to certain values of i and j and defines M_s^{ij} according to the following:

For $l_1 = 4$ to 7 and/or $l_2 = 4$ to 7 the corresponding $M_s^{ij} = 0$; otherwise, the component of the mass matrix is given by

$$M_S^{ij} = \int_S \overline{N}_{k_1} \, \overline{N}_{k_2} \, \delta \, (l_1 l_2) \, \rho_s \, h(s) \, ds \qquad\qquad (4.11)$$

where $\delta(l_1 l_2)$ is the kroneker delta function, i.e. $\delta(l_1 l_2) = 1$ for $l_1 = l_2$ and $\delta(l_1 l_2) = 0$ for $l_1 \neq l_2$. The integration of Equation 4.11 is performed numerically by employing the Gaussian Quadrature scheme in the r-s plane as given in Section 2-7.

4-2-2 Free Vibration Analysis using the Consistent Shell Element

The linear stiffness matrix of the shell element $[K_o]$ is obtained by omitting the terms which are multiplied by the initial strains $u'_{i,j}{}^{T\,(k-1)}$ from the non-linear stiffness matrix $[K_L]$ given in Chapter Two. Both the linear stiffness matrix $[K_o]$ and the mass matrix $[M_s]$ are used to calculate the natural frequencies of a shell ω_n and the corresponding mode shapes $\{q_n\}$ by solving the following equations:

$$([K_o] - \omega^2 [M_s]) \{q\} = \{0\}. \tag{4.12}$$

The non-trivial solution of Equation 4.12 exists if the determinant of the coefficients vanishes, i.e.

$$| [K_o] - \omega^2 [M_s] | = 0. \tag{4.13}$$

This is solved to obtain the natural frequencies of the shell and subsequently the mode shape $\{q_n\}$, typically for a limited number.

4-2-3 Non-Linear Time History Analysis using the Consistent Shell Element

In view of Equation 2.22, the incremental equations of motion for the non-linear dynamic analysis which include both the inertia and the damping forces is given by

$$[M_s] \{\ddot{U}^T\} + [C] \{\dot{U}^T\} + [K_L^{T~(k-1)} + K_S^{T~(k-1)}] \{\Delta U\} = \{R^T\} - \{F^{T~(k-1)}\} \tag{4.14}$$

where [C] is the viscous damping matrix; [K_L] and [K_S] are the non-linear stiffness matrices; {F} is the unbalanced load vector as given in Chapter Two and {R} is the external load vector. The implicit time integration of Equation 4.14 is performed using Newmark's method (see Bathe, 1982) with the implicitness parameters known as $\delta(=0.5)$ and $\alpha(=0.25)$. Iterations are performed using the Newton-Raphson method within each time step ΔT, until equilibrium is reached. Following the procedure described by Bathe (1982), the incremental solution $\{\Delta U\}$ which corresponds to the kth iteration during the time step ΔT, can be obtained by solving the following equation:

$$[K^{*T\ (k-1)}]\{\Delta U\}=\{R^T\}-\{F^{T\ (k-1)}\}-[M_S]\{A^{T\ (k-1)}\}-[C]\{B^{T\ (k-1)}\}.\qquad(4.15)$$

The matrix $[K^{*T\ (k-1)}]$ is an effective stiffness matrix of the following form:

$$[K^{*T\ (k-1)}]=[K_L^{T\ (k-1)}]+[K_S^{T\ (k-1)}]+\frac{4}{(\Delta T)^2}[M_S]+\frac{2}{(\Delta T)}[C]\ .\qquad(4.16)$$

The vectors $\{A^{T\ (k-1)}\}$ and $\{B^{T(k-1)}\}$ are updated after each iteration during the time step ΔT and are obtained by the following:

$$\{A^{T\ (k-1)}\}=\frac{4}{\Delta T^2}\ [\{U^{T\ (k-1)}\}-\{U^{T-\Delta T}\}]\ -\frac{4}{\Delta T}\{\dot{U}^{T-\Delta T}\}-\{\ddot{U}^{T-\Delta T}\}\qquad(4.17)$$

$$\{B^{T\ (k-1)}\}=\frac{2}{\Delta T}\ [\{U^{T\ (k-1)}-\{U^{T-\Delta T}\}]\ -\{\dot{U}^{T-\Delta T}\}\qquad(4.18)$$

where $\{U^{T\ (k-1)}\}$ is the vector which includes the total displacement degrees of freedom after the (k-1) iteration for the current time T; $\{U^{T-\Delta T}\}$, $\{\dot{U}^{T-\Delta T}\}$ and $\{\ddot{U}^{T-\Delta T}\}$ are the vectors of the total nodal displacement, the total nodal velocity and the total nodal acceleration at the equilibrium configuration corresponding to the time (T-ΔT). Based on the trapezoidal rule, the vectors $\{\dot{U}^{T-\Delta T}\}$ and $\{\ddot{U}^{T-\Delta T}\}$ are evaluated using the displacements $\{U^{T-2\Delta T}\}$, the velocities $\{\dot{U}^{T-2\Delta T}\}$ and the accelerations $\{\ddot{U}^{T-2\Delta T}\}$ which correspond to the equilibrium solution at the previous time step (T-2ΔT) as follows:

$$\{\ddot{U}^{T-\Delta T}\}= [\{U^{T-\Delta T}\}-\{U^{T-2\Delta T}\}] \ \frac{2}{\Delta T} -\{\dot{U}^{T-2\Delta T}\} \qquad (4.19)$$

$$\{\ddot{U}^{T-\Delta T}\}= [\{\dot{U}^{T-\Delta T}\}-\{\dot{U}^{T-2\Delta T}\}] \ \frac{2}{\Delta T} -\{\ddot{U}^{T-2\Delta T}\} \ . \qquad (4.20)$$

Similar to the solution procedure for the non-linear static analysis in Section 2-7, the solution of Equation 4.15 proceeds iteratively during the load increment until equilibrium is reached within a specified tolerance. The convergence criterion is based on the energy tolerance which uses the ratio of the work done during the current iteration to the work done during the first iteration.

4-2-4 Numerical Examples

4-2-4-1 Simply Supported Plate under Uniform Step Pressure

The simply supported square plate shown in Figure 4.1 has the following material properties: Modulus of Elasticity $E=10^7$ psi (68950 MPa), Poisson's ratio $\nu=0.3$ and mass density $\rho_s =2.588*10^{-4}$ lb sec^2/in^4 (2765.8 Kg / m^3). Using double symmetry, eight consistent shell elements are used to model one quarter of the plate and the boundary conditions along the edges of the quarter plate are described by the following equations:

$u=v=w=\alpha=\phi=0$ along AB

$u=v=w=\beta=\psi=0$ along BC

$u=\alpha=\phi=0$ along OA

$v=\beta=\psi=0$ along OC.

The mass matrix $[M_s]$ and the linear stiffness matrix $[K_s]$ of the quarter plate are evaluated and incorporated into a free vibration analysis as described in Section 4-2-2,

to give the fundamental period of the structure equal to 0.00108 sec. The vertical fundamental mode shape along the centre line of the plate is displayed in Figure 4.2. The same plate was analyzed by Saigal and Yang (1985) using a 48 D.O.F curved shell element and the quarter plate was also modelled using four elements. The free vibration analysis carried out by Saigal and Yang predicted a fundamental period equal to 0.00111 seconds which is very slightly higher than the consistent shell element result.

Using the consistent shell element, a large deformation dynamic analysis of the plate subject to a uniformly distributed transverse step pressure of 300 psi (2.0685 MPa) is carried out with a time step ΔT of 22.3 μsec. The variation of the central deflection of the plate with time is plotted in Figure 4.3. The corresponding deflections obtained from a large deformation dynamic analysis carried out by Saigal and Yang (1985) using the 48 D.O.F curved shell element are also given in the figure. From both the free vibration and the non-linear time history analyses, excellent agreement of the results obtained using both shell elements can be observed.

4-2-4-2 Cylindrical Shell under Impulsive Load

The cylindrical panel shown in Figure 4.4 has two free straight longitudinal edges and two circular edges which are supported on diaphragms. The elastic material properties of the shell are: Modulus of Elasticity $E=3*10^6$ psi (20685 MPa), Poisson's ratio $\nu=0.3$ and the weight density $\gamma_s=37.5$ psf (1.795 KPa). Again, using double symmetry for the cylindrical panel, one quarter of the shell is modelled using eight consistent shell element as shown in Figure 4.4. The rigid diaphragms and the double symmetry lead to the following boundary conditions on the edges:

$u=w=\alpha=\phi=0$ along BC

$u=\alpha=\phi=0$ along CD

$v=\beta=\psi=0$ along AD

while AB being a free edge involves no restraint condition.

A free vibration analysis is first performed for the panel using the consistent shell element and the results are given in Table 4.1 and are compared with those obtained by Clough and Wilson (1971) using a conforming plate element. Good agreement in natural frequencies between the two analyses can be observed. The fundamental vertical mode shapes along the two centre lines of the shell, which are obtained from the consistent shell element analysis, are plotted in Figures 4.5 and 4.6.

The cylindrical panel is then subjected to a uniformly distributed half-sinusoidal wave with a peak intensity 90 psf (4.3 KPa) as shown in Figure 4.4. The large deflection dynamic analysis of the panel under the applied dynamic load is carried out using eight consistent shell elements and a time step ΔT of 0.025 sec. The vertical deflection at point A (see Figure 4.4) versus time are plotted in Figure 4.7. An alternative solution was provided by Saigal and Yang (1985) using four 48 D.O.F. curved shell elements to model one quarter of the cylindrical panel. The deflections of point A resulting from their analysis is also presented in Figure 4.7. It can be observed that the two results are very close indeed.

4-3 Hydrodynamic Pressure due to Seismic Excitation

Hydrodynamic pressure develops inside liquid-filled tanks when they are subjected to a seismic excitation and acts as a dynamic force on the walls of the tanks. The

dynamic pressure P_d which results from an earthquake motion can be viewed as the sum of two components as follows, i.e. $P_d = P_s + P_I$, where P_s is the long period component (convective) due to sloshing at the free surface of the fluid and P_I is the impulsive fluid pressure which varies in phase with the vibrations of the walls of the tank.

Previous studies concerning seismic analysis of liquid-filled cylindrical tanks indicate that the fundamental sloshing frequencies are much lower than those of the vibrating walls of the shell and, as such, the coupling between vibrations of the walls and the sloshing action was usually neglected. In this study, the same assumption is employed for liquid-filled conical tanks. Therefore, the surface waves at the top of the fluid are neglected and only the impulsive hydrodynamic pressure P_I is considered in the dynamic analysis. The fluid inside the tank is assumed to be inviscid, incompressible and irrotational, i.e. ideal fluid. This assumption is very reasonable for the case of a tank filled with water. Previous studies on liquid-filled cylindrical tanks also indicate that the flexibility of their walls has a major contribution to the impulsive pressure P_I. The base of the conical vessel is usually resting on a rigid diaphragm. Assuming that this base is restricted from rocking, the displacements and consequently the accelerations will be constant at all points on the base during a certain time T.

In view of the assumptions above, the hydrodynamic pressure P_d resulting from vibrations of a flexible conical vessel filled with water (see Figure 4.8), is governed by the following set of equations and boundary conditions:

$$\nabla^2 P_d(r,\theta,z,T) = 0 \qquad \text{inside the fluid volume } \Omega \qquad (4.21)$$

$$\frac{\partial P_d(r,\theta,z,T)}{\partial n} = -\rho_F \, \underline{\ddot{u}}(r,\theta,z,T) \cdot \underline{n} \qquad \text{at the surface } S_1 \qquad (4.22)$$

$$P_d = 0 \qquad \text{at the surface } S_3 \qquad (4.23)$$

$$\frac{\partial P_d(T)}{\partial n} = -\rho_F \, \underline{\ddot{u}}_s(T) \cdot \underline{n} \qquad \text{at the surface } S_2 \qquad (4.24)$$

where P_d is the hydrodynamic pressure exerted in the tank in access to the hydrostatic pressure; $\underline{\ddot{u}}(r,\theta,z,T)$ is the acceleration vector at any point of the tank's walls; $\underline{n}$ is the unit vector normal to the surface of the tank; ρ_F is the fluid density and $\underline{\ddot{u}}_s(T)$ is the acceleration vector at the base of the vessel. Surfaces S_1, S_2 and S_3 are as shown in Figure 4.8. The boundary condition given by Equation 4.24 implies that the dynamic pressure at the surface S_2 ($z=0$) does not vary with the coordinates r and θ.

It is clear from the set of equations above that the fluid hydrodynamic pressure P_d depends on the acceleration of the walls of the tank. In turn, this pressure acts as a force on the walls of the tank and hence affects the acceleration of the structure. Therefore, a fluid-structure interaction results and has to be considered to obtain a reasonable estimate of the seismic response of the liquid-filled tanks.

4-3-1 Boundary Integral Method to Obtain Hydrodynamic Pressure

The boundary integral method was used by Haroun (1980) to obtain the hydrodynamic pressure acting on the walls of a cylindrical tank due to a seismic excitation. A similar approach is used here to obtain the hydrodynamic pressure for the

case of liquid-filled conical tanks subjected to a seismic movement.

The general idea is to interpolate the dynamic pressure using shape functions (modes) which satisfy the partial differential equation governing the initial value problem and also the time-independent boundary conditions as applicable to the problem. The amplitude of each mode is then obtained by satisfying the rest of the time-dependent boundary conditions in an integral sense.

The solution of the partial differential equation given by Equation 4.21 was derived by Haroun (1980), and is presented in Appendix G as a series solution. Considering the terms which satisfy both the free surface boundary condition, given by Equation 4.23, and the condition of constant dynamic pressure at the base resulting from Equation 4.24, the hydrodynamic pressure can be interpolated using the linearly independent functions H_{in} as follows:

$$P_d(r, \theta, z, T) = \sum_{n=0}^{N_2} \sum_{i=1}^{N_1} A_{in}(T) H_{in}(r, \theta, z) + B(T) (z-h) . \tag{4.25}$$

The shape functions H_{in}, a combination of Bessel's function and transcendental functions, are given in Appendix G as

$$H_{in}(r, \theta, z) = I_n(\alpha_j r) \cos(\alpha_j z) \cos(n\theta) \tag{4.26}$$

where I_n are the modified Bessel's functions of the first kind and the coefficients α_j depend on the height of the fluid in the tank h as

$$\alpha_i = (2i-1) \frac{\pi}{2h} \, . \tag{4.27}$$

The variational functional J for this initial value problem described by Equations 4.21 to 4.24 is given by

$$J = \int_{t_1}^{t_2} [\frac{1}{2} \int_\Omega (\underline{\nabla} P_d \cdot \underline{\nabla} P_d) \, dV + \int_S \rho_F \, \underline{\ddot{u}} \cdot \underline{n} \, P_d \, dS] \, dt \tag{4.28}$$

where Ω is the volume of the fluid inside the tank and S is the sum of the surfaces S_1, S_2 and S_3 which are shown in Figure 4.8.

Green's Formula is applied to the first term on the right hand side of Equation 4.28 to give the following expression:

$$J = \int_{t_1}^{t_2} [\frac{1}{2} \{ \int_S P_d \, \frac{\partial P_d}{\partial n} \, dS - \int_V P_d \, \nabla^2 P_d \, dV \} + \int_S \rho_F \, \underline{\ddot{u}} \cdot \underline{n} \, P_d \, dS] \, dt . \tag{4.29}$$

Since the shape functions and consequently the dynamic pressure P_d, given by Equation 4.25, satisfy Equation 4.21 and the free surface boundary condition in Equation 4.23, the variational functional J can be reduced to the following

$$J = \int_{t_1}^{t_2} [\frac{1}{2} \int_{(S_1+S_2)} P_d \, \frac{\partial P_d}{\partial n} \, dS + \int_{(S_1+S_2)} \rho_F \, \underline{\ddot{u}} \cdot \underline{n} \, P_d \, dS] \, dt . \tag{4.30}$$

Equation 4.25 is substituted into Equation 4.30 to obtain the variational functional J as a quadratic equation in amplitudes $A_{in}(T)$ and $B(T)$. The first variation of the functional J is taken for the extremum condition which leads to a satisfaction of the

boundary condition on the surfaces S_1 and S_2, given in Equations 4.22 and 4.24, in an integral sense. This results in determination of the amplitudes $A_m(T)$ and $B(T)$ in terms of the acceleration of the walls of the tank $\ddot{u}(T)$. These amplitudes are then back substituted into Equation 4.25 to obtain the dynamic pressure P_d as a function of the coordinates r, θ, z and the acceleration $\ddot{u}(T)$.

Assuming virtual displacements $\{\delta(\Delta u)\}$ and using the consistent shell element to interpolate both the virtual displacements and the accelerations of the walls of the tank, the virtual work done by the hydrodynamic pressure δW can be expressed in the following manner:

$$\delta W = \delta \{\Delta U\}^{TRANS} [DM] \{\ddot{U}\} \tag{4.31}$$

where [DM] represents a fluid added-mass matrix which results from the fluid hydrodynamic pressure. Its elements include both the interpolation functions used in the consistent shell formulation and the mode shapes employed to interpolate the dynamic pressure in the boundary element formulation.

In the following subsections, the fluid added-masses due to the horizontal and the vertical seismic accelerations acting on the liquid-filled conical tanks are obtained, and the effect of each added-mass on the stability of liquid-filled conical tanks is discussed. It should be noted here that because the static analysis of liquid-filled conical tanks shows more sensitivity to axisymmetric imperfections, the seismic study is also limited to conical tanks which are either perfect or have axisymmetric deviation in geometry.

4-3-2 Horizontal Excitation

4-3-2-1 Fluid Added Mass due to Horizontal Excitation

Due to horizontal excitation acting on a liquid-filled conical tank which is prevented from rocking, the base of the tank has no movement in the vertical direction. As a consequence, the boundary condition on surface S_2 is given by

$$\frac{\partial P_d}{\partial n} = 0 \quad . \tag{4.32}$$

To satisfy this boundary condition, the coefficient B(T) given in Equation 4.25 must vanish and hence the hydrodynamic pressure distribution can be simplified to the following:

$$P_d(r, \theta, z, T) = \sum_{n=0}^{N_2} \sum_{i=1}^{N_1} A_{in}(T) H_{in}(r, \theta, z) \quad . \tag{4.33}$$

Also, the preliminary analyses have shown that only the $\cos\theta$-type modes are excited due to the horizontal acceleration applied to either a perfect tank or a tank with axisymmetric imperfections. This result agrees with the numerical studies in the literature for liquid-filled cylindrical tanks subjected to horizontal excitation. It should be noted that the $\cos(n\theta)$ modes can be excited for tanks which have non-axisymmetric imperfections. Hence, the expression for the dynamic pressure can be simplified to the following:

$$P_d(r, \theta, z, T) = \sum_{i=1}^{N_1} A_{i1}(T) H_{i1}(r, \theta, z) \tag{4.34}$$

where

$$H_{j1}(r, \theta, z) = I_1(\alpha_j r) \cos(\alpha_j z) \cos(\theta) \tag{4.35}$$

The first four mode shapes (H_{11} to H_{41}) along the generator ($\theta=0$) of typical tall and broad tanks, as described in Section 3.9, are plotted in Figure 4.9 and 4.10. The resulting fluid added-mass matrix $[DM]_H$ due to a horizontal acceleration, based on Equation 4.34, is derived in Appendix H.

4-3-2-2 Effect of a Horizontal Excitation on Conical Tanks

As mentioned above, a horizontal excitation along the x-axis (see Figure 4.11) results in a $\cos\theta$-type variation of the hydrodynamic pressure in the circumferential direction. This dynamic pressure distribution is symmetric about the x-axis. Its variation about the y-axis leads to two resultant forces, P, normal to the surface of the tank. The first resultant acts downward at a certain location on the generator defined by $\theta=0$ and the second resultant acts upward at a similar location on the generator defined by $\theta=180$ as shown in Figure 4.11. These two forces exert a base shear and an overturning moment at the base of the conical tank which might lead to plastification or to dynamic instability of the tank.

4-3-3 Vertical Excitation

4-3-3-1 Fluid Added-Mass due to Vertical Excitation

When a liquid-filled conical tank is subjected to a vertical acceleration, the expected motion of the tank and the resulting hydrodynamic pressure are axisymmetric. Accordingly, the dynamic pressure given by Equation 4.25 can be simplified to the following:

$$P_d(r, z, T) = \sum_{i=1}^{N_1} A_{io}(T) H_{io}(r, z) + B(T) (z-h)$$
(4.36)

where the shape functions H_{io} are given by

$$H_{io}(r, z) = I_0(\alpha_j r) \cos(\alpha_j z) .$$
(4.37)

The distribution of the first four shapes for H_{io} (H_{10} to H_{40}) along the generator of the tall and the broad tanks are shown in Figures 4.12 and 4.13, respectively. These mode shapes are used to derive the fluid added-mass $[DM]_V$, resulting from a vertical acceleration, as given in Appendix I.

4-3-3-2 Effect of a Vertical Excitation on Conical Tanks

A vertical acceleration acting on a liquid-filled conical tank is expected to lead to an axisymmetric dynamic pressure distribution as shown in Figure 4.14. Due to this dynamic pressure, upward and downward vertical accelerations will exert added compressive and reduced compressive meridional forces on the tank, respectively. Thus, unlike the case of liquid-filled cylindrical tanks, the vertical acceleration is expected to have an important contribution on the dynamic stability of a liquid-filled conical tank and, therefore, it is important to consider the vertical component of an earthquake when performing seismic analysis of liquid-filled conical tanks.

4-4 Dynamic Formulation of the Liquid-Shell System

4-4-1 Free Vibration Formulation of the Liquid-Shell System

The natural frequencies ω_n and the corresponding mode shapes $\{q_n\}$ of the liquid-shell system can be obtained by solving the following matrix equation:

$$([K_o] - \omega^2 [M]) \{q\} = \{0\} \tag{4.38}$$

where the matrix [M] is the effective mass matrix of the liquid-shell system and is given by the sum of the mass matrix of the structure $[M_S]$ and the fluid added-mass matrix [DM] as

$$[M] = [M_S] + [DM] . \tag{4.39}$$

Now, the fluid added-mass [DM] is either $[DM]_H$ or $[DM]_V$ depending on whether lateral or vertical natural frequencies are sought, respectively. An evaluation of these mass matrices is described in Sections 4-3-2-1 and 4-3-3-1.

The solution of equation 4.38 proceeds as described in Section 4-2-2. It should be noted that the free vibration analysis is based on the linear stiffness matrix $[K_o]$ and, as such, it does not take into account the change in the stiffness of the tank due to the effect of both the stresses resulting from the hydrostatic pressure and the geometric imperfections. However, the free vibration results give an insight into the time step which can be used to perform time history analysis. They also provide a guidance in choosing an input ground motion which contains the liquid-filled tank fundamental frequencies in its dominant frequency range. It is pointed out here that a free vibration analysis can be performed through use of the total mass matrix, i.e . $[M_s]$ + $[DM]_H$ + $[DM]_V$. However, the purpose here is to determine a reasonable range of the frequencies of the liquid-shell system. Therefore, a decoupled analysis in terms of the mass matrix for horizontal and vertical motions, as described earlier, seems reasonable and hence is employed here.

4-4-2 Non-Linear Time History Analysis of Liquid-Shell System due to Seismic Motion

The non-linear dynamic equations of motion for a liquid-shell system subject to both horizontal and vertical components of a ground motion are given by

$$[M]\{\ddot{U}^T\}+[C]\{\dot{U}^T\}+[K_L^{T\ (k-1)}+K_S^{T\ (k-1)}]\{\Delta U\}=\{R^T\}-\{F^{T\ (k-1)}\}-[M]\{H\}a_H^T-[M]\{V\}a_V^T.$$

$$(4.40)$$

The effective mass matrix [M] is the sum of the structure's mass and the fluid added-mass matrices due to both the horizontal and vertical accelerations, i.e.

$$[M] = [M_S] + [DM]_H + [DM]_V.$$ $$(4.41)$$

The sum of the matrices $[K_L + K_S]$ represents the tangential stiffness matrix $[K_{Tan}]$. The damping matrix [C] appearing in Equation 4.40, is obtained using the Rayleigh method, as a linear combination of the effective mass matrix [M] and the tangential stiffness matrix $[K_{Tan}]$, i.e.

$$[C] = \alpha [M] + \beta [K_{Tan}].$$ $$(4.42)$$

The coefficients α and β are obtained by solving the following equations:

$$\alpha + \beta \omega_1^2 = 2\omega_1 \xi_1$$ $$(4.43)$$

$$\alpha + \beta \omega_2^2 = 2\omega_2 \xi_2$$ $$(4.44)$$

where ω_1, ξ_1 and ω_2, ξ_2 are the frequencies and the damping ratios for the first and the second mode shapes, respectively, of the liquid-filled tank. Other terms in Equation 4.40

are the vectors $\{\Delta U\}$, $\{\dot{U}^T\}$ and $\{\ddot{U}^T\}$ which represent the incremental nodal displacements, the total nodal velocities and the total nodal accelerations relative to the ground motion. The load vector $\{R^T\}$ results from the hydrostatic pressure acting on the walls of the tank while the terms $a_H{}^T$ and $a_V{}^T$ are the components of the ground acceleration in the horizontal and vertical directions, respectively, at time T. Finally, the vectors $\{H\}$ and $\{V\}$, which correspond to the consistent shell element, are given by

$$\{H\}_{1 \cdot 91}^{TRANS} = \{1\ 0\ 0\ 0\ 0\ 0\ 0\ 1\ 0\ 0\ 0\ 0\ 0\ 0\ .\ .\ .\ 1\ 0\ 0\ 0\ 0\ 0\ 0\} \quad (4.45)$$

$$\{V\}_{1 \cdot 91}^{TRANS} = \{0\ 1\ 0\ 0\ 0\ 0\ 0\ 0\ 1\ 0\ 0\ 0\ 0\ 0\ .\ .\ .\ 0\ 1\ 0\ 0\ 0\ 0\ 0\} \quad (4.46)$$

In view of equation 4.15, the incremental solution $\{\Delta U\}$ corresponding to the kth iteration of a time step ΔT can be obtained by solving the following equations:

$$[K^{*T\ (k-1)}]\{\Delta U\} = R^T - F^{T\ (k-1)} - [M]\{A^{T\ (k-1)}\} - [C]\{B^{T\ )k-1)}\} - [M]\{H\}a_H^T - [M]\{V\}a_V^T.$$

$$(4.47)$$

Note that the vectors $\{A^{T\ (k-1)}\}$ and $\{B^{T\ (k-1)}\}$ are defined by Equations 4.17 and 4.18 while the effective stiffness matrix $[K^{*T\ (k-1)}]$ can be obtained from Equation 4.16 by replacing the shell element mass matrix $[M_S]$ by the effective mass matrix $[M]$.

In order to obtain the non-linear time history of a liquid-filled tank subject to seismic motion, the following procedure is followed:

Constant Quantities at Start of Solution

The following quantities are evaluated at the beginning of the solution and are kept constant through the subsequent time steps.

a) The fluid added-masses $[DM]_H$ and $[DM]_V$ are evaluated using the procedure described in Appendices H and I and are added to the mass matrix of the tank $[M_S]$ to obtain the effective mass matrix $[M]$.

b) The load vector $\{R^T\}$ due to the hydrostatic pressure acting on the walls of the tank, is calculated when it is filled with water, i.e the load vector corresponding to a load factor p=unity as described in Section 3.8.

c) Using the first two frequencies ω_1 and ω_2, obtained from the free vibration analysis of the liquid-filled tank, the coefficients α and β are evaluated by solving Equations 4.43 and 4.44.

<u>Quantities Updated at each Time Step</u>

The components of the input ground acceleration a_H and a_V are updated at each time step according to the time history of the applied earthquake. The accelerations a_H^T and a_V^T are multiplied by the quantities $[M]\{H\}$ and $[M]\{V\}$, respectively, to obtain the load vectors resulting from the ground motion at time T.

<u>Quantities Updated at each Iteration</u>

a) The stiffness matrices $K_L^{T\ (K-1)}$ and $K_S^{T\ (K-1)}$ and the unbalanced load vector $F^{T\ (K-1)}$ are updated at each iteration as described in Section 2-7.

b) The vectors $\{A^{T\ (k-1)}\}$ and $\{B^{T\ (k-1)}\}$ are also updated at each iteration using Equations 4.17 and 4.18, respectively. ·

c) The stiffness matrices $K_L^{T\ (k-1)}$ and $K_S^{T\ (k-1)}$ are added together to obtain the tangential stiffness matrix $K_{Tm}^{T\ (k-1)}$ which is substituted in Equation 4.42 to obtain

the damping matrix [C].

The solution of Equation 4.47 proceeds iteratively during each load increment corresponding to the time step ΔT until equilibrium is achieved as described in Section 4-2-3. A non convergent solution at any iteration during the time history of the earthquake is an indication of dynamic instability due to the stiffness deterioration caused by yielding of the material and/or localized buckling. This means that the design of the tank being analyzed is expected to be unsafe under the applied seismic excitation.

4-4-3 Free Vibration Analysis of Liquid-Filled Cylinders

The natural frequencies of a number of cylindrical tanks which are filled with liquid and subjected to both $\cos\theta$-type and axisymmetric vibrations were determined numerically by Haroun (1980) and Haroun and Tayel (1985b). The numerical model used by Haroun had been verified by comparison with tests results (Haroun 1980). Since cylindrical tanks can be viewed as special conical vessels having equal top and bottom radii, the boundary integral formulation used for the analysis of liquid-filled conical tanks can be checked by evaluating the fluid added-mass matrices $[DM]_H$ and $[DM]_V$ for the cylinders considered by Haroun using the procedures outlined in Appendices H and I, respectively. These matrices are then incorporated into the eigen value analysis as described in Section 4-4-1 to evaluate the natural frequencies of such liquid-filled cylinders due to $\cos\theta$-type (horizontal excitation) and axisymmetric (vertical excitation) vibrations. Results of the free vibration analyses are presented in the following subsections.

4-4-3-1 Natural Frequencies of the Cosθ-Vibration of Liquid-Filled Cylinders

A cylindrical tank with radius (R) and height (H) equal to 24´ (7.32 m) and 72´ (21.95m), respectively, is assumed to be filled with water (ρ_F=0.94*10^{-4} lb.sec^2 /in^4, 1000 Kg/m^3). The tank is made of steel with ρ_s = 0.733*10^{-3} lb.sec^2/in^4 (7833 Kg/m^3), E=30*10^6 lb/in^2 (2.068*10^5 MPa) and ν=0.3. Three different values for the thickness (t) of the tank are assumed as given in Table 4.2. The fundamental natural frequencies of the cosθ-type vibration of the cylinders are obtained by modelling the wall of the tank using the consistent shell element and evaluating the fluid added-mass [DM]$_H$ as given in Appendix H. The calculated natural frequencies are tabulated in Table 4.2 and are compared to the corresponding frequencies given by Haroun (1980). Excellent agreement can be observed, thus verifying the formulation of the added-mass matrix [DM]$_H$.

4-4-3-2 Natural Frequencies of the Axisymmetric Vibration of Cylinders

Three steel cylindrical tanks of the same material properties described above and having the dimensions given in Table 4.3, are assumed to be filled with water and subjected to an axisymmetric vibration. The steel shells are also modelled using the consistent shell element. Meanwhile, the fluid added-mass resulting from the axisymmetric vibration [DM]$_V$ is evaluated as presented in Appendix I and added to the mass matrix of the shell. The eigen value analyses of the liquid-filled cylindral tanks lead to the fundamental natural frequencies given in Table 4.3. In addition, free vibration analysis results are piesented for the empty cylindrical tanks. These are compared, once again, to the corresponding values given by Haroun and Tayel (1985b). Again, excellent agreement can be observed which then verifies the accuracy of the

formulation of the added-mass matrix $[DM]_v$. It should be mentioned here that for this particular example, the base of the tank is assumed to be restrained from any vertical motion. This leads to the requirement that the coefficient $B(T)$ in Equation 4.36 must vanish in order to satisfy the condition of zero acceleration normal to the base of the tank.

4-5 Seismic Analysis of Elevated Liquid-Filled Conical Tanks

4-5-1 Modelling of Tanks

As previously mentioned in Section 3-7, elevated conical tanks usually consist of a steel vessel which is supported by a circular steel plate resting on a heavily reinforced concrete slab supported in turn by a reinforced concrete tower. In practice, the steel vessel usually consists of a short cylinder superimposed on a cone. Similar to what was done in the static analysis, the cylindrical part is omitted in the dynamic analysis and a full cone steel vessel is considered in the finite element modelling. This simplification is reasonable since the critically stressed area is near the bottom of the tank. Due to the presence of a heavily reinforced concrete slab underneath the steel vessel, the base of the vessel can be assumed infinitely rigid and hence can only tilt as a rigid body rotation due to differential axial deformation between the extremities of the concrete tower. For this study, the conical vessels are assumed to be resting on four rigid frames. (See Figure 4.15). The tilting at the base of the vessel can be neglected due to the rigidity of the frames in the axial direction relative to the lateral direction. As such, the supporting tower can be replaced by horizontal and vertical springs as shown in Figure 4.16. The stiffness of the horizontal spring k_h is obtained by applying a horizontal force F_x at the

top point of one of the rigid frames and using a plane frame program to calculate the corresponding lateral deflection Δ_x at that point. The stiffness k_h is then given by

$$k_h = \frac{2F_x}{\Delta_x} .$$
(4.48)

Meanwhile, the stiffness of the vertical spring k_v is directly given by

$$k_v = \frac{4EA}{L}$$
(4.49)

where E is the modulus of elasticity of the concrete; A is the cross sectional area of the columns of the frames and L is the height of the frames.

In the dynamic analysis, both the walls and the base of the tanks are modelled using the consistent shell element. For the free axisymmetric vibration analysis, double symmetry exists and therefore twenty six elements are used to model one quarter of the tank as shown in Figure 4.17. For the cases of non-linear time history and lateral free vibration analyses, only symmetry about the axis of excitation exists. As such, one half of each tank is modelled using fifty two elements, forty eight of which are needed to model the walls and four elements for the base. The finite element mesh employed is shown in Figure 4.18. It can be observed from the figure that a finer mesh is used at the bottom region of the tank where buckling is anticipated for the case of uniform thickness. The element lengths at the bottom region are chosen to be smaller than one quarter the buckling wave length resulting from the static analysis.

Due to the rigid diaphragm action of the reinforced concrete slab, the displacement degrees of freedom of different nodes at the base of the tank are all

assumed to be equal, when directed along the same axis. The rotational degrees of freedom at the base are restricted because of the bending rigidity of the underlying reinforced concrete slab. As was the case for the static analysis, the rotational restraint at the weld between the base plate and the wall of the tank is neglected and hence the wall of the tank is assumed to be free to rotate at its connection to the base.

It should be also noted that in the stiffness formulation of the structure, the stiffnesses of the horizontal and vertical springs, simulating the supporting rigid frames, are added to the stiffness terms which correspond to the horizontal and vertical nodal displacements at the base plate.

4-5-2 Stiffness Values for Supporting Towers of Tall and Broad Tanks

In order to perform seismic analysis for both the tall and the broad tanks described in Section 3.9, it is necessary to determine the stiffness of the springs k_h and k_v which simulate the supporting tower as described in Section 4-5-1. The preliminary analyses show that the fundamental frequencies of both the tall and the broad tanks are relatively high. This means that such structures will be more excited when subjected to an earthquake having a high peak acceleration to peak velocity ratio (a/v). According to the National Building code of Canada NBCC (1990), Quebec city is located in an active seismic zone which can expect such an earthquake type of motion. Based on this, it is assumed that the tall and broad tanks are located there. Consequently, the reinforced concrete supporting frames of both tanks have to be designed to withstand the flexural stresses resulting from either the seismic load or the wind pressure intensity for that location, and in accord with the NBCC (1990). In addition, they must resist direct

compressive stresses due to the weight of the liquid, the self weight of the shell and the snow load on the roof. The heights of the supporting towers for tall and broad tanks are assumed to be 10 m and 6 m, respectively.

Some preliminary analyses show that for both the tall and broad tanks, the induced flexural stresses due to the seismic motion are much larger than those resulting from the wind pressure. The dimensions of the reinforced concrete frames for each tank are chosen based on the maximum compressive strength of concrete, assumed to be 13.3 MPa (based on 33.3% of a 28 day nominal compressive strength of 40MPa). Using the moment of inertia and the cross sectional area values that confirm safe design for the supporting rigid frames, the stiffnesses of the horizontal and the vertical springs for modelling are calculated for each tank as described in Section 4-5-1 and are given by:

For Tall Tanks

$k_h = 0.708*10^9$ N/m, $k_v = 2.33*10^{10}$ N/m

For Broad Tanks

$k_h = 0.220*10^9$ N/m, $k_v = 0.765*10^{10}$ N/m

4-5-3 Free Vibration Analysis of Tall and Broad Tanks

Constant thicknesses of 12 mm and 9.6 mm are chosen for the tall and broad tanks, respectively. The other dimensions of the tanks (r_1, h and θ_v) as well as the material properties are the same as given in Section 3-9. The tanks are assumed to be filled with water ($\rho_F = 1000$ kg/ m^3). To perform the free vibration analysis, the two tanks are modelled using the consistent shell element as described in Section 4-5-1, while the stiffnesses of the horizontal and vertical springs, replacing the supporting frames, are

given in Section 4-5-2. Also required are the fluid added-masses $[DM]_H$ and $[DM]_V$ which are obtained for each tank following the procedures described in Appendices H and I. Each added-mass is then individually incorporated into the free vibration analysis to obtain the natural frequencies of the tanks due to horizontal and vertical vibrations.

The results of the free vibration analyses show that considering only the first four modes of the pressure functions H_{i0} and H_{i1}, i.e. i=1 to 4, gives sufficiently accurate values for the natural frequencies of the first four modes of vibration. This has been confirmed by considering only the first three pressure modes in the free vibration analysis, since the results remained almost the same as those obtained by including the fourth pressure mode. The natural frequencies from the free vibration analyses of both tanks using four pressure modes are shown in Tables 4.4 and 4.5. The horizontal and vertical components of the fundamental mode shapes for both the $\cos\theta$-type and the axisymmetric vibrations are plotted along the generator of the tall tank in Figures 4.19 and 4.20, respectively. The fundamental mode shapes along the generator of the broad tank are presented in Figures 4.21 and 4.22. Although there are no results available in the literature for comparison, the mode shapes appear very reasonable.

4-5-4 Time History Analysis of the Tall and Broad Tanks

4-5-4-1 Choice of an Input Ground Motion

Non-linear time history analysis of both the broad and tall conical-shaped reservoirs filled with water are performed using the San Fernando, California, Feb. 1971 earthquake as the input ground motion. In this study, the S21W component of the earthquake which was recorded at Lake Hughes St.4, is used as a horizontal excitation

along the x-axis (Figure 4.11), while the vertical component of the same record provides

vertical accelerations for the tanks. The reason for choosing this particular record as an

input ground motion for the tanks is that the dominant frequencies of this earthquake

contain the fundamental modes of vibrations of the tanks which are given in Tables 4.4

and 4.5. The acceleration time histories as well as the response spectra for this record

are given by Naumoski et al. (1988).

The two components of the acceleration records of the San Fernando earthquake

are scaled down such that the maximum velocity of the input record is equal to the zonal

velocity of Quebec city as specified in the NBCC (1990). This leads to a maximum

horizontal and vertical accelerations equal to 0.28 g and 0.167 g, respectively, where g

is the acceleration due to gravity. Only the strongest six seconds of the records are used

in the analyses because of the very long computer time associated with this type of time

history analysis problem. The response spectra of the earthquake as well as the scaled

horizontal and vertical accelerations are shown in Figures 4.23 to 4.25.

4-5-4-2 Non-Linear Time History Analysis

Non-linear time history analysis of seven elevated conical tanks filled with water

and subjected to the horizontal and the vertical components of the San Fernanado, 1971

earthquake are performed. The dimensions of the seven tanks (DB1 and DT1 to DT6)

as well as the magnitudes of the axisymmetric imperfections, assumed to exist in the shell

structures before loading, are given in Table 4.6. The wave length of the imperfections

is taken equal to the buckling wave length of the perfect structure resulting from the

elastic static analysis as shown in Section 3.10. This is deemed to result in a conservative

estimate of buckling resistance for the shell.

Based on the static analysis described in Chapter Three, the prescribed dimensions listed in Table 4.6 provide safe designs for these tanks under hydrostatic load. The static analysis yields a critical load factor p_{cr} which implies that the hydrostatic pressure can be multiplied by any value up to this value prior to the tank becoming unsafe. The load factors p_{cr} are tabulated in Table 4.6 from which it can be observed that p_{cr} depends on both the tank thickness and the magnitude of imperfections existing in the tank.

The seven tanks are modelled using the consistent shell element as described in Section 4-5-1. The spring constants which simulate the supporting shaft of the broad tank (DB1) and the tall tanks (DT1 to DT6) are as given in Section 4-5-2. The fluid added-mass matrices $[DM]_H$ and $[DM]_V$ for both the broad and tall tanks, are calculated following the procedures in Appendices H and I, respectively. Both $[DM]_H$ and $[DM]_V$ are added to the mass matrix of the shell to obtain the effective mass matrix $[M]$. To evaluate the damping matrix $[C]$ as a linear combination of the tangential stiffness matrix $[K_{Tan}]$ and the effective mass matrix $[M]$, the frequencies of the first two modes of vibrations must be known. For tanks DB1 and DT1 to DT3 the first two frequencies can be obtained from Tables 4.4 and 4.5, respectively. The free vibration analyses are performed for tanks DT4, DT5 and DT6 resulting in the following values for the first two frequencies:

$f_1 = 2.63$ (cps), $f_2 = 3.52$ (cps),   (for tank DT4)

$f_1 = 2.68$ (cps), $f_2 = 3.50$ (cps),   (for tank DT5)

$f_1 = 2.83$ (cps), $f_2 = 3.47$ (cps),   (for tank DT6).

Assuming a 2% damping for the first two modes of vibration, the coefficients α and β are evaluated for each tank through Equations 4.43 and 4.44 and then the matrix [C] is obtained using Equation 4.42.

A time step Δt of 0.02 sec is used in the analysis and at each time step the horizontal acceleration a_H and the vertical acceleration a_V of the ground motion are obtained according to Figures 4.24 and 4.25, respectively. It should be noted that a ΔT of 0.02 sec is much smaller than any of the fundamental periods of the tanks. As mentioned previously, the external load which is acting on the tank at each load increment consists of the inertia force due to the ground acceleration as well as the hydrostatic pressure (with multiplication of a load factor equal to unity).

4-5-4-3 Discussion of Results of Analyses

Results of the time history analysis are presented at different horizontal cross sections at the location shown in Figure 4.26. At each cross section the response at three points corresponding to $\theta=0°$, $\theta=90°$ and $\theta=180°$ are considered. (See Figure 4.26). It should be noted here that in the time history plots, the response at $T=0$ corresponds to the effect of the hydrostatic pressure before applying any seismic load to the structure.

In Figure 4.27 horizontal, vertical, transverse meridional and axial displacements of tank DT1 along the generator ($\theta=0°$) of the tank are displayed. In this figure, the dotted plots represent the displacement shapes resulting from the static load while the solid lines show the displacements just prior to dynamic instability. From the plots it can be observed that the dynamic buckling which is localized at the bottom of the tank has the same pattern as that of the static displacements. Also to be noted, are the large

horizontal and vertical movements at the upper region of the tank due to the seismic motion. In Figure 4.28, the same displacements are plotted along the generator ($\theta=180°$) of the tank. The displacement plots show no evidence of buckling along that generator. This means that the buckling is localized near the base and is confined to the region subjected to high compressive axial stresses resulting from the overturning moment.

The response of the tall tank DT5, which survived the earthquake without any inelastic behaviour is presented in Figures 4.29 to 4.43. The relative displacements along the x-axis at sections 1-1, 2-2 and 3-3 are displayed in Figures 4.29, 4.31 and 4.33, respectively, for $\theta=0°$, $\theta=90°$ and $\theta=180°$. It can be noted from these plots that the horizontal displacement takes the $\cos\theta$-type variation, i.e. no out of roundness effect is noticed at any section of the tank. In Figure 4.30, 4.32 and 4.34, the vertical displacements relative to the ground motion are also presented at sections 1-1, 2-2 and 3-3, respectively, for $\theta=0°$, $\theta=90°$ and $\theta=180°$. It is important to point out that the response at $\theta=90°$ is only due to the vertical acceleration, while the response at $\theta=0°$ and $\theta=180°$ results from both the vertical and the horizontal accelerations. It can be seen from the figures that the vertical displacements resulting from the horizontal excitation are larger than those resulting from the vertical excitation, especially at the top section of the reservoir. It is also interesting to note that the vertical displacements at section 2-2 ($\theta=90°$) are slightly larger than those at section 1-1 ($\theta=90°$). This is in correspondence with the fundamental mode shape resulting from the vertical acceleration which has a peak value in the middle region of the tank as shown in Figure 4.20. Also, the plots of the vertical displacements at $\theta=0°$ and $\theta=180°$ show the coupling effect between both the

vertical and the horizontal excitations especially at sections located in the bottom region of the vessel. The meridional stresses at section 4-4 (bottom section of the vessel) are plotted in Figure 4.35 for $\theta=0°$, $\theta=90°$ and $\theta=180°$. Similar to the plots for vertical displacements, the results for stresses at $\theta=90°$ are only affected by the vertical acceleration, while the stresses at $\theta=0°$ and $\theta=180°$ are due to both the vertical and the horizontal components. From the plots of the stresses, it can be observed that the maximum stresses induced at the bottom section of the tank by the vertical acceleration are almost 32% of the maximum stresses induced at the same section by the horizontal accelerations. It can also be observed from the plots that the stresses in the critical region due to the seismic motion are larger than those resulting from the hydrostatic pressure. In Figure 4.36, the time history of the base shear, normal force and overturning moment at section 4-4 (the base of the tank) are plotted. The normal forces are due to the effect of the vertical acceleration, while both the base shear and the overturning moment result from the effect of the horizontal acceleration. By simple calculation, the absolute base shear Q_{max}, normal force N_{max} and overturning moment M_{max} are found to be related to the maximum ground horizontal acceleration ($a_H = 0.28$ g) and the maximum vertical acceleration ($a_V = 0.167$ g) through the mass of the fluid inside the tank M_F as follows: $Q_{max} = 0.53 \, M_F \, a_H$ and $N_{max} = 2.70 \, M_F \, a_V$. These results suggest that more than half the fluid acts as a rigidly connected mass causing base shear and overturning effects. Meanwhile, a factor of 2.7 amplifies the fluid mass under vertical acceleration thus adding the equivalent of about 45% (2.7*0.167) to the hydrostatic effect at the base of the cone.

The effect of the flexibility of the supporting tower in amplifying the ground motion is shown by plotting the relative displacements at the base of the vessel (section 4-4) in Figure 4.37. It can be concluded from the plots that the relative vertical displacements are very small which means that the supporting frames are very rigid in their axial directions. The relative horizontal and vertical accelerations at different locations for the tank DT5 are plotted in Figures 4.38 to 4.40, from which it can be seen that maximum horizontal and vertical relative accelerations of about 0.50 g and 0.75 g are obtained.

The time history of the dynamic pressure resulting from the horizontal excitation is plotted in Figure 4.41 at $\theta=180°$ for different sections of tank DT5. In Figure 4.42, the time history of the dynamic pressure due to vertical excitation is plotted at the same sections. Comparison of the numerical values indicates that the absolute value of the dynamic pressure resulting from the vertical acceleration is larger than the one resulting from the horizontal acceleration. Figure 4.43 shows the pressure distribution along the generator of tank DT5 ($\theta=180°$). Figure 4.43(a) shows the distribution of the absolute dynamic pressure resulting from the horizontal acceleration (at T=5.46 sec), while the absolute dynamic pressure due to vertical acceleration (at T=5.1 sec) is displayed in Figure 4.43(b). In Figures 4.43(c) and 4.43(d), the absolute total dynamic pressure resulting from both the horizontal and the vertical excitations are plotted at T=5.46 sec and T=5.1 sec, respectively. It should be noted that in the last figures the dotted lines represent the hydrostatic pressure distribution. From these figures, it can be concluded that the value of the total dynamic pressure is always less than the hydrostatic pressure,

This means that no suction pressure is expected to happen at any point of the structure.

Despite the occurrence of early plastification in the broad tank DB1, it has survived the six seconds of the ground input acceleration. The results are presented in Figures 4.44 to 4.51. Similar response observations are found for DB1 as noted above for tank DT5. The former has sustained noticeably smaller values for displacements and stresses due to the seismic motion. However, the behaviour of the tank is not affected by the plastification which is localized at the very bottom region of the tank. Based on the absolute values for the base shear, the normal force and the overturning moment given in Figure 4.44, equivalent mass values of 0.25 M_F for Q_{max} and 2.52 M_F for N_{max} are obtained. It is obvious that the broad tank is subjected to somewhat less vertical force from the acceleration component a_V than does the tall tank. However, the base shear is very much reduced.

The results from the time history analysis are summarized in Table 4.6. The last column denotes the most critical state experienced by the structure during the six seconds of record. The term "safe" denotes that the tank has survived the earthquake motion, while the tanks which have suffered from dynamic instability during the six seconds of the input ground motion are described by the term "failed". In the same column, tanks which have a complete elastic response during the record are described by "elastic", while the term "plastification" denotes the tanks which have an inelastic response during the seismic motion.

In light of the static limit load factor p_{cr} tabulated in the seventh column of Table 4.6, the following observations can be concluded from the dynamic analysis:

1)   Broad tanks are much less critical to seismic load than tall tanks. This is concluded from the fact that a limit load factor of 1.5 provides a safe design for the broad tank DB1 under the input ground motion, in spite of the early plastification which occurred in the tank. Meanwhile, the same seismic excitation applied to the tall tank DT3 leads to dynamic instability of the tank, despite a high load factor of 2.25.

2)   The results of the analyses of tanks DT4, DT5 and DT6 show that under a seismic excitation which has the frequency content of the fundamental modes of the tall tank and has a maximum acceleration equal to 0.28 g, a load factor under static conditions of 2.8 has to be provided to assure the safety of the structure from dynamic instability, with a full elastic response. Meanwhile, a load factor of 2.65 leads to a safe inelastic response of the tall tank under the same excitation. These load factors can be achieved either by increasing the thickness of the tank or assuring a low level of imperfections in the tank.

Mode	1	2	3	4
Present Solution	9.974	24.00	36.06	50.3
Clough (1971)	9.777	24.09	34.08	45.95

Table 4.1 Natural Frequencies ω (rad/sec) of a Cylindrical Panel

Thickness t (mm)	f (cps) Present Analysis	f (cps) Haroun (1980)
25.4	5.35	5.31
10.92	3.609	3.56
7.32	3.00	2.93

(R=7.32 m , H=21.95 m)

Table 4.2 Cos θ-Vibrations for Cylindrical Tanks

Tank Dimensions (m)	Empty Current Study f (cps)	Empty Haroun and Tayel (1985b) f (cps)	Full Current Study f (cps)	Full Haroun and Tayel(1985b) f (cps)
R=7.32 H=21.95	57.19	57.8	6.92	6.86
R=7.32 H=14.64	83.58	83.96	10.26	10.11
R=18.29 H=12.19	44.0	44.41	6.442	6.40

(t=25.4 mm)

Table 4.3 Axisymmetric vibrations for Cylindrical Tanks.

r_1 (m)	h (m)	θ_v	t (mm)	Mode 1	Mode 2	Mode 3	Mode 4
3.0	9.0	45	12	2.51	3.54	6.67	12.04
3.0	4.5	60	9.6	3.21	4.37	7.61	10.35

Table 4.4 Natural Frequencies f (cps) of Conical Tanks due to Horizontal Excitation.

r_1 (m)	h (m)	θ_v	t (mm)	Mode 1	Mode 2	Mode 3	Mode 4
3.0	9.0	45	12	7.44	14.95	19.06	24.46
3.0	4.5	60	9.6	8.12	13.52	15.46	31.35

Table 4.5 Natural Frequencies f (cps) of Conical Tanks due to Vertical Excitation.

Tank	r_1 (m)	h (m)	θ_v	t (mm)	Imperf. (mm)	p_{cr}	Results description.
DB1	3.0	4.5	60	9.6	9.6	1.5	Safe (plastic)
DT1	3.0	9.0	45	12.0	12.0	1.4	Failed (plastic)
DT2	3.0	9.0	45	12.0	3.0	2.1	Failed (plastic)
DT3	3.0	9.0	45	12.0	0.0	2.25	Failed (plastic)
DT4	3.0	9.0	45	13.5	0.0	2.65	Safe (plastic)
DT5	3.0	9.0	45	14.0	0.0	2.8	Safe (elastic)
DT6	3.0	9.0	45	16.0	7.0	2.8	Safe (elastic)

Table 4.6 Results of the Time History Analyses for Conical Tanks.

* Please Refer to Figure 3.11 for the Notations Description.
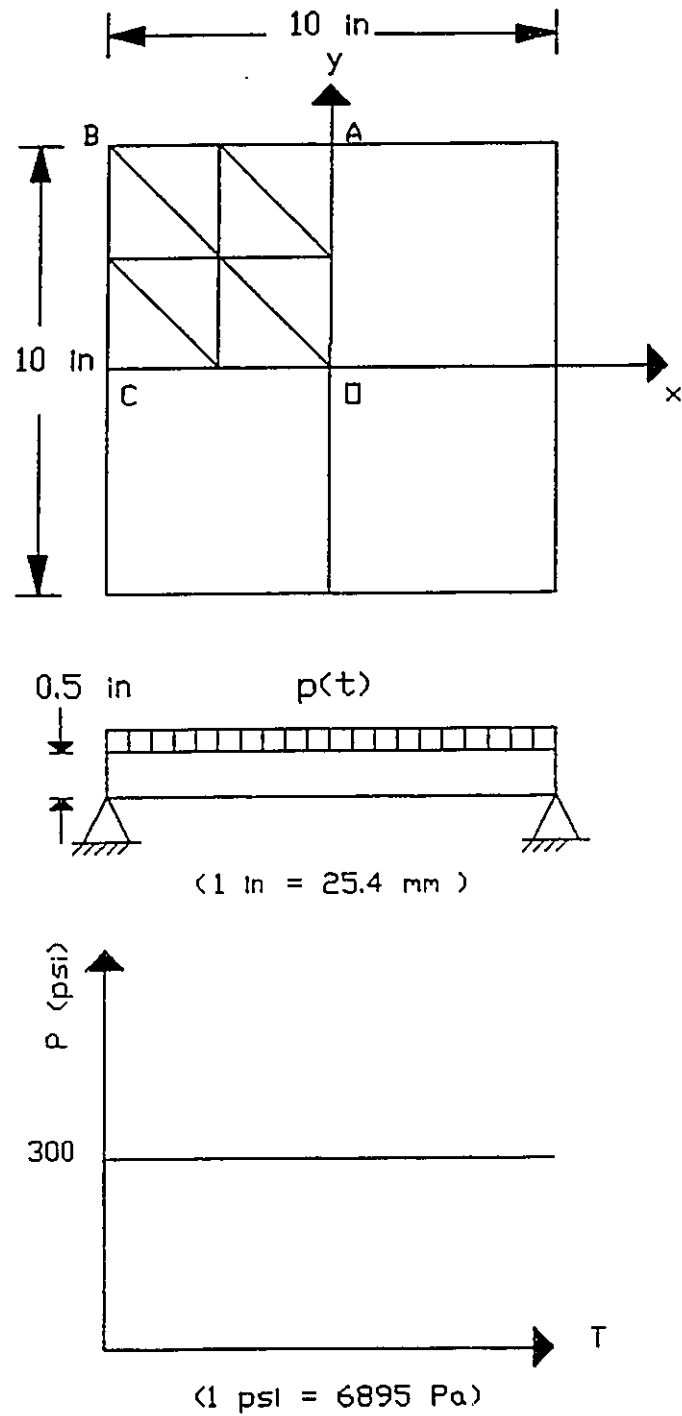
Figure 4.1 Simply Supported Plate Subjected to Uniform Step Load.
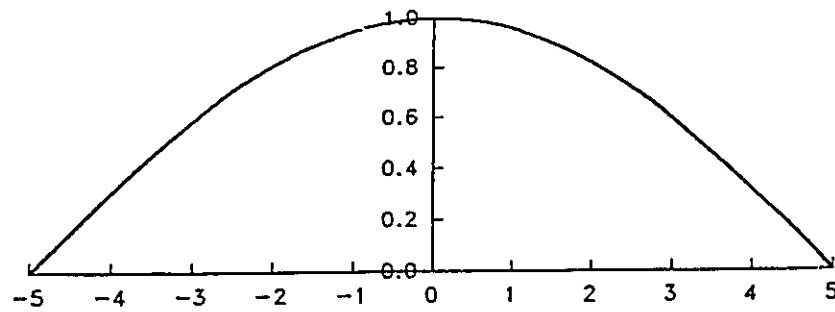
Figure 4.2 Fundamental Vertical Mode Along Centre Line
of a Simply Supported Plate.
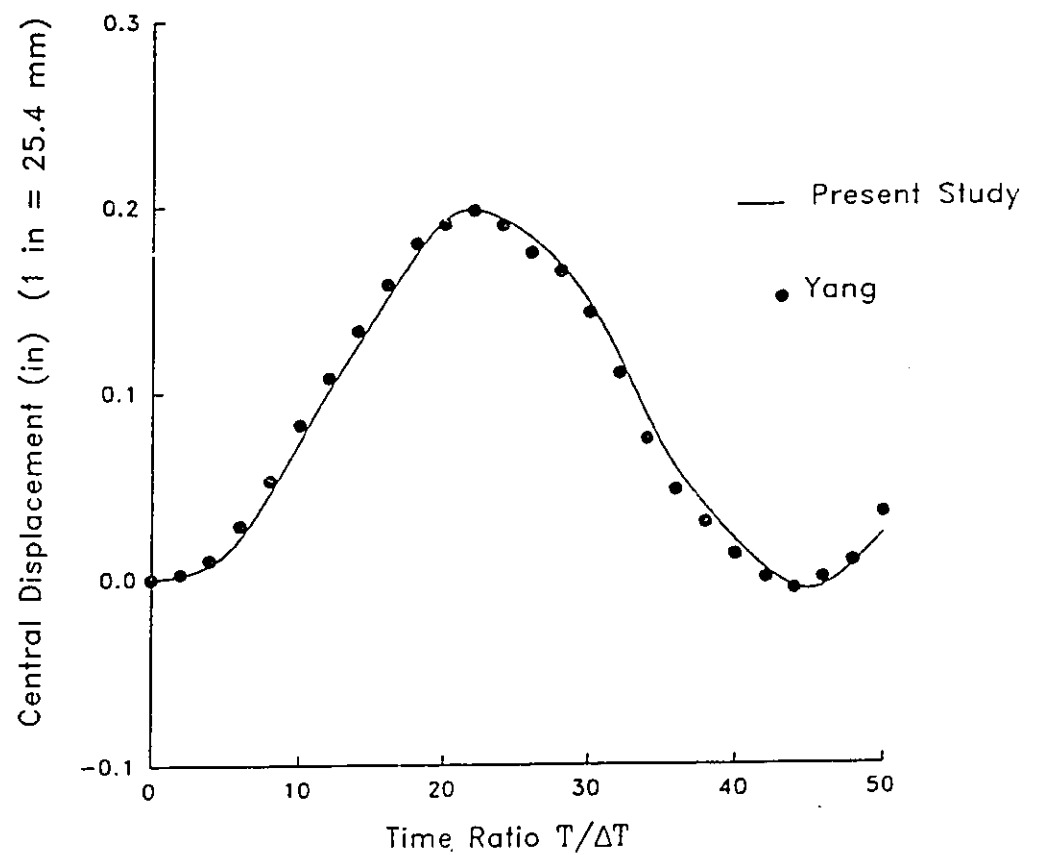
Figure 4.3 Central Displacement of a Simply Supported Plate
Under Uniformly Distributed Step Load.
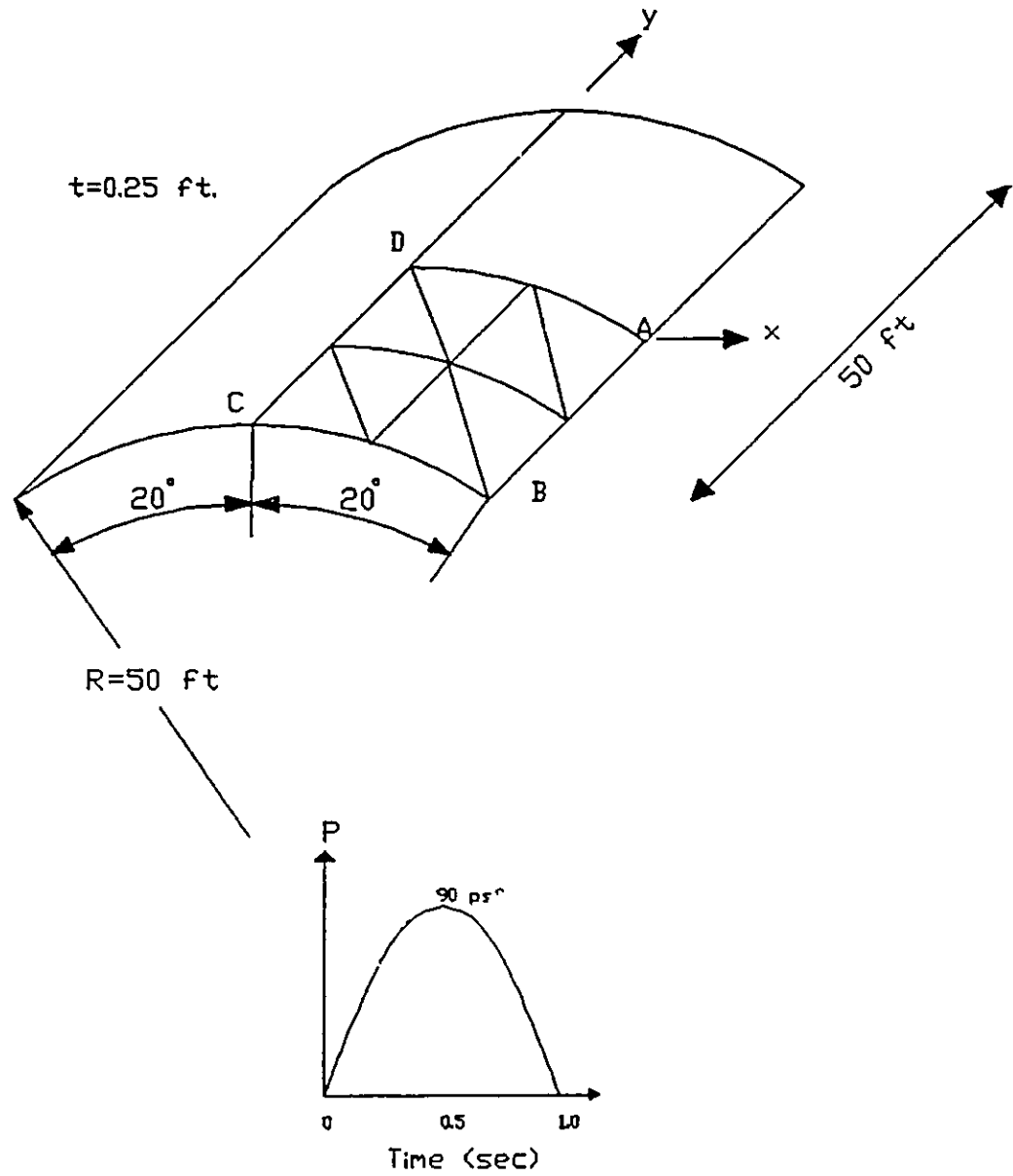
Figure 4.4 Cylindrical Panel Subjected to a Sinusoidal Load.
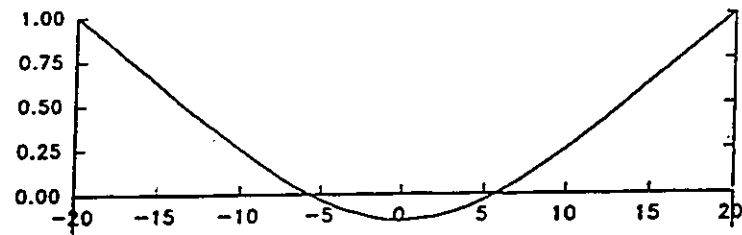
Figure 4.5 Fundamental Vertical Mode Along the Circular Centre Line of a Cylindrical Panel.
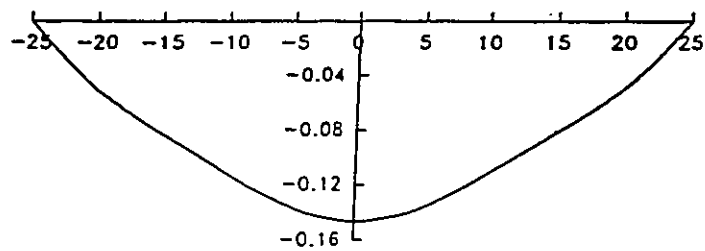
Figure 4.6 Fundamental Vertical Mode Along Longitudinal Centre Line of a Cylindrical Panel.
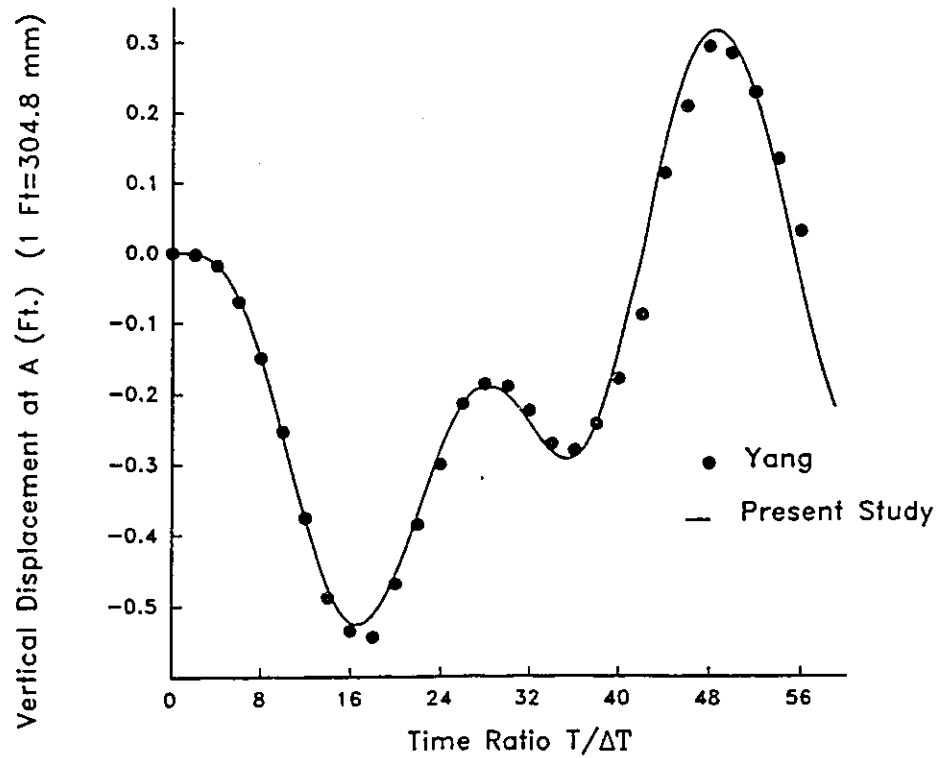
Figure 4.7 Nonlinear Dynamic Response of a Cylindrical Panel.
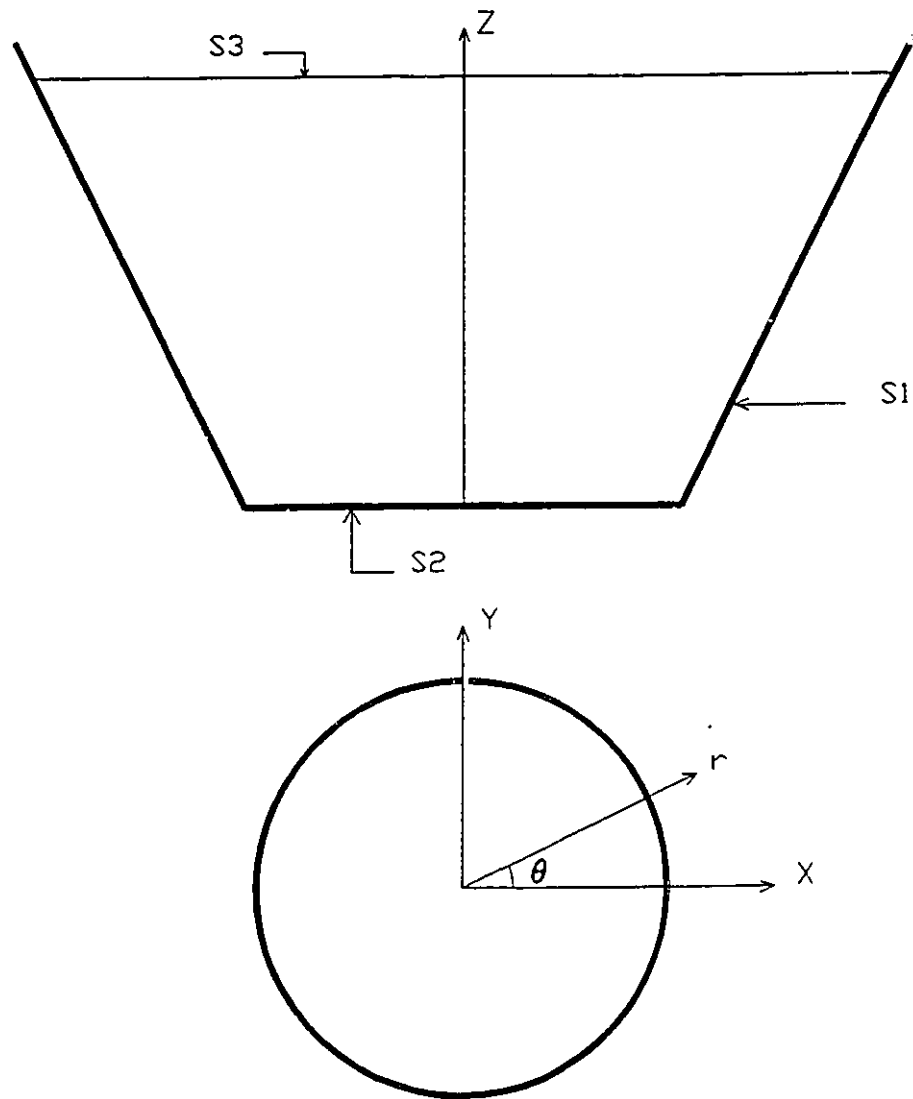
Figure 4.8 Coordinate System for the Hydrodynamic Pressure Formulation.
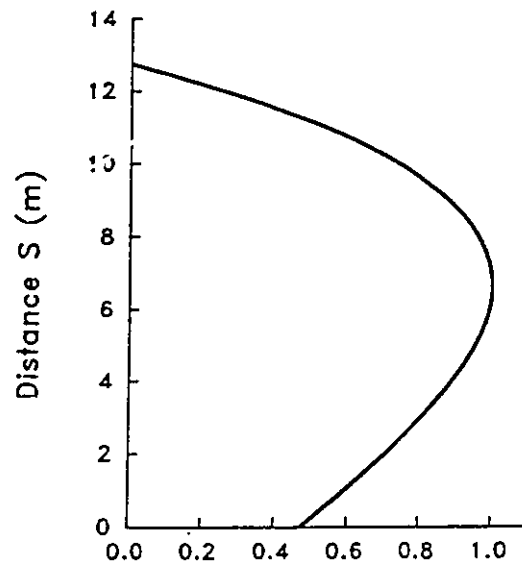
(a) First Mode
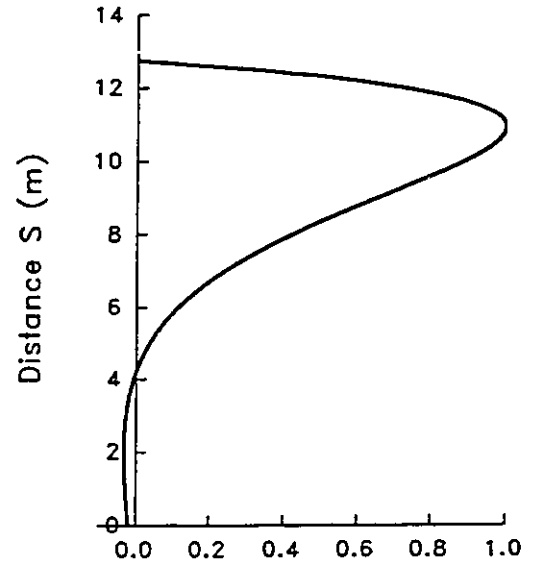
(b) Second Mode
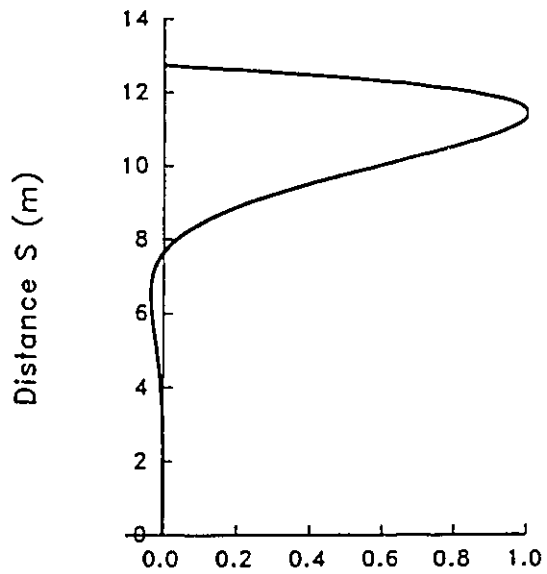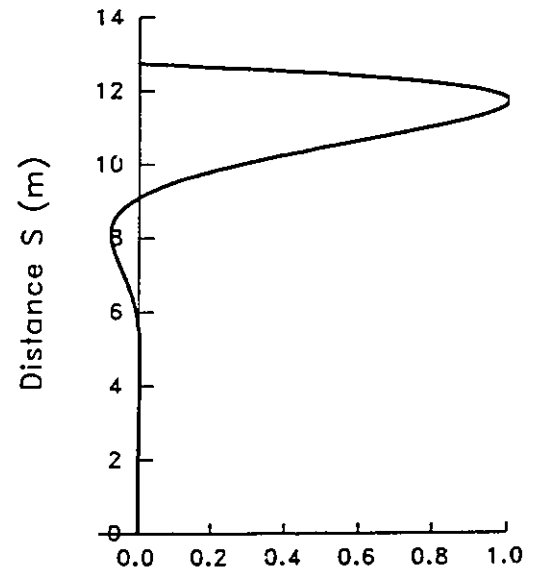
(c) Third Mode

(d) Fourth Mode

Figure 4.9   Cos θ —Type Pressure Modes Along the Generator
of the Tall Tanks ($\theta=0°$)
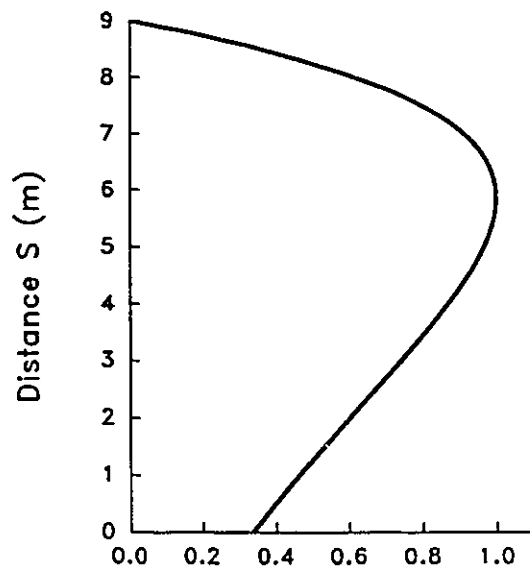
(a) First Mode
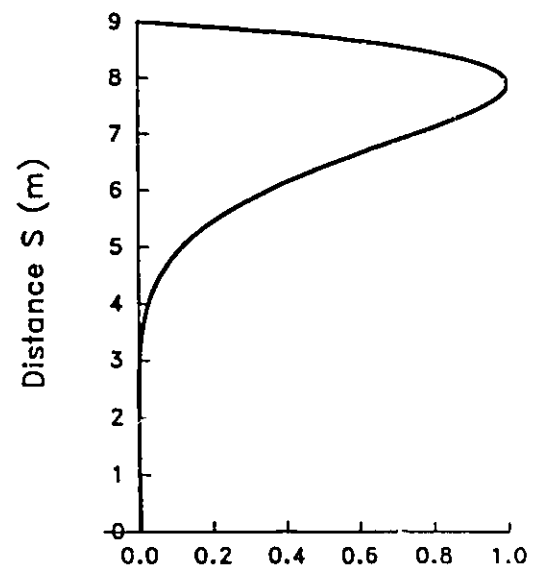
(b) Second Mode
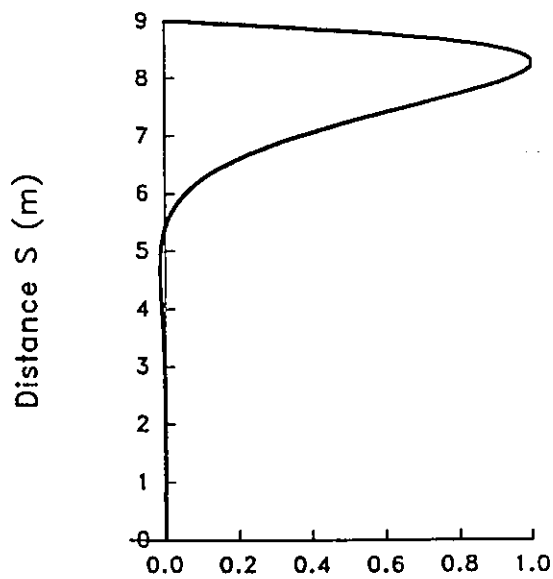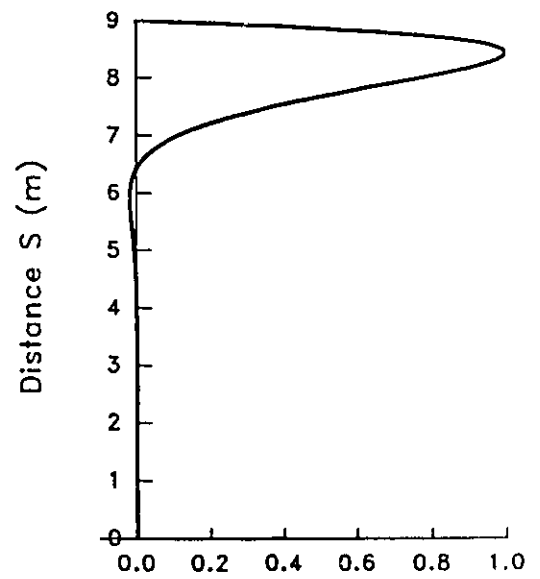
(c) Third Mode

(d) Fourth Mode

Figure 4.10 Cos θ −Type Pressure Modes Along the Generator

of the Broad Tanks ($\theta = 0°$)
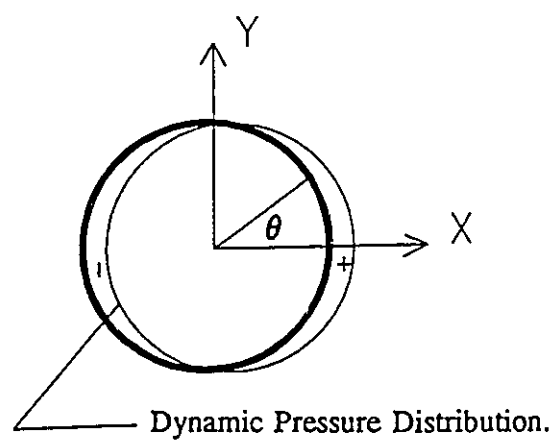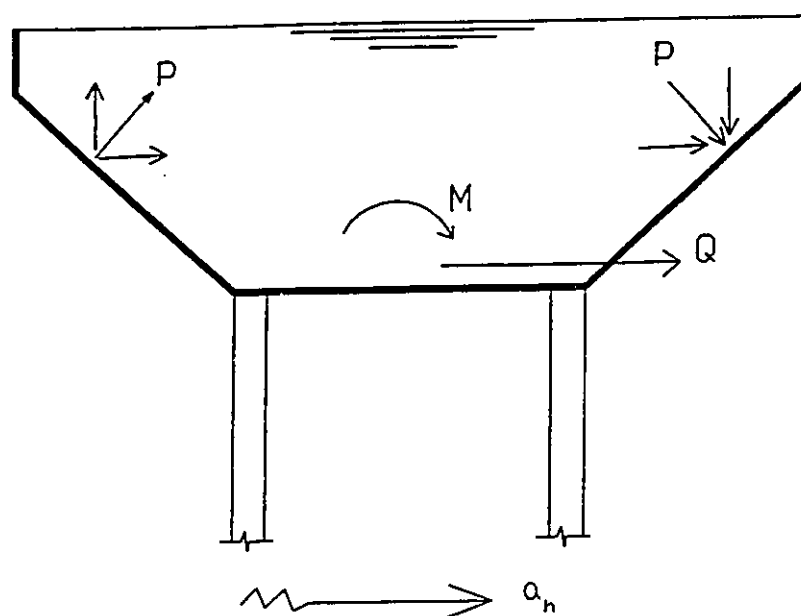
Figure 4.11 Effect of the Horizontal Acceleration on Conical Tanks.
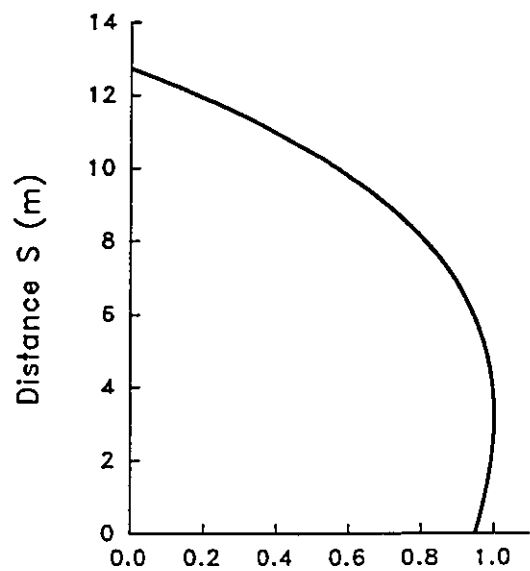
(a) First Mode
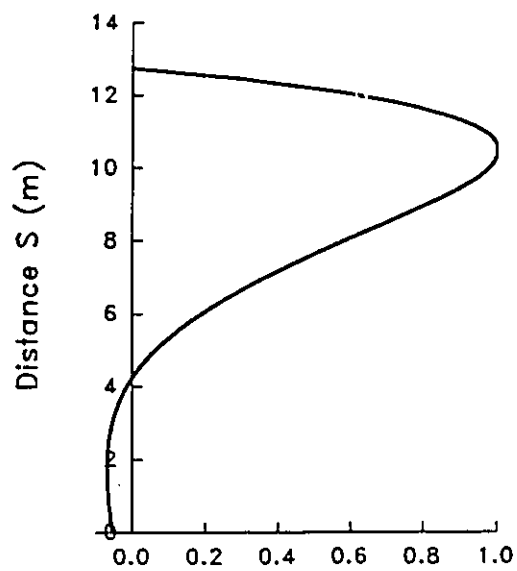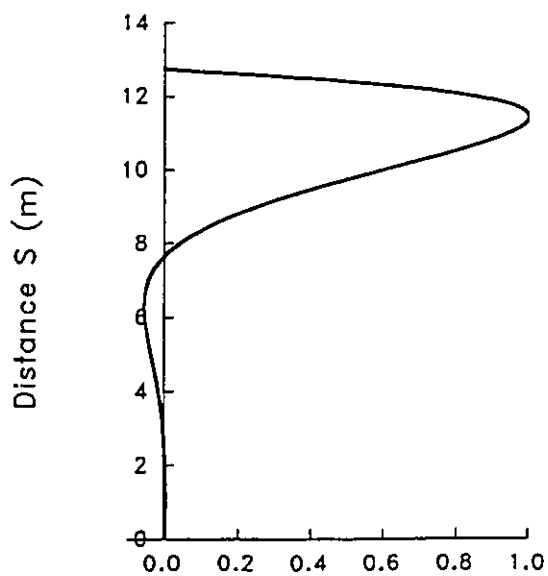
(b) Second Mode
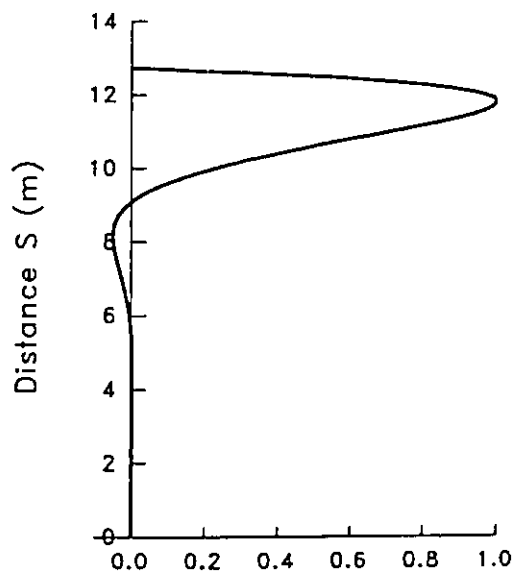
(c) Third Mode

(d) Fourth Mode

Figure 4.12   Axisymmetric Pressure Modes Along the Generator
of the Tall Tanks .
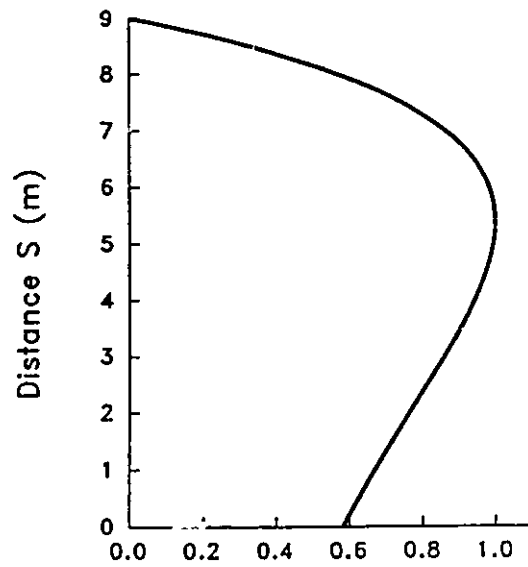
(a) First Mode
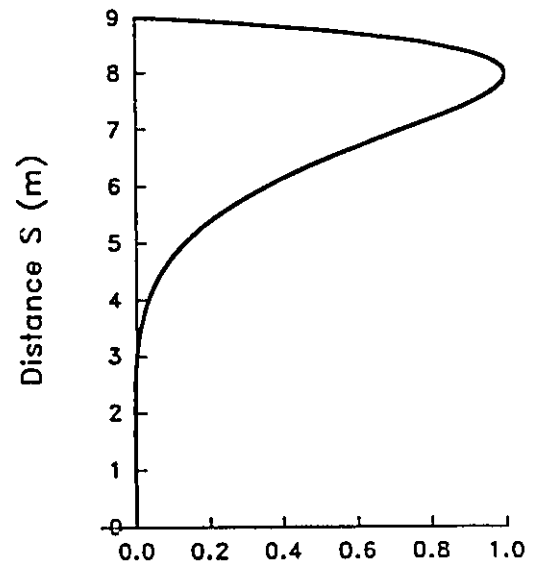
(b) Second Mode
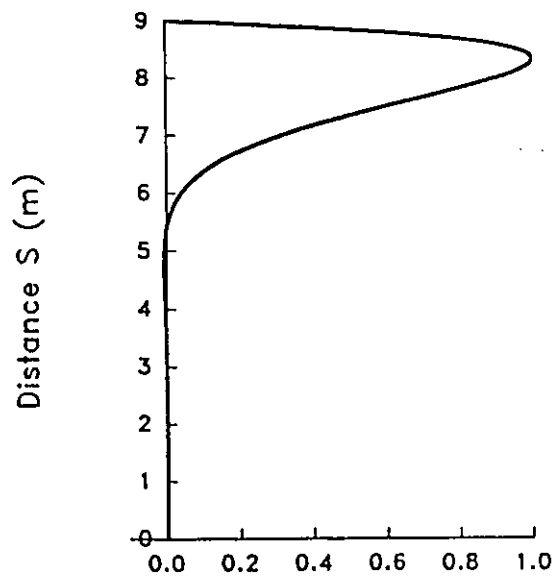
(c) Third Mode
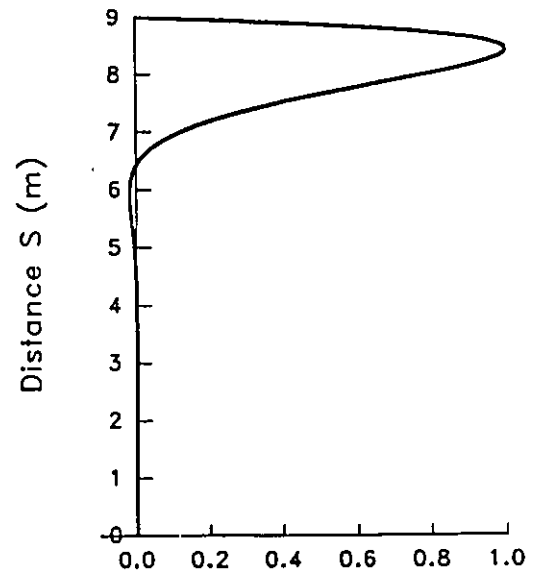
(d) Fourth Mode

Figure 4.13 Axisymmetric Pressure Modes Along the Generator
of the Broad Tanks .
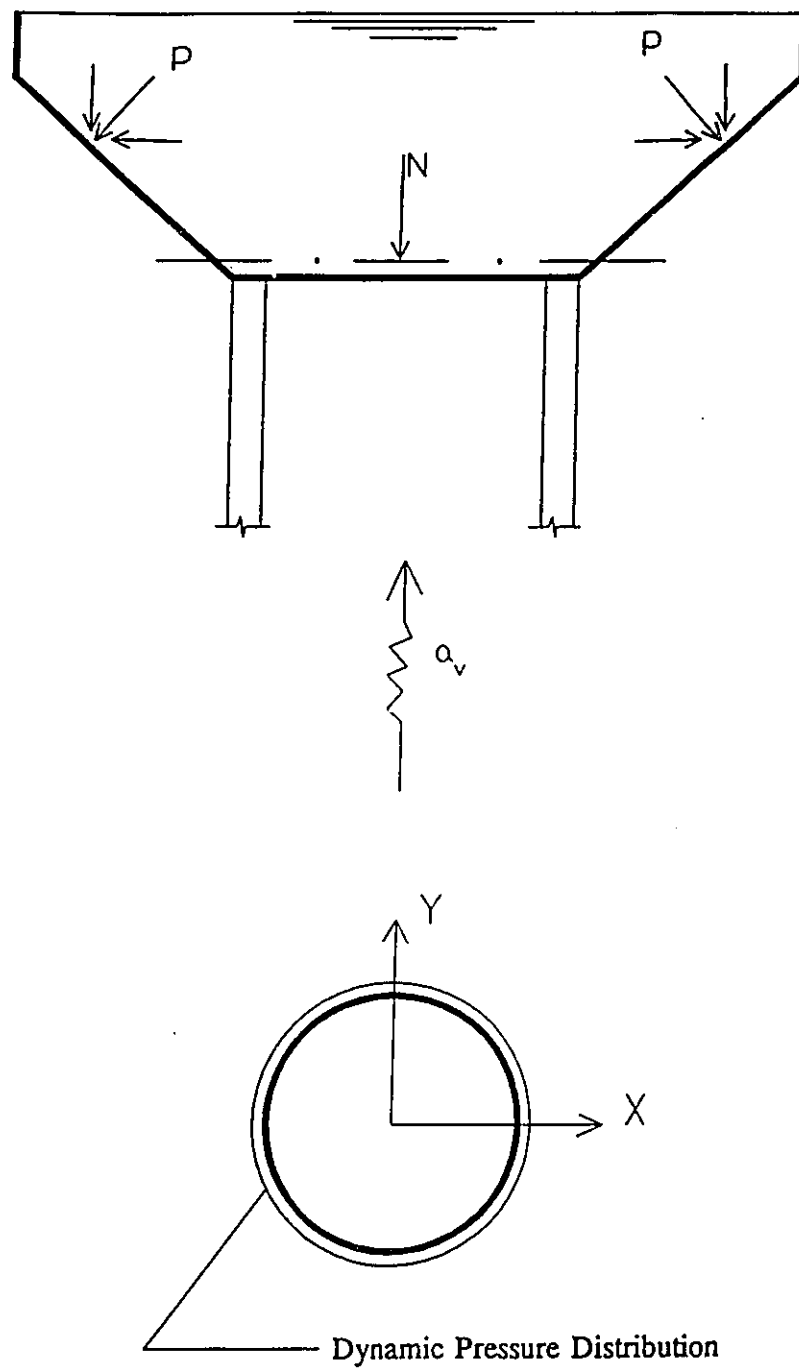
Figure 4.14 Effect of the Vertical Acceleration on Conical Tanks.
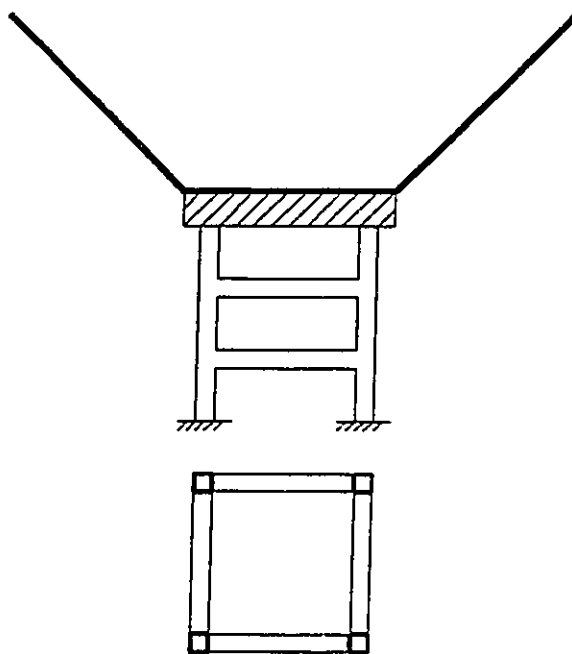
Figure 4.15 Frames Supporting the Steel Conical Vessels.
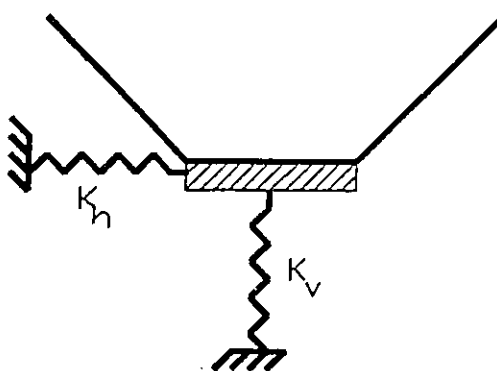
Figure 4.16 Springs Simulating the Supporting Frames.
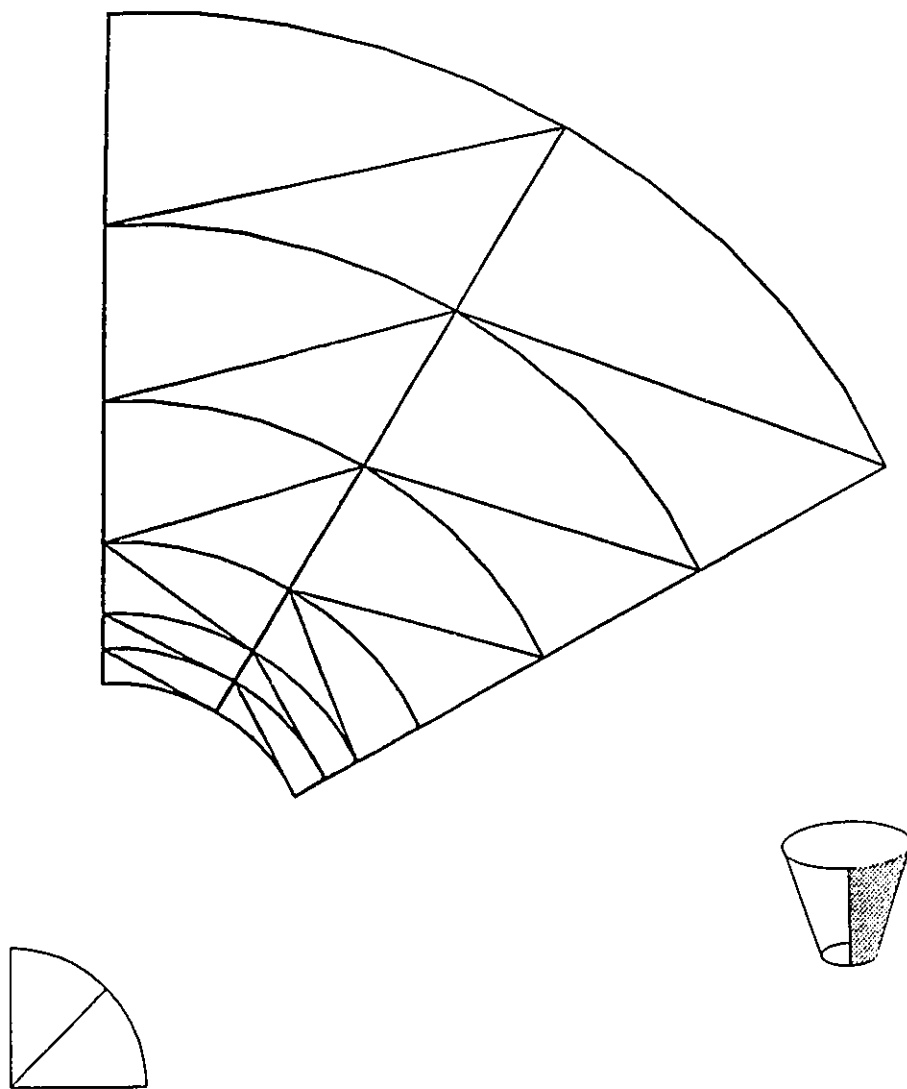
Mesh for the Base

Figure 4.17 Finite Element Mesh for Dynamic Analysis (Quarter Cone).
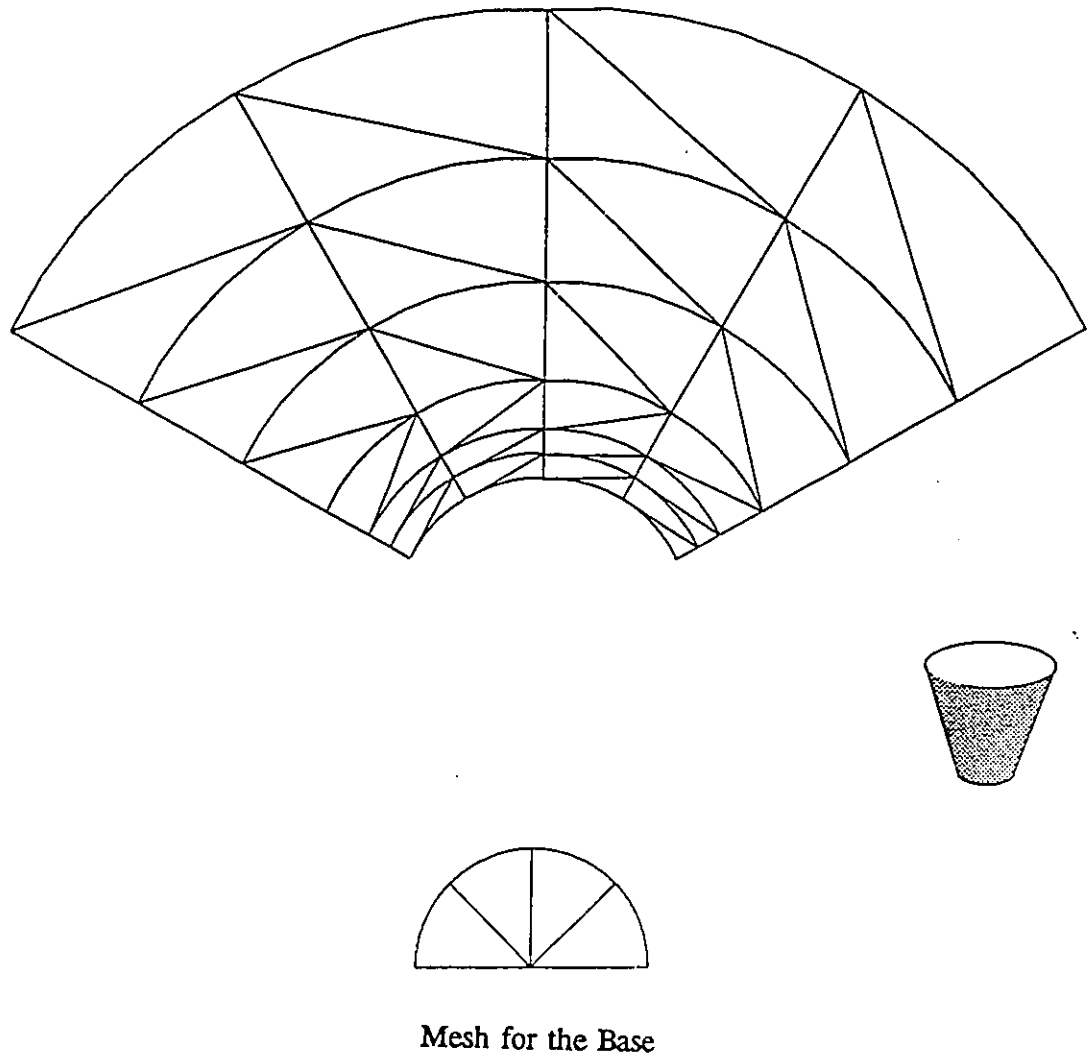
Mesh for the Base

Figure 4.18 Finite Element Mesh for Dynamic Analysis (Half Cone).
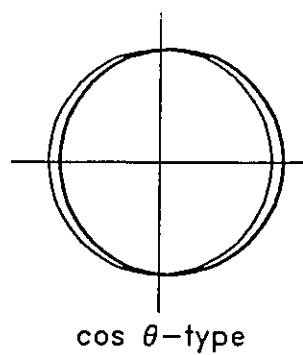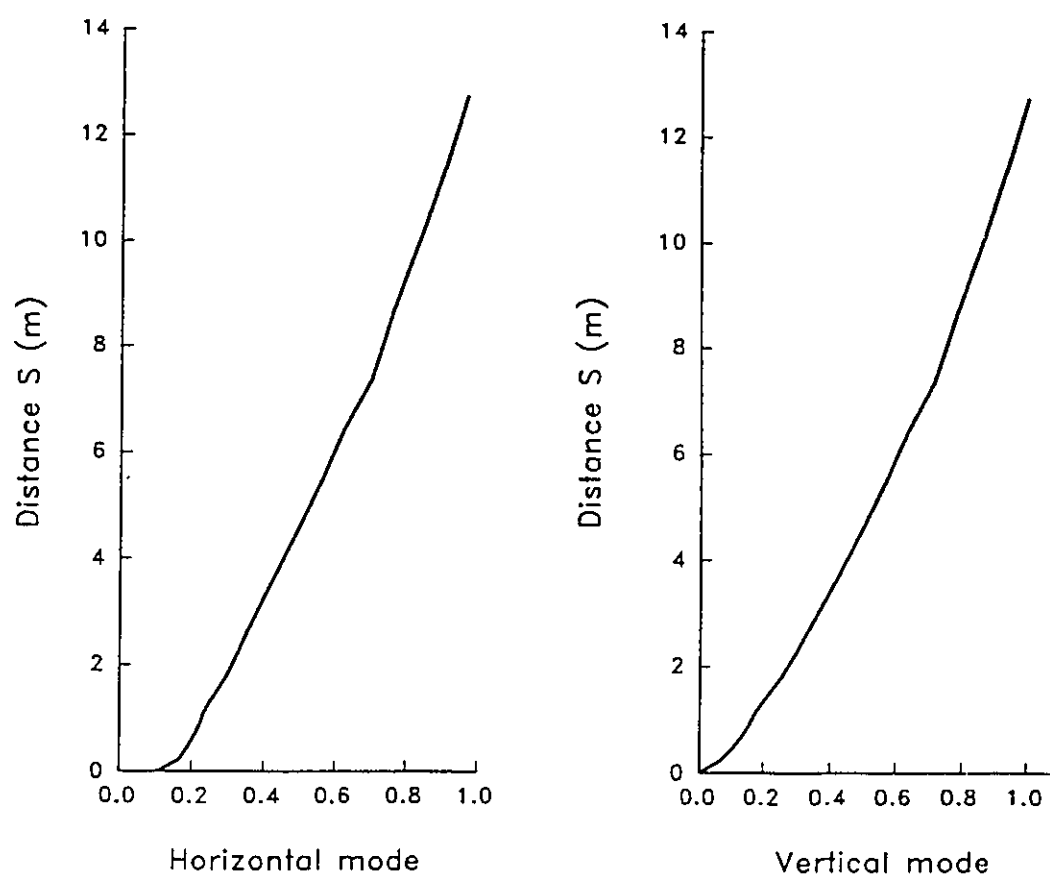
Figure 4.19 Fundamental modes of the cos—θ vibration
for the Tall Tank $\theta=0°$.
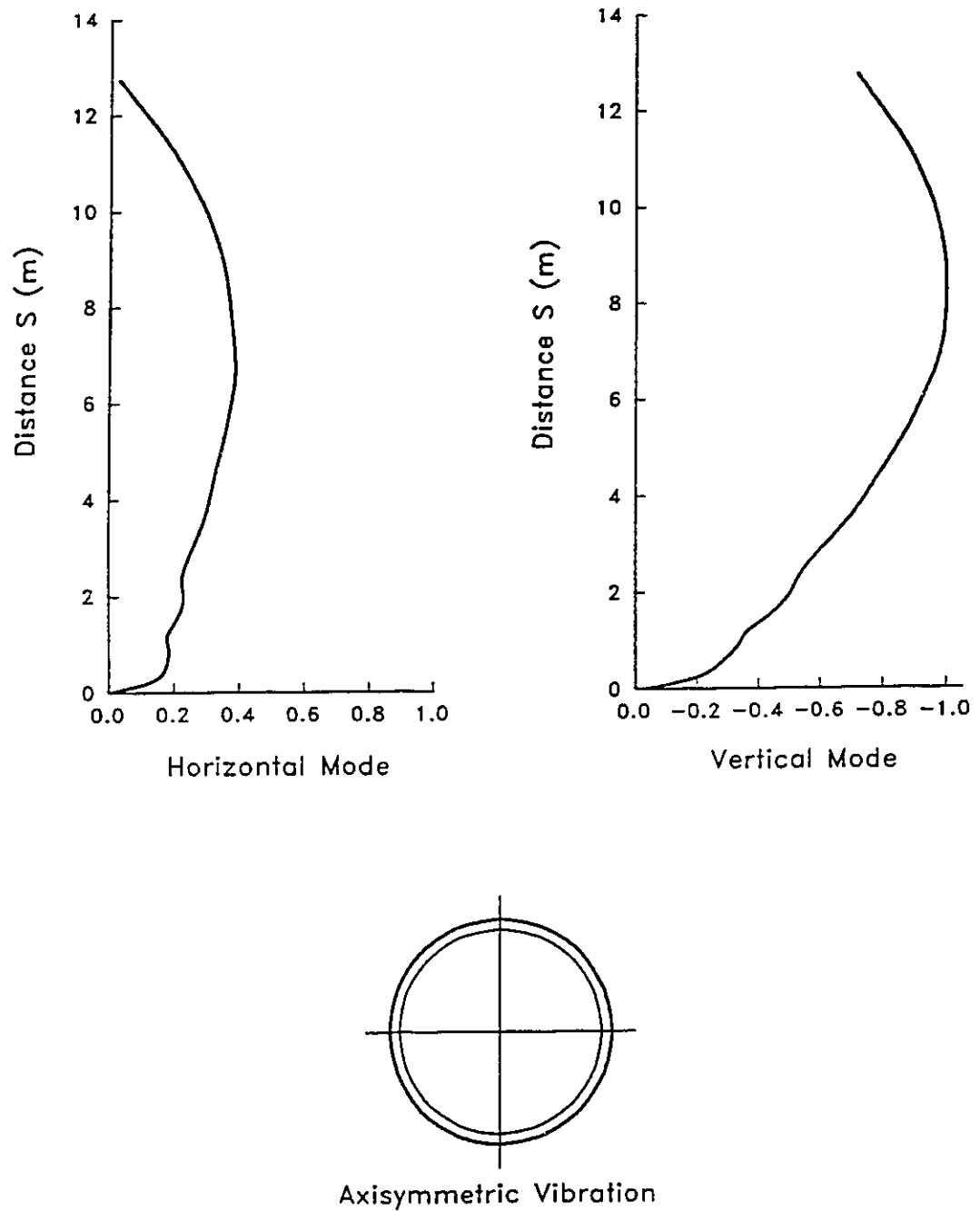
Figure 4.20 Fundamental Modes of the Axisymmetric Vibration for the Tall Tank.
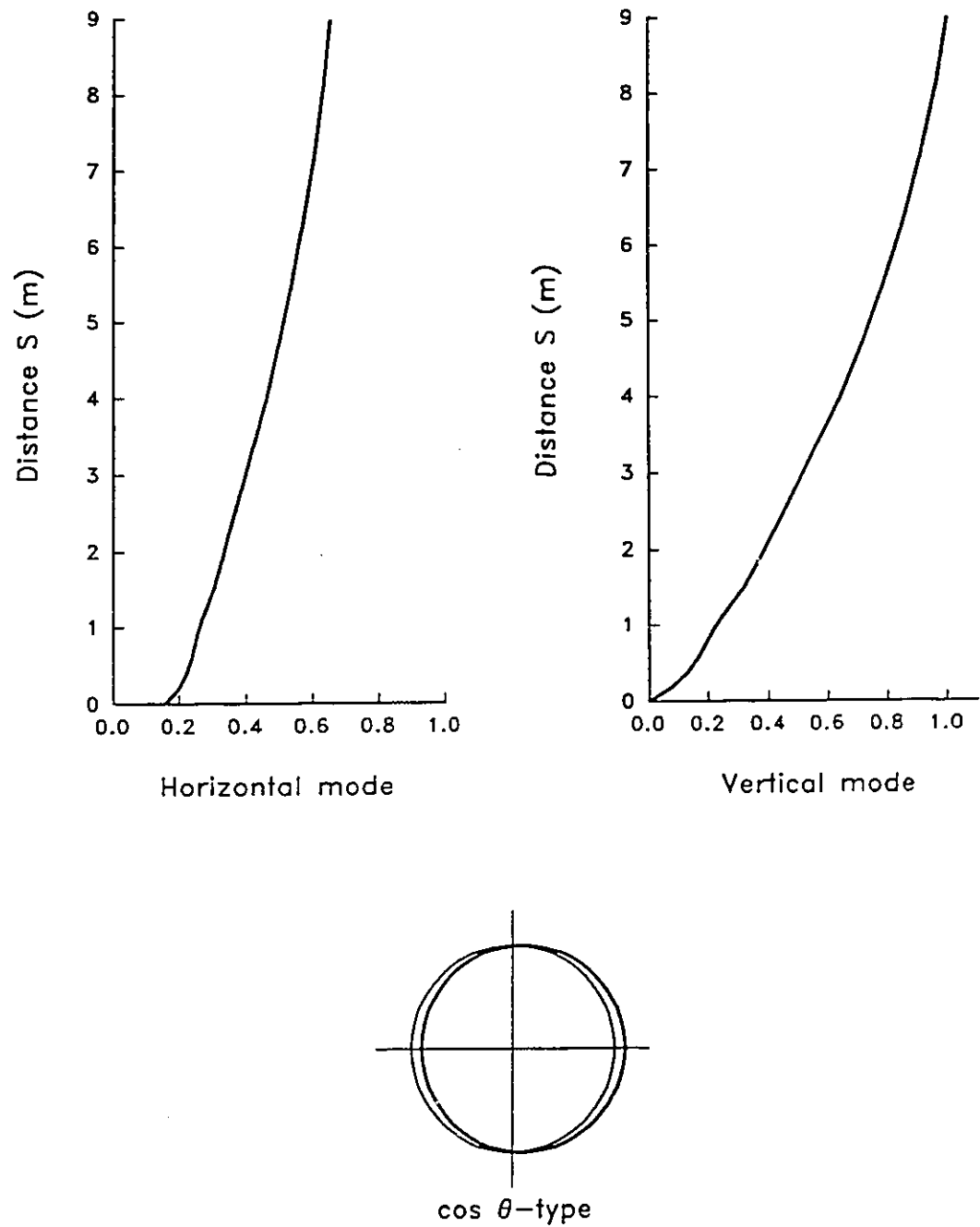
Figure 4.21 Fundamental modes of the cos−θ vibration for the Broad Tank (θ=0°).
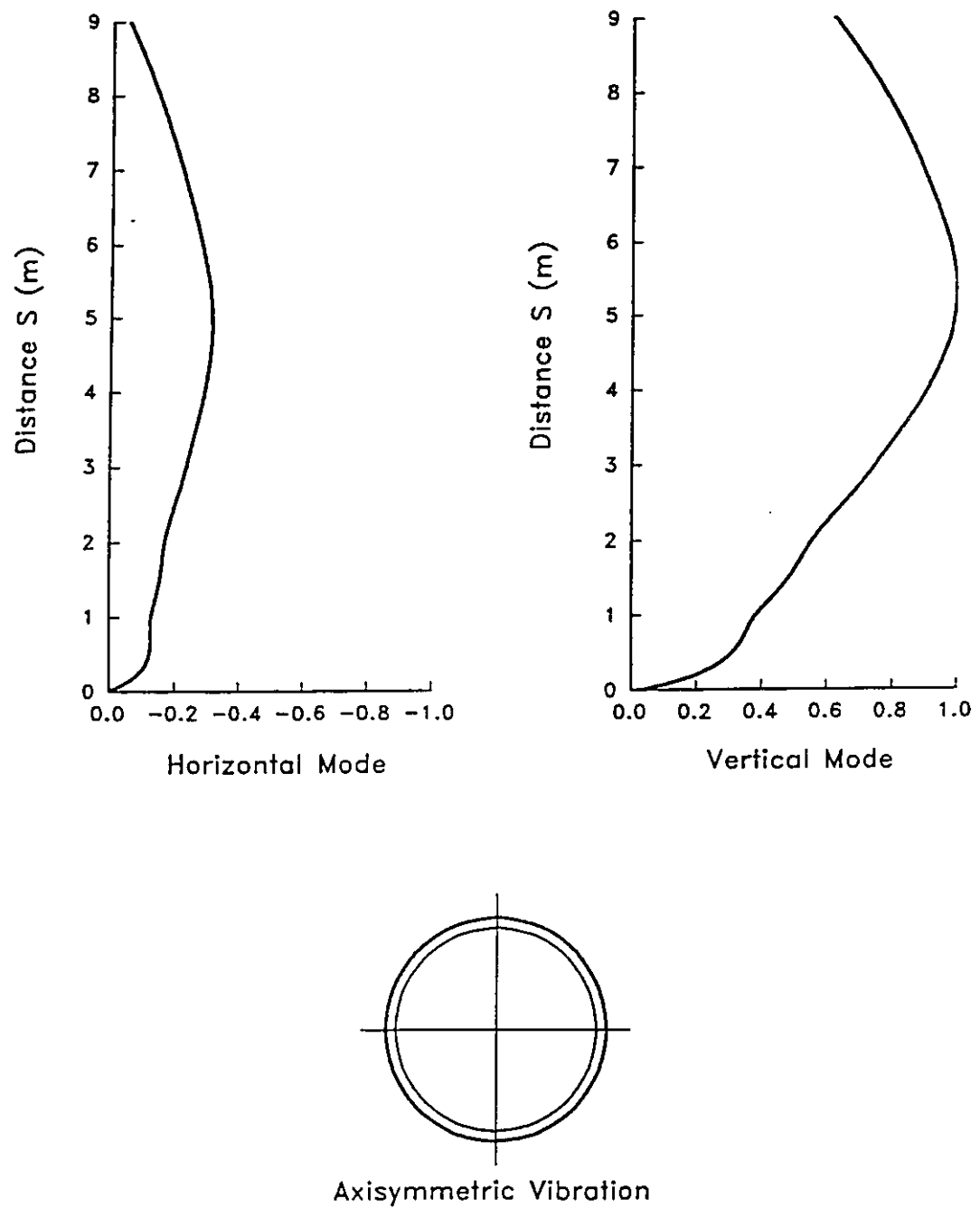
Figure 4.22 Fundamental Modes of the Axisymmetric Vibration for the Broad Tank.
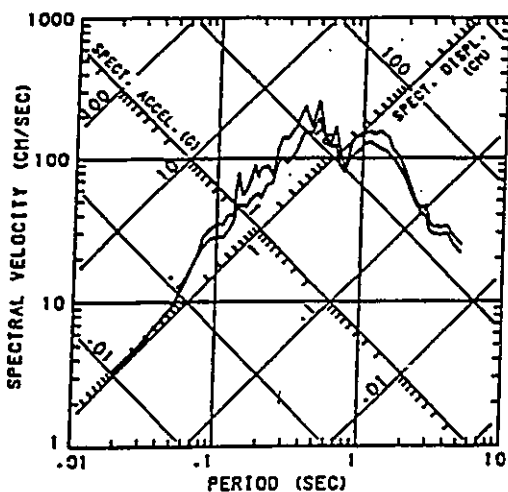
Figure 4.23 Response Spectrum for the San Fernanado Earthquake
(2% and 5% Damping)
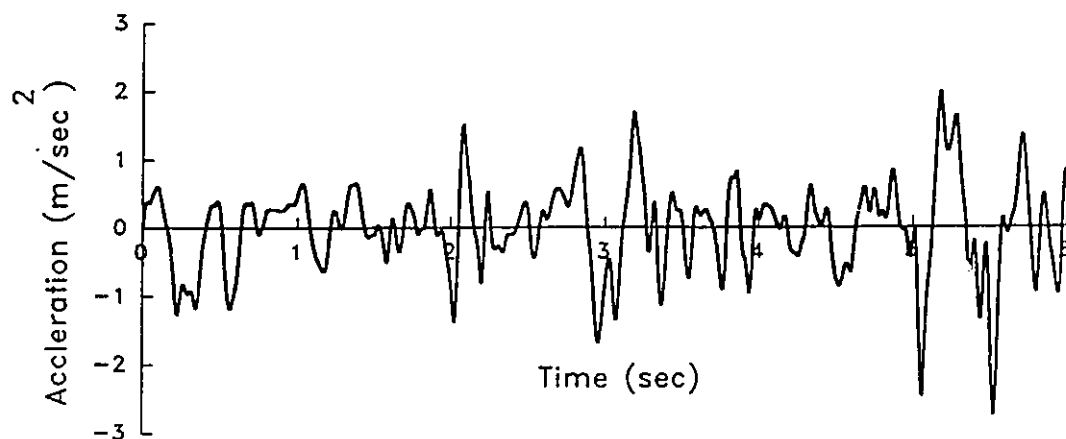
Figure 4.24 Scaled Horizontal Component of the Ground Acceleration.
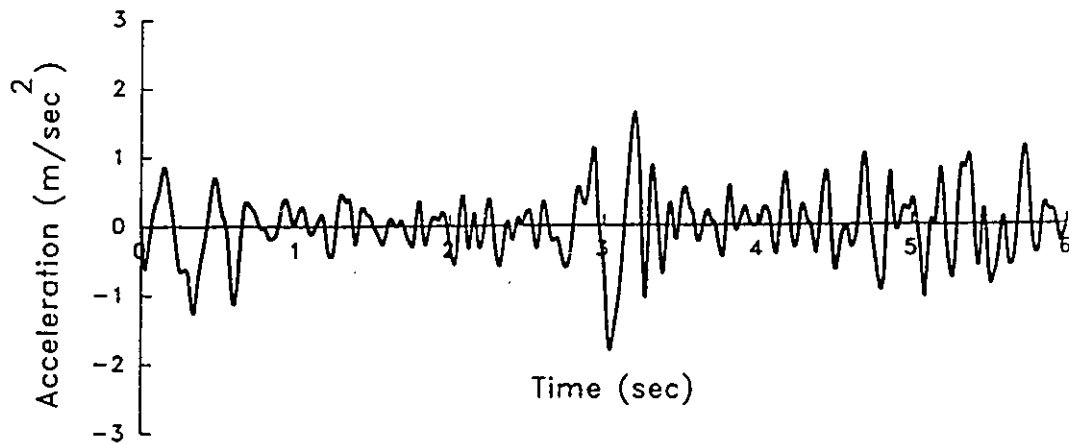
Figure 4.25 Scaled Vertical Component of the Ground Acceleration.
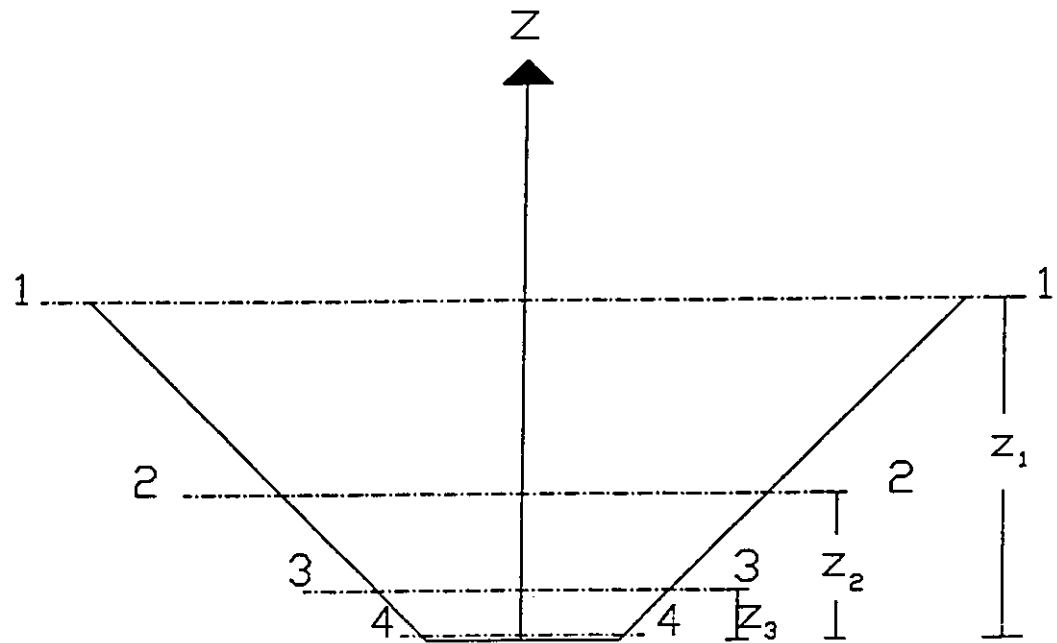
For the Broad Tanks

$z_1 = 4.5$ m
$z_2 = 1.97$ m
$z_3 = 0.56$ m
$z_4 = 0.0$ m

For the Tall Tanks

$z_1 = 9.0$ m
$z_2 = 3.79$ m
$z_3 = 0.95$ m
$z_4 = 0.0$ m
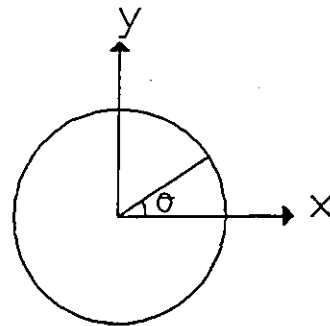
Figure 4.26 Sections at which Dynamic Results Are Displayed.

(a) Horizontal displacement (mm)

(b) Vertical Displacement (mm)

·········· Static.

——— Failure due to Dynamic.

(c) Transverse displacement (mm)

(d) Axial Displacement (mm)
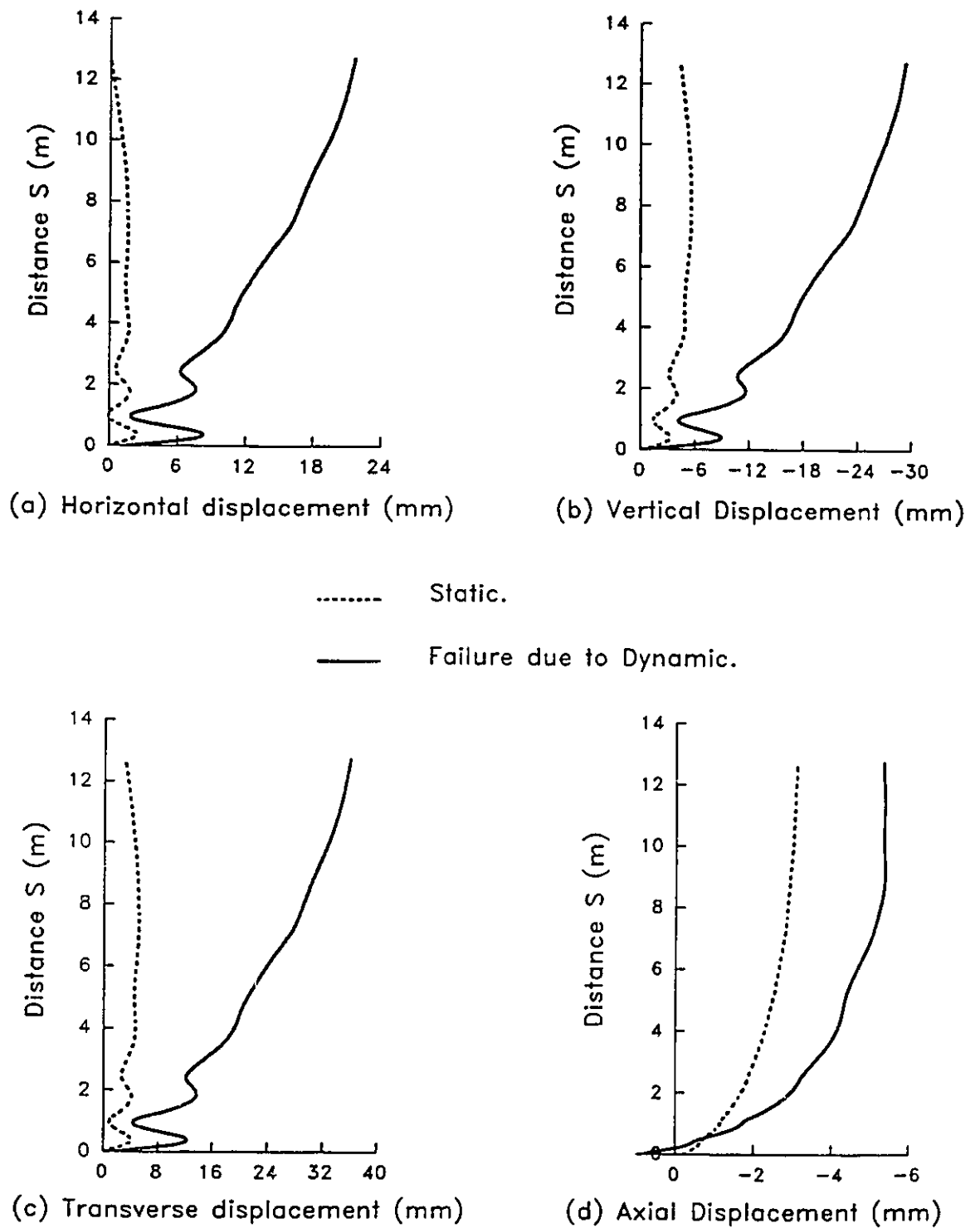
Figure 4.27 Displacement shapes Along the Generator ($\theta=0°$) of Tank DT1 at Failure.

(a) Horizontal displacement (mm)

(b) Vertical Displacement (mm)

.... Static.

———— Failure due to Dynamic.

(c) Transverse displacement (mm)

(d) Axial Displacement (mm)
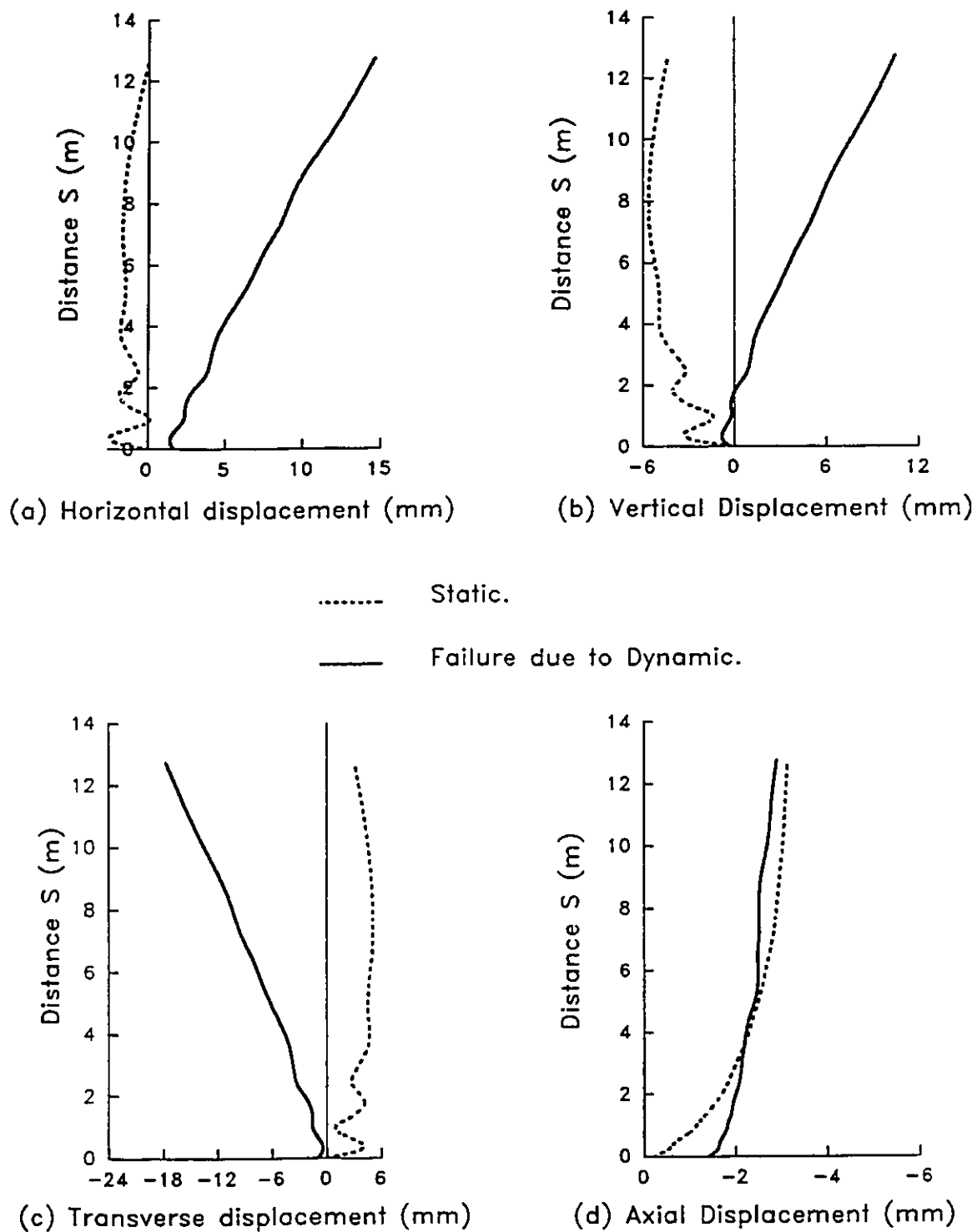
Figure 4.28 Displacement shapes Along the Generator ($\theta=180°$) of Tank DT1
at Failure.
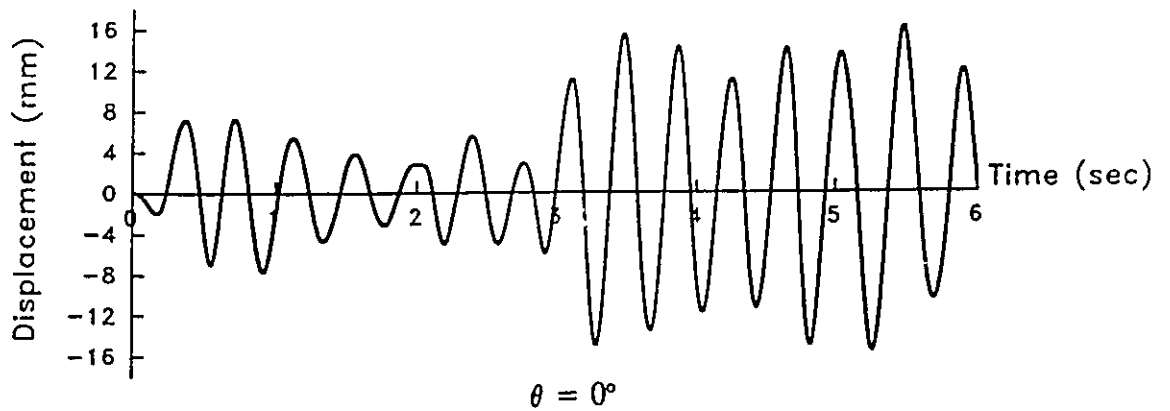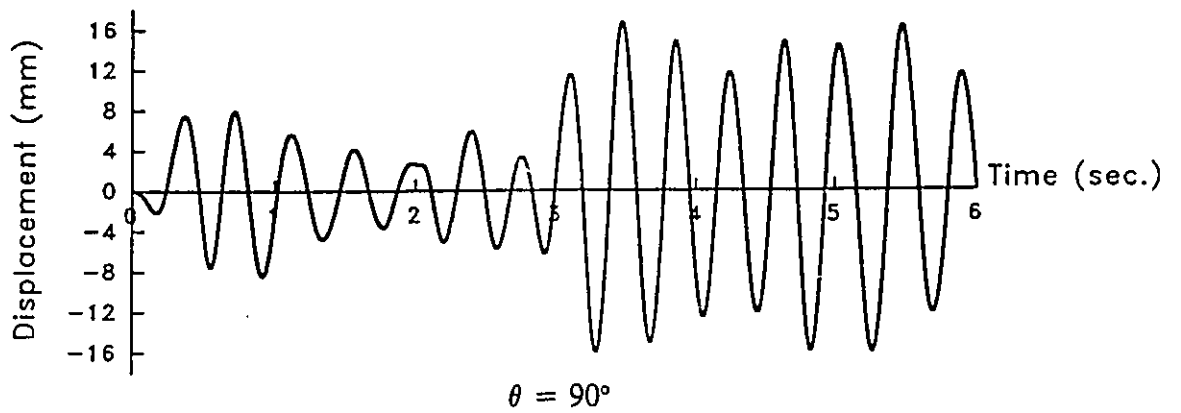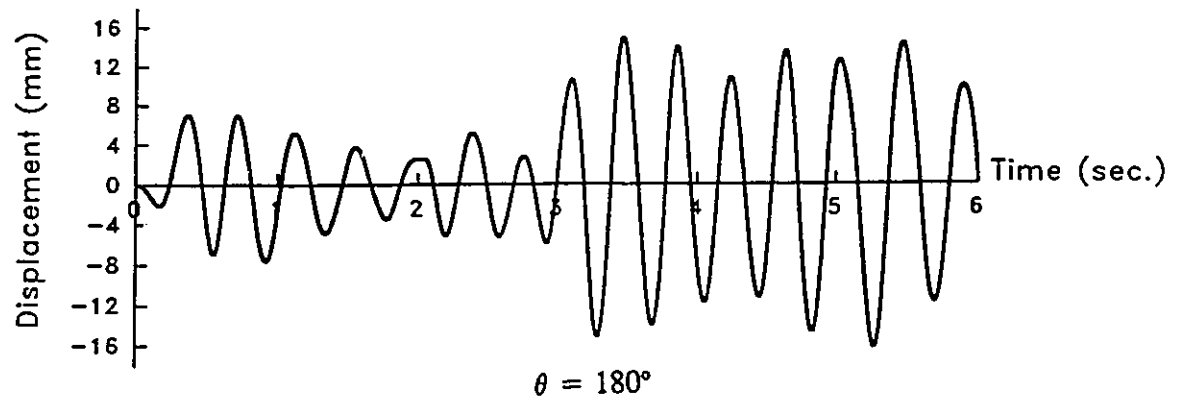
Figure 4.29 Time History of the Relative Displacements Along the X—Axis at Section 1—1 for Tank DT5.
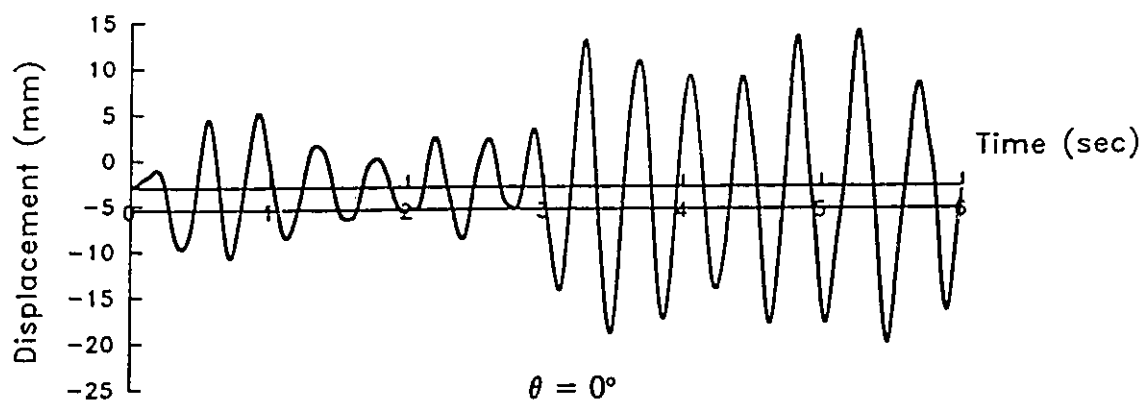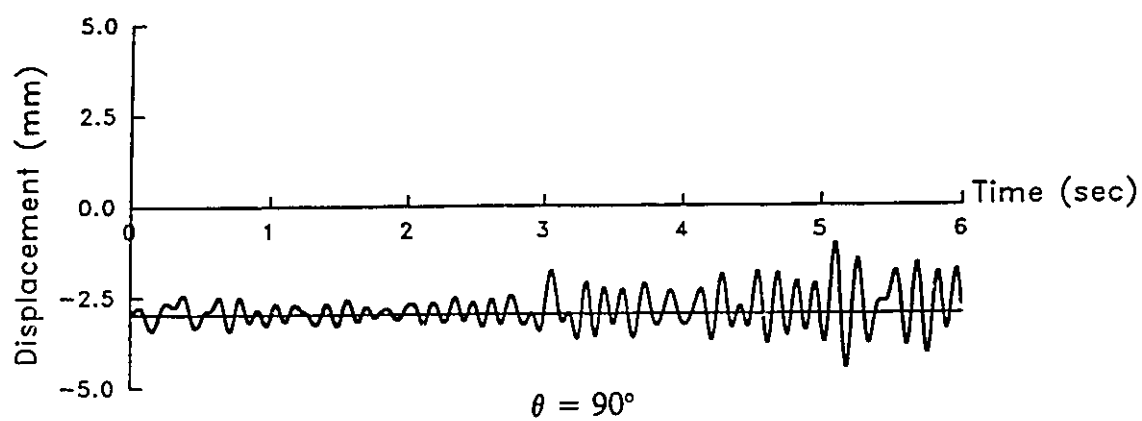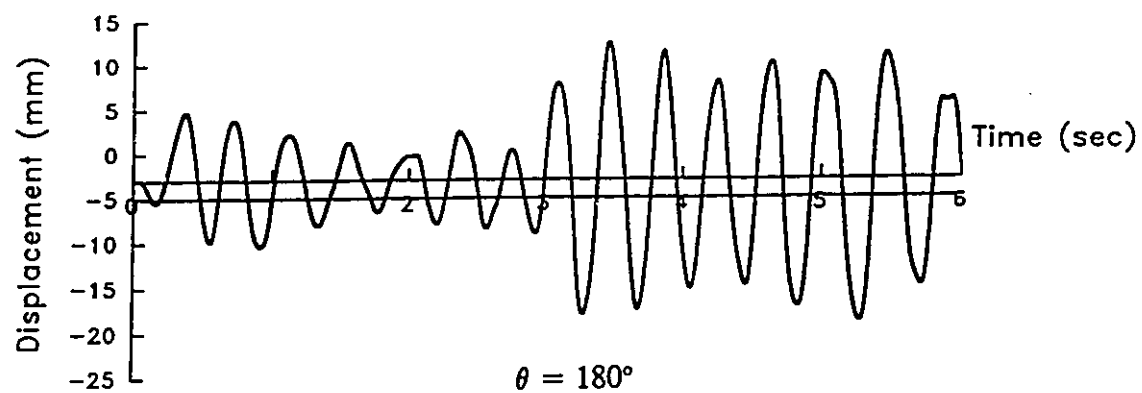
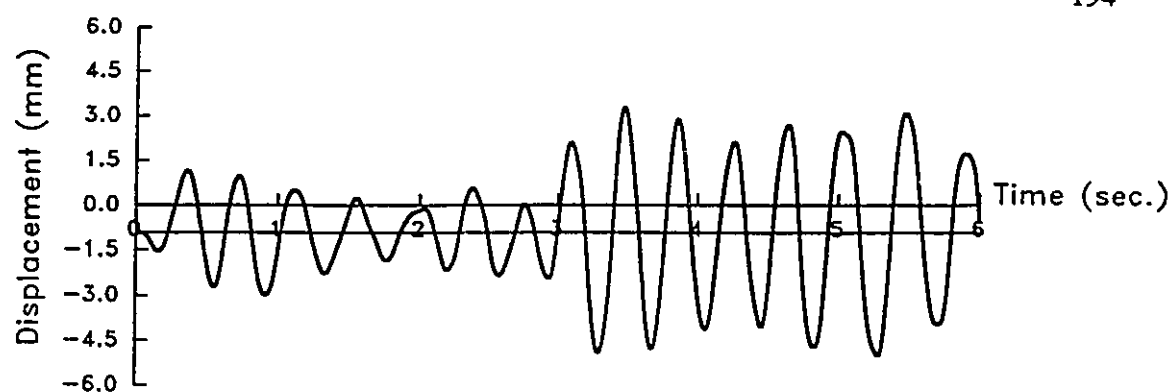Figure 4.30 Time History of the Relative Vertical Displacements at Section 1-1 for Tank DT5.
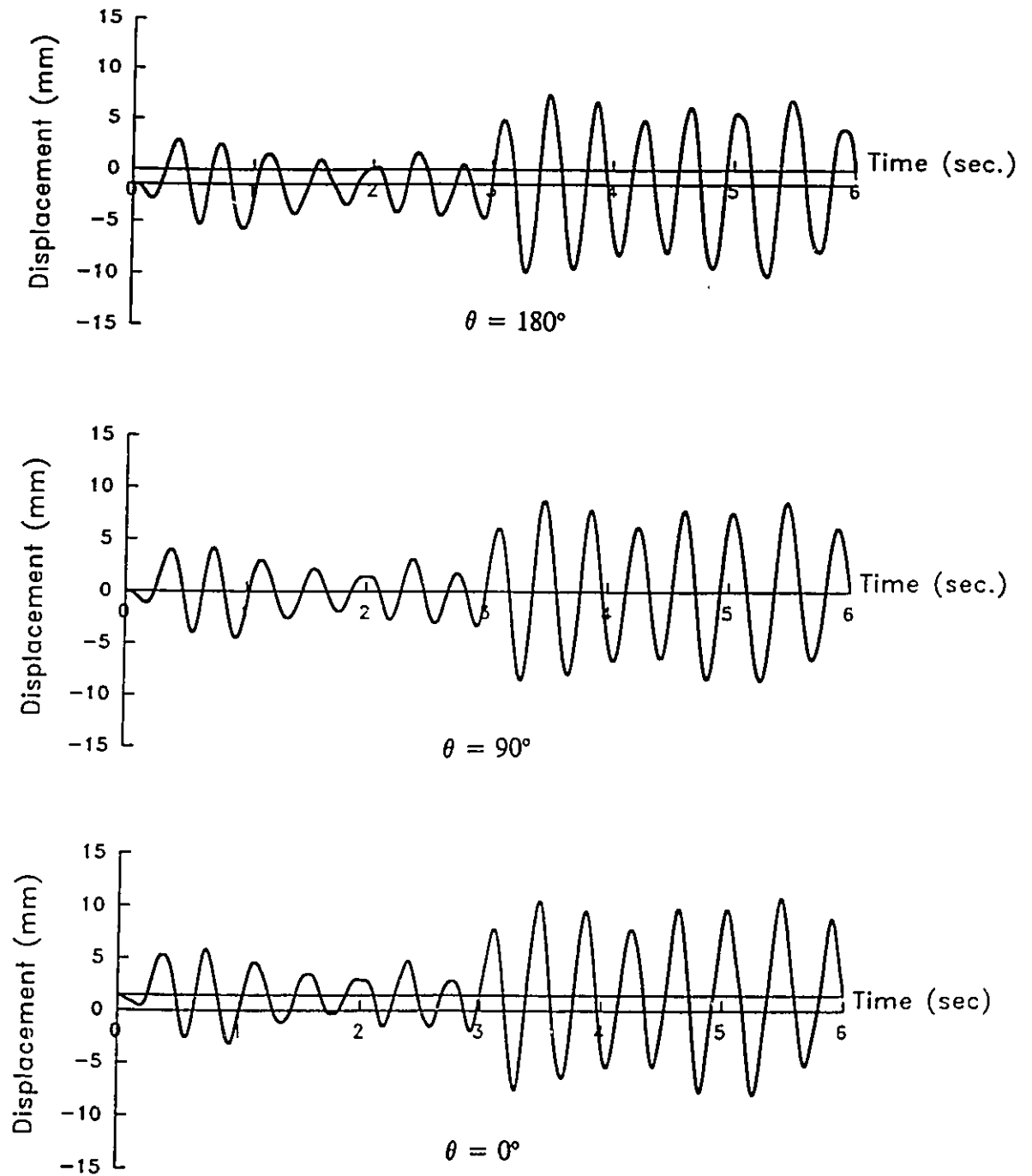
Figure 4.31 Time History of the Relative Displacements Along the X—Axis at Section 2—2 for Tank DT5.
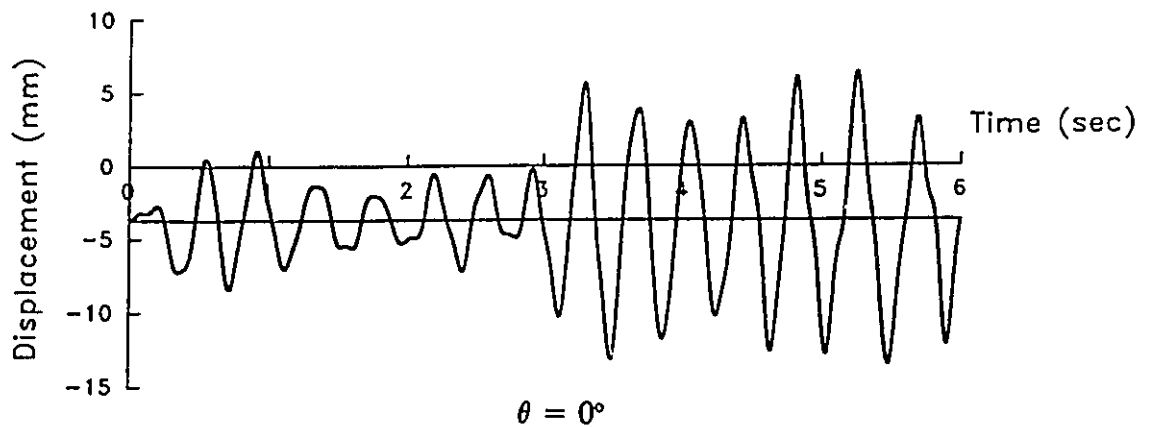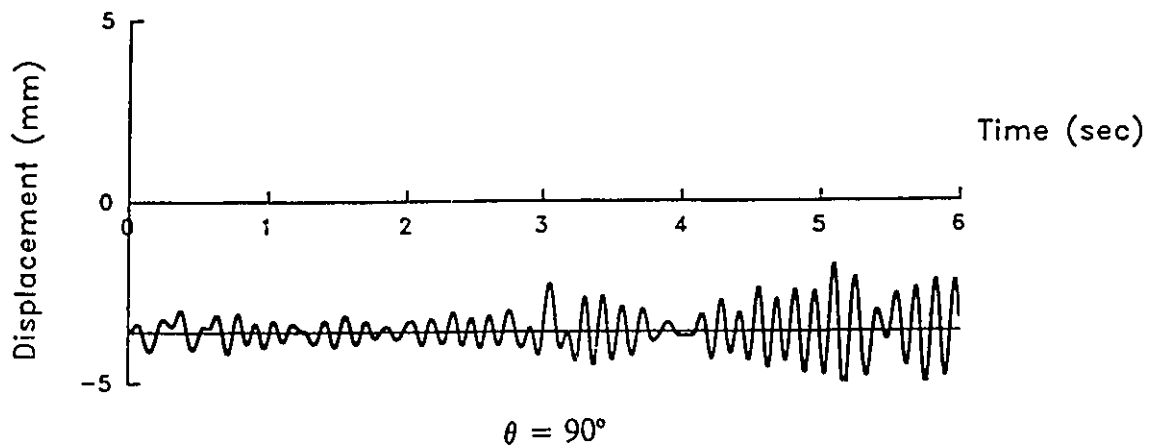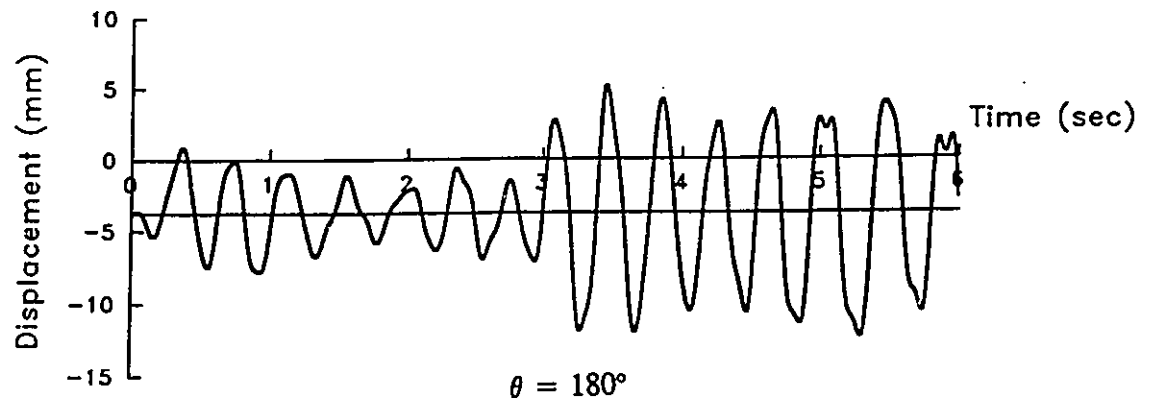
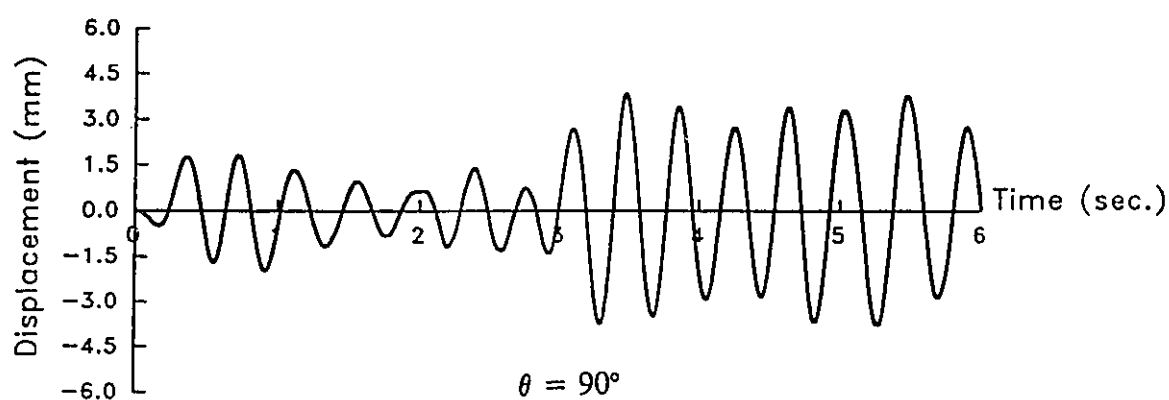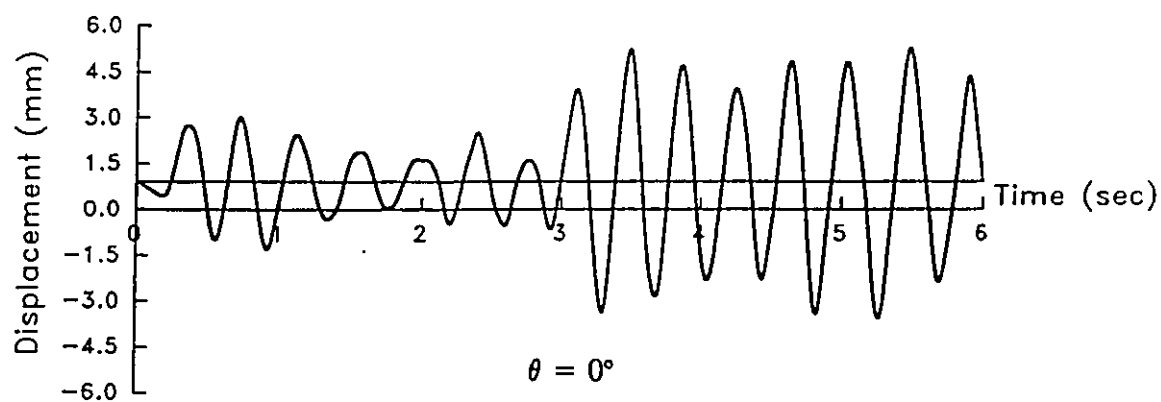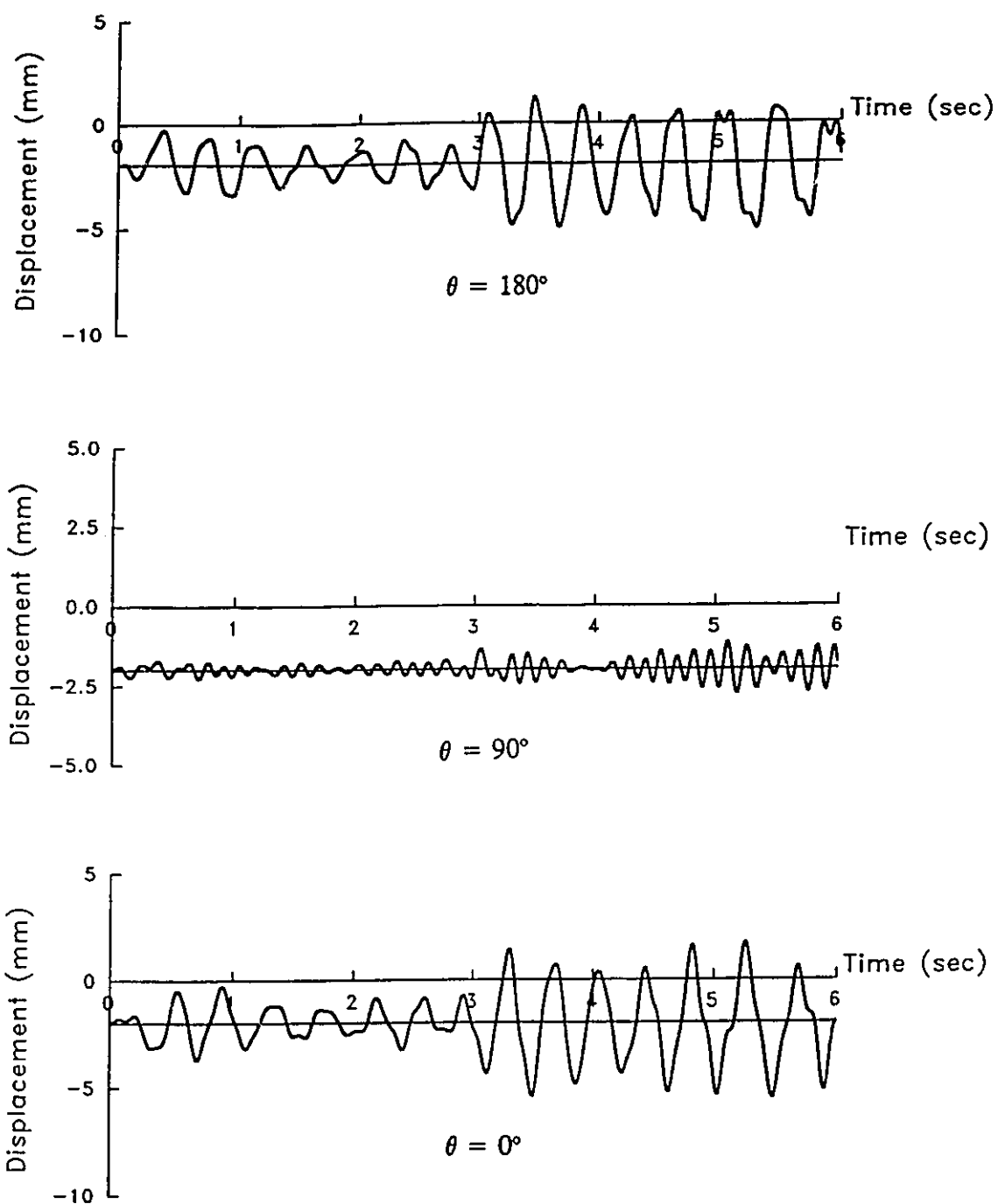Figure 4.32 Time History of the Relative Vertical Displacements at Section 2-2 for Tank DT5.

Figure 4.33 Time History of the Relative Displacements Along the X—Axis at Section 3—3 for Tank DT5.

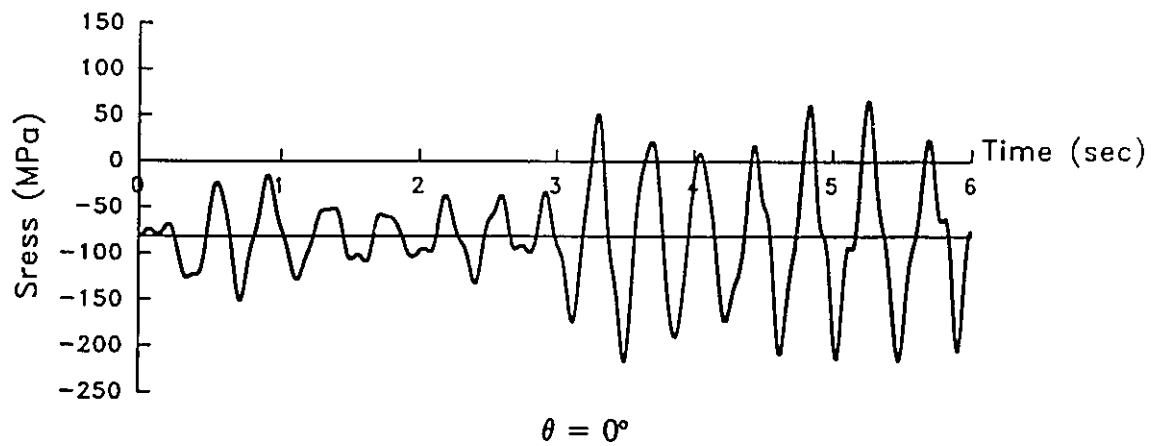Figure 4.34 Time History of the Relative Vertical Displacements at Section 3-3 for Tank DT5.
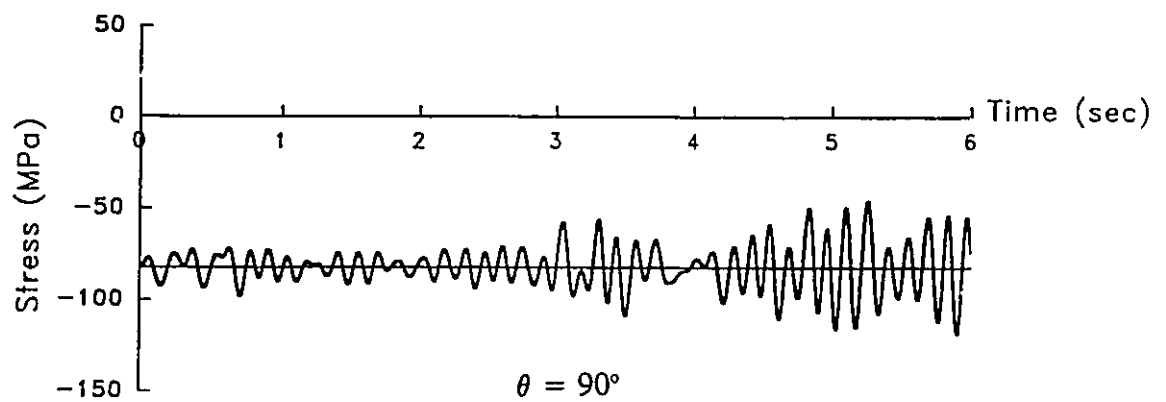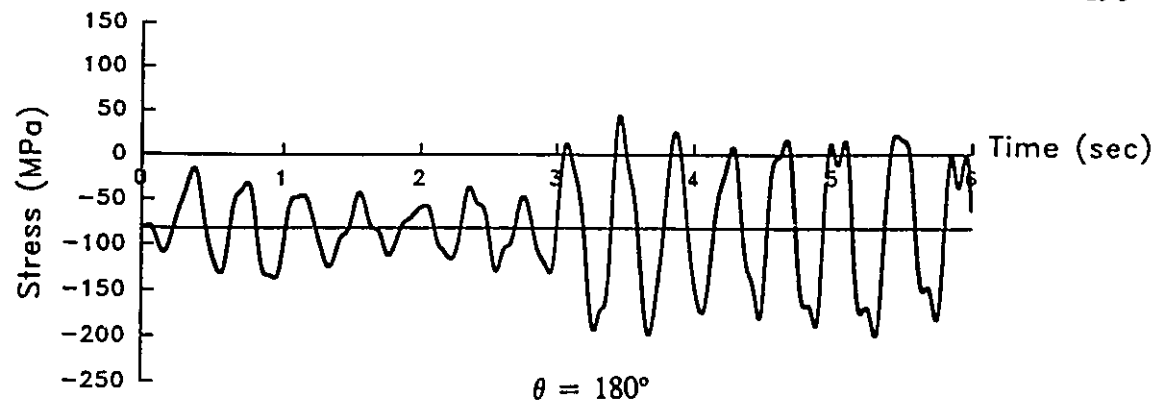
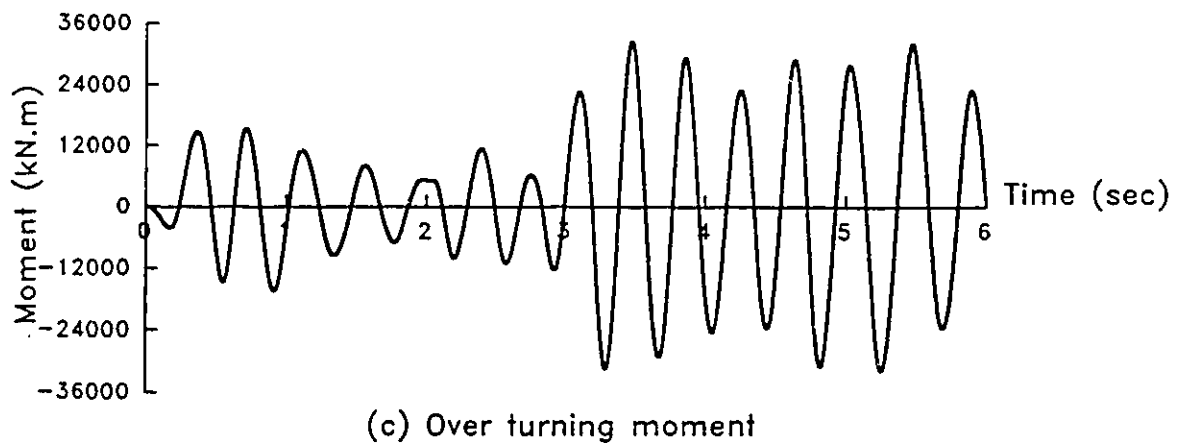Figure 4.35 Time History of the Meridional Stresses at Section 4—4 for Tank DT5.

(a) Base shear

(b) Normal force

(c) Over turning moment
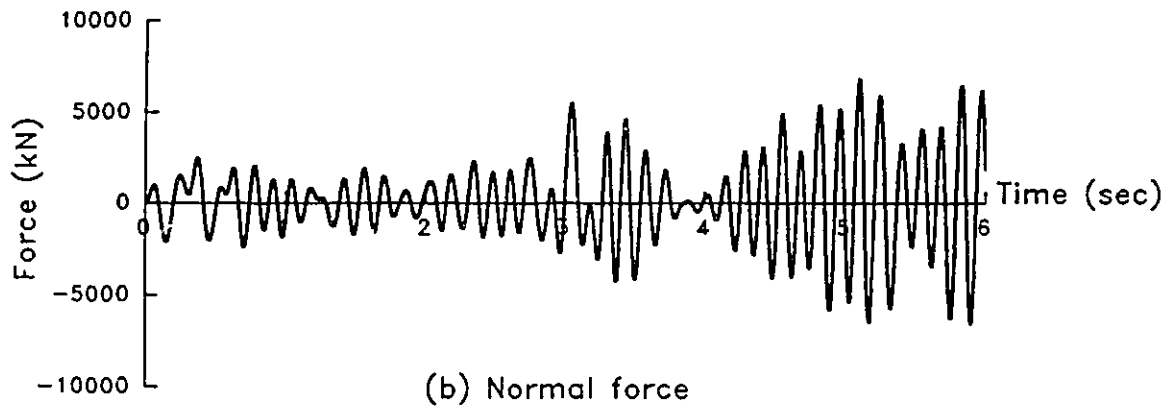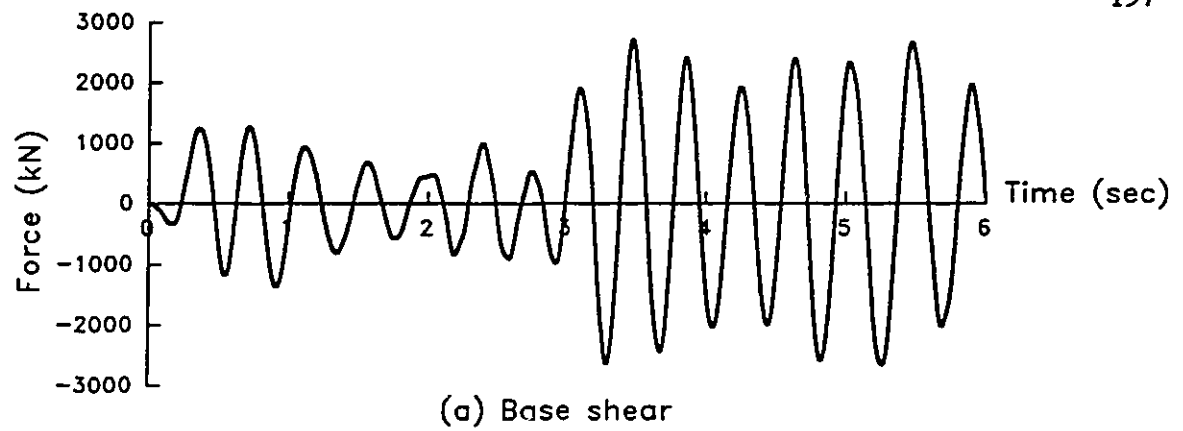
Figure 4.36 Time History of the Base Reactions at Section 4—4
for Tank DT5.
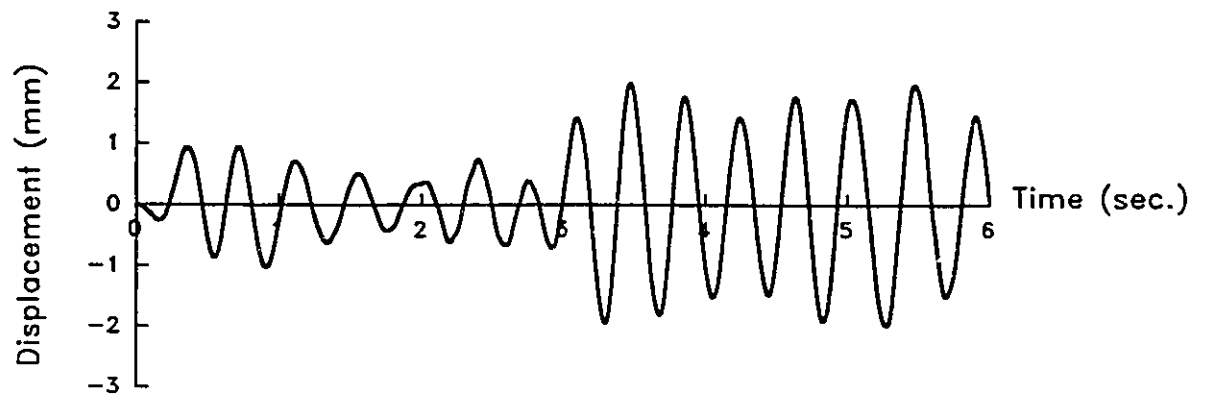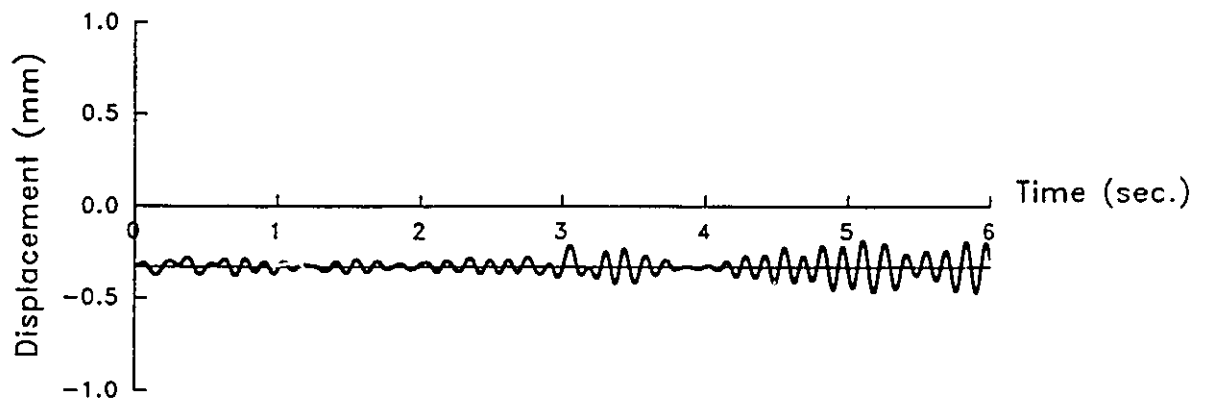
Figure 4.37 Time History of the Relative Displacements at Section 4-4
for Tank DT5.
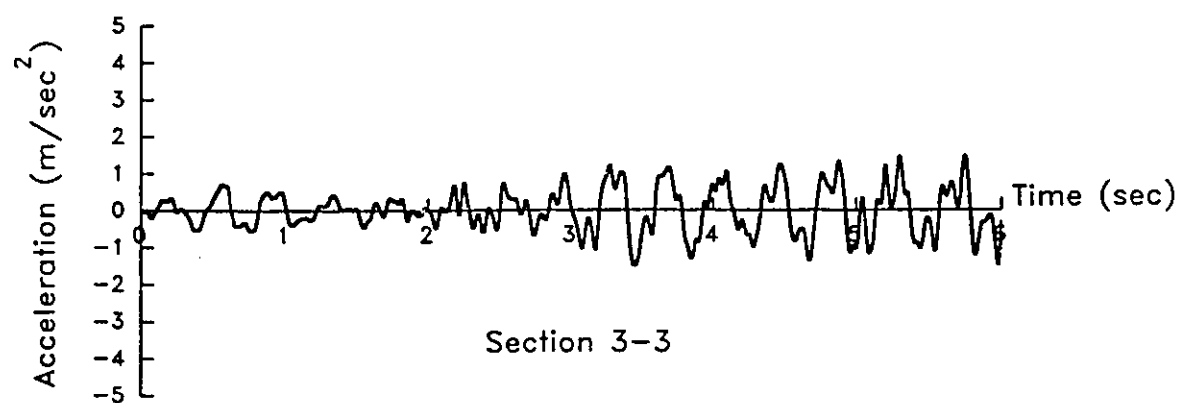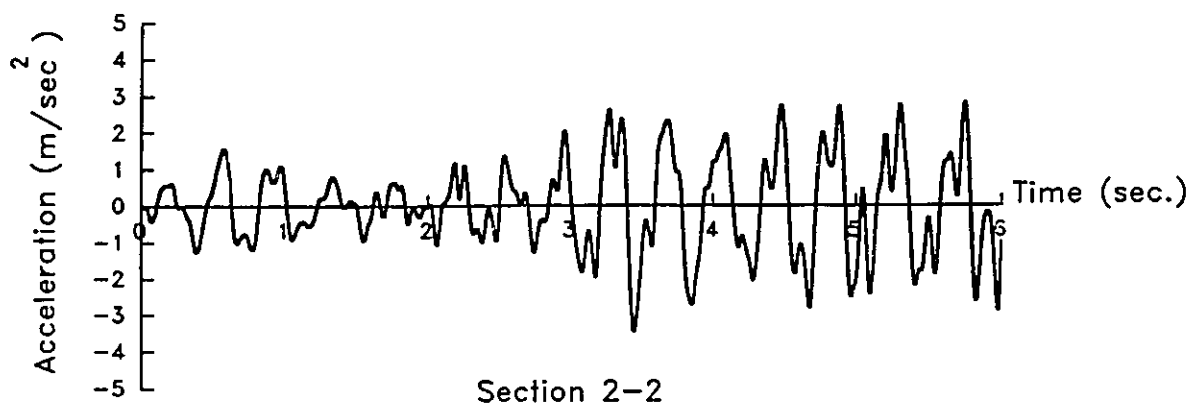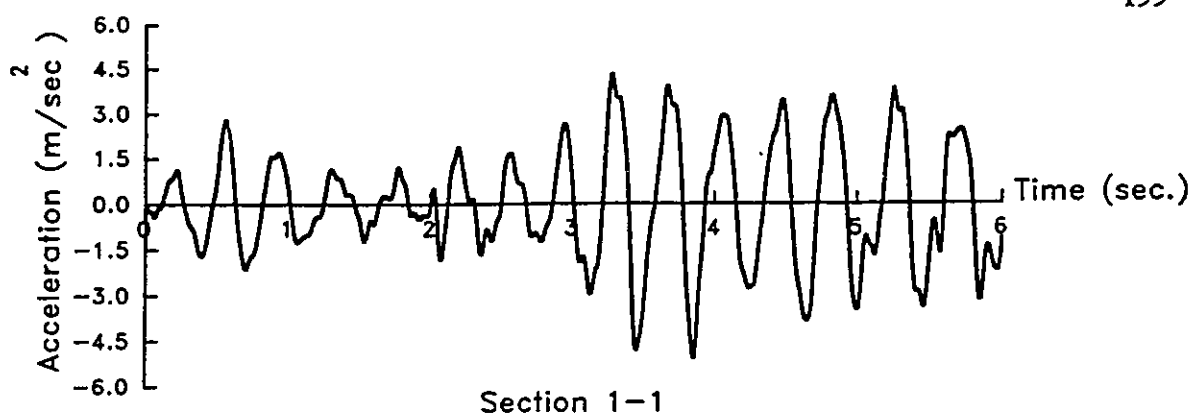
Figure 4.38 Time History of the Relative Accelerations Along the X—Axis at θ=180° for Tank DT5.
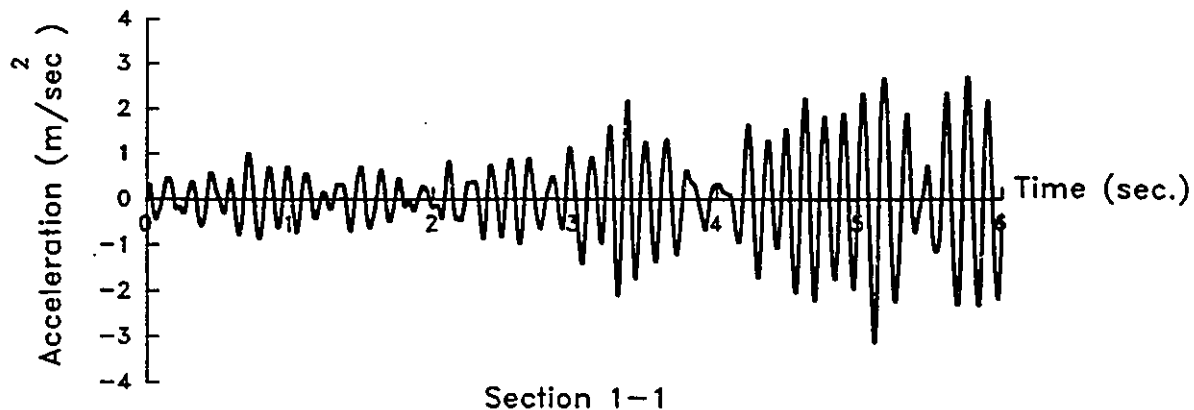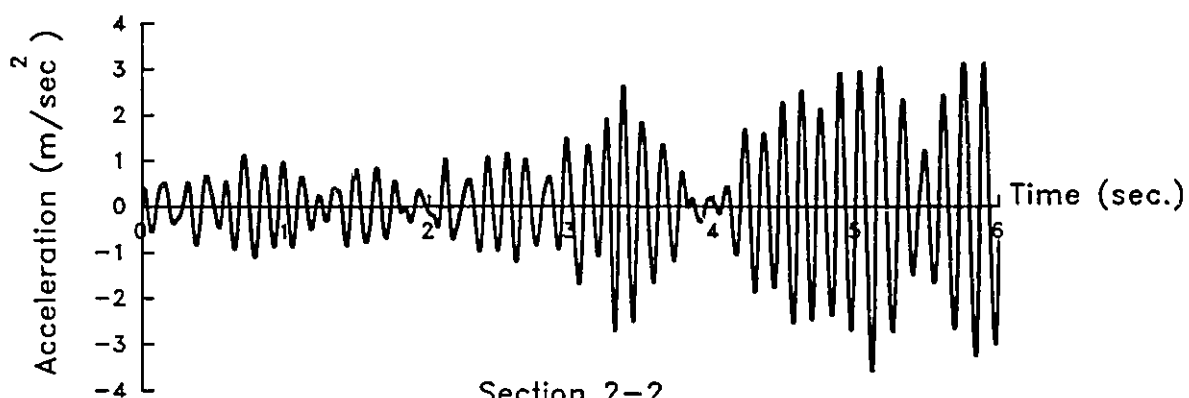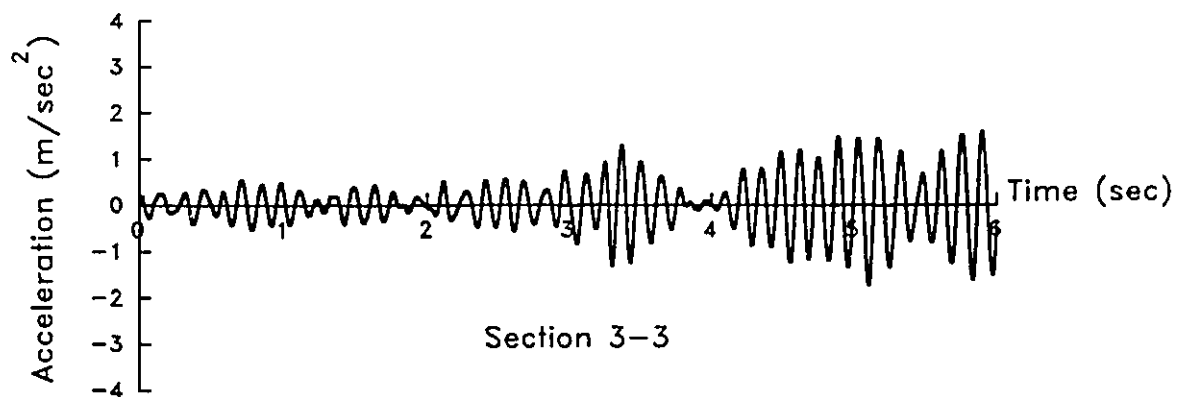
Figure 4.39 Time History of the Relative Vertical Accelerations at $\theta=90°$ for Tank DT5.
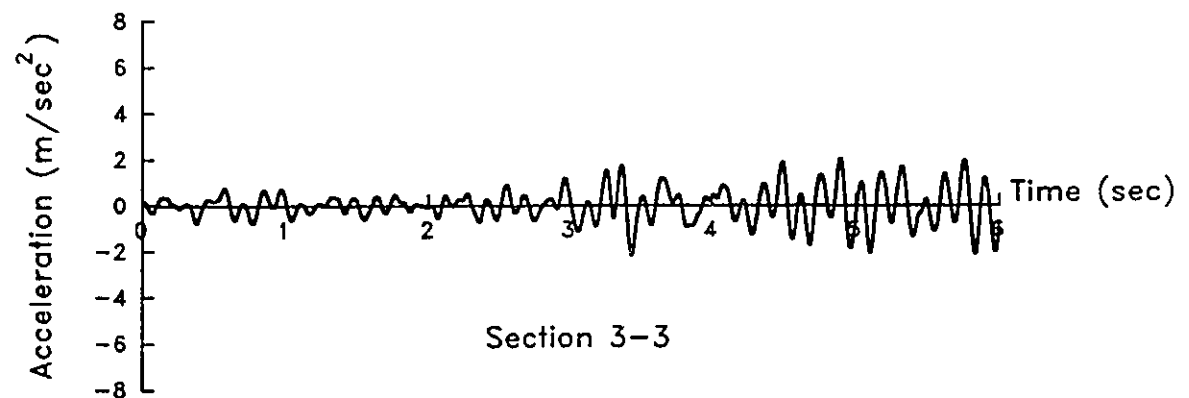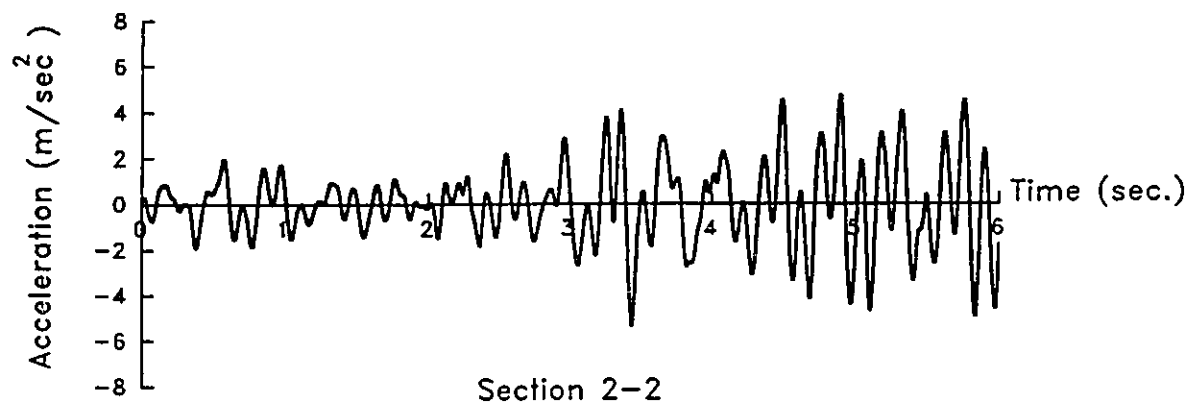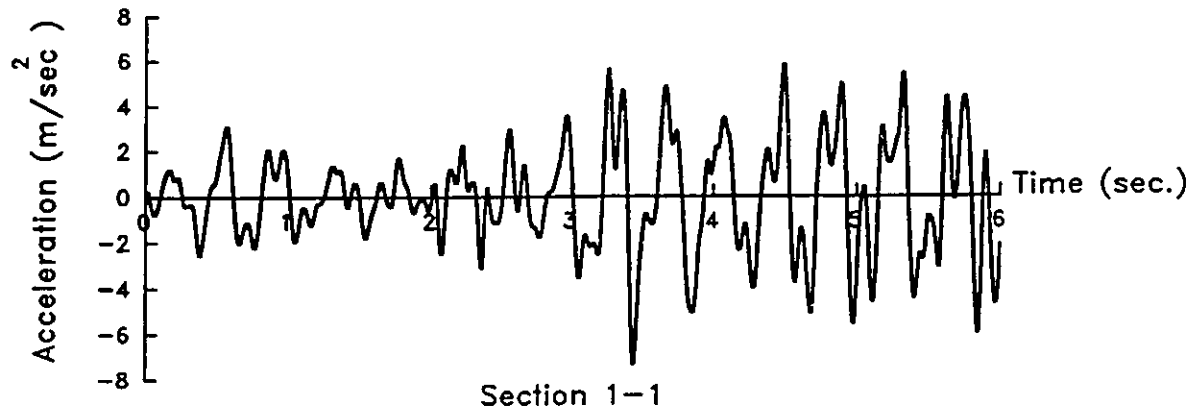
Figure 4.40 Time History of the Relative Vertical Accelerations
at $\theta=180°$ for Tank DT5.
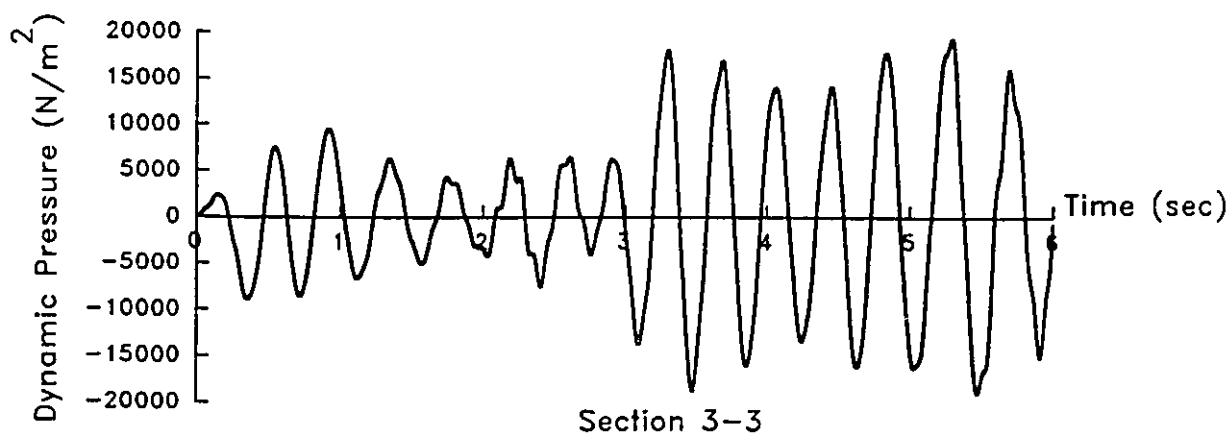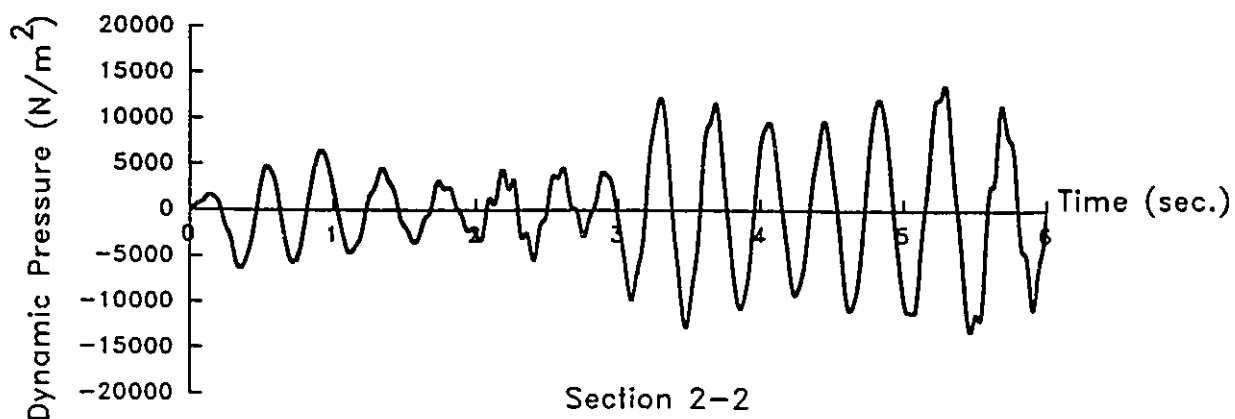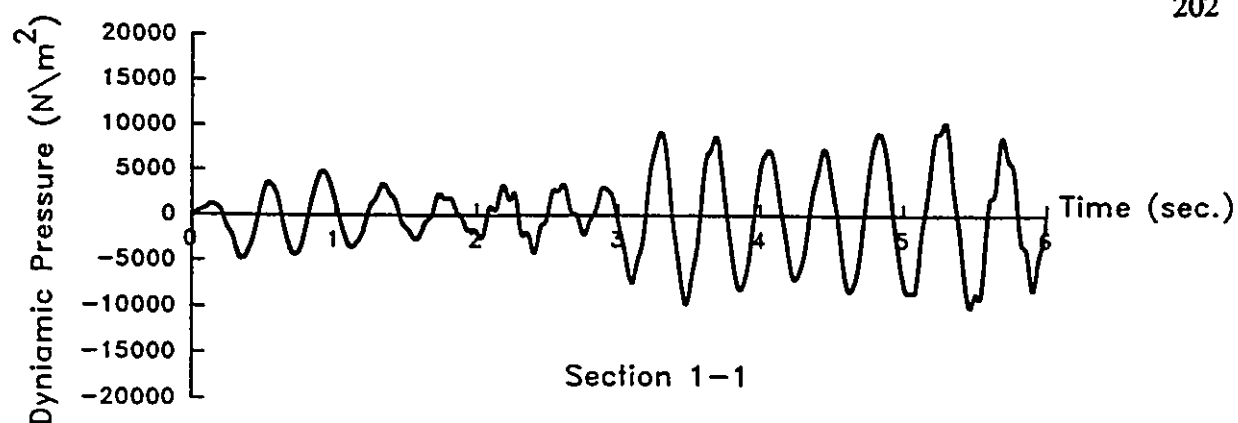
Figure 4.41 Time History of the Dynamic Pressure Resulting from
Horizontal Excitation, for Tank DT5, at $\theta = 180°$.
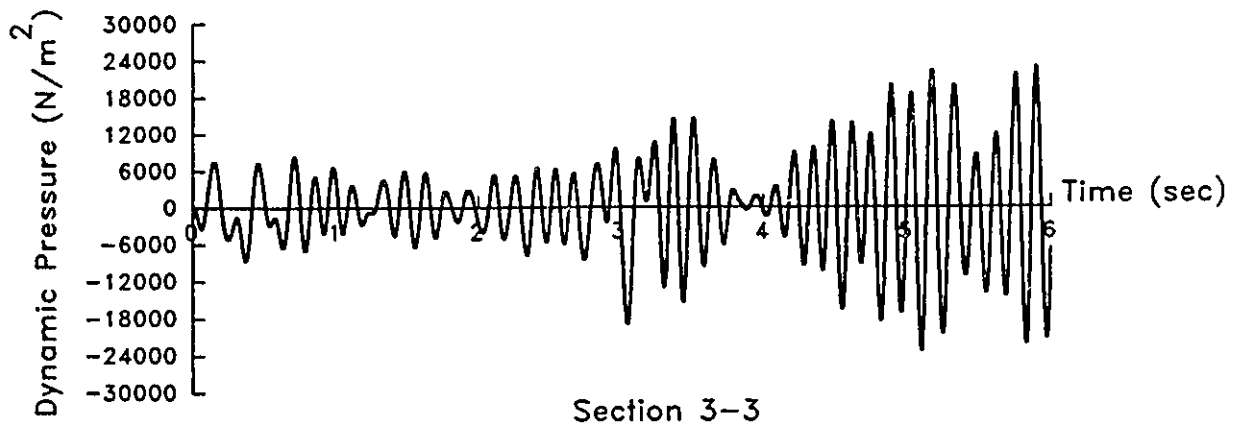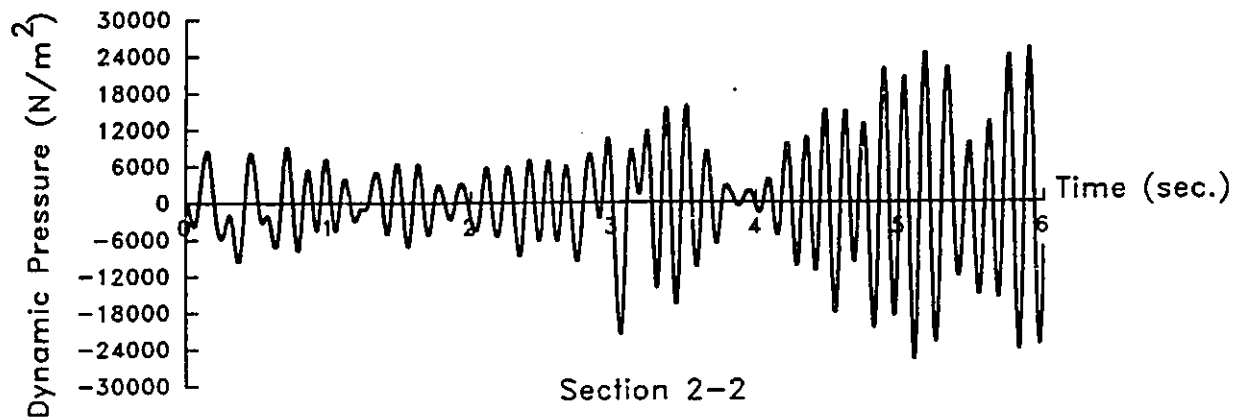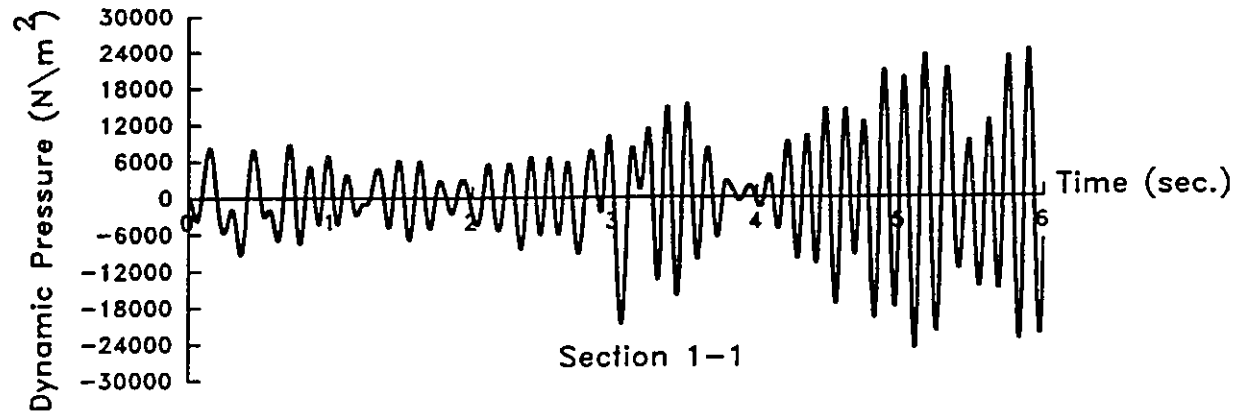
Figure 4.42 Time History of the Dynamic Pressure Resulting from Vertical Excitation, for Tank DT5.
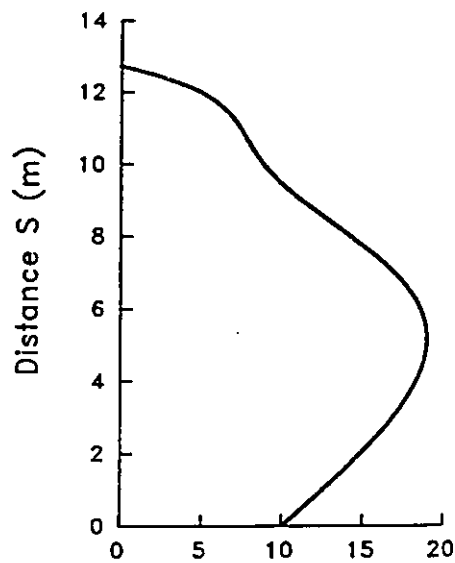
(a) Absolute Dynamic Pressure (KPa)
Due to Horizontal Acceleration
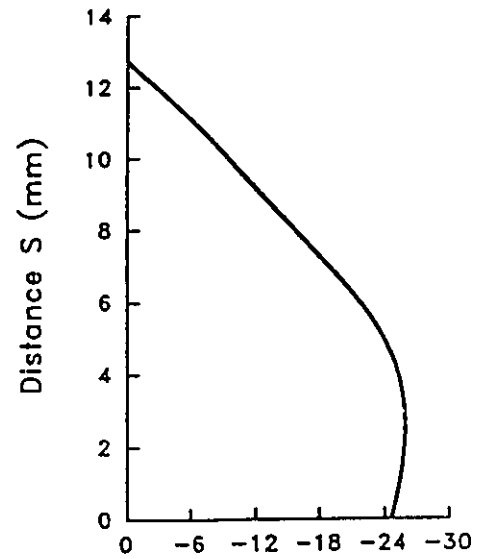
(b) Absolute Dynamic Pressure (KPa)
Due to Vertical Acceleration
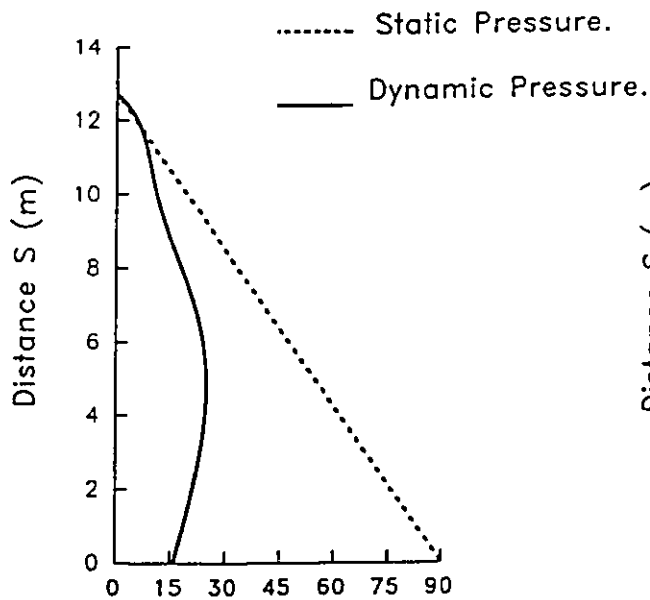
(c) Total Pressure (KPa)
(at T=5.46 sec)
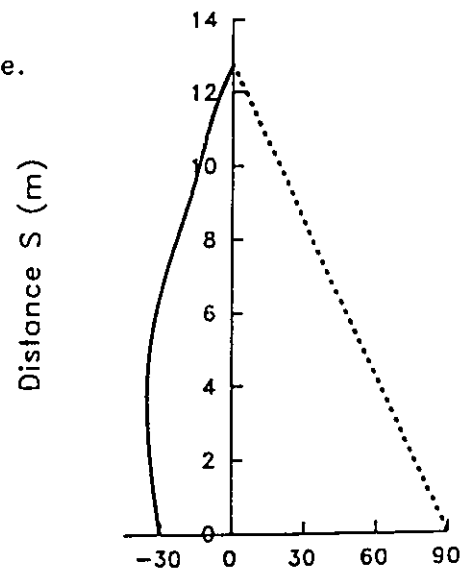
(d) Total Pressre (KPa)
(at T=5.1 sec)

Figure 4.43 Dynamic Pressure Distributions Along the Generator of Tank DT5.
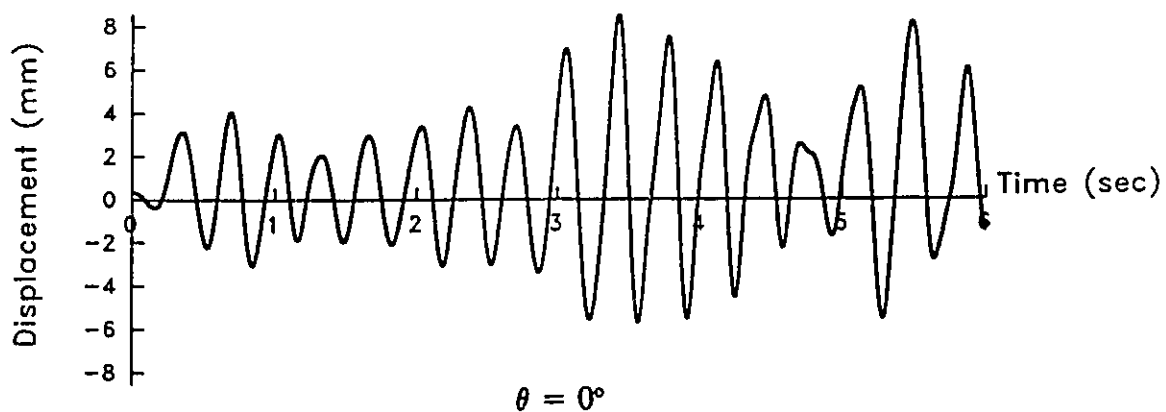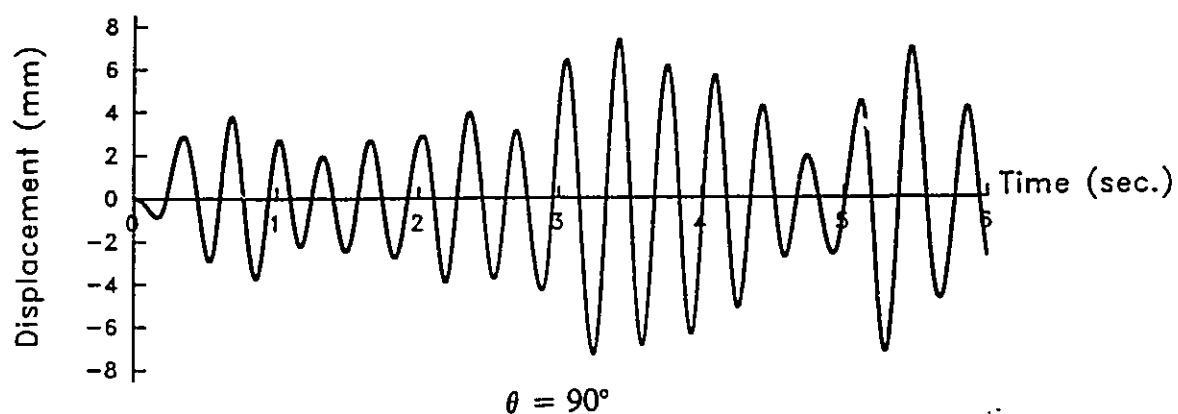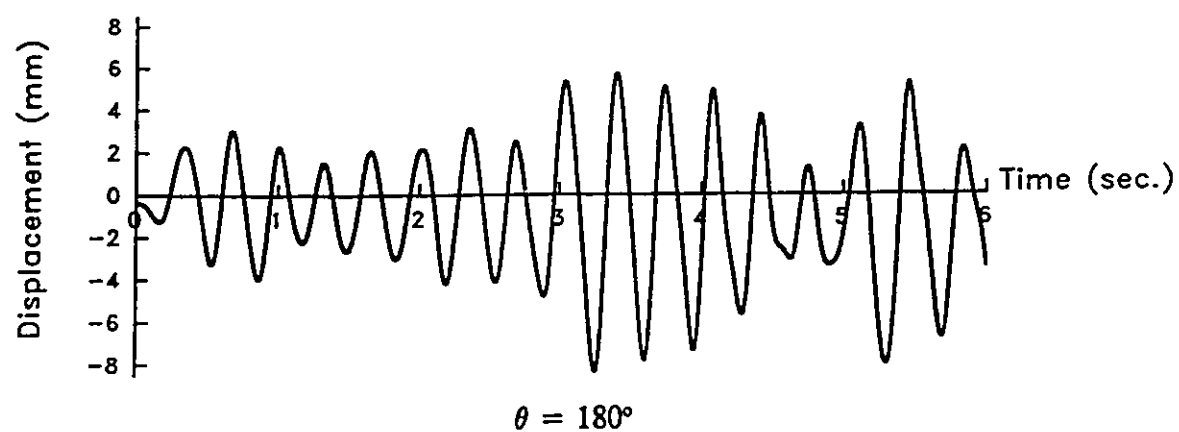
Figure 4.44 Time History of the Relative Displacements Along the X−Axis at Section 1−1 for Tank DB1.
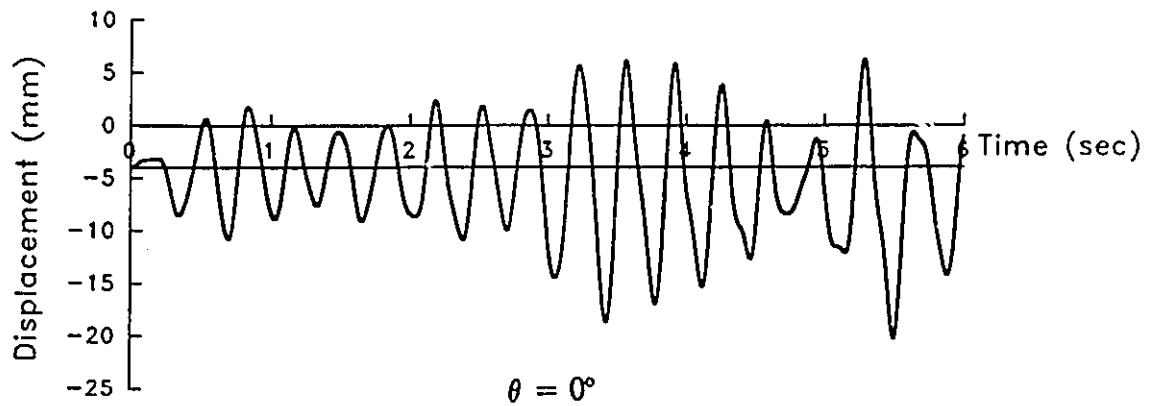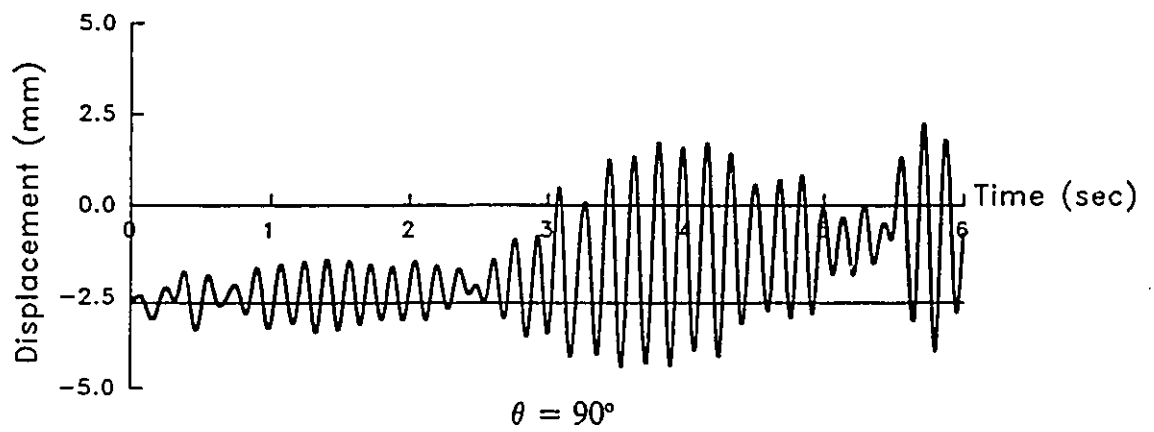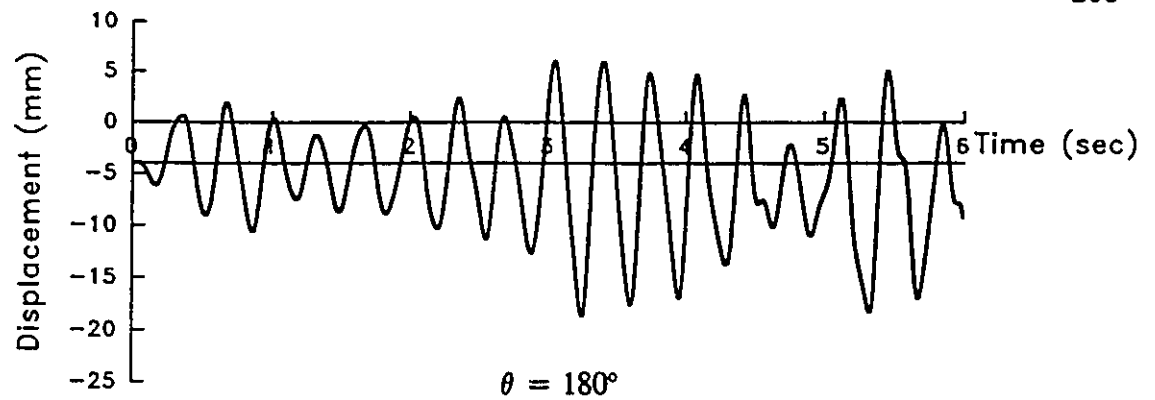
Figure 4.45 Time History of the Relative Vertical Displacements
at Section 1—1 for Tank DB1.
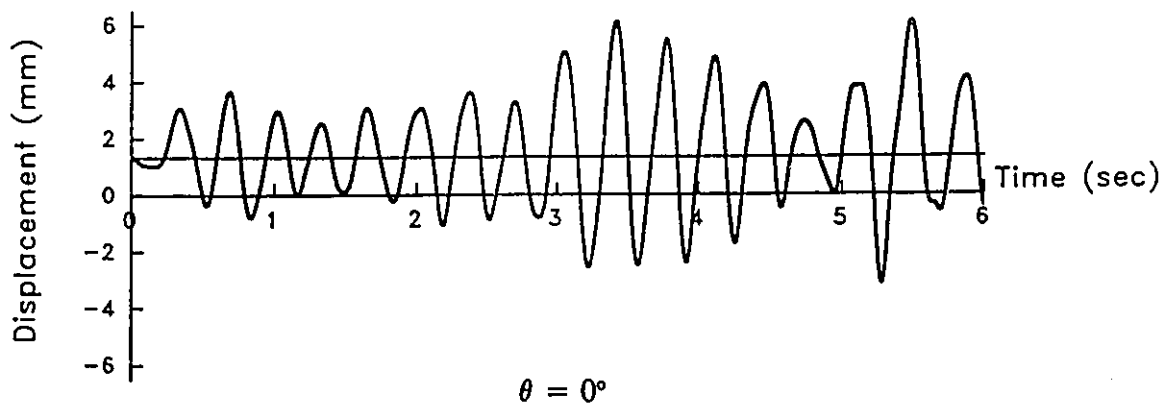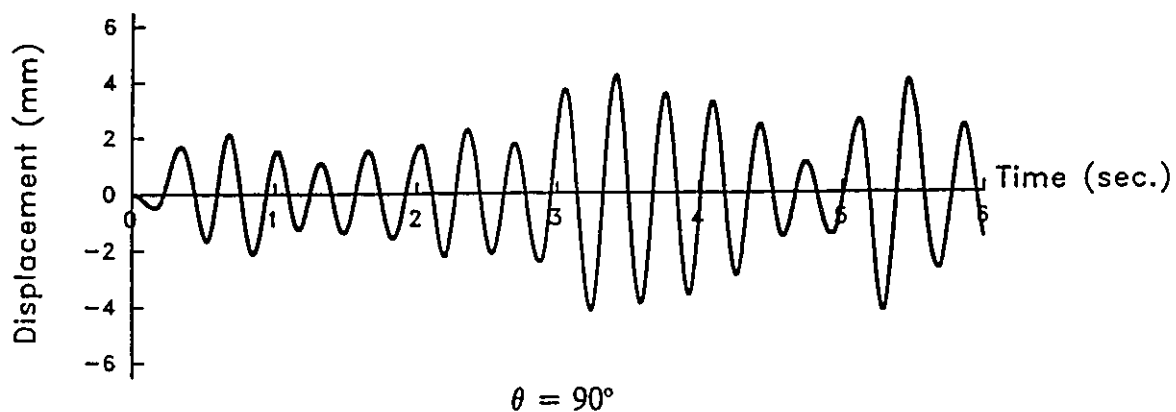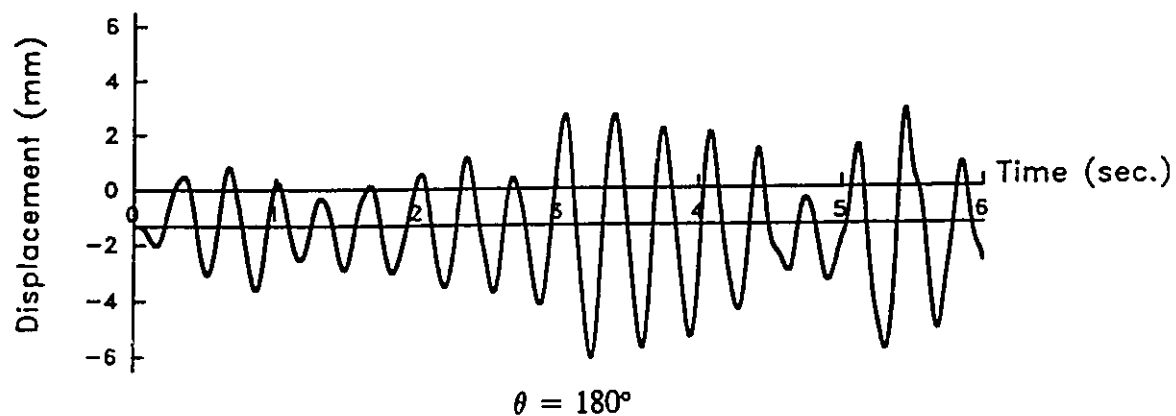
Figure 4.46 Time History of the Relative Displacements Along the X—Axis at Section 2—2 for Tank DB1.
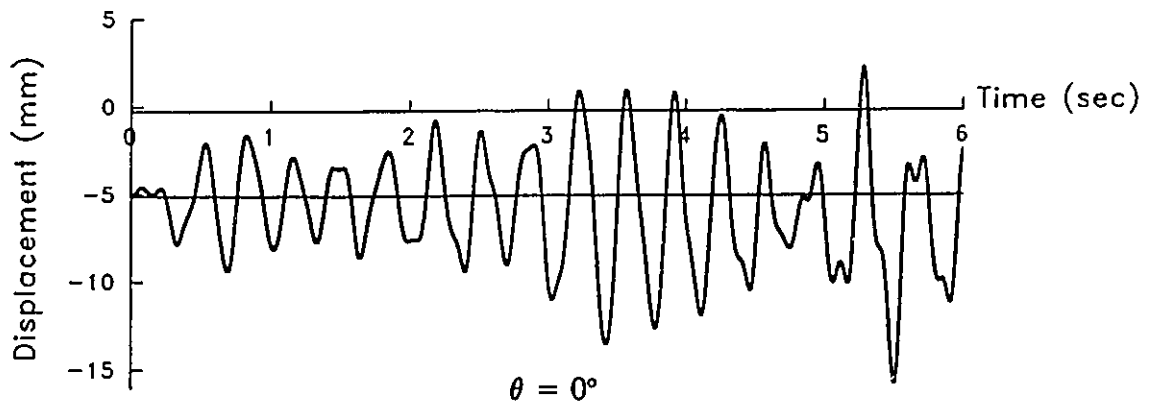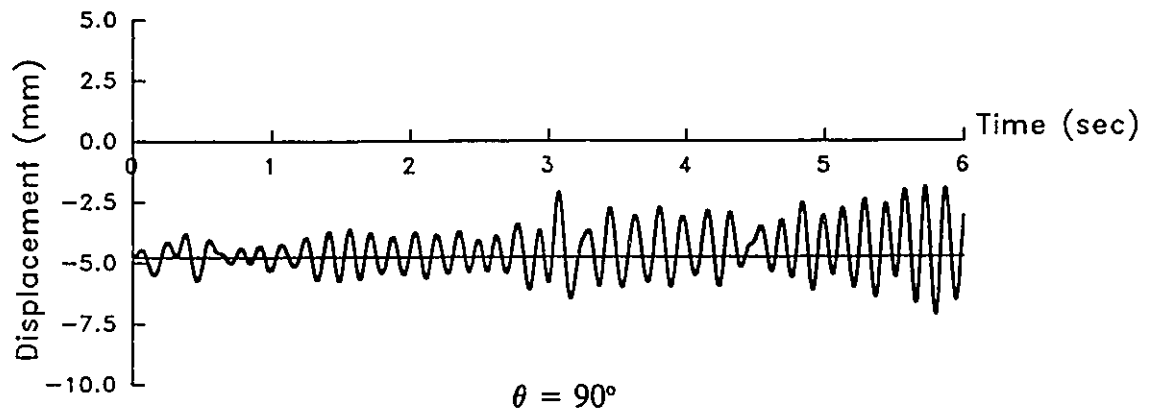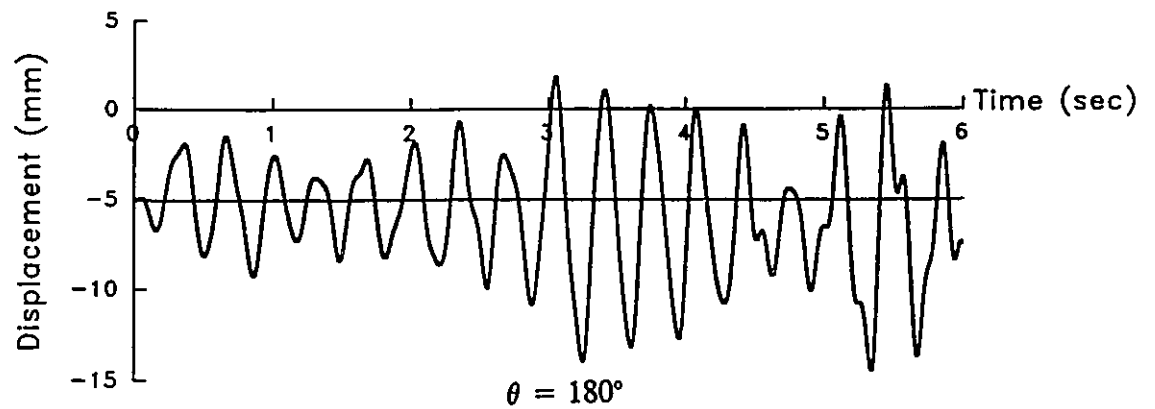
Figure 4.47 Time History of the Relative Vertical Displacements at Section 2-2 for Tank DB1.
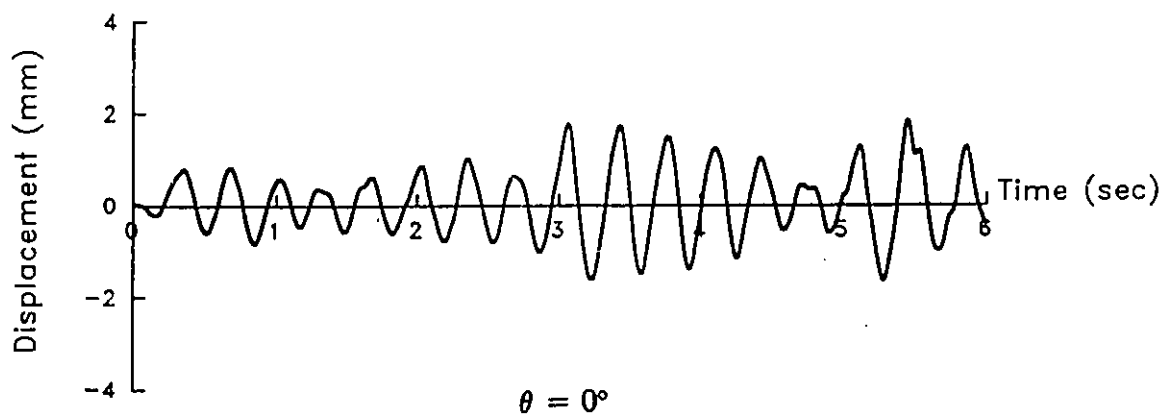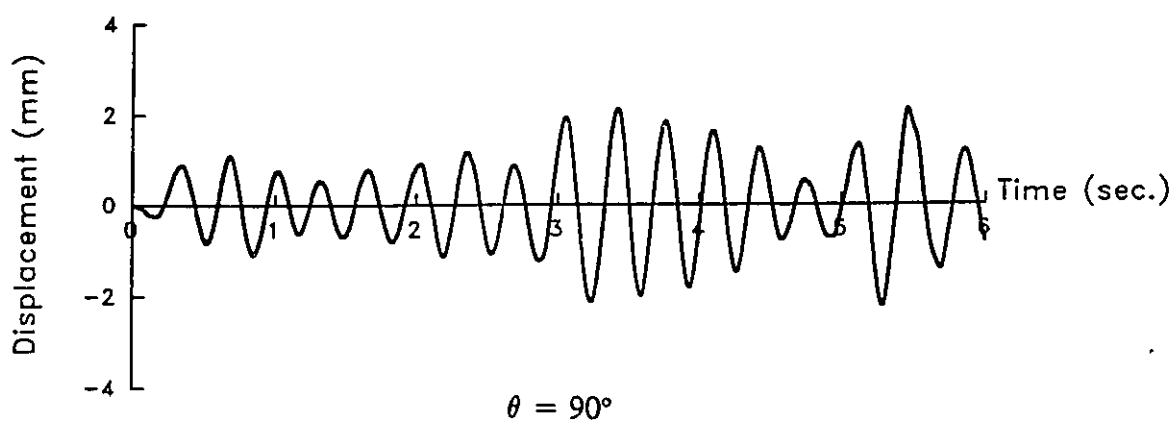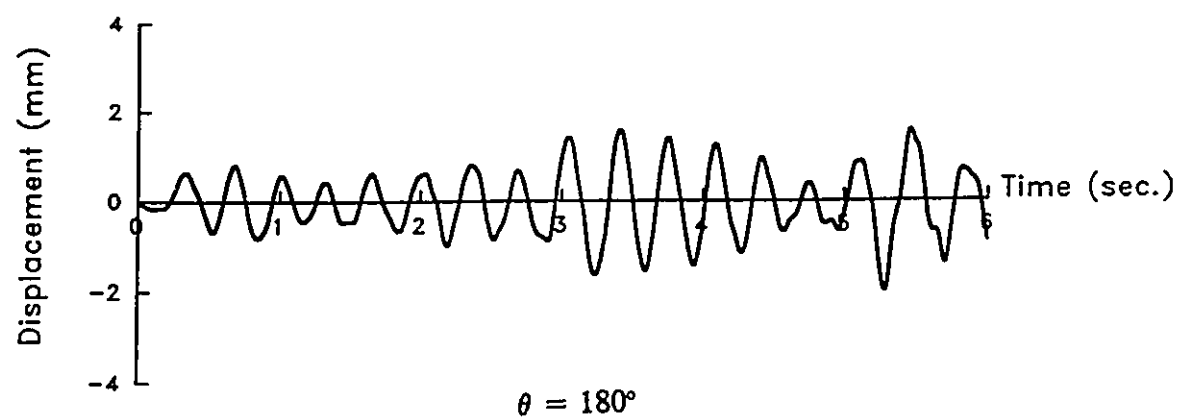
Figure 4.48 Time History of the Relative Displacements Along the X—Axis at Section 3-3 for Tank DB1.
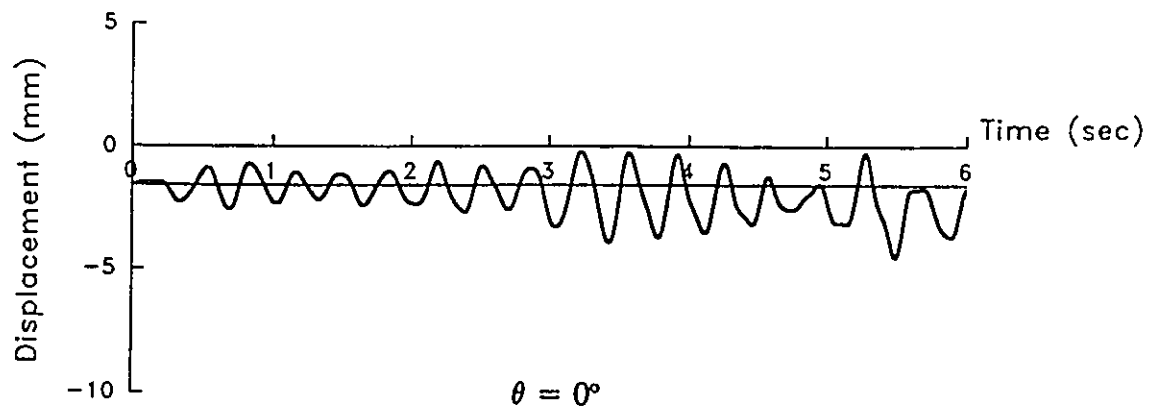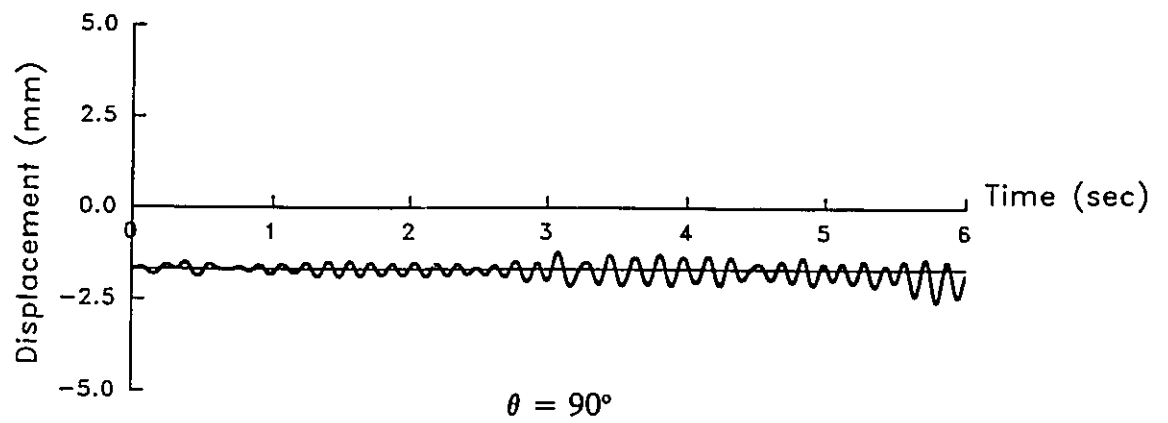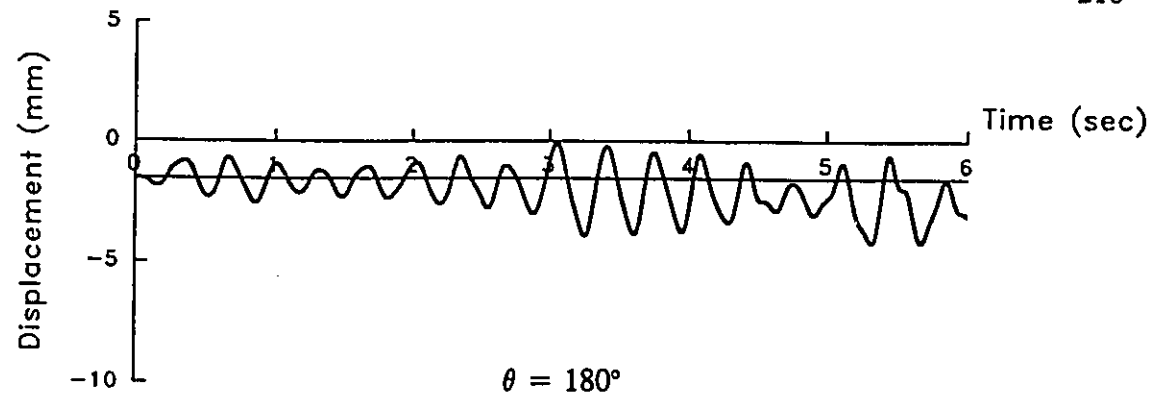
Figure 4.49 Time History of the Relative Vertical Displacements at Section 3-3 for Tank DB1.
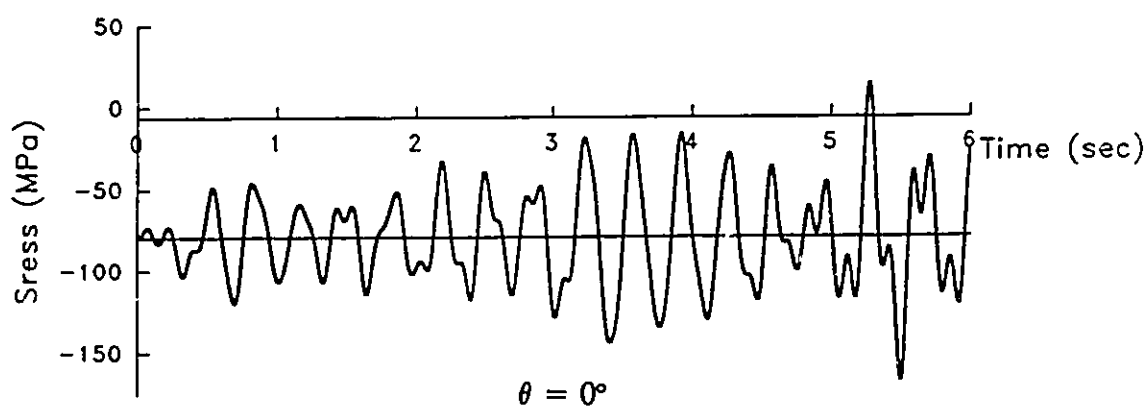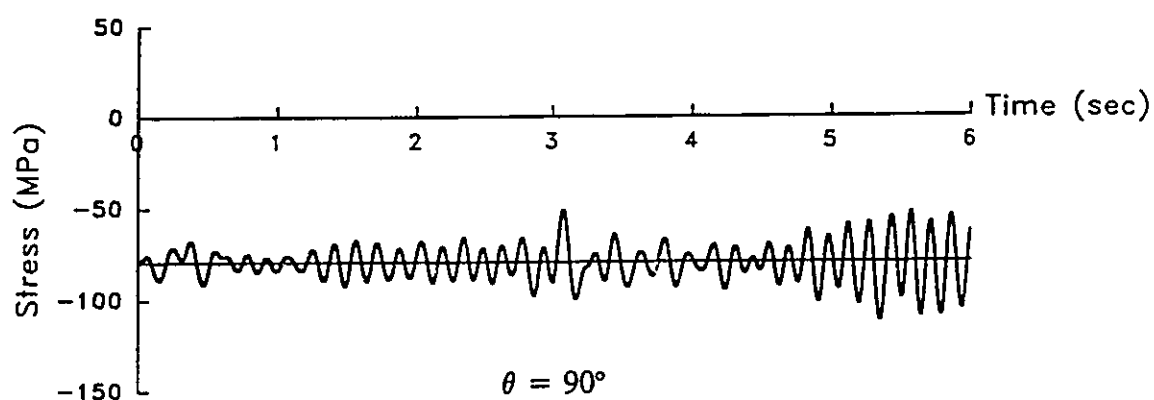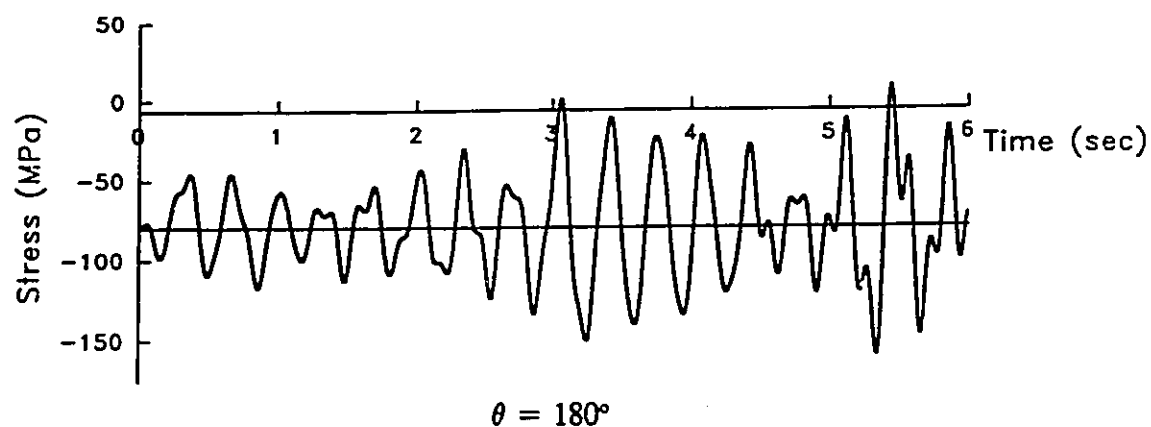
Figure 4.50 Time History of the Meridional Stresses at Section 4—4
for Tank DB1.
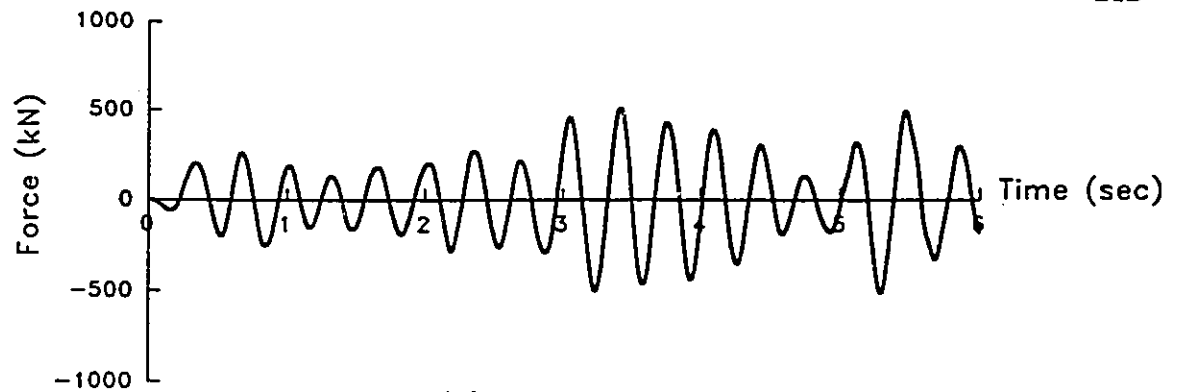
(a) Base shear
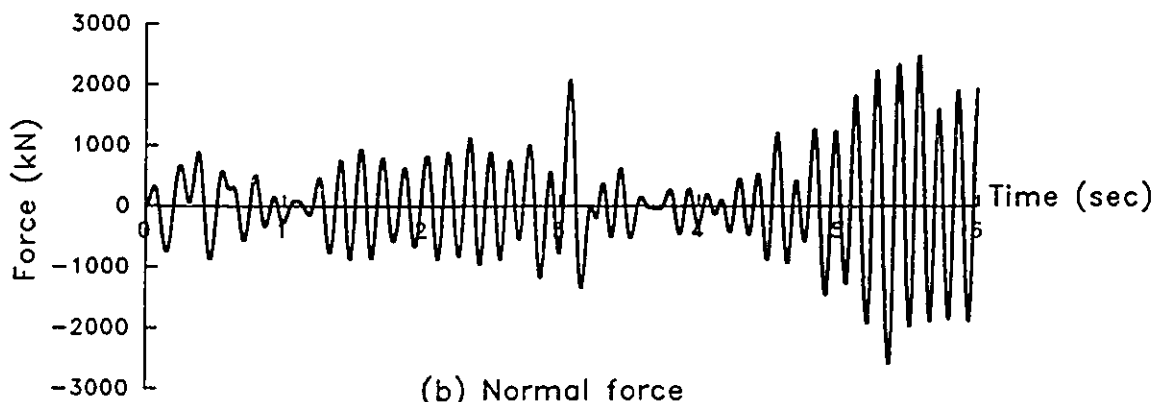
(b) Normal force
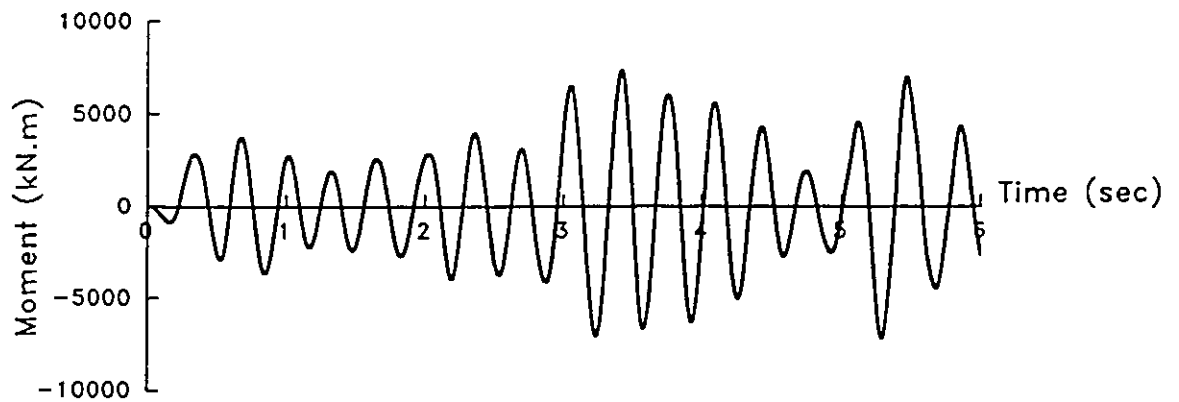
(c) Over turning moment

Figure 4.51 Time History of the Base Reactions at Section 4—4
for Tank DB1.

CHAPTER FIVE

CONCLUSIONS

5-1 Introduction

The research work accomplished and reported in this thesis consists of three parts. The first part involved extension and verification of the consistent shell element to large displacement static and dynamic analyses. The second part focused on the application to solve the problem of inelastic stability of perfect and imperfect hydrostatically loaded elevated conical tanks. The third part of the study involved applications, again to study the inelastic stability of liquid-filled elevated conical tanks, subjected to seismic motion with proper fluid-structure interaction accommodated through the boundary integral method to include the hydrodynamic effect.

5-2 Summary and Conclusions

5-2-1 Consistent Shell Element

The formulation of the consistent shell element is extended to include geometric non-linearities as well as non-linear dynamic analysis. The results of large displacement static and dynamic analyses of a number of plate and shell problems using the consistent shell element are compared with the numerical and experimental results available in the literature. These comparisons reveal superior performance of the consistent shell element in all examples, even with very small number of elements used to model such structures.

Therefore, this modified consistent shell element, which is free from spurious shear modes that exist in the isoparametric shell elements, provides an excellent tool to handle the non-linear static and dynamic analyses of thin and thick plates and shells.

5-2-2 Stability of Hydrostatically Loaded Conical Tanks

The stability investigation of liquid-filled conical vessels under hydrostatic loading is undertaken using the consistent shell element with geometric non-linearities included. Elastic stability analyses of perfect vessels show localized buckling near the bottom of the shell due to the effect of high compressive meridional stresses. The limit or buckling loads are found to be in excellent agreement with the corresponding numerical results available in the literature. The elastic analyses of conical vessels, with different imperfection patterns, indicate that the presence of an axisymmetric imperfection shape leads to the lowest limit load for hydrostatically loaded conical vessels.

By including a strain hardening plasticity model, the inelastic stability analyses reveal that for tanks which have practical dimensions, yielding precedes the elastic stability limit. Therefore, the inelastic behaviour has to be considered when studying the stability of such structures. The effect of the meridional and the hoop residual stresses due to welding is investigated. It is found from the inelastic stability analyses undertaken that the limit load of hydrostatically loaded conical shells is reduced by the presence of hoop residual stresses resulting from circumferential welding. Longitudinal welding has no appreciable effect on the limit loads. A comparison of the results from the inelastic stability analysis of perfect liquid-filled conical tanks with those which have axisymmetric geometric imperfections show significant reduction in capacity. For the case where the

initial displacements are of the order of one thickness, the shell's limit load is reduced by about 35% to 40%. When residual stresses are included, there is a further reduction of 5% to 10%. Comparison of the results of the inelastic stability analyses for the imperfect tanks with those obtained from the experimental investigation carried out by Vandepitte at al. (1982) shows very good agreement in terms of the limit load. Analyses also show that the reduction in the buckling strength due to the presence of the geometric imperfections is more pronounced in a tall tank than in a broad one. Furthermore, the smaller the thickness of a conical tank, the more sensitive is the structural response to geometric imperfections.

Inelastic stability analyses, employing 128 consistent shell elements to model the tank that failed in Fredericton, New Brunswick, are carried out. Two degrees of geometric imperfection are assumed - one having a small amplitude (good cone) and the other with a large amplitude (poor cone). It is found that the load factor for the small imperfection case is about 1.3, whereas the value dropped to 0.9 when the larger imperfection values are used. The larger values used are reasonable estimates of the imperfection states in civil engineering shell structures. Furthermore, an additional 10% reduction can be anticipated when residual stresses are included. Therefore, the author believes that the Fredericton tank, which had a design not complying with the code requirements, was unsafe and would very likely collapse under full tank conditions. A comparison of the limit loads obtained from the analyses above, indicates that the codes recommendations are in general overly conservative. Meanwhile, a comparison with the design formulae given by Vandepitte suggests that they provide a more reasonable margin

of safety.

5-2-3 Stability of Liquid-Filled Conical Tanks Under Seismic Loading

The seismic analysis presented in this thesis represents the first attempt, to the best of author's knowledge, to study the stability of liquid-filled conical tanks under earthquake loading. In this investigation, the consistent shell element is used to model the steel vessel, while the boundary integral method is employed to obtain the impulsive component of the hydrodynamic pressure resulting from the horizontal and the vertical components of an earthquake. The free vibration analyses of a number of liquid-filled cylindrical tanks show very good agreements with the published results, thus, also confirming the accuracy of the boundary integral method.

The towers supporting liquid-filled conical tanks are modelled using horizontal and vertical springs. The free vibration analyses of these elevated tanks indicate that the fundamental modes of vibration arise from the horizontal excitation. Thereafter, the non-linear time history analyses of tall and broad conical tanks, using the horizontal and the vertical components for the San Fernando 1971 earthquake scaled down to meet the code specification for Quebec City, Canada, are carried out. These analyses reveal that, for a number of tall tanks, the inelastic behaviour sets in during the earthquake record. This is followed by localized inelastic buckling near the base of the tank. This dynamic instability state occurs for tall tanks which are designed under a static load factor less than 2.65. Therefore, it can be concluded that the liquid-filled conical tanks, especially the tall superstructures, are very sensitive to seismic loading and must be designed for large static load factors in order to survive strong seismic motion. Meanwhile, the broad

tank, designed for a static load factor of just 1.5, survived the earthquake in spite of an early plastification. The compressive meridional stresses, which are the main cause of instability of conical tanks, are mainly caused by three effects: the horizontal acceleration, the hydrostatic pressure and the vertical acceleration. The numerical results indicate that the largest contribution to these stresses comes from the overturning moment resulting from the horizontal acceleration. The second most important factor is the hydrostatic pressure. However, all three factors are important. The ratio of the maximum meridional stresses resulting from the vertical acceleration to the maximum stresses due to the horizontal acceleration is approximately one to three. Therefore, it is concluded that the vertical acceleration does contribute significantly to the dynamic instability of liquid-filled conical vessels and cannot be ignored in a seismic analysis of such structures.

5-3 Recommendations for Further Research

The consistent shell element model with geometric and material non-linearities, which also includes the geometric imperfections and the residual stresses, can be used to develop charts and/or formulae for the design of water filled conical tanks under hydrostatic loads for possible implementation in the codes for design of such structures. In addition, the static analysis should be extended to study the stability of stiffened liquid-filled conical tanks. To achieve this, a curved beam element compatible with the consistent shell element can be used to model the stiffeners. The analysis formulated in this work can be easily extended to include the effect of the non-axisymmetric imperfections on the dynamic stability of conical tanks to confirm some of the

assumptions used. The model may also be extended to include the effects of the free surface sloshing and the rocking motion of the base of the vessel. The rocking of the base is expected to be significant when studying the dynamic stability of conical vessels resting on cylindrical shafts.

REFERENCES

Ahmad, S., Irons, B., and Zienkiewicz, O.C. 1970, "Analysis of Thick and Thin Shell Structures by Curved Finite Elements.", International Journal for Numerical Methods in Engineering, Vol. 2, pp. 419-451.

Amazigo, J.C., and Budiansky, B. 1972, "Asymptotic Formulas for the Buckling Stresses of Axially Compressed Cylinders with Localized or Random Axisymmetric Imperfections.", ASME, Journal of Applied Mechanics Division, pp. 179-184.

Arbocz, J., Abramovich, H. 1979, "The Initial Imperfection Data Bank of Delft University of Technology.", Part I, Report LR-290, Delft University of Technology, Netherlands.

AWWA 1984. " AWWA Standard for Welded Street Tanks for Water Storage.", AWWA D100-1984, Denver, Colorado.

Balendra, T., Ang, K.K., Paramasivan, P., and Lee, S.L., 1982, "Seismic Design of Flexible Cylindrical Liquid Storage Tanks.", Earthquake Engineering and Structural Dynamics, Vol. 10, pp. 477-496.

Barton, D.C., and Parker, J.V. 1987, "Finite Element Analysis of the Seismic Response of Anchored and Unanchored Liquid Storage Tanks.", Earthquake Engineering and Structural Dynamics, Vol. 15, pp. 299-322.

Bathe, K.J. 1982, "Finite Element Procedures in Engineering Analysis.", Prentice-Hall Inc., Englewood Cliffs, NJ.

Bathe, K.J., Ramm, E., and Wilson, E.L. 1975, "Finite Element Formulations for Large Deformation Dynamic Analysis.", International Journal for Numerical Methods in Engineering, Vol. 9, pp. 353-386.

Belytschko, T., Wong, B.L., and Stolarski, H. 1989, "Assumed Strain Stabilization Procedure for the 9-Node Lagrange Shell Element.", International Journal for Numerical Methods in Engineering, Vol. 28, pp. 385-414.

Bornscheuer, F.W., and Hafner, L. 1983, "The Influence of an Imperfect Circumferential Weld on the Buckling Strength of Axially Loaded Circular Cylindrical Shells.", Prelim. Report, 3rd International Colloqium on Stability of Metal Structures, Paris, pp. 407-414.

219

Bornscheuer, F.W., Ramm, E., and Stegmuller, H. 1883, "Stability and Ultimate Load Analysis of Liquid-Filled Conical Shells.", Prelim. Report, 3rd International Colloqium on Stability of Metal Structures, Paris, pp. 391-398.

Brebbia, C., and Connor, J. 1969, "Geometrically Nonlinear Finite-Element Analysis.", Journal of Eng. Mech. Div. ASCE, Vol. 95, pp. 413-483.

Briassoulis, D. 1988, "The Zero Energy Modes Problem of the Nine-Node Lagrangian Degenerated Shell Element.", Computers and Structures, Vol.30, No.6, pp. 1389-1402.

Chen, W.F., and Han, D.J. 1988, "Plasticity for Structural Engineers.", Springer-Verlag Inc., New York, NY.

Clough, R.W., and Wilson, E.L. 1971, "Dynamic Finite Element Analysis of Arbitrary Thin Shells.", Computers and Structures, Vol. 1, pp. 33-56.

Concrete Design Handbook 1985. Canadian Portland Cement Association, Ottawa, Ontario.

Conners, J.M., 1990, 'City of Fredericton, N.B. Regent Street Tower Reservoir Project.", Design Report.

Crisfield, M.A. 1991, "Non-Linear Finite Element Analysis of Solids and Structures", Vol. 1, John Wiley & Sons.

Daali, M.L., and Korol, R.M. 1994, "Damage Assessment in Locally Stiffened Beams Under Seismic Type of Loading.", Eng. Mech. Symp. , CSCE 94, Vol IV, Winnipeg, Manitoba, pp. 209-214.

Dawe, J.L., Seah, C.K., and Abdel-Zaher, A.K. 1993, "Collapse of a Water Tower.", Proceeding of the CSCE Conference, Fredericton, N.B., Canada, June 8-11, pp. 315-323.

Det Norske Veritas (DNV-CN) 1982, "Buckling Strength Analysis.", Classification Notes, Note No. 30.1, Høvik, Norway, 1982.

Deutscher Ausschuss Fur Stahlbau (DAST) 1980, Cologne, Germany.

Ellinas, C.P., Supple, W.J., and Walker, A.C. 1984, "Buckling of Offshore Structures." Gulf Publishing Company.

Esslinger, M., Geier, B., and Wendt, V. 1984, "Berechnung der Spannungen und Deformationen Von Rotationsschalen im elastoplastichen Bereich.", Der Stahlbau 53, pp.17-25.

European Convention for Constructional Steel Work 1988, "Buckling of Steel Shells.", Fourth Edition, 1988, No. 56, Brussels.

Gilewski, W. and Radwanska, M. 1991, "A Survey of Finite Element Models for the Analysis of Moderately Thick Shells.", Finite Element in Analysis and Design 9, pp. 1-21.

Gjelsvik, A., and Bodner, S.R. 1962, "The Energy Criterion and Snap Buckling of Arches.", Journal of Eng. Mech. Div., ASCE, Vol. 88, pp. 87-134.

Haroun, M.A. 1980, "Dynamic Analyses of Liquid Storage Tanks.", Report No. EERL 80-04, Earthquake Engineering Research Laboratory Report, California Institute of Technology, Pasadenas, CA.

Haroun, M.A., and Ellaithy, H.M. 1985a, "Model for Flexible Tanks Undergoing Rocking.", Journal of Engineering Mechanics, ASCE, Vol. III, No. 2, pp. 143-157.

Haroun, M.A., and Ellaithy, H.M. 1985b, "Seismically Induced Fluid Forces on Elevated Tanks.", Journal of Technical Topics in Civil Engineering, Vol III, No.1, pp. 1-15.

Haroun, M.A., and Housner, G.W. 1981, "Seismic Design of Liquid Storage Tanks.", Journal of the Technical Councils of ASCE, Vol. 107, No. TC1, pp. 191-207.

Haroun, M.A., and Tayel, M.A. 1985a, "Axisymmetrical Vibrations of Tanks - Analytical.", Journal of Eng. Mech. Div. , ASCE, III, pp. 346-358.

Haroun, M.A., and Tayel, M.A. 1985b, "Axisymmetrical Vibrations of Tanks - Numerical.", Journal of Eng. Mech. Div., ASCE, III, pp. 329-345.

Haroun, M.A., and Tayel, M.A. 1985c, "Response of Tanks to Vertical Seismic Excitations.", Earthquake Engineering and Structural Dynamics, Vol. 13, pp. 583-595.

Hinton, E., and Owen, D.R.J. 1977, "Finite Element Programming.", Academic Press Inc., London.

Housner, G.W. 1957, "Dynamic Pressures on Accelerated Fluid Containers.". Bull. Seism. Soc. Am. 47, pp. 15-35.

Hutchison, J.W., Tennyson, R.C., and Muggeridge, D.B. 1971, "Effect of a Local Axisymmetric Imperfectrion on the Buckling Behavior of a Circular Cylindrical Shell under Axial Compression.", AIAA, Vol. 9, No. 1, pp. 48-52.

Irons, B.M. 1970, "A Frontal Solution Program.", International Journal for Numerical Methods in Engineering, Vol. 2, pp. 5-32.

Koitter, W.T. 1963, "The Effect of Axisymmetric Imperfections on the Buckling of Cylindrical Shells under Axial Compression.", TR 6-90-63-86, Lockheed Missiles and space Cooperation.

Korol, R.M. 1991, "An Assessment of Fredericton's Regent Steel Tower Reservoir Failure.", Technical Report, McMaster University, Hamilton, Canada.

Koziey, B. 1993, "Formulation and Applications of Consistent Shell and Beam Elements.", Ph.D.Thesis, McMaster University, Hamilton, Ontario, Canada.

Lin, T.H., Lin, S.R., and Mazelsky, B. 1972, "Elastoplastic Bending of Rectangular Plates with Large Deflection.", ASME, Applied Mechanics Division, Vol. 39, pp. 978-982.

Liu, W.K., Chen, Y. J., Tsukimori, K., and Uras, R.A. 1991, "Recent Advances in Dynamic Buckling Analysis of Liquid-Filled Shells.", Journal of Pressure Vessel Technology, Vol. 113, pp. 314-320.

Liu, W.K., and Uras, R.A. 1989a, "Transient Failure Analysis of Liquid-Filled Shells Part I: Theory", Nuclear Engineering and Design, Vol. 117, pp. 107-140.

Liu, W.K., and Uras, R.A. 1989b, "Transient Failure Analysis of Liquid-Filled Shells Part II: Applications", Nuclear Engineering and Design, Vol. 117, pp. 141-157.

Mackerle, J. 1993, "Finite and Boundary Element Analyses of Shells - A Bibliography (1990-1992).", Finite Element in Analysis and Design, Vol. 14, pp. 73-83.

Mallet, R.H., and Berlee, L. 1966, "Automated Method for the Large Deflection and Instability Analysis of 3-Dimensional Truss and Frame Assemblies.", AFF DL-TR-66-102.

Manos, G., and Clough, R.W. 1985, "Tank Damage During the May 1983 Coalinga Earthquake.", Earthquake Engineering and Structural Dynamics, Vol. 13, pp. 449-466.

Manos, G., Shibata, H., and Shigeta, T. 1989, "Correlation of Cylindrical Tank Wall Buckling with an Earthquake Motion Recorded at a Small Distance from the Tank.",

Earthquake Engineering and Structural Dynamics, Vol. 18, pp. 169-184.

Mindlin, R.D. 1951, "Influence of Rotary Ineitia and Shear Deformation on Flexural Motion of Isotropic Elastic Plates.", ASME Journal of Applied Mechanics, Vol. 18, pp. 31-38.

National Building Code of Canada. 1990 (NBCC 1990), National Research Council of Canada, Ottawa, Ontario.

Naumoski, N., Tso, W.K., and Hei de brecht, A.C., 1988, "A Selection of Representative Strong Motion Earthquake Records Having Different A/V Ratio.", Earthquake Engineering Group, McMaster University, Hamilton, Ontario, EERG, Report 88-01.

Niwa, A., and Clough, R.W. 1982, "Buckling of Cylindrical Liquid-Storage Tanks Under Earthquake Loading.", Earthquake Engineering and Structural Dynamics, Vol. 10, pp. 107-122.

Ostrowski, P. 1984, "Finite Element Modelling of Single Chord RHS Gap K-Joint.", Ph.D Thesis, McMaster University, Hamilton, Ontario, Canada.

Parish, H. 1979, "A Critical Survey of the 9-Node Degenerated Shell Element with Special Emphasis on Thin Shell Application and Reduced Integration.", Computer Methods in Applied Mechanics and Engineering, Vol. 20, pp.323-350.

Rotter, M., and Teng, J. 1989, "Elastic Stability of Cylindrical Shells with Weld Depressions.", Journal of Structural Engineering, ASCE, Vol. 115, No. 5, pp. 1244-1263.

Saigal, S. and Yang, T.Y. 1985, "Nonlinear Dynamic Analysis with a 48 D.O.F. Curved Thin Shell Element.", International Journal for Numerical Methods in Engineering, Vol. 21, pp. 1115-1128.

Seide, P., Weingarten, V.I., and Morgan, E.J. 1965, "Elastic Stability of Thin-Walled Cylindrical and Conical Shells Under Combined Internal Pressure and Axial Compression.", AIAA, pp. 1118-1125.

Singer, J., Abramovich, H., and Yaffe, R. 1978, "Initial Imperfection Measurements of Integrally Stringer-Stiffened Shells.", TAE Report No. 330, Technion, Haifa, Israel.

Vandepitte, D. 1992, "Report About the Failure of a Water Tower, Fredericton, New Brunswick.", Technical Report, Ghent University, Belgium.

Vandepitte, D., Rathe, J., Verhegghe, B., Paridaens, R. and Verschaeve, C. 1982, "Experimental Investigation of Hydrostatically Loaded Conical Shells and Practical Evaluation of the Buckling Load.", Proceeding of a State-of the-Art Colloquium, Universitat Stuttgart, Germany, pp. 375-399.

Van Impe, I.R. 1992, "Water Tower of Fredericton, New Brunswick-Canada, Numerical Buckling Analysis.", Report No. LMO-91-1001, Laboratory for Research on Models, ghent University, Belgium.

Veletsos, A.S. 1974, "Seismic Effects in Flexible Liquid Storage Tanks.", Proc. 5th World Conf. Earthquake Eng., Roma, Italy, pp. 630-639.

Vu-Quoc, L., and Mora, J.A., 1989. "A Class of Simple and Efficient Degenerated Shell Elements - Analysis of Global Spurious - Mode Filtering.", Computer Method in Applied Mechanics and Engineering, Vol. 74, pp. 117-175.

Zeinkiewicz, O.C., Taylor, R.L., and Too, J.M. 1971, "Reduced Integration Technique in General Analysis of Plates and Shells.", International Journal for Numerical Methods in Engineering, Vol. 3, pp. 275-290.

Zhou, M., Zheng,S., and Zhang, W. 1992, "Study on Elephant-Foot Buckling of Broad Liquid Storage Tanks by Nonlinear Theory of Shells.", Computers & Structures, Vol. 44, pp. 783-788.

APPENDIX A

INTERPOLATION FUNCTIONS FOR CONSISTENT

SHELL ELEMENT

Quadratic Interpolation Functions:

$$N_1(L_1,L_2,L_3) = L_1(2L_1-1) \qquad N_2(L_1,L_2,L_3) = L_2(2L_2-1)$$

$$N_3(L_1,L_2,L_3) = L_3(2L_3-1) \qquad N_4(L_1,L_2,L_3) = 0$$

$$N_5(L_1,L_2,L_3) = 4L_1L_2 \qquad N_6(L_1,L_2,L_3) = 0$$

$$N_7(L_1,L_2,L_3) = 0 \qquad N_8(L_1,L_2,L_3) = 4L_2L_3 \qquad\qquad \text{(A.1 a-m)}$$

$$N_9(L_1,L_2,L_3) = 0 \qquad N_{10}(L_1,L_2,L_3) = 0$$

$$N_{11}(L_1,L_2,L_3) = 4L_1L_3 \qquad N_{12}(L_1,L_2,L_3) = 0$$

$$N_{13}(L_1,L_2,L_3) = 0$$

Cubic Interpolation Functions:

$$\bar{N}_1(L_1,L_2,L_3) = \tfrac{1}{2}L_1(3L_1-1)(3L_1-2) \qquad \bar{N}_2(L_1,L_2,L_3) = \tfrac{1}{2}L_2(3L_2-1)(3L_2-2)$$

$$\bar{N}_3(L_1,L_2,L_3) = \tfrac{1}{2}L_3(3L_3-1)(3L_3-2) \qquad \bar{N}_4(L_1,L_2,L_3) = 9\{\tfrac{1}{2}L_1L_2(3L_1-1)\}$$

$$\bar{N}_5(L_1,L_2,L_3) = 0 \qquad \bar{N}_6(L_1,L_2,L_3) = 9\{\tfrac{1}{2}L_1L_2(3L_2-1)\}$$

$$\bar{N}_7(L_1,L_2,L_3) = 9\{\tfrac{1}{2}L_2L_3(3L_2-1)\} \qquad \bar{N}_8(L_1,L_2,L_3) = 0 \qquad\qquad \text{(A.2 a-m)}$$

$$\bar{N}_9(L_1,L_2,L_3) = 9\{\tfrac{1}{2}L_2L_3(3L_3-1)\} \qquad \bar{N}_{10}(L_1,L_2,L_3) = 9\{\tfrac{1}{2}L_3L_1(3L_3-1)\}$$

$$\bar{N}_{11}(L_1,L_2,L_3) = 0 \qquad \bar{N}_{12}(L_1,L_2,L_3) = 9\{\tfrac{1}{2}L_1L_3(3L_1-1)\}$$

$$\bar{N}_{11}(L_1,L_2,L_3) = 27L_1L_2L_3$$

APPENDIX B

DERIVATION OF THROUGH THICKNESS

INTERPOLATION FUNCTION M_2

Rotation ϕ is allowed to vary quadratically through the thickness and is approximated by

$$\phi(\bar{z}) = a + b\bar{z} + c\bar{z}^2 \tag{B.1}$$

where $\bar{z}$ is the dimensional coordinate in the thickness direction and a, b and c are constants, yet to be determined. The inplane displacement u_ϕ, due to ϕ can be calculated by

$$u_\phi(\bar{z}) = \int \phi(\bar{z}) \, d\bar{z}. \tag{B.2}$$

Substituting $\phi(\bar{z})$ given by Equation B.1, into Equation B.2 and integrating yields

$$u_\phi(\bar{z}) = a\bar{z} + \frac{b\bar{z}^2}{2} + \frac{c\bar{z}^3}{3} + d. \tag{B.3}$$

The boundary conditions used for determining the constants above are as follow:

$$u_\phi(\frac{h}{2}) = 0 \qquad u_\phi(-\frac{h}{2}) = 0 \qquad u_\phi(0) = 0 \qquad \phi(0) = \phi_i \tag{B.4,a-d}$$

where ϕ_i is the additional rotational degree of freedom used in the consistent shell element. The use of the boundary conditions above when applied to the expression for

226

u and ϕ (Equations B.1 and B.3), respectively gives the following four equations for the unknowns:

$$a \frac{h}{2} + b \frac{h^2}{8} + c \frac{h^3}{24} + d = 0$$

$$-a \frac{h}{2} + b \frac{h^2}{8} - c \frac{h^3}{24} + d = 0 \qquad \text{(B.5,a-d)}$$

$$d = 0 \qquad a = \phi_i.$$

Hence, the constants a, b, c and d can be solved for, to give the following values:

$$a = \phi_i \qquad b = 0 \qquad c = -\frac{12}{h^2} \qquad d = 0. \qquad \text{(B.6,a-d)}$$

The constants above are then substituted into the approximations for ϕ and u_ϕ in Equation B.1 and Equation B.3, respectively, to give the following:

$$\phi(\overline{z}) = [1 - \frac{12}{h^2} \overline{z}^2] \phi_i.$$

$$u_\phi(\overline{z}) = [\overline{z} - \frac{4}{h^2} \overline{z}^3] \phi_i \qquad \text{(B.7,a-b)}$$

At the same time, the non-dimensional coordinate t and the dimensional coordinate z are related by

$$\overline{z} = \frac{h \, t}{2} \qquad \text{(B.8)}$$

which allows re-writing Equations B.7 in terms of t as

$$\phi(t) = (1 - 3t^2) \phi_i$$

$$u_\phi(t) = \frac{ht}{2}(1 - t^2) \phi_i = M_2 \phi_i.$$ (B.9,a-b)

The through thickness interpolation function M_2 yields the displacement variation across the thickness due to rotation ϕ.

APPENDIX C

CONSTRUCTION OF ORTHOGONAL BASIS

The Jacobian matrix can be written as

$$[J] = \left\{ \begin{array}{c} \underline{R} \\ \underline{S} \\ \underline{T} \end{array} \right\} \qquad (C.1)$$

where the vectors $\underline{R}$ and $\underline{S}$ are tangent to the surface defined by t = constant . A normal vector $\underline{V}_3$ to this surface can be obtained by applying the following cross product:

$$\underline{V}_3 = \underline{R} * \underline{S} \qquad (C.2)$$

The other two vectors $\underline{V}_1$ and $\underline{V}_2$ of the orthogonal basis are obtained from the following equations:

$$\underline{V}_2 = \underline{j} * \underline{V}_3 \qquad (C.3)$$

$$\underline{V}_1 = \underline{V}_2 * \underline{V}_3 \qquad (C.4)$$

where j is the unit vector along the global y-axis. It should be mentioned here that in case that the vector $\underline{V}_3$ is parallel to the global y-axis , the unit vector $\underline{k}$ along the z axis can be used instead of j in Equation C.3.

The normalization of the vectors $\underline{V}_1$, $\underline{V}_2$ and $\underline{V}_3$ then leads to the unit vectors $\underline{v}_1$, $\underline{v}_2$ and $\underline{v}_3$ which can be used in the transformation matrix as follows:

229

$$[\theta] = \begin{Bmatrix} \underline{v}_1 \\ \underline{v}_2 \\ \underline{v}_3 \end{Bmatrix} = \begin{matrix} x' \\ y' \\ z' \end{matrix} \begin{matrix} x & y & z \\ \begin{bmatrix} l_{11} & l_{12} & l_{13} \\ l_{21} & l_{22} & l_{23} \\ l_{31} & l_{32} & l_{33} \end{bmatrix} \end{matrix} \qquad (C.5)$$

APPENDIX D1

STRESS MATRIX AND VECTORS FOR THE

SHELL ELEMENT FORMULATION

$$
[S^{T(k-1)}]_{9 \times 9} =
\begin{bmatrix}
S_{x'x'}^{T(k-1)} & 0 & 0 & S_{x'y'}^{T(k-1)} & 0 & 0 & S_{x'z'}^{T(k-1)} & 0 & 0 \\
0 & S_{x'x'}^{T(k-1)} & 0 & 0 & S_{x'y'}^{T(k-1)} & 0 & 0 & S_{x'z'}^{T(k-1)} & 0 \\
0 & 0 & S_{x'x'}^{T(k-1)} & 0 & 0 & S_{x'y'}^{T(k-1)} & 0 & 0 & S_{x'z'}^{T(k-1)} \\
S_{x'y'}^{T(k-1)} & 0 & 0 & S_{y'y'}^{T(k-1)} & 0 & 0 & S_{y'z'}^{T(k-1)} & 0 & 0 \\
0 & S_{x'y'}^{T(k-1)} & 0 & 0 & S_{y'y'}^{T(k-1)} & 0 & 0 & S_{y'z'}^{T(k-1)} & 0 \\
0 & 0 & S_{x'y'}^{T(k-1)} & 0 & 0 & S_{y'y'}^{T(k-1)} & 0 & 0 & S_{y'z'}^{T(k-1)} \\
S_{x'z'}^{T(k-1)} & 0 & 0 & S_{y'z'}^{T(k-1)} & 0 & 0 & 0 & 0 & 0 \\
0 & S_{x'z'}^{T(k-1)} & 0 & 0 & S_{y'z'}^{T(k-1)} & 0 & 0 & 0 & 0 \\
0 & 0 & S_{x'z'}^{T(k-1)} & 0 & 0 & S_{y'z'}^{T(k-1)} & 0 & 0 & 0
\end{bmatrix}
$$

(D1.1)

$$
\{S^{T(k-1)}\}^{TRANS} = \left\{ S_{x'x'}^{T(k-1)} \quad S_{y'y'}^{T(k-1)} \quad S_{x'y'}^{T(k-1)} \quad S_{x'z'}^{T(k-1)} \quad S_{y'z'}^{T(k-1)} \right\}
$$

(D1.2)

$$
\{\Delta S\}^{TRANS} = \{ \Delta S_{x'x'} \quad \Delta S_{y'y'} \quad \Delta S_{x'y'} \quad \Delta S_{x'z'} \quad \Delta S_{y'z'} \}
$$

(D1.3)

APPENDIX D2

PLASTIC CONSTITUTIVE MATRIX FOR

STRAIN HARDENING MATERIALS

The inelastic constitutive matrix for isotropic strain hardening material used in a shell element formulation is of the following form.

$$[D'_p] = \frac{1}{H} \begin{bmatrix} \overline{S}^2_{x'x'} & & & & \text{Symmetry} \\ \overline{S}_{y'y'}\overline{S}_{x'x'} & \overline{S}^2_{y'y'} & & & \\ \overline{S}_{x'y'}\overline{S}_{x'x'} & \overline{S}_{x'y'}\overline{S}_{y'y'} & \overline{S}^2_{x'y'} & & \\ \overline{S}_{z'x'}\overline{S}_{x'x'} & \overline{S}_{z'x'}\overline{S}_{y'y'} & \overline{S}_{z'x'}\overline{S}_{x'y'} & \overline{S}^2_{z'x'} & \\ S_{y'z'}S_{x'x'} & S_{y'z'}S_{y'y'} & S_{y'z'}S_{x'y'} & S_{y'z'}S_{z'x'} & S^2_{y'z'} \end{bmatrix} \tag{D2.1}$$

The parameter H is obtained from the following set of equations:

$$H = \frac{h}{36\,G^2} \tag{D2.2}$$

$$h = 4\,(3\,G + H_p)\,\sigma_e^2 \tag{D2.3}$$

$$H_p = \frac{E_T E}{E - E_T} \tag{D2.4}$$

where E, E_T and G are the elastic, the tangential and the shear modulii, respectively, and σ_e is as given in Section 2.6.

APPENDIX E

[B$_L$] AND [B$_S$] MATRICES

In order to obtain expressions for the matrices [B$_L$] AND [B$_S$] which can be easily

coded for a computer program, the components of these matrices are related to the

components of two other matrices [B$_{01}$] and [B$_{02}$] which are as follows:

$$[B_{01}]_{5 \cdot 91} = \sum_{n=1}^{13} \begin{bmatrix} l_{11}h_{n,1} & l_{12}h_{n,1} & l_{13}h_{n,1} & C_n^{11}H_n^1 & -C_n^{12}H_n^1 & C_n^{11}G_n^1 & -C_n^{12}G_n^1 \\ l_{21}h_{n,2} & l_{22}h_{n,2} & l_{23}h_{n,2} & C_n^{21}H_n^2 & -C_n^{22}H_n^2 & C_n^{21}G_n^2 & -C_n^{22}G_n^2 \\ l_{11}h_{n,2} & l_{12}h_{n,2} & l_{13}h_{n,2} & C_n^{11}H_n^2 & -C_n^{12}H_n^2 & C_n^{11}G_n^2 & -C_n^{12}G_n^2 \\ l_{11}h_{n,3} & l_{12}h_{n,3} & l_{13}h_{n,3} & C_n^{11}H_n^3 & -C_n^{12}H_n^3 & C_n^{11}G_n^3 & -C_n^{12}G_n^3 \\ l_{21}h_{n,3} & l_{22}h_{n,3} & l_{23}h_{n,3} & C_n^{21}H_n^3 & -C_n^{22}H_n^3 & C_n^{21}G_n^3 & -C_n^{22}G_n^3 \end{bmatrix} \quad (E.1)$$

$$[B_{02}]_{5 \cdot 91} = \sum_{n=1}^{13} \begin{bmatrix} 0 & 0 & 0 & 0 & 0 & 0 & 0 \\ 0 & 0 & 0 & 0 & 0 & 0 & 0 \\ l_{21}h_{n,1} & l_{22}h_{n,1} & l_{23}h_{n,1} & C_n^{21}H_n^1 & -C_n^{22}H_n^1 & C_n^{21}G_n^1 & -C_n^{22}G_n^1 \\ l_{31}h_{n,1} & l_{32}h_{n,1} & l_{33}h_{n,1} & C_n^{31}H_n^1 & -C_n^{32}H_n^1 & C_n^{31}G_n^1 & -C_n^{32}G_n^1 \\ l_{31}h_{n,2} & l_{32}h_{n,2} & l_{33}h_{n,2} & C_n^{31}H_n^2 & -C_n^{32}H_n^2 & C_n^{31}G_n^2 & -C_n^{32}G_n^2 \end{bmatrix} \quad (E.2)$$

where l$_{ij}$ are the direction cosines between the local and the global set of axes and are

given in appendix C. The functions C, h, H and G are defined by Equations 2.8, 2.42,

2.43 and 2.44, respectively. The sum of the above two matrices leads to the [B] matrix

used in the linear analysis of the consistent shell element.

The components of the matrix $[B_S]$ can be related to the components of the matrices in Equations E.1 and E.2 in the following manner:

$$[B_S]_{9 \cdot 91} = \begin{bmatrix} \text{First} & \text{row} & \text{of} & [B_{01}] \\ \text{Third} & \text{row} & \text{of} & [B_{02}] \\ \text{Fourth} & \text{row} & \text{of} & [B_{02}] \\ \text{Third} & \text{row} & \text{of} & [B_{01}] \\ \text{Second} & \text{row} & \text{of} & [B_{01}] \\ \text{Fifth} & \text{row} & \text{of} & [B_{02}] \\ \text{Fourth} & \text{row} & \text{of} & [B_{01}] \\ \text{Fifth} & \text{row} & \text{of} & [B_{01}] \\ l_{31}h_{n,3} & l_{32}h_{n,3} & l_{33}h_{n,3} & C_n^{31}H_n^3 \quad -C_n^{32}H_n^3 \quad C_n^{31}G_n^3 \quad -C_n^{32}G_n^3 \end{bmatrix} \qquad (E.3)$$

It should be noted that for the last row of the matrix $[B_S]$, n takes values from 1 to 13 to give the 91 columns of the $[B_S]$ matrix.

The components of the matrix $[B_L]$ can also be related to the components of the matrices $[B_{01}]$, $[B_{02}]$ and $[B_S]$ through the local initial strain terms $u'_{i,j}$ as follows:

$$[B_L]_{5 \cdot 91} = \begin{bmatrix} u'_{,x'}(\text{row 1 of } [B_{01}]) + v'_{,x'}(\text{row 3 of } [B_{02}]) + w'_{,x'}(\text{row 4 of } [B_{02}]) \\ \\ u'_{,y'}(\text{row 3 of } [B_{01}]) + v'_{,y'}(\text{row 2 of } [B_{01}]) + w'_{,y'}(\text{row 5 of } [B_{02}]) \\ \\ \begin{aligned} &u'_{,y'}(\text{row 1 of } [B_{01}]) + v'_{,y'}(\text{row 3 of } [B_{02}]) + W'_{,y'}(\text{row 4 OF } [B_{02}]) \\ &+ \\ &u'_{,x'}(\text{row 3 of } [B_{01}]) + v'_{,x'}(\text{row 2 of } [B_{01}]) + w'_{,x'}(\text{row 5 of } [B_{02}]) \end{aligned} \\ \\ \begin{aligned} &u'_{,z'}(\text{row 1 of } [B_{01}]) + v'_{,z'}(\text{row 3 of } [B_{02}]) + w'_{,z'}(\text{row 4 of } [B_{02}]) \\ &+ \\ &u'_{,x'}(\text{row 4 of } [B_{01}]) + v'_{,x'}(\text{row 5 of } [B_{01}]) + w'_{,x'}(\text{row 9 of } [B_S]) \end{aligned} \\ \\ \begin{aligned} &u'_{,z'}(\text{row 3 of } [B_{01}]) + v'_{,z'}(\text{row 2 of } [B_{01}]) + w'_{,z'}(\text{row 5 of } [B_{02}]) \\ &+ \\ &u'_{,y'}(\text{row 4 of } [B_{01}]) + v'_{,y'}(\text{row 5 of } [B_{01}]) + w'_{,y'}(\text{row 9 of } [B_S]) \end{aligned} \end{bmatrix}$$

(E.4)

The matrix $[B_L^{T\,(k-1)}]$ which is used to update the stiffness matrix $[K_L^{T\,(k-1)}]$ at the beginning of the kth iteration for the load increment corresponding to the time T, can be obtained by replacing the terms $(u'_{i,j})$ in Equation E.4 by the initial local strains for the kth iteration $(u'_{i,j}^{T\,(K-1)})$ which are derived in Section 2-5-3.

APPENDIX F

COMPRESSIVE STRENGTH OF THE EQUIVALENT

CYLINDER ACCORDING TO DIFFERENT CODES.

The maximum compressive strength of an equivalent cylinder σ_{cr} can be obtained, according to the Danish code DNV (1982) and the AWWA D100 (1984) specifications, by applying the following set of equations.

a) DNV Code

A geometric parameter M_{eq} is first calculated as

$$M_{eq} = \frac{l_{eq}}{\sqrt{r_{eq}t}} .$$

(F.1)

Based on the value of M_{eq} a buckling coefficient C_L and a knock-down factor ρ accounting for imperfections can be obtained from the following equations:

$$C_L = \begin{cases} 0.605 & \text{for } M_{eq} \geq 1.73 \\ \dfrac{0.904}{M^2_{eq}} + 0.1013 M^2_{eq} & \text{for } M_{eq} < 1.73 \end{cases}$$

(F.2)

$$\rho = \begin{cases} 0.35 - 0.0002\dfrac{r_{eq}}{t} & \text{for } M_{eq} \geq 4.58 \\ 0.76 - (0.615 + 0.00031\dfrac{r_{eq}}{t})\ \log M_{eq} & \text{for } M_{eq} < 4.58 \end{cases} .$$

(F.3)

The elastic buckling σ stress may then be calculated from

$$\sigma = \rho \, C_L E \left(\frac{t}{r_{eq}} \right) .$$ (F.4)

The compressive strength σ_{cr} can then be calculated as

$$\sigma_{cr} = \frac{\sigma_y}{\sqrt{1 + \lambda^4}}$$ (F.5)

where σ_y is the yield stress, E is Young's Modulus and λ is the reduced slenderness parameter given by

$$\lambda = \sqrt{\frac{\sigma_y}{\sigma}} .$$ (F.6)

b) AWWA D100-84 Specifications

According to AWWA D100 (1984) specifications, the maximum permissible compressive strength in psi of a cylinder can be calculated from the following equations:

$$\sigma_{cr} = XY$$ (F.7)

$$Y = \begin{cases} \frac{2}{3} \left(100 \frac{t}{r_{eq}} \right) \left[2 - \left(\frac{2}{3} \right) \left(100 \frac{t}{r_{eq}} \right) \right] & for \quad \frac{t}{r_{eq}} < 0.015 \\ 1.0 & for \quad \frac{t}{r_{eq}} \geq 0.015 \end{cases}$$ (F.8)

$$X = \frac{18000}{\left[1 + \frac{L^2_{eq}}{18000 \, r'^2_{eq}} \right]} \quad and \quad X \leq 15000 \; psi.$$ (F.9)

where L_{eq} and r'^2_{eq} are the effective length and the radius of gyration of the equivalent, respectively.

APPENDIX G

SOLUTION OF THE LAPLACIAN EQUATION

IN CYLINDRICAL COORDINATES

The impulsive component of the hydrodynamic pressure P_d ,developed inside a liquid-filled tank due to seismic excitation is governed by the Laplacian Equation, i.e.

$$\nabla^2 P_d = 0. \tag{G.1}$$

Using the separation of variables technique, the solution of the Laplacian Equation in the cylindrical coordinates (r,θ,z) is given by (for details see Haroun 1980)

$$P_d(r,\theta,z,T) = A_{in}(T)\cos(n\theta)\begin{Bmatrix} J_n(ir)\cosh(iz) \\ J_n(ir)\sinh(iz) \\ r^n z \\ r^n \\ I_n(ir)\cos(iz) \\ I_n(ir)\sin(iz) \end{Bmatrix} \tag{G.2}$$

where J_n and I_n are the Bessel's and the modified Bessel's functions of order n, respectively; i is a separation constant and n is the circumferential wave number. It should be noted that the terms in the solution to the Laplacian Equation, which lead to singularity at $r=0$, are not present in Equation G.2.

APPENDIX H

DERIVATION OF THE FLUID ADDED-MASS

MATRIX RESULTING FROM HORIZONTAL EXCITATION

The hydrodynamic pressure P_d resulting from a horizontal acceleration acting on a conical tank, as presented in Section 4-3-2-1, can be assumed as

$$P_d(r,\theta,z,T) = \sum_{i=1}^{N_1} A_{i1}(T) H_{i1}(r,\theta,z). \tag{H.1}$$

The functions H_{i1} are given by

$$H_{i1}(r,\theta,z) = I_1(\alpha_i r) \cos(\alpha_i z) \cos(\theta) \tag{H.2}$$

where $I_1(\alpha_i r)$ is the modified Bessel's function of the first kind, $\alpha_i = (2i-1)\pi/(2h)$, and h is the height of the fluid in the vessel.

Following the procedure described in Section 4-3-1, the variational function for the dynamic fluid pressure is given by

$$J = \int_{t_1}^{t_2} [\frac{1}{2} \int_{S_1} P_d \frac{\partial P_d}{\partial n} ds + \int_{S_1} \rho_F \underline{\ddot{u}}^T \underline{n} P_d ds] dt \tag{H.3}$$

where surface S_1 is as shown in Figure 4.8 and n is the unit outward normal to the surface.

The first term on the R.H.S of Equation H.3 can be written as

239

$$\frac{1}{2} \int_{S_i} P_d \frac{\partial P_d}{\partial n} \, ds = \frac{1}{2} \{A_{il}(T)\}_{1 \cdot N_i}^{Trans} [C^*]_{N_i \cdot N_i} \{A_{il}(T)\}_{N_i \cdot 1} \tag{H.4}$$

where

$$C_{ij}^* = \int_{S_i} H_{il} \frac{\partial H_{jl}}{\partial n} \, ds. \tag{H.5}$$

The derivative $\partial H_{jl}/\partial n$ can be evaluated using the chain rule as follows:

$$\frac{\partial H_{jl}}{\partial n} = \frac{\partial H_{jl}}{\partial r} \frac{\partial r}{\partial n} + \frac{\partial H_{jl}}{\partial z} \frac{\partial z}{\partial n} \tag{H.6}$$

For conical tanks, $(\partial r/\partial n)$ and $(\partial z/\partial n)$ are equal to $(\cos \theta_v)$ and $(-\sin \theta_v)$, respectively, where θ_v is the angle of inclination of the generator of the tank with the vertical direction. The derivatives $(\partial H_{jl}/\partial r)$ and $(\partial H_{jl}/\partial z)$ can be obtained from Equation H.2. The derivatives above are substituted into Equation H.6 which leads to

$$\frac{\partial H_{jl}}{\partial n} = \alpha_i I_1'(\alpha_i r) \cos(\alpha_i z) \cos(\theta) \cos(\theta_v) + \alpha_i I_1(\alpha_i r) \sin(\alpha_i z) \cos(\theta) \sin(\theta_v). \tag{H.7}$$

Equations H.2 and H.6 are then substituted into Equation H.5, and the integration is performed by discretizing the surface S_1 using triangular elements and the Gaussian quadratic scheme for numerical integration to obtain components of the matrix $[C^*]_{N1 \cdot N1}$. Note that $[C^*]$ is a symmetric full matrix. It is also pointed out here that 79 Gaussian integration points are used to achieve the numerical integration. This integration order insures an accurate numerical integration of polynomials of the 20th degree and is found to be sufficient for the discretization employed.

The second integral I on the R.H.S of Equation H.3 is given by

$$I = \int_{S_1} \rho_F \, p_d \, \underline{\ddot{u}} \cdot \underline{n} \, ds. \tag{H.8}$$

The rotatory inertia is neglected and the acceleration $\underline{\ddot{u}}^T$ at any point on the surface S_1 is approximated using the cubic interpolation functions $\overline{N}$ of the consistent shell element to give:

$$I = \rho_F \sum_{i=1}^{N_1} A_{il} \, (T) \sum_{Elem} \int_{SEL} H_{il}(r,\theta,z) \, \{n^*\}_{1 \bullet 39}^{Trans} \, dS \, \{\overline{U}^T\}_{39 \bullet 1} \tag{H.9}$$

where

$$\{n^*\}^{Trans} = \{\, l_{31} \quad l_{32} \quad l_{33} \quad \cdot \quad \cdot \quad \cdot \quad l_{31} \quad l_{32} \quad l_{33} \,\} \tag{H.10}$$

$$\{\overline{U}\}^{Trans} = \{\, \overline{N}_1 \ddot{U}_1^T \quad \overline{N}_1 \ddot{V}_1^T \quad \overline{N}_1 \ddot{W}_1^T \quad \cdot \quad \cdot \quad \cdot \quad \overline{N}_{13} \ddot{U}_{13}^T \quad \overline{N}_{13} \ddot{V}_{13}^T \quad \overline{N}_{13} \ddot{W}_{13}^T \,\} \tag{H.11}$$

l_{3i} are the direction cosines of the unit outward normal to the surface; Elem is the number of consistent shell elements and SEL is the area of each shell element used to discretize the surface S_1.

Substituting Equations H.4 and H.9 into Equation H.3 and taking the first derivative with respect to the amplitude function $A_{il}(T)$ gives the following:

$$\{\, A_{il}(T) \,\}_{N_1 \bullet 1} = -\rho_F \, [C^*]_{N_1 \bullet N_1}^{-1} \sum_{Elem} [F]_{N_1 \bullet 39} \, \{\ddot{U}^T\}_{39 \bullet 1} \tag{H.12}$$

where matrix $[F]_{N1 \bullet 39}$ is given by

$$[F_{N_i \bullet 39}] = \begin{bmatrix} \int_{SEL} \bar{N}_1 l_{31} H_{11} ds & \int_{SEL} \bar{N}_1 l_{32} H_{11} ds & \int_{SEL} \bar{N}_1 l_{33} H_{11} ds & \cdots & \cdots & \cdots & \cdots \\ \cdots & \cdots & \cdots & \cdots & \cdots & \cdots & \cdots \\ \cdots & \cdots & \cdots & \cdots & \cdots & \cdots & \cdots \\ \cdots & \cdots & \cdots & \cdots & \cdots & \cdots & \cdots \\ \int_{SEL} \bar{N}_1 l_{31} H_{N_i 1} ds & \int_{SEL} \bar{N}_1 l_{32} H_{N_i 1} ds & \int_{SEL} \bar{N}_1 l_{33} H_{N_i 1} ds & \cdots & \cdots & \cdots & \cdots \end{bmatrix}$$

$$\begin{bmatrix} \cdots & \cdots & \cdots & \cdots & \int_{SEL} \bar{N}_{13} l_{31} H_{11} ds & \int_{SEL} \bar{N}_{13} l_{32} H_{11} ds & \int_{SEL} \bar{N}_{13} l_{33} H_{11} ds \\ \cdots & \cdots & \cdots & \cdots & \cdots & \cdots & \cdots \\ \cdots & \cdots & \cdots & \cdots & \cdots & \cdots & \cdots \\ \cdots & \cdots & \cdots & \cdots & \cdots & \cdots & \cdots \\ \cdots & \cdots & \cdots & \cdots & \int_{SEL} \bar{N}_{13} l_{31} H_{N_i 1} ds & \int_{SEL} \bar{N}_{13} l_{32} H_{N_i 1} ds & \int_{SEL} \bar{N}_{13} l_{33} H_{N_i 1} ds \end{bmatrix}$$

$$\text{(H.13)}$$

and $\{\ddot{U}^T\}_{39 \bullet 1}$ is the vector which includes the accelerations of the nodal displacements of the shell element (excluding the rotational degrees of freedom). The integration of the components of the matrix [F] is also carried out numerically using the 79 Gaussian integration points.

It is important to note that before carrying the multiplication $[C^-]^{-1} \Sigma[F]$, the matrices $[F]_{N1 \bullet N1}$ of all elements on the surface S_1 have to be assembled into the global matrix $[F_1]$, i.e.

$$[F_1]_{N_1 \bullet M} = \sum_{Elem} [F]_{N_1 \bullet 39} \qquad \text{(H.14)}$$

where M is the total number of degrees of freedom due to the shell elements employed

to discretize surface S_1.

Let the matrix $[F^*]$ result from performing the multiplication $\rho_F [C^*]^{-1} [F_1]$, i.e

$$[F^*]_{N_1 \bullet M} = \rho_F [C^*]^{-1}_{N_1 \bullet N_1} [F_1]_{N_1 \bullet M} \qquad \text{(H.15)}$$

Then, in view of Equations H.1, H.12 and H.15, the hydrodynamic pressure on any

point on the surface of the tank is given by

$$P_d(r,\theta,z,T) = - \{H(T)\}^{TRANS}_{1 \bullet N_1} [F^*]_{N_1 \bullet M} \{\ddot{U}_1^T\}_{M \bullet 1} \qquad \text{(H.16)}$$

where

$$\{H(T)\}^{TRANS} = \{ H_{11}(T) \quad H_{21}(T) \quad . \quad . \quad . \quad H_{N_1 1}(T) \} \qquad \text{(H.17)}$$

and the vector $\{ \ddot{U}_1^T \}$ is the global vector which includes the acceleration of all degrees

of freedom of the surface (excluding the rotational degrees of freedom). Now the virtual

work $V_{(i}$, by the hydrodynamic pressure can be obtained as follows:

$$V_M = \sum_{Elem} \int_{SEL} P_d(r,\theta,z,T) \sum_{i=1}^{13} \bar{N}_i \{\delta(\Delta \underline{U})\} . \underline{n} \, ds \qquad \text{(H.18)}$$

or

$$V_M = \sum_{Elem} \{\delta \Delta U \}^{TRANS}_{1 \cdot 39} \int_{SEL} \{G\}_{39 \cdot 1} \{H(T)\}^{TRANS}_{1 \cdot N_1} [F^*]_{N_1 \cdot M} \, dS \{ \bar{U}_1 \}_{M \cdot 1} \, ds \qquad \text{(H.19)}$$

where

$$\{\delta(\Delta U)\}^{TRANS}_{1 \cdot 39} = \{\delta(\Delta U_1) \quad \delta(\Delta V_1) \quad \delta(\Delta W_1) \quad . \quad \delta(\Delta U_{13}) \quad \delta(\Delta V_{13}) \quad \delta(\Delta W_{13})\} \qquad \text{(H.20)}$$

$$\{G\}^{TRANS}_{1 \cdot 39} = \{ \bar{N}_1 l_{31} \quad \bar{N}_1 l_{32} \quad \bar{N}_1 l_{33} \quad . \quad . \quad . \quad \bar{N}_{13} l_{31} \quad \bar{N}_1 l_{32} \quad \bar{N}_{13} l_{33} \}. \qquad \text{(H.21)}$$

From Equation H.19, it can be concluded that the fluid added-mass $[DM]_H$ is given by

$$[DM]_H = \sum_{Elem} \int_{SEL} \{G\}_{39 \cdot 1} \{H(T)\}^{TRANS}_{1 \cdot N_1} [F^*]_{N_1 \cdot M} \, ds. \qquad \text{(H.22)}$$

After having evaluated $[F^*]_{N1 \cdot M}$ using Equation H.15, it is substituted into Equation H.22. The integration is again carried out numerically using the 79 Gaussian integration points. It is important to note here that the added-mass matrix $[DM]_H$ can be obtained only globally and, furthermore, it is a fully populated matrix.

APPENDIX I

DERIVATION OF THE FLUID ADDED-MASS

MATRIX RESULTING FROM VERTICAL EXCITATION

The hydrodynamic pressure P_d resulting from a vertical acceleration acting on a conical tank, as presented in Section 4-3-3-1, can be assumed as

$$P_d(r,\theta,z,T) = \sum_{i=1}^{N_1} A_{i0}(T) H_{i0}(r,z) + B(t) H^*(z). \tag{I.1}$$

The functions H_{i0} and H^* are given by

$$H_{i0}(r,z) = I_0(\alpha_i r) \cos(\alpha_i z) \quad , \quad H^*(z) = (z-h) \tag{I.2}$$

where $I_0(\alpha_i r)$ is the modified Bessel's function of the first kind, $\alpha_i = (2i-1)\pi/(2h)$, and h is the height of the fluid inside the tank.

Following the procedure described in Appendix H, the fluid added-mass matrix $[DM]_V$ due to vertical acceleration is given by

$$[DM]_V = \sum_{Elem} \int_{SEL} \{G\}_{39 \cdot 1} \{H^*\}_{1 \cdot N_1}^{TRANS} [F^*]_{N_1 \cdot M} \, ds \tag{I.3}$$

where $N_2 = N_1 + 1$; the vector $\{G\}$ is as given in Equation H.21; Elem is the number of consistent shell elements and SEL is the area of each shell element used to discretize the surfaces S_1 and S_2 (see Figure 4.8). The vector $\{H\}^{TRANS}$ and the matrix $[F^*]$ are as follows:

245

$$\{H^{\substack{TRANS}}\}_{1 \cdot N_2} = \{ H_{10}(T) \quad H_{20}(T) \quad . \quad . \quad . \quad H_{N_10}(T) \quad H^{\bullet}(T) \} \tag{1.4}$$

$$[F^{\bullet}]_{N_2 \cdot M} = \rho_F [C^{\bullet}]^{-1}_{N_2 \cdot N_2} [F_1]_{N_2 \cdot M} \tag{1.5}$$

where

$$[F_1]_{N_2 \cdot M} = \sum_{Elem} [F]_{N_2 \cdot 39} . \tag{1.6}$$

and the matrix $[F]_{N2 \cdot 39}$ is of the following form:

$$[F]_{N_1 \cdot 39} = \begin{bmatrix} \int_{SEL} \bar{N}_1 l_{31} H_{10} ds & \int_{SEL} \bar{N}_1 l_{32} H_{10} ds & \int_{SEL} \bar{N}_1 l_{33} H_{10} ds & \cdots & \cdots & \cdots & \cdots \\ \cdots & \cdots & \cdots & \cdots & \cdots & \cdots & \cdots \\ \cdots & \cdots & \cdots & \cdots & \cdots & \cdots & \cdots \\ \cdots & \cdots & \cdots & \cdots & \cdots & \cdots & \cdots \\ \int_{SEL} \bar{N}_1 l_{31} H_{N_1 0} ds & \int_{SEL} \bar{N}_1 l_{32} H_{N_1 0} ds & \int_{SEL} \bar{N}_1 l_{33} H_{N_1 0} ds & \cdots & \cdots & \cdots & \cdots \\ \int_{SEL} \bar{N}_1 l_{31} H^{\cdot} ds & \int_{SEL} \bar{N}_1 l_{32} H^{\cdot} ds & \int_{SEL} \bar{N}_1 l_{33} H^{\cdot} ds & \cdots & \cdots & \cdots & \cdots \end{bmatrix}$$

$$\begin{bmatrix} \cdots & \cdots & \cdots & \cdots & \int_{SEL} \bar{N}_{13} l_{31} H_{10} ds & \int_{SEL} \bar{N}_{13} l_{32} H_{10} ds & \int_{SEL} \bar{N}_{13} l_{33} H_{10} ds \\ \cdots & \cdots & \cdots & \cdots & \cdots & \cdots & \cdots \\ \cdots & \cdots & \cdots & \cdots & \cdots & \cdots & \cdots \\ \cdots & \cdots & \cdots & \cdots & \cdots & \cdots & \cdots \\ \cdots & \cdots & \cdots & \cdots & \int_{SEL} \bar{N}_{13} l_{31} H_{N_1 0} ds & \int_{SEL} \bar{N}_{13} l_{32} H_{N_1 0} ds & \int_{SEL} \bar{N}_{13} l_{33} H_{N_1 0} ds \\ \cdots & \cdots & \cdots & \cdots & \int_{SEL} \bar{N}_{13} l_{31} H^{\cdot} ds & \int_{SEL} \bar{N}_{13} l_{32} H^{\cdot} ds & \int_{SEL} \bar{N}_{13} l_{33} H^{\cdot} ds \end{bmatrix} \quad (I.7)$$

where $\bar{N}_n$ are the cubic interpolation functions for the shell element; l_{3i} are the direction cosines of the unit vector normal to the surface and M is the global number of degrees of freedom of the shell elements (excluding the rotational degrees of freedom)

The matrix $[C^{\cdot}]_{N2 \cdot N2}$ is partitioned in the following way:

$$[C^{\cdot}]_{N_1 \cdot N_1} = \begin{bmatrix} [C^{11}]_{N_1 \cdot N_1} & [C^{12}]_{N_1 \cdot 1} \\ [C^{21}]_{1 \cdot N_1} & [C^{22}]_{1 \cdot 1} \end{bmatrix} \quad (I.8)$$

where

$$C_{ij}^{11} = \int_S H_{io} \frac{\partial H_{jo}}{\partial n} ds \qquad (I.9)$$

$$C_{ij}^{12} = C_{ji}^{21} = \int_S H_{io} \frac{\partial H^*}{\partial n} ds \qquad (I.10)$$

$$C^{22} = \int_S H^* \frac{\partial H^*}{\partial n} ds \qquad (I.11)$$

S is the sum of the surfaces S_1 and S_2 shown in Figure 4.8 and n is the unit outward normal to the surface.

The derivatives of the functions H_{io} and H^* with respect to the normal direction n are obtained by following the same procedure described in Appendix H to give

$$\frac{\partial H_{io}}{\partial n} = \alpha_i I_0'(\alpha_i r) \cos(\alpha_i z) \cos(\theta_v) + \alpha_i I_0(\alpha_i r) \sin(\alpha_i z) \sin(\theta_v) \qquad (I.12)$$

$$\frac{\partial H^*}{\partial n} = - \sin(\theta_v) \qquad (I.13)$$

where θ_v is the angle of inclination of the generator of the tank with the vertical direction.

Note that when the integration of Equations I.9 to I.11 is carried out over the surface S_2, θ_v is replaced by zero in Equations I.12 and I.13.

In the above formulation, all integrations are carried out numerically, using 79 Gaussian integration points within the triangular elements used to discretize surfaces S_1 and S_2.